12-2010

Experimental and computational analysis of an energy storage composite ankle foot orthosis

Michelle C. Hawkins
University of Nevada, Las Vegas

EXPERIMENTAL AND COMPUTATIONAL ANALYSIS OF AN ENERGY STORAGE COMPOSITE ANKLE FOOT ORTHOSIS

by

Michelle Cameron Hawkins

Bachelor of Science
University of Nevada, Las Vegas
2001

Master of Science
University of Nevada, Las Vegas
2003

A dissertation submitted in partial fulfillment
of the requirements for the

Doctor of Philosophy in Mechanical Engineering
Department of Mechanical Engineering
Howard R. Hughes College of Engineering

Graduate College
University of Nevada, Las Vegas
December 2010

UNLV
UNIVERSITY OF NEVADA LAS VEGAS

THE GRADUATE COLLEGE

We recommend the dissertation prepared under our supervision by

Michelle Cameron Hawkins

entitled

Experimental and Computational Analysis of an Energy Storage Composite Ankle Foot Orthosis

be accepted in partial fulfillment of the requirements for the degree of

Doctor of Philosophy in Mechanical Engineering

Brendan O'Toole, Committee Co-Chair

Edward Neumann, Committee Co-Chair

Mohamed Trabia, Committee Member

Woosoon Yim, Committee Member

Janet Dufek, Graduate Faculty Representative

Ronald Smith, Ph. D., Vice President for Research and Graduate Studies
and Dean of the Graduate College

December 2010

ABSTRACT

Experimental and Computational Analysis of an Energy Storage Composite Ankle Foot Orthosis

by

Michelle Cameron Hawkins

Dr. Edward Neumann, Examination Committee Co-Chair
Professor of Civil Engineering
University of Nevada, Las Vegas

Dr. Brendan O'Toole, Examination Committee Co-Chair
Associate Professor of Mechanical Engineering
University of Nevada, Las Vegas

Ankle Foot Orthotics (AFOs) are used by individuals presenting with Charcot-Marie-Tooth (CMT) to assist with improving gait. Mitch Warner, CPO, has developed a composite AFO made from woven carbon-Kevlar and carbon fiber lamina. The overall goals of the research are to characterize the HELIOS brace and to determine its effect on the gait of CMT subjects. Human motion analysis, experimental mechanical testing, and Finite Element Analysis (FEA) are used to gain a better understanding of how the materials and geometric design of the HELIOS AFO contribute to gait.

Human motion experiments are performed to determine the relationship between ground reaction forces and strain measurements. Experimental mechanical tests replicate brace deformation observed during the gait study and provide the force applied to the brace to produce the measured strains during the human tests. In addition, the amount of energy storage and return can be calculated from the force vs. displacement curves of the experimental tests. An FEA model is developed to determine how the materials can affect the energy storage properties.

ACKNOWLEDGEMENTS

Thank you to my advisors, Dr. Edward Neumann and Dr. Brendan O'Toole for the countless hours provided to assist me in producing my best work. I would also like to thank my committee members, Dr. Mohamed Trabia, Dr. Woosoon Yim, and Dr. Janet Dufek for agreeing to be on my committee and reading over my work. Appreciation is extended to the Hereditary Neuropathy Foundation, Ortho Rehab Designs of Las Vegas, and the Applied Research Initiatives Program at UNLV for funding the project. A special thank you is extended to Mitch Warner, CPO, of Ortho Rehab Designs for providing the opportunity to analyze the HELIOS braces as well as fabricating duplicate sets of the braces that were used for instrumentation.

Thank you to all of my friends and fellow graduate students for assisting me during times of need. Thanks to Dave DeLion and Dana Forrest for assistance with human motion capture. Thanks to Richard Jennings for assistance with AFO instrumentation and photography. Thanks to Sean Sheehan for the hours you devoted to helping me with AFO instrumentation. I am very thankful to Jeff Markle for his assistance with AFO instrumentation data collection and experimental testing. Thanks to Thomas Higgins for assistance with AFO instrumentation and scanning all eight instrumented braces. Thanks to Jason Mulvey for providing some good insights. Thanks to Stan Brewster for allowing me to take time off from work to finish my dissertation. Thanks to Stacy Nelson and Jagadeep Thota for assisting with finite element analysis.

Many things can happen in the span of six years: starting a new job, buying a car, buying a house, having a baby, earning a dissertation. I venture to guess that very few people decide to do it all at once. One of my friends told me that I was an overachiever. I

never really thought of myself this way, just that I was a hard worker. A lot of blood, sweat, and tears went into the making of what is now a 235 page document. I have a lot of family and friends in my life to thank for my success. I would not be the person I am today without their help and understanding.

I hope that one day my son Logan will learn to appreciate the value of life long learning. I will most likely remind him always of the increasing challenges I faced attempting to draft my dissertation while taking care of a newborn. Having experienced both, I can now say that a dissertation is almost like having a child. I would also like to thank my husband Edward for providing me with much love and support throughout the last thirteen years. You have always told me that you fully support my educational pursuits. I really do appreciate all that you do for me.

TABLE OF CONTENTS

LIST OF FIGURES

LIST OF TABLES

CHAPTER 1

INTRODUCTION

1.1 Purpose of Study

The HELIOS, an advanced composite carbon fiber/epoxy ankle-foot-orthotic (AFO) developed by Ortho Rehab Designs, aids patients with drop foot to improve gait. Foot drop is a common symptom of Charcot-Marie-Tooth (CMT) syndrome, which is a hereditary neuropathy disease [1] that has no cure. Affected people experience nerve degeneration and weakened muscles, resulting in loss of normal use of the extremities.

An interdepartmental collaboration at the University of Nevada, Las Vegas was formed between the Mechanical Engineering and Kinesiology departments to analyze the HELIOS in a series of experiments. Funded by the Hereditary Neuropathy Foundation, Ortho Rehab Designs of Las Vegas, and a grant from the Applied Research Initiatives Program, the goals of the research were to measure and characterize the effect that the HELIOS has on the gait of individuals with CMT, and to develop a finite element model of the HELIOS that could be used to explain the performance of the HELIOS and examine the role that its materials and geometric design features play in its performance. Successful accomplishment of these goals will contribute to the understanding of how the effectiveness of orthotic interventions can be improved for individuals with CMT.

1.2 Research Questions/ Objectives

- Question 1: Which biomechanical characteristics of gait are improved when the HELIOS is worn? Objective 1: Determine the improvement in gait when patients are wearing the HELIOS brace by collecting and comparing data on the gait and

ground reaction forces (GRF) of CMT patients when wearing the HELIOS brace and when walking unbraced.

- Question 2: How does strain in the brace relate to ground reaction force? Objective 2: Measure strain in the HELIOS when it is worn by CMT patients and determine the relationship between measured strain values and ground reaction force.
- Question 3: What forces are input to the brace to produce the measured strains? Objective 3: Perform mechanical testing of the brace to collect data on force, strain, and displacement. Determine the laboratory test machine loading condition that is needed to replicate brace deformation observed during human motion study. This will show approximately how much force the subject is placing on the brace during gait.
- Question 4: What amount of energy storage and return occurs during gait? Objective 4: Use the mechanical testing of the brace to determine the extent to which the brace is acting as an energy storing and releasing device by calculating energy storage, energy release, and energy dissipated.
- Question 5: How will changing the types of materials used in the HELIOS alter its energy storing characteristics? Objective 5: Develop and validate a finite element analysis (FEA) model of the brace, and use the model to examine how alteration of brace material properties could affect energy exchanges between the brace and the individual.

1.3 Study Procedures and Methodology

Several different types of testing and analysis were performed and combined to create an overall understanding of the HELIOS brace. The flowchart shown in Figure 1.1 shows these different phases of data collection and how they are related.

Gait data were collected at the Sports Injury Research Center (SIRC) at the University of Nevada, Las Vegas (UNLV). A 12 camera motion capture system was used to collect kinematics data and two floor mounted force plates were used to obtain ground reaction force data. Eight of the subjects were CMT patients and one was a normal individual not diagnosed with CMT. Since CMT affects individuals differently and is asymmetric [1], which means a single patient could have different degrees of degeneration in the left leg versus the right leg, the 'normal' subject allowed comparison between a healthy individual and one who has CMT. Data were collected during the human motion tests to provide the ground reaction forces and gage strain data from the HELIOS braces. These data were used to determine if the gait of individual subjects was improved by wearing the braces and also yields the relationship between gait and the strain seen in the brace.

Three of the CMT subjects and the one normal subject were provided braces instrumented with strain gages to analyze and relate the deformation of the AFO to gait. These instrumented braces were also used in experimental tests using an axial compression/tension machine to analyze the relationship between force, strain, and displacement. The mechanical performance of the brace was better understood by completing experimental mechanical testing of the braces. This testing allowed the determination of the forces and displacements applied to the brace that produce the

measured strains seen during gait. Ultimately, the human motion testing and mechanical testing were combined to provide the relationship between gait, gage strain, pretibial force, and pretibial displacement. The mechanical testing also allowed the calculation of energy storage of the brace.

The mechanical test data can then be used to validate a finite element (FE) model of the HELIOS brace. A 3D scanner was used to transfer the geometry of the brace used in human testing into a digitized form for analysis. The FE model allowed a greater understanding of the energy storage characteristics by being able to change the brace materials.

The experimental data and computational models of the braces can be used to quantify which aspects of the brace are most relevant to improving gait. A fundamental understanding of this may help improve the design process and material selection process for future CMT patients.

1.4 Paper Format

This dissertation consists of six chapters. Chapter 1 provides an introduction to the thesis including detail on research objectives, study procedures, and methodology. Chapter 2 includes background information on gait analysis, and material properties and springs. It also includes a review of related literature on AFO design, AFO experimental work, and materials used in AFO fabrication. The third chapter presents procedures and results for human motion testing. Chapter 4 presents procedures and results for experimental mechanical testing of the HELIOS braces. A discussion of FEA analysis

and results which include effects of materials is provided in Chapter 5. Finally, conclusions are supplied in Chapter 6.

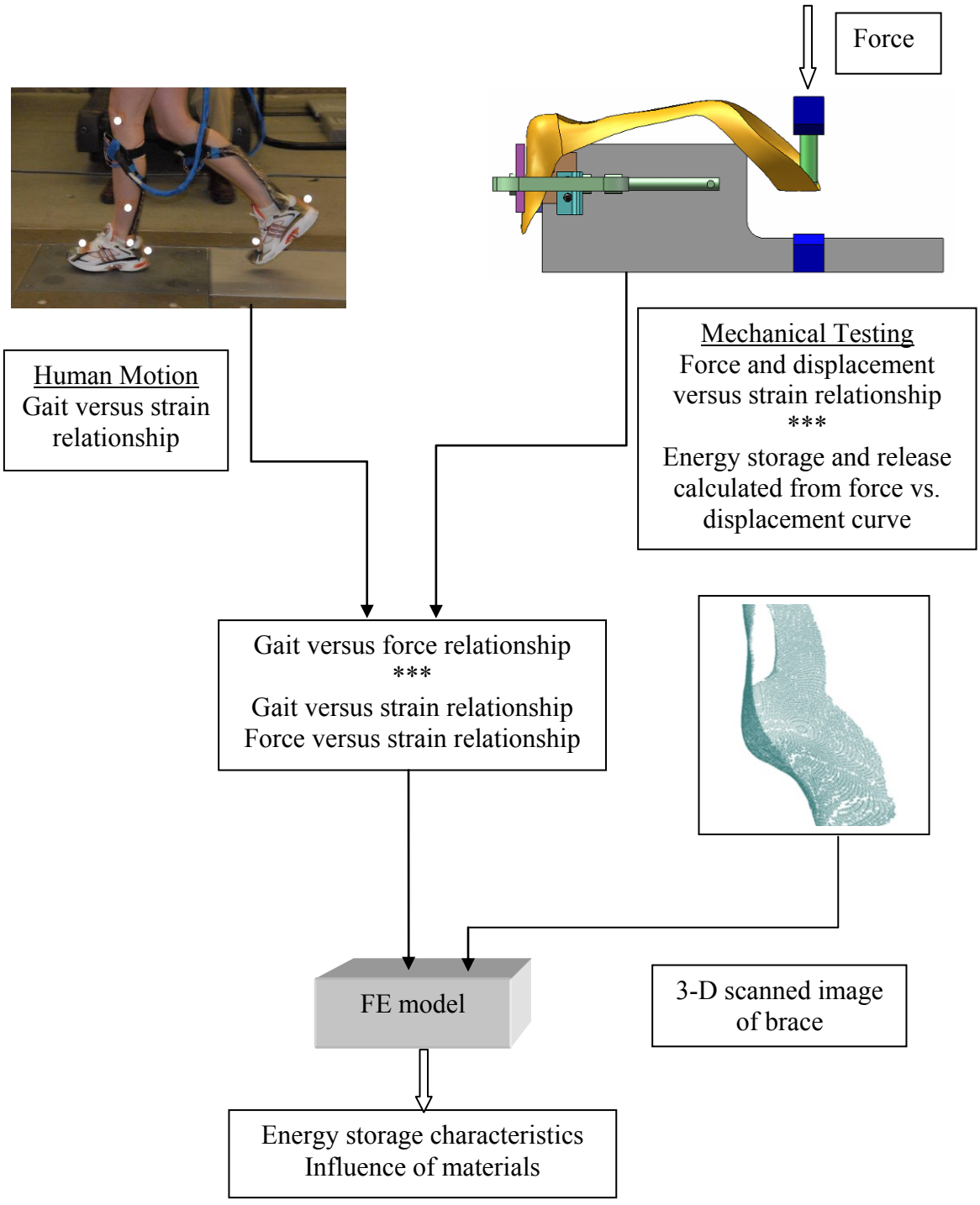

Figure 1.1: Research flowchart

CHAPTER 2

REVIEW OF RELATED LITERATURE

2.1 Gait Analysis Background

A human motion study allows for the collection of gait kinematics which includes joint angles, linear and angular displacements, velocities, and accelerations [2]. These kinematics variables can then be used in conjunction with the ground reaction forces (GRF) to calculate from inverse dynamics the gait kinetics which includes joint torques and powers [2].

The gait cycle is defined as the movement of one leg through a stride. The gait cycle can be divided into two phases, the stance phase and the swing phase. The stance phase occurs at initial contact of the heel, termed Heel Contact (HC), and ends as the toe of the same leg leaves the ground, termed Toe Off (TO). On average, the stance phase represents 60% of the gait cycle and the swing phase represents 40% of the gait cycle. The stance and swing phases can be further separated into several phases as shown in Figure 2.1 [3].

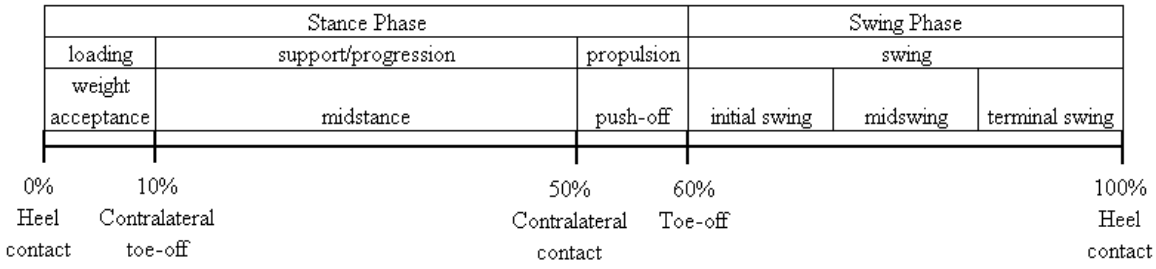

Figure 2.1: Gait cycle [3]

The ground reaction force of the stance phase is typically separated into three components: vertical (F_z), anterior-posterior shear (F_y), and medial-lateral shear (F_x) as shown in Figure 2.2. The vertical force is created due to the weight of the individual plus the vertical acceleration of that individual's center of mass. The shear forces are created due to friction between the foot and the force platform [3].

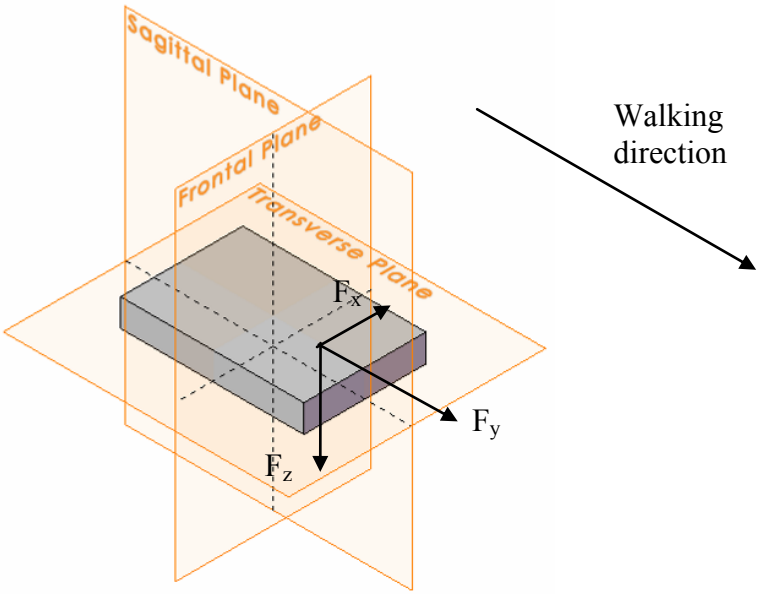

Figure 2.2: Force plate force definitions of F_z, F_y, and F_x

The three ground reaction forces for a typical healthy individual are shown in Figure 2.3. Several key variables can be taken from the graph which includes those listed in Table 2.1. Typical values for some of these variables are shown in Table 2.2.

The walking speed can alter the GRF curve; an increase in walking speed tends to increase the force of the F_1 peak and decrease the force of the F_{min} peak on the F_z GRF curve [3]. An increase in walking speed also tends to increase the braking (F_{yb}) and propulsive (F_{yp}) peaks on the F_y GRF curve [3].

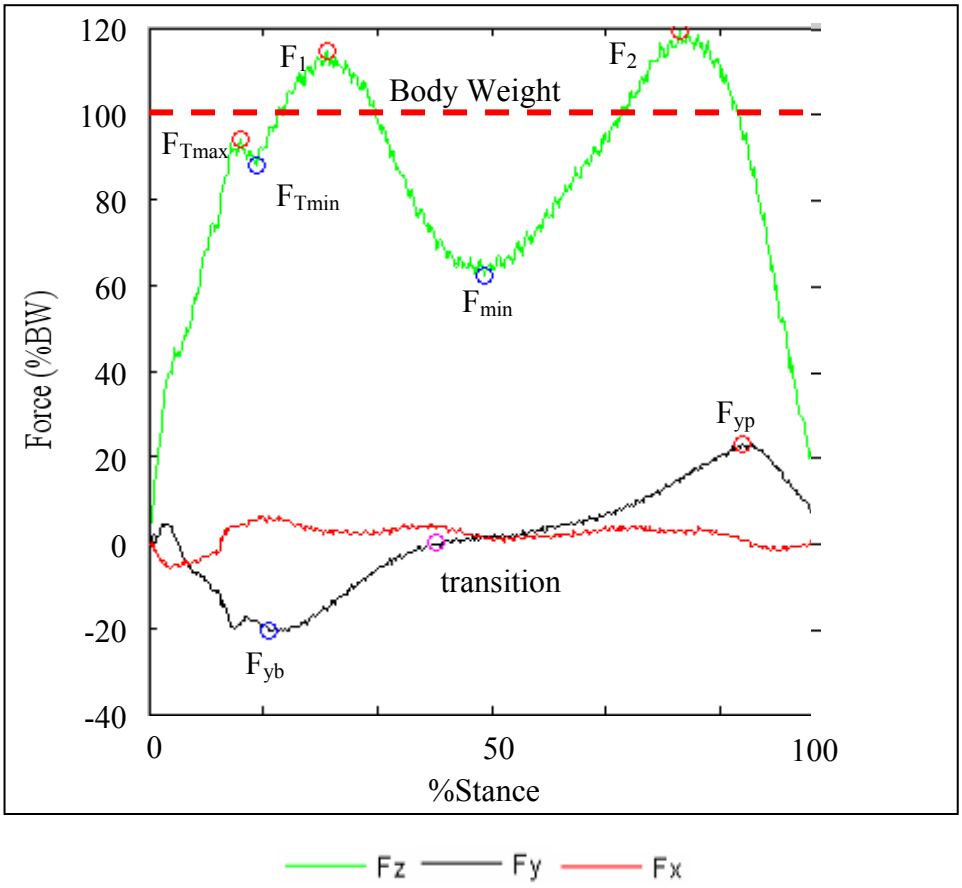

Figure 2.3: Typical ground reaction force (GRF) curves with key variables

Table 2.1: GRF variables [3]

Variable	Definition
stance time	entire stance phase time from HC to TO
F_1	peak of F_z during braking
t_1	time to reach F_1
F_2	peak of F_z during propulsion
t_2	time to reach F_2
F_{min}	force at midstance
t_{min}	time to reach F_{min}
F_{Tmax}	heel-strike transient (typically 10% BW)
t_{Tmax}	time to reach F_{Tmax}
F_{Tmin}	force after heel-strike transient
t_{Tmin}	time to reach F_{Tmin}
F_{yb}	peak of F_y during braking
t_{yb}	time to reach F_{yb}
F_{yp}	peak of F_y during propulsion
t_{yp}	time to reach F_{yp}
transition time	time for F_y to reach zero force

Table 2.2: Typical values for normal gait [4]

Force (%BW)		Time (%Stance)	
Variable	Mean ± 1Standard Deviation	Variable	Mean ± 1Standard Deviation
F_1	117 ± 9	t_1	23 ± 2
F_2	75 ± 6	t_2	48 ± 3
F_{min}	109 ± 5	t_{min}	76 ± 2
F_{yb}	-19 ± 3	t_{yb}	17 ± 2
F_{yp}	22 ± 3	t_{yp}	86 ± 2

2.2 Background of Mechanical Properties and Mechanical Springs

It is common to classify a material based on the material's stress-strain curve. The curve is created by testing a piece of material in compression or tension at a constant rate. The force and displacement are recorded and then the stress of the material is calculated using Eq 2.1 and the strain is calculated using Eq 2.2. Most materials can be assumed to be linear-elastic and exhibit a linear stress-strain curve at the beginning of loading. The modulus of elasticity or Young's modulus is defined as the initial slope in the linear elastic portion of the stress-strain curve as shown in Figure 2.4(a). The modulus is calculated as the stress divided by the strain of the linear portion of the stress-strain curve [5].

$$\sigma = \frac{F}{A}, \qquad \text{(Eq 2.1)}$$

where F is the recorded force and A is the cross sectional area

$$\varepsilon = \frac{\Delta L}{L}, \qquad \text{(Eq 2.2)}$$

where ΔL is the change in length and L is the original length

The force-displacement curve can be used to calculate the spring constant by dividing the force by the displacement of the linear portion of the curve as shown in Figure 2.4(b). The spring constant describes the stiffness of the spring. If the spring constant is large, then the spring is considered a hard spring. If the spring constant is small, then the spring is considered a soft spring. Also, if stretched far enough, a linear spring could show a non-linear curve before the spring yields as shown in Figure 2.5 [6].

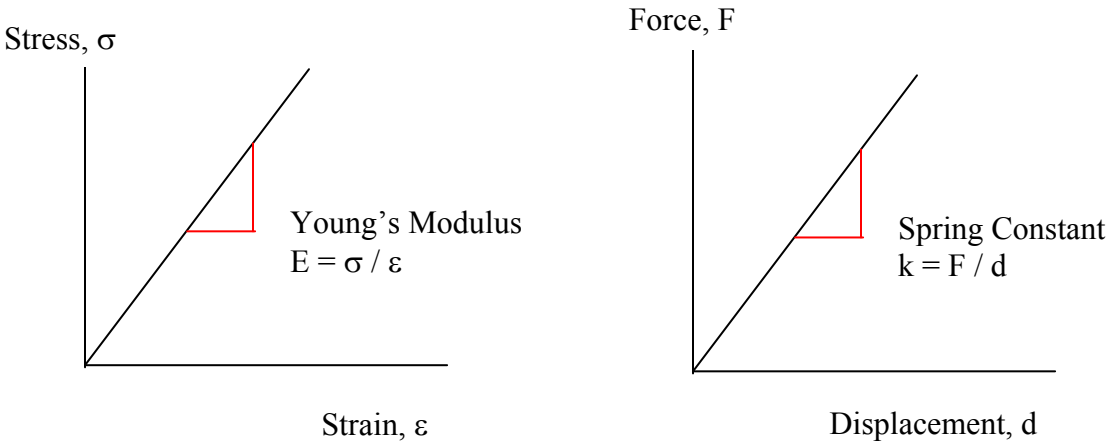

Figure 2.4: Linear-elastic (a) stress-strain curve (b) force-displacement curve

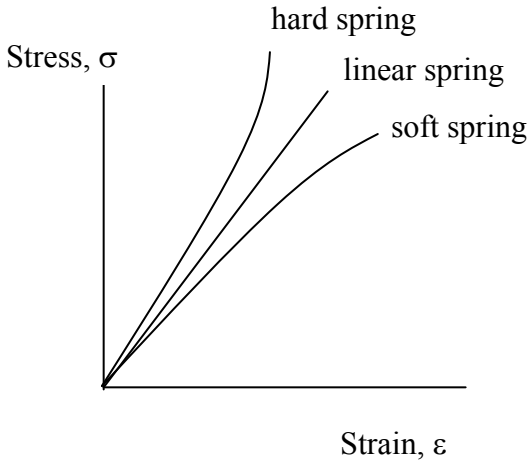

Figure 2.5: Nonlinear and linear hard and soft springs [6]

The area under the stress-strain curve is the "work done on the materials to elongate them or the restoring force within the materials" and is defined as the modulus of resilience [7]. The work done, W, to deform a spring can be calculated using Eq 2.3. The energy, e, to perform the work (elastic energy or strain energy) can be calculated as the area under the load-displacement curve and can also be calculated using Eq 2.4.

$$W = F \cdot d, \quad \text{(Eq 2.3)}$$

where F is the force used to displace the material a perpendicular distance d

$$e = \tfrac{1}{2} \cdot F \cdot d = \tfrac{1}{2} \cdot k \cdot d^2, \quad \text{(Eq 2.4)}$$

where F is force, d is perpendicular distance, and k is spring constant

Materials and springs that are linear-elastic, load and unload with the same force displacement profile as shown in Figure 2.6(a). The work used to deform the spring (shown in green) is stored as potential energy and is the energy released as the force returns to zero. This is also true for a nonlinear material/spring as shown in Figure 2.6(b), even though the load/unload path is curved. This is not the case for a viscoelastic material/spring as shown in Figure 2.6(c). The material/spring is loaded to a certain point before yield and then unloads taking a different path [8, 9]. The work to deform the spring still creates potential energy that is equal to the area under the load curve, but the energy released as the force returns to zero is smaller. The envelope created by the different load and unload paths is the amount of energy dissipated during unloading due to internal energy, friction, heat, or sound [5, 9].

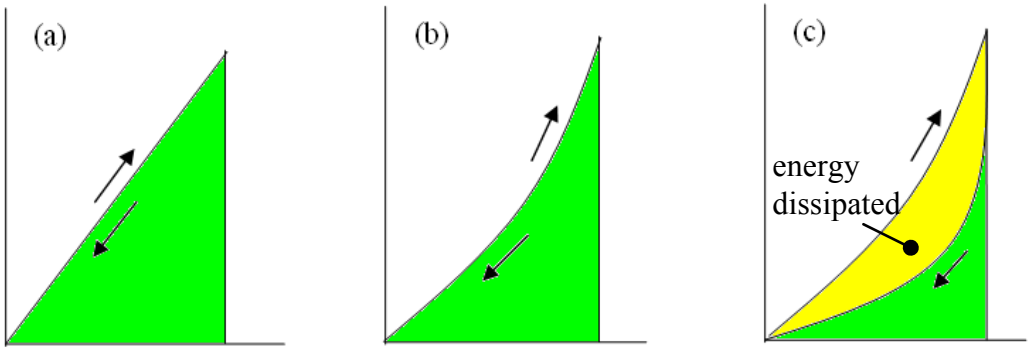

Figure 2.6: Curves showing different behavior

(a) linear-elastic (b) nonlinear (c) nonlinear viscoelastic

A material that has been yielded will exhibit hysteresis when unloaded or loaded in the opposite direction. The unload line will be parallel to the original load line, but will be offset a certain distance, termed residual strain. This effect is caused by the permanent deformation of the material and is shown graphically in Figure 2.7(a). The original load/unload curve of the raw material is shown in red. When the material is loaded again (shown in green) the unload line will be traced during loading [7].

A hyperelastic material will show a similar profile termed the Mullins effect. For example, when a rubber-like material is loaded it will reload following the load profile as shown in Figure 2.7(b) because of micro-tears in the material. The material will also show stress softening if reloaded to the previous maximum strain. If the material is loaded in one direction and then reloaded in another direction, the stress-strain profile for the new direction will not exhibit the Mullins effect until it is loaded again in the same orientation. This implies that rubberlike viscoelastic materials are also anisotropic [8,10,11].

A ductile polymer such as polypropylene exhibits hyperelastic and viscoelastic properties as shown in the load/unload curve of Figure 2.7(c) [12, 13, 14]. The material is nonlinear both in the load and unload direction and as the maximum strain is increased, the area between the load and unload curves (hysteresis area) increases. However, the hysteresis area decreases if the same maximum strain is reached in cyclic loading [14]. Similar to hyperelastic materials, polymers exhibit cyclic stress softening and can have changes in microstructure during loading. These changes can sometimes be reversed if the material is allowed to recover at zero stress [13].

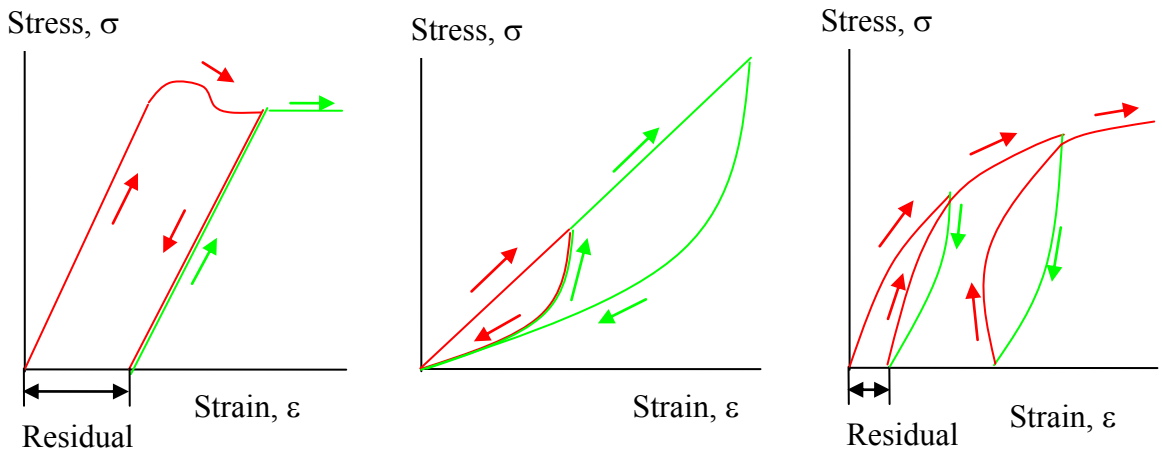

Figure 2.7: (a) Linear-elastic material (b) Hyperelastic material (c) Polymer material

A mechanical system can be thought of as a simple system of inertia elements (mass), spring elements, and damper elements. The spring elements are deflected by the force and the damping elements resist the deflection by absorbing energy and dissipating it as heat to the surroundings [6]. The Maxwell model describes an isotropic visco-hyperelastic material as parallel springs and dampers in series as shown in Figure 2.8 [8].

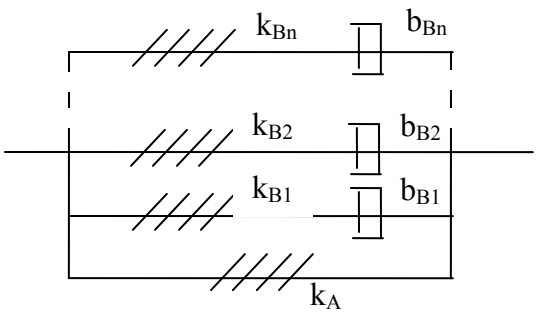

Figure 2.8: Maxwell model describing rubberlike materials [8]

Composite materials with long fibers will have anisotropic material properties; the properties are dependant on orientation of the fibers and the load direction. A unidirectional ply will have the highest strength and modulus in the direction of the fibers. The fibers hold the majority of the load when forces are applied. The matrix serves to hold the fibers together and protect the fibers from environmental factors and mechanical abrasion. The matrix and fiber interface is important to material properties since any delaminating effects could weaken the composite material strength [15, 16].

Tsuji et al. performed compressive tests on a carbon fiber composite and found that the load-deflection curve was non-linear and found no permanent deformation or large residual strains. The test specimens showed the same loading and unloading path during testing. In most other materials, a non-linear stress-strain curve would be associated with permanent deformation or large residual strains. Only a 0.5% strain was seen at the end of loading the composite. The non-linearity was explained by the local or microscopic buckling of individual fibers [15].

Wang et al. performed loading and unloading tensile tests on a carbon fiber composite. The material followed the same load/unload path in the linear portion of the

curve. Once the material yielded, due to microcracks in the matrix and fractures of the fibers, the material exhibited a hysteresis effect similar to a linear-elastic material [17].

2.2.1 Beam and Leaf Springs

There are three common configurations of beam springs: quarter-elliptic, semi-elliptic, and full elliptic as shown in Figure-2.9 [5]. The HELIOS brace most resembles a quarter-elliptic beam spring which can be modeled as a simple cantilever beam as shown in Figure 2.10(a). Beam springs are commonly fabricated as multileaf springs, Figure 2.10(b), where individual beams are layered to create a constant stress along the length of the beam [5]. However, leaf springs are also made from composite materials and changes in geometry are used to create the constant stress across the beam [18, 19]. Leaf springs are unique since they are able to hold structural loads as well as spring loads and as long as the maximum deflection is less than 30% of the spring length, significant changes in geometry are avoided [5].

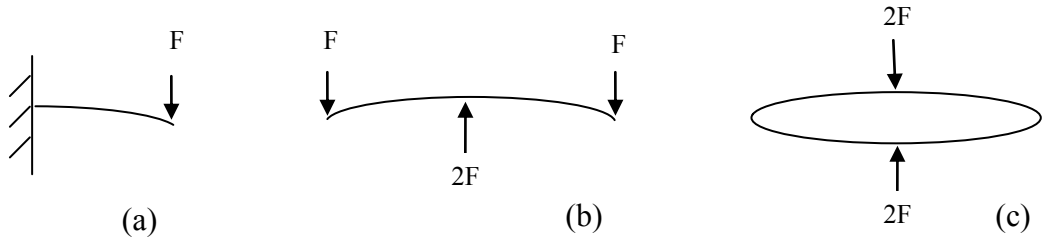

Figure 2.9: (a) quarter-elliptic, (b) semi-elliptic, (c) full-elliptic

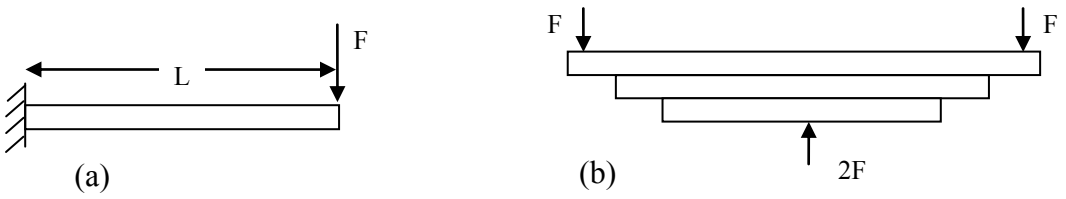

Figure 2.10: Beam springs (a) quarter-elliptic (b) multileaf [5]

The stress, deflection, and stiffness of a cantilever beam spring can be calculated using Eq 2.5, Eq 2.6, and Eq 2.7, respectively.

$$\sigma = \frac{6 \cdot F \cdot L}{b \cdot h^2}, \quad \text{(Eq 2.5)}$$

where F is applied force, L is beam length, b is height, and h is width

$$\delta = \frac{6 \cdot F \cdot L^3}{E \cdot b \cdot h^3}, \quad \text{(Eq 2.6)}$$

where F is force, L is beam length, E is modulus, b is height, and h is width

$$k = \frac{F}{\delta} = \frac{E \cdot b \cdot h^3}{6 \cdot L^3}, \quad \text{(Eq 2.7)}$$

where F is force, L is beam length, E is modulus, b is height, and h is width

Tsuji et al. tested a carbon fiber composite in a cantilever beam configuration. Experimental data were compared to beam theory calculated values. It was shown that the experimental results on the tension side of the beam were higher than the beam theory results. This difference was from softening occurring on the compression side of the beam and hardening occurring on the tensile side of the beam, which causes the neutral axis to move toward the tensile side of the beam. Both the tensile and compressive properties were shown to be nonlinear at high deformations when the composite was tested in bending. It was concluded that linear beam theory is only applicable for calculating beam bending stiffness, but not beam failure stress and deformation [15].

Forces applied to a leaf spring create deflection and this potential energy is stored as strain energy. Elastic energy, S_e, of a leaf spring can be calculated using Eq 2.8 [18]. This

equation shows that a material with a high allowable stress and a low modulus of elasticity would yield the optimum amount of elastic energy. The strain energy, S_s, for a leaf spring is written as Eq 2.9 [18]. Materials with higher strain energies are considered to have better energy storage capabilities [19]. Shokrieh et al. show that a carbon fiber composite is able to store the greatest amount of energy as compared to steel and glass fiber composites. As with material properties, energy is stored best in the direction of the fibers [18].

$$S_e = \frac{\sigma^2}{2 \cdot E}, \qquad \text{(Eq 2.8)}$$

where, σ is longitudinal maximum allowable stress and E is longitudinal modulus

$$S_s = \frac{\sigma_t^{\,2}}{2 \cdot \rho \cdot E}, \qquad \text{(Eq 2.9)}$$

where, σ_t is allowable stress, E is modulus of elasticity, and ρ is density

Leaf springs are commonly used for automotive suspension [16,18,19,20]. In this application the springs "buffer the vertical vibrations or impacts due to road irregularities by means of variations in the spring deflection". Essentially, the spring deflects and absorbs and/or releases the potential energy. It is therefore important for the leaf spring to have high energy storage capabilities. Yu et al. discuss the importance of the leaf spring material and geometry on the energy storage capabilities [19]. A glass fiber composite is usually chosen for the automotive spring since it is better suited to continued contact with metal and has high impact strength compared to carbon fiber composites which have the ability to store the most energy [18].

2.3 AFO Design

Charcot-Marie-Tooth (CMT) syndrome is a genetic disorder where patients exhibit weakness in the extremities. Muscle atrophy is seen which results "in flail calcaneocavus and cavovarus foot deformities, with clawing of the toes" [3]. Foot-drop is seen in gait and is the result of weak dorsiflexor muscles, which can severely impact normal gait [3]. Young, et al., performed a review on treatments used for CMT disease. Five types of studies were identified and included exercise, oral creatine monohydrate, parenteral Neurotrophin-3, subcutaneous preparation of purified bovine ganglisides, and foot orthoses. The review concluded that none of these interventions provide a significant benefit for those diagnosed with CMT [21].

An Ankle Foot Orthosis (AFO) is typically prescribed to CMT [6], stroke [22], polio [23], and multiple sclerosis [24] patients to prevent foot-drop and assist with normal gait. It has been shown that a properly prescribed AFO can reduce perceived exertion and enhance physiologic performance [25]. Ezenwa, et al., showed that AFO braces increase stability and improve gait during propulsion [26].

Many braces in industry are considered to be commercial-off-the-shelf (COTS) models since they are mass produced and based on average anthropometric measurements. It has been suggested that only 10% of individuals in need of an AFO could be fitted with a COTS model [27]. For the remaining 90%, a custom brace would be needed, which provides a much better fit and follows the biomechanical needs of the patient [27, 28].

There are several types of AFO braces and many different materials used to make these braces. Metal and leather braces were commonly used to make AFO braces until

plastics were introduced. Metal was good for rigidity and strength but was often heavy and bulky for the user [29]. Metal braces were often so heavy that the user was fatigued by walking [30]. Plastics are easily formed to the complex geometry of the leg and are lightweight, but are often less durable than metals due to their viscoelastic properties [31]. Polypropylene is one of the more popular plastics used for AFO braces [32, 33] and extensive research is available with regard to polypropylene AFO braces. In recent years composite materials have been used to create a lightweight AFO that has better strength properties than the plastic AFO braces [33].

Four common types of AFO braces are posterior spring, anterior spring, side stay, and spiral [34]. Each of these braces is different with respect to flexibility/stiffness due to differences in geometry. The posterior type is rigid in dorsiflexion and plantar flexion, the anterior type more flexible in dorsiflexion than in plantar flexion, the side-stay has similar flexibility in dorsiflexion and plantar flexion, and the full spiral is flexible in both dorsiflexion and plantar flexion [34]. The stiffness of AFO braces can also be altered by changing the amount of trim on the brace or by combining the plastic orthosis with metal cams and hinges [29]. Sumiya, et al., showed that as the width of the posterior spring brace was decreased, the stiffness of the brace in plantar flexion and dorsiflexion decreased linearly [35]. Lee, et al., also found that the ankle width affected the rigidity of a polypropylene posterior spring brace [36]. Chu, et al., determined that as the neck decreases in width, the stresses become higher and therefore the brace fails [37].

Singerman, et al., showed that a posterior spring brace provides low but constant stiffness from plantar flexion to dorsiflexion [29]. Designs that showed low stiffness values in dorsiflexion may not provide the stability needed during the latter part of stance

and may give the patient the false sense that the brace is collapsing [29]. It could be argued that dorsiflexion stiffness is more important in the design of an AFO than plantar flexion stiffness since the dorsiflexion stiffness is used to stabilize the individual during terminal stance whereas plantar flexion stiffness is used to prevent the affected foot from dropping, which does not require as much stiffness.

2.4 Mechanical Analyses of AFOs

Abu-Hasaballah, et al., performed an FEA optimization analysis on a posterior spring brace using 3D hexagonal 8-node elements [38]. It was found that the high stress regions of the brace existed in the lower neck region which correlates with other studies [38]. It was then suggested that optimization of the brace could be achieved by reducing material in the upper neck region and thereby reduce the overall weight of the brace [38].

Several studies performed to determine the mechanical characteristics of AFO braces tend to test the AFO strapped to a dummy leg [29, 31, 35, 39, 40] or to a human subject [34, 37, 41]. This infers the major concern is the flexibility only about the ankle joint and does not take into account the stiffness of the brace as a whole.

Another issue with testing AFO braces for stiffness is the application of the applied force. Polliack, et al., attempted to create a fixture to test AFO braces that would flex the neck region of the brace in addition to the foot plate of the brace. It was suggested that the footplate of the braces may fail and should not be fixed during testing. Three setups were tested to simulate heel contact, midstance, and toe off. A wedge was placed at the top of the brace to angle it by 30 degrees to simulate heel contact, 0 degrees to simulate midstance, and -20 degrees to simulate toe off. In all three cases the applied force was

applied vertically to the brace [40]. While this setup provides a force vs. displacement relationship and provides a stiffness value for the brace, it does not adequately simulate the force applied to the brace during gait.

Prior studies indicate high stress concentrations in the lower neck of polypropylene posterior spring braces near the medial and lateral edges of the brace [36]. Polypropylene braces have also been shown to have weakened mechanical properties after cyclic loading [31, 42]. The problem with viscoelastic polypropylene braces is that prolonged use of the brace makes the material stretch or elongate. A 0.125 in thick polypropylene pediatric AFO was tested to reveal stiffness and effects of cyclic loading. The base of the AFO was fixed while force was applied at the top of the brace to create motion from 10 degrees of dorsiflexion to 15 degrees of plantarflexion. A force of 366 N applied at the top of the brace was required to induce 10 degrees of dorsiflexion. Crazing of the plastic, which is permanent plastic deformation, was seen proximal to the malleolus [31].

Chu, et al., did extensive research on the stress measurement of a polyethylene brace using FEA and experimental testing. A study was conducted to validate clinical observations and FEA analysis. Only two strain gages were used for the study since it was difficult to bond the strain gages to the polypropylene material. A normal subject was asked to walk in the braces at a slow rate, a fast rate, and to jump in the braces. A known weight of 80 lbs was also placed on the instrumented brace. Results showed that failure occurred in the middle-lower lateral neck region of the polypropylene posterior spring AFO [41].

Chu, et al., performed two more studies involving several polypropylene posterior spring AFO braces of varying stiffness to determine stress distribution and how body

weight changes the stress distribution in AFO braces [32, 37]. Each brace was instrumented with eight strain gages located at the neck region of the brace. Similar to the previous study, it was determined that the high stress location of a standard polypropylene brace would be in the middle-lower lateral neck region [37, 41].

During the stress distribution study a normal subject was asked to walk slow, walk fast, run, jump, stand up/ sit down, and lift an object. Maximum compressive stress was seen at heel contact and the maximum tensile stress was seen at toe off during slow walking. It was also determined that the geometry and the physical activity being performed both altered the magnitude and distribution of the peak stress [37].

The weight differences were introduced by using three different subjects who were asked to perform a slow walk in addition to a stand up/sit down action. No correlation was made between stress and weight. This is most likely due to the differences in subject gait or from the fact that each brace was not custom fit to each individual [32].

Syngellakis, et al., state that large deformations exist at the ankle region of the AFO as the brace is used during plantar flexion and dorsiflexion. Material non-linearity exists in polypropylene when it is loaded beyond a certain range. This is why there was a better correlation of results to actual physical experiments when the non-linear behavior of the polypropylene material was taken into account. The authors show this to be true when analyzing a polypropylene brace using ANSYS. A 3D model of the polypropylene posterior spring brace was modeled by measuring points on the brace and then creating splines which were connected to create a surface. The model was meshed using 8-node quad shell elements [43].

Most FEA studies analyze the AFO brace by itself; however it can be argued that different results could surface by modeling the foot since it adds viscoelastic properties to the model [34]. Chu, et al., analyzed a polypropylene posterior spring AFO brace and modeled it with the foot [42, 44]. Both were represented by 3D solid elements in PATRAN and the model was analyzed using ADINA [42, 44]. It was shown that the peak compressive stress occurred in the heel region during heel contact and that the peak tensile stress occurred in the neck region during toe off [42]. These results tend to correlate with other studies but since the foot was modeled for the analysis, it was found that the AFO stress distributions change depending on the properties of the muscles as well as the ground contact point during heel strike [42]. This is an important finding since it reveals each individual will stress the brace differently depending on their condition.

Modeling the foot as well as the AFO could provide a more accurate analysis, however to simplify the model the foot was modeled only including the ligaments, bones, and soft tissue which were all assumed to have linear properties. After performing the analysis, Chu, et al., discussed that the stress distribution was affected more by the mechanical properties of the AFO than by the mechanical properties of the soft tissues [44].

Prior studies have been performed that model the foot exclusively using CT or MRI images to determine foot pressures and effects of changing mechanical properties of certain elements of the foot (i.e. muscles, ligaments, etc). In these studies the foot model was generally more complex than in AFO FEA analysis [45, 46, 47].

2.5 Use of Composite Materials in AFO Design

Composite materials have been researched to replace the traditional polypropylene material for AFO braces. These materials offer better mechanical properties than polypropylene and can still be shaped to the complex geometry of the leg. The stiffness properties of a polypropylene brace can be altered by shape, thickness, and trimline whereas the stiffness of a composite brace can also be altered by adjusting matrix and fiber properties, fiber loading, fiber-matrix interface, and fiber architecture [33].

Composites have been considered as a possible replacement for metal braces as early as the 1960s. Hill, et al., suggests the use of fiberglass-epoxy for a drop-foot brace and cites the reduced weight and excellent strength and fatigue properties of the composite material. In this brace design metal rods were replaced with fiberglass-epoxy rods [30].

Carbon fiber composites have been considered a suitable material in orthotics since the late 80s and early 90s. Composites offer excellent strength properties and a reduction in weight as compared to plastic [28]. Glass fibers and light curable resin have also been considered since they offer a much higher flexural strength and modulus than polypropylene [33]. Materials and fabrication for a composite brace are more costly than for a plastic brace [28] which is probably why custom-off-the-shelf (COTS) polypropylene AFO braces are still being used.

Stallard, et al., addressed a concern regarding possible catastrophic failure when using composite materials for AFO braces [48]. A carbon fiber orthotic was tested and showed increased stiffness, slightly lower strength, and a similar plastic deformation after yield compared to a ductile metal orthotic.

Several designs have been proposed and studied to use lightweight composites in lieu of traditional plastics. The use of carbon composites in full leg braces used by paraplegic patients was considered to reduce weight while maintaining high strength values [49]. A knee-ankle-foot-orthotic (KAFO) traditionally made from polyethylene and aluminum was redesigned and made from a thermoplastic matrix carbon fiber reinforced plastic composite. This increased fatigue strength in addition to reducing weight by 40%. No catastrophic failure was seen from switching to the composite material [50].

A Passive Dynamic (PD) or energy storage orthosis is of interest to further improve gait [51]. These devices use material properties, component thickness, AFO shape, springs, and fluid pressure dynamics to provide support and mechanical energy return during gait [51].

Hafner, et al., reviewed literature on energy storage prosthetic devices (feet), highlighting nomenclature confusion and variations in measuring energy-storage and energy-return features [9]. A prosthetic foot consists of a compressible heel and a flexible keel spring that acts as an elastic spring and returns energy to the amputee. Considered to be more advanced, carbon fiber shank prosthetic feet with a heel spring were introduced in 1987. Both of these prosthetic feet designs are considered passive devices. Energy-storage prosthetics and orthotics are similar "by storing energy during weight-bearing in the stance phase, and releasing it as the foot is unloaded for swing initiation" [52]. It was shown that the peak power produced by the prosthetic foot "can be 15-20% of normal push-off, reducing the energy (as measured by oxygen consumption) expended by the amputee" [52].

CHAPTER 3

HUMAN MOTION

3.1 Human Subjects Protocol and Collection of Gait Data

A study of gait was undertaken to determine if the HELIOS brace improved the gait of CMT subjects. Since the research involved human subjects, the project was reviewed and approved by the UNLV Institutional Review Board (IRB) and informed consent was obtained for all participants before tests were conducted. The date of approval was 02-15-08 for the initial protocol, 02-02-09 for the continuing review, and 10-16-08 for a modification that allowed collection from previous wearers. Dr. Edward Neumann administered Informed Consent to all participating subjects.

Gait was analyzed before (pre-test) and after (post-test) the subject was acclimated to the brace, which was at least a seven week period. Nine total subjects were used in the study with eight being CMT subjects and one being a non CMT subject or 'normal' subject. Of these, three CMT subjects in addition to the one 'normal' subject were analyzed while wearing instrumented braces during the post-test. This provided a way to understand the relationship between the gait and the motion of the brace through the ground reaction force (GRF) and the strain gage readings.

The 'normal' subject completed extra trials to determine how a change in weight would affect the HELIOS braces. The weight trials were performed pre- and post-test as well as braced and unbraced. In addition to normal body weight, the three weights used were 5% of body weight (26.7 N), 10% of body weight (53.4 N), and 15% of body weight (80.1 N). A weight belt was worn around the subject's waist with the weights evenly distributed, as shown in Figure 3.1. A total of sixteen conditions were formulated

and are shown in Table 3.1. Not all subjects completed all sixteen conditions as shown by the table. All subsequent data are labeled by the subject number and condition number.

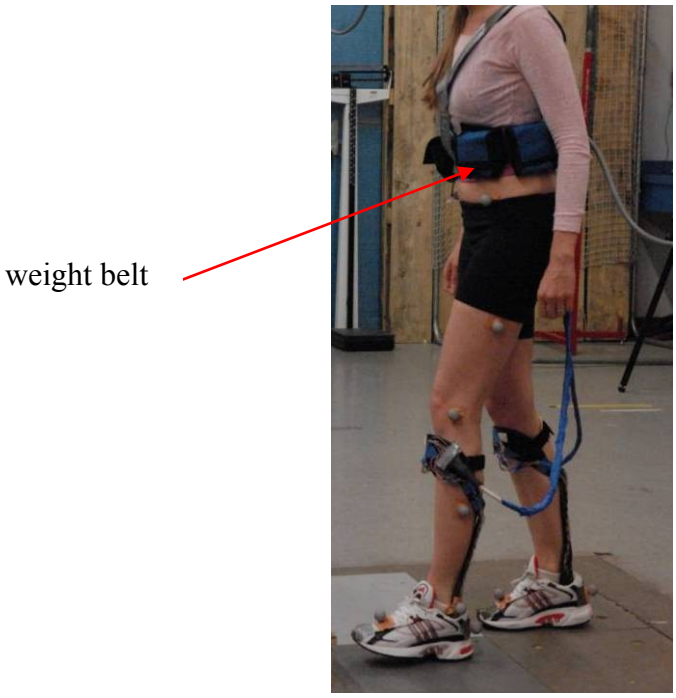

Figure 3.1: 'Normal' subject wearing weight belt

Two Kistler 9281C force plates were used to collect GRF data from the left and right foot for each trial. The force plates used four built-in piezoelectric 3-component force sensors to measure the vertical GRF component (F_z) as well as the two shear GRF components (F_y and F_x) acting along the force plate surface. The measurement range for the F_x and F_y directions was -10 kN to 10 kN whereas the range for the F_z direction was -10 kN to 20 kN.

Table 3.1: Data collected for each subject by condition number
(An 'X' indicates data were collected)

					Subject Number								
					1	2	3	4	5	6	7	8	'normal'
Condition Number	1	Pre-Test	Unbraced	no added weight	X		X			X	X	X	X
	2			5% body weight added									X
	3			10% body weight added									X
	4			15% body weight added									X
	5		Braced (current brace)	no added weight	X		X					X	X
	6			5% body weight added									X
	7			10% body weight added									X
	8			15% body weight added									X
	9	Post-Test	Unbraced	no added weight	X	X	X	X	X	X	X	X	X
	10			5% body weight added									X
	11			10% body weight added									X
	12			15% body weight added									X
	13		Braced (HELIOS)	no added weight	X	X	X	X	X	X	X	X	X
	14			5% body weight added									X
	15			10% body weight added									X
	16			15% body weight added									X

Most of the subjects were able to walk across the force plates in the standard layout as shown in Figure 3.2 as the 'normal setup'. If the subject's stride length was not long enough the plates would be rearranged as shown in Figure 3.2 as the 'alternate setup'. This was done to ensure the subject was walking at a normal pace without altering their gait. Table 3.2 shows which force plate setup was used for each subject/test.

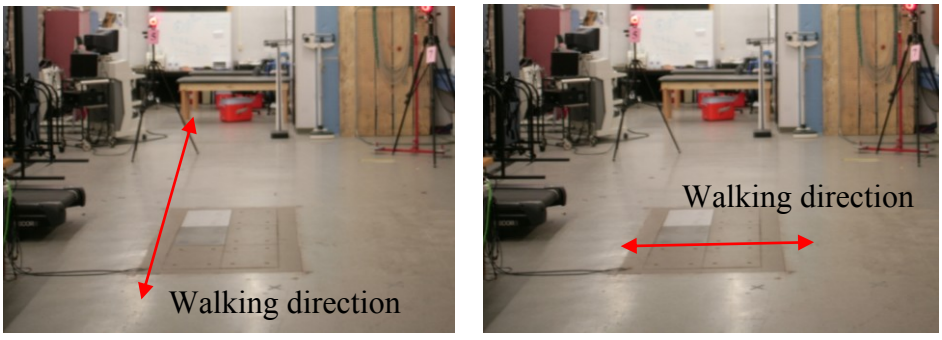

Figure 3.2: Kistler force plate (left) normal setup, (right) alternate setup

Table 3.2: Setup of force plates

	Pre-Test		Post-Test	
Subject No.	Unbraced (condition 1)	Braced [current] (condition 5)	Unbraced (condition 9)	Braced [HELIOS] (condition 13)
CMT 1	normal setup	normal setup	normal setup	normal setup
CMT 2	n/a	n/a	normal setup	normal setup
CMT 3	alternate setup	normal setup	normal setup	normal setup
CMT 4	n/a	n/a	normal setup	normal setup
CMT 5	n/a	n/a	normal setup	normal setup
CMT 6	alternate setup	n/a	normal setup	normal setup
CMT 7	normal setup	n/a	normal setup	normal setup
CMT 8	normal setup	normal setup	normal setup	normal setup
'normal'	normal setup	normal setup	normal setup	normal setup

3.2 Collection of Data on Brace Mechanical Performance

3.2.1 AFO Fabrication

Each HELIOS AFO brace was custom designed and fabricated at Ortho Rehab Designs. Patients were cast and the cast was modified by a certified prosthetist/orthotist to incorporate corrections for ankle and foot deformities resulting from CMT. This customization allowed for maximum correction of the patient's alignment for improved balance and joint stability, in addition to providing customized spring based on the patient's activity level and condition. The typical HELIOS brace is made from multiple layers of bidirectional carbon, bidirectional carbon-Kevlar, and is vacuum formed with an epoxy matrix.

The HELIOS differs in geometry from traditional AFO braces. It is considered a posterior spring brace since the main structure of the brace is posterior to the leg. However, the brace structure wraps around to the anterior side of the leg with a strap connecting posterior. This allows the individual to lean into the brace without concern of

falling forward. A traditional posterior brace has a strap that connects anterior to the leg, which does not provide as much stability if the individual leans forward.

The HELIOS design reduces the material in the upper neck region as suggested by Abu-Hasaballah, et al. [38]. The HELIOS has unique geometry of the posterior section of the brace since it is separated into two individual struts instead of one solid section. This allows the brace to bend and flex during gait. It is also possible that this geometric design coupled with the carbon fiber material provide an energy storage and release that assists in gait. In addition, it could also improve the structure and life span of the brace since the brace is not being stressed in the neck region such as a solid posterior section made out of polypropylene would be stressed.

The experimental braces were fabricated in the same manner and used the same materials as the actual HELIOS braces that were delivered to the patients to take home with them. However, the experimental braces were turned over to the research team at UNLV for instrumentation, and were not worn by the subjects until they returned for post-test data collection approximately 8 to 12 weeks following delivery of the braces the subjects took home after fitting.

3.2.2 AFO Instrumentation

Affixed to each brace were a total of eight 350 Ω Omega strain gages (Model SGD-7/350-LY11) which were numbered and split evenly on the two struts of the brace as shown in Figure 3.3. Due to project time constraints the 350 Ω strain gages used for the 'normal' subject instrumented braces were Vishay (Model EA-06-250BF-350), since these gages were more readily available. Strain gages were applied using standard application procedures. The first gage was placed just below the top curve so it was

positioned in the straight section of the strut. The second gage was placed approximately in the middle of the strut between the top and bottom. The third gage was placed in the straight section of the lower curve. The fourth gage was placed near the ankle and as close to the shoe line as possible without being placed in the shoe. All gages were placed in the center of the strut and ran parallel to the strut direction. The gages were chosen to be placed in these selected locations to provide a general indication of the strain along the length of the struts.

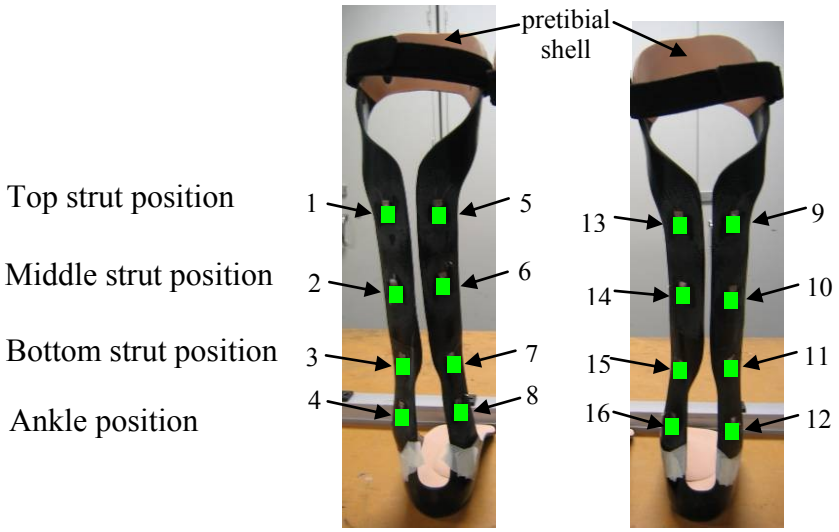

Figure 3.3: Gage placement on left and right HELIOS braces

A 20 m cable suspended on an overhead guide-wire connected the gages, using D-sub 25 pin connectors mounted on the pretibial shell of each HELIOS brace, to the National Instruments (NI) data acquisition system (Figure 3.4). The NI system consisted of the following components:

- NI SCXI-1520: 8 channel strain conditioner
- NI SCXI-1600: data acquisition and control module

- NI SCXI-1314: 8 channel terminal block for quarter bridge gages
- NI SCXI-1000: 4 slot chassis

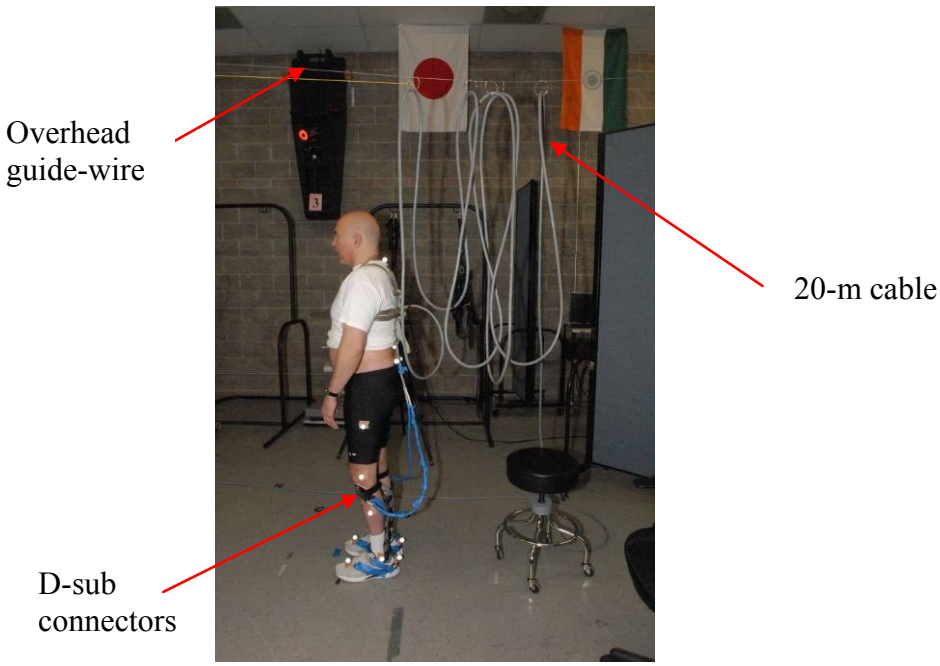

Figure 3.4: 20 m cable connected to braces

3.2.3 Human Testing

All subjects were asked to walk at a normal pace across two force plates in the UNLV Sports Injury Research Center (SIRC) laboratory (Figure 3.5) following the protocol described previously. Each force plate recorded the vertical force (F_z), anterior/posterior force (F_y), and medial/lateral force (F_x) of one foot. The Kistler force plates were calibrated up to 20 kN in the F_z direction and up to 5 kN in the F_x and F_y directions. Ten trials were collected for each subject. Pre-test data were collected only for those subjects that were new users of the HELIOS brace, as shown in Table 3.1. Post-test data were collected for all nine subjects.

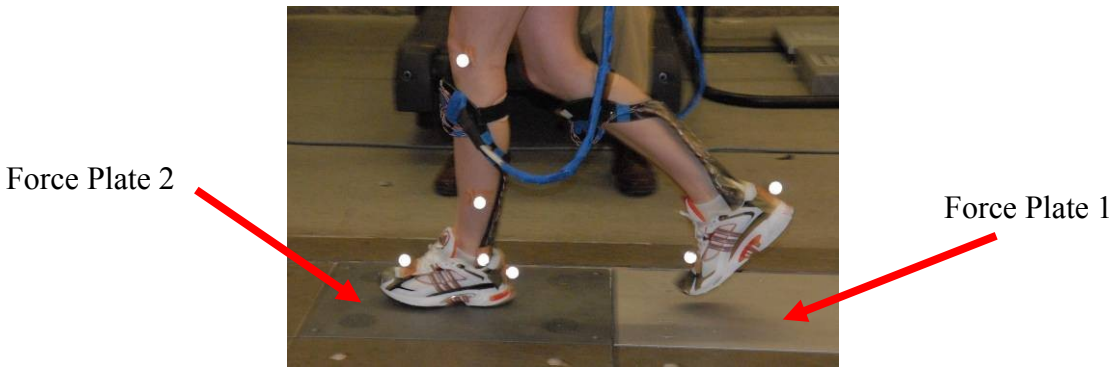

Figure 3.5: Subject walking across force plate

The Kistler Bioware system was used to collect pre-test GRF data at 1116 Hz whereas post-test GRF data were collected using the Vicon 8i motion capture system (12 camera system) at 1080 Hz. Each subject had retro-reflective markers applied to the lower half of the body as shown in Figure 3.6 for post-test data collection. Marker data were collected by Vicon at 120 Hz. These markers were used by the software to calculate the kinematics. The kinematics data will not be presented in this dissertation due to the vast amount of testing and analysis being completed on the brace itself. Instead, the collected kinematics data will be analyzed and presented in another report.

During the post-test trials of the subjects with instrumented braces, data from all sixteen strain gages were collected via a LabView program at 1080 Hz. The raw strain data were filtered to remove high frequency noise using a 4-pole Butterworth filter at 10 kHz. A string was attached to the cable and lightly pulled to ensure the subject did not alter gait by pulling the 20 m cable from behind.

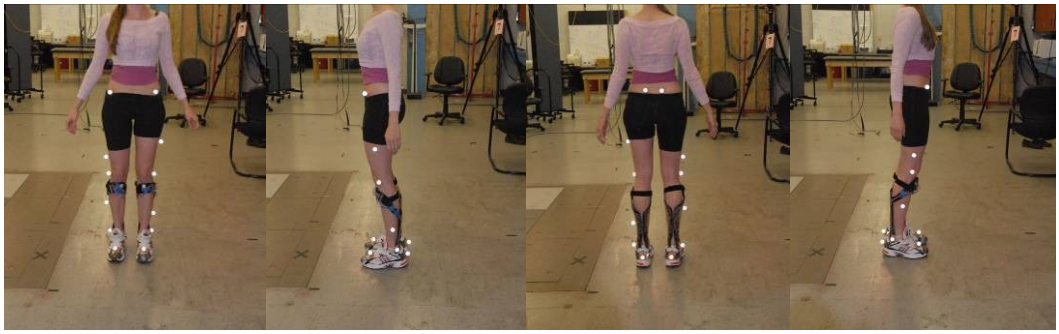

Figure 3.6: Markers attached for post-test

3.2.4. Data Reduction

All raw GRF and strain data trials were analyzed using Matlab. The two sets of GRF data were analyzed for each trial; the first set corresponded to one foot and the second set corresponded to the other foot. Figure 3.7 shows the raw GRF curves for one trial. All of the raw GRF curves (F_x, F_y, and F_z) were clipped to include only the time where the subject's foot was in contact with the force plate. This is termed the stance phase, where heel contact (HC) occurs at the beginning of the curve and toe off (TO) occurs at the end of the curve. Figure 3.8 shows these two conditions. All were clipped at the time where the F_z curve reached 20 N. This is a nominal weight chosen to ensure the data would be clipped above the noise level of the data collection system. The data were then normalized for stance so that heel contact occurs at 0% stance and toe off occurs at 100% stance. The data were also normalized for body weight by dividing the raw forces by the subject's body weight. This was done to eliminate the differences between the weights of the subjects, so a more direct comparison could be made between different subjects. This normalization provided a non-dimensional number that is a percentage of body weight.

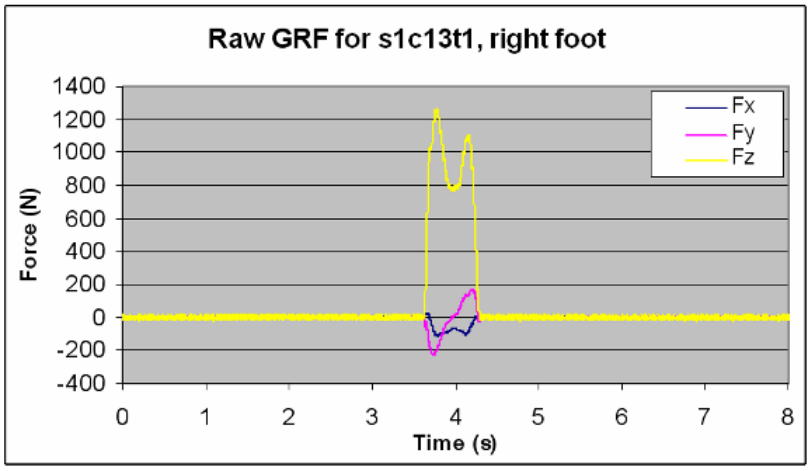

Figure 3.7: Raw GRF data collected for CMT1, condition 13, trial 1

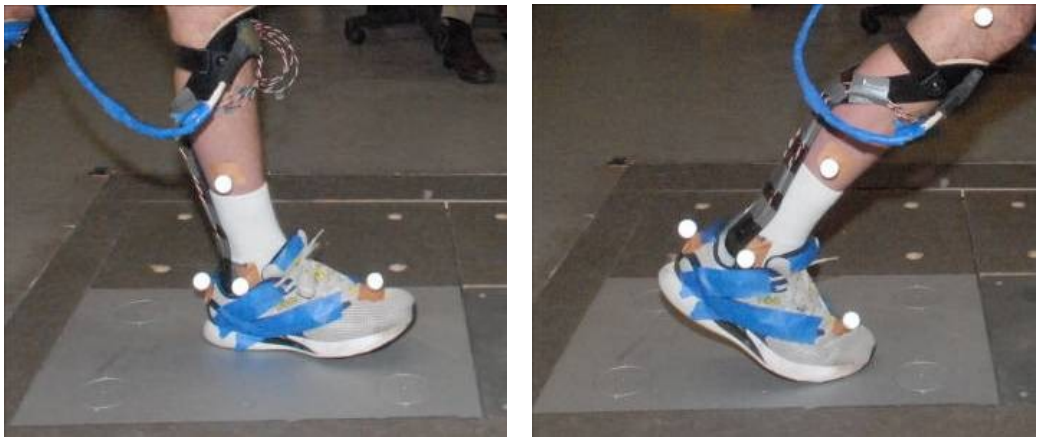

Figure 3.8: (left) Heel contact at 0% stance, (right) Toe off at 100% stance

Since the force plate data and strain gage data were collected for the same trials it was possible to line up the two sets of data to determine when HC and TO occurred in the strain data. A square wave was inserted into the GRF file during data collection so the force and strain data could be aligned. An example of the raw strain data collected for one trial is shown in Figure 3.9. Once the strain data were clipped based on the GRF

curves, the strain data were normalized for stance so that HC would occur at 0% stance and TO would occur at 100% stance.

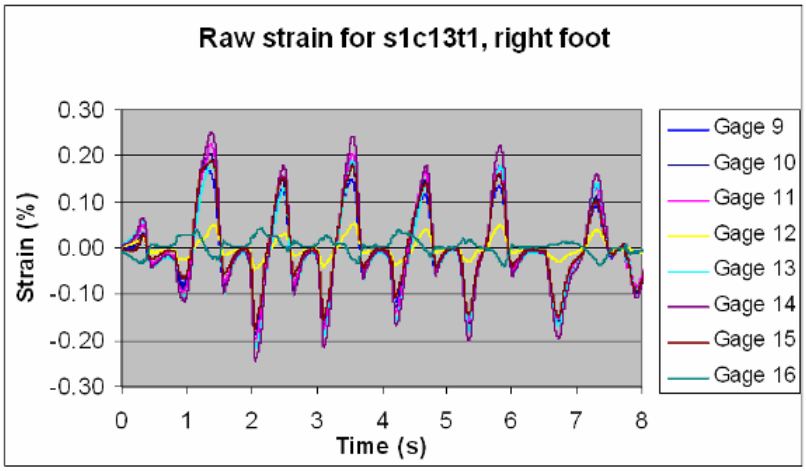

Figure 3.9: Raw strain data collected for CMT1, condition 13, trial 1

All trials of GRF data for the same subject and condition were averaged and are included in Appendix A. Linear interpolation was used to produce curves with the same number of intervals (1001) so the curves could be averaged and a standard deviation could be calculated. Figure 3.10 verifies that the number of points was large enough to produce an interpolated curve that matched the raw data closely. All trials of strain gage data for the same gage, subject, and condition were averaged and are included in Appendix B. Linear interpolation was also used to produce curves with the same number of points (1001) so the curves could be averaged. Standard deviations are not shown on these graphs for ease of viewability.

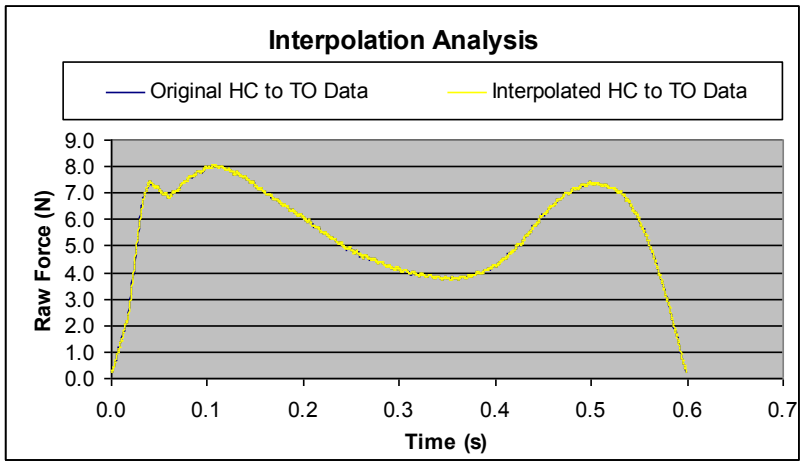

Figure 3.10: Linear interpolation of raw data

3.3 Results of Human Motion Testing

There are two types of data that resulted from the human motion tests that will be discussed in this section. The first type of data is the ground reaction force (GRF), both the vertical force (F_z) and the anterior/posterior force (F_y). The results of how the brace influences these forces will be discussed in the second subsection. The second type of data produced by the human motion tests is the strain of the brace collected by the eight strain gages. The strain data will be discussed in the third subsection.

3.3.1. Walking Speed

Table 3.3 shows the subject numbers for the study with associated information for the subjects. Table 3.4 shows the gender, age, and anthropometric data of the subjects. Figure 3.11 shows the increase in walking speed from the unbraced to braced condition for all subjects in ascending order. These increases were calculated based on the subject's average walking speeds calculated during trials in the gait lab, which could alter the subject's true walking speed due to the testing conditions (i.e. trying to aim for the force plate).

Table 3.3: Subject numbers and information for human study

Subject No.	Type of CMT	New or Current Wearer	Years of HELIOS Use	Instrumented Braces	Pre-Test Data	Post-Test Data
CMT1	Ia	New	<1	Yes	Yes	Yes
CMT2	II	Current	12	Yes	No	Yes
CMT3	NA	New	<1	No	Yes	Yes
CMT4	II	Current	4	Yes	No	Yes
CMT5	X-link	Current	1	No	No	Yes
CMT6	I	New	<1	No	Yes	Yes
CMT7	I	New	<1	No	Yes	Yes
CMT8	NA	New	<1	No	Yes	Yes
'normal'	None	New	<1	Yes	Yes	Yes

I = inherited in an autosomal dominant pattern; Ia = duplication of PMP22 gene on Chromosome 17;
II = dominantly inherited, X-link = inherited through the X chromosome

Table 3.4: Subject gender, age and anthropometric data

				Mass (kg)		Self-Selected Walking Speed (m/s)	
Subject No.	Gender	Age (yr)	Height (m)	Pre-Test	Post-Test	Post-Test Unbraced	Post-Test Braced
CMT1	F	59	1.65	105.23	105.69	1.26	1.27
CMT2	F	37	1.70	n/a	61.69	0.99	1.28
CMT3	F	56	1.70	100.24	97.52	0.86	0.99
CMT4	M	51	1.75	n/a	92.99	1.07	1.11
CMT5	M	62	1.73	n/a	80.29	0.96	1.16
CMT6	M	69	1.83	85.73	87.54	1.02	1.14
CMT7	M	62	1.65	61.23	62.14	1.06	1.11
CMT8	M	50	1.83	76.66	78.93	0.77	0.99
'normal'	F	30	1.65	52.16	52.16	1.43	1.33

It should be noted that the average self-selected walking speed of normal males is 1.3-1.6 m/s while that of normal females is 1.2-1.5 m/s [3]. CMT1 was the only subject able to meet the normal range of walking speed without the use of the HELIOS brace. This is perhaps why this subject also showed the smallest increase in walking speed while

wearing the HELIOS brace. CMT2 was the only subject who was able to reach the normal range of walking speed while wearing the HELIOS brace. Coincidently, this subject also had the largest increase in walking speed, 0.29 m/s, from the unbraced to braced condition. CMT2 did not have the lowest walking speed during the unbraced condition, three other subjects (CMT3, CMT5, and CMT8) had a lower unbraced speed and did not increase walking speed as much as CMT2.

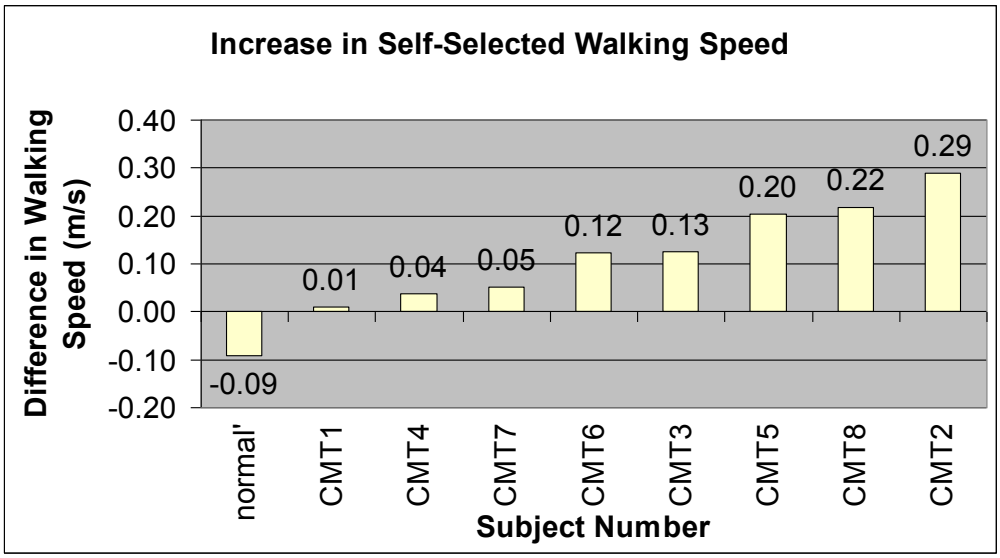

Figure 3.11: Increases in self-selected walking speed from unbraced to braced condition

Table 3.4 shows that the walking speed of the 'normal' subject actually decreased from the unbraced to braced condition. The 'normal' subject was the only one chosen to perform walking trials with extra added weight, pre-test and post-test, so it was possible to calculate the change in walking speed for these extra trials. Table 3.5 includes the walking speeds for the 'normal' subject for pre- and post-trials with 0%BW and 15%BW. Results show that for the 'normal' subject the self selected walking speed was

consistently lower with the brace. This implies that the brace may naturally lower the walking speed of a normal individual; therefore, any small increase in speed (i.e. CMT1) would be a positive outcome. Even though the overall walking speed did not increase as much for subjects like CMT1, it is possible that using the brace requires less exertion by the subject.

The raw vertical and anterior/posterior (A/P) ground reaction forces of all ten walking trials are graphed for each subject and included in Appendix A. Graphs were broken down into left and right feet since the CMT condition is not symmetric. When the average curves were calculated, this separation reduced the standard deviations of some of the graphs, but not all. The graphs could show higher deviations if the subject was not able to walk at the same velocity during every trial. Mentioned in Chapter 2 was the effect of velocity on the ground reaction forces. As the velocity increases, the amplitude of the F_1 peak increases and the F_{min} peak decreases on the F_z GRF curve and on the F_y GRF curve the braking (F_{yb}) and propulsive (F_{yp}) peaks increase [3].

Table 3.5: Self selected walking speed of 'normal' subject

	Self-Selected Walking Speed (m/s)	
	Unbraced	Braced
pre-test 0%BW	1.38	1.30
pre-test 15%BW	1.41	1.38
post-test 0%BW	1.43	1.33
post-test 15%BW	1.37	1.32

3.3.2 Ground Reaction Forces and Temporal Parameters

Sixteen ground reaction force variables, as shown in Table 3.6, were analyzed for differences between the unbraced and braced conditions for each foot. The variables with

significant changes for the subject are highlighted red or blue, indicating if the variable increased ('up') or decreased ('down'), respectively. Those changes that were not significant are also shown and indicated by the symbols not highlighted. These provide the general increase (+) or decrease (-) of the variable.

Table 3.6: GRF variables with significant changes (unbraced vs. braced conditions)

Placed in order of increasing walking speed.

Significant increases are highlighted in red. Significant decreases highlighted in blue.

	Subject, Foot																	
	'normal'		CMT1		CMT4		CMT7		CMT6		CMT3		CMT5		CMT8		CMT2	
	L	R	L	R	L	R	L	R	L	R	L	R	L	R	L	R	L	R
Stance time	+	+	+	+	-	-	-	-	+	-	-	-	-	-	-	-	-	-
F_1	+	+	+	+	+	+	+	+	-	-	-	-	-	-	-	+	+	+
t_1	-	-	+	+	+	+	+	+	+	+	+	+	+	+	+	+	+	+
F_{min}	+	+	+	+	-	-	-	+	-	+	-	-	-	-	-	-	+	+
t_{min}	-	-	-	+	-	-	+	-	-	+	+	+	+	+	+	-	+	-
F_2	+	+	+	+	+	+	-	+	+	-	-	-	-	-	+	-	+	+
t_2	-	-	-	-	-	-	+	-	+	+	+	+	+	+	+	-	+	+
F_{Tmax}*	-**	n/a	-	-	+	+	-	-	-**	-**	-**	-**	-	-**	+	-	-**	n/a
t_{Tmax}	n/a	n/a	+	+	+	+	-	-	n/a	n/a	n/a	n/a	+	+	+	-	n/a	n/a
F_{Tmin}*	-**	n/a	-	-	+	+	-	-	-**	-**	-**	-**	+	-**	+	-	-**	n/a
t_{Tmin}	n/a	n/a	+	+	+	+	-	-	n/a	n/a	n/a	n/a	+	+	+	-	n/a	n/a
$F_{y\,b}$	-	-	-	-	-	-	-	-	-	-	-	-	-	-	-	-	-	-
t_{yb}	+	+	+	+	+	+	+	+	+	+	+	+	+	+	+	+	+	+
F_{yp}	-	-	-	-	-	+	-	-	+	+	+	-	-	+	+	-	-	-
t_{yp}	-	-	-	-	+	+	+	+	+	+	+	+	+	+	+	-	+	+
transition	-	-	+	+	+	+	+	+	+	+	+	+	+	+	+	-	+	+
Number of GRF Variables with Significant Changes	8	7	10	14	9	5	6	6	4	5	9	7	11	8	8	6	6	8

* relative to F_1 peak

n/a less than three transient peaks reported for either condition (9 or 13)

** when including all trials (no reported transient peaks treated as zero)

Significant values were determined using the Model Statistic (single subject t-test approach) procedure with $p<.01$ [53]. This approach was used since the study was a repeated-measure of within-subject design. The p-value determines the chance that a difference in the values could be due to sampling error. In this case, with a chosen p-value of $p<.01$ there was a 1% chance that the significant difference could be due to sampling error. This p-value was chosen over the more widely used $p<.05$ because multiple comparisons are being used.

Each subject showed a significant difference in at least one GRF variable. CMT4, CMT6, and CMT7 had the lowest number of variables with significant changes, while CMT1, CMT3, and CMT5 showed the most variables with significant changes. The remaining three subjects, CMT2, CMT8, and 'normal' were in-between. The number of variables with changes does not correspond to an improvement in self-selected walking speed. It is possible that not all changes were positive changes to the subject's gait. It is also possible that each subject showed a different improvement in the GRF variables because each subject's gait needed improvement in different areas. Changes in variables might be a function of problems with the original gait or the brace could change the gait for each subject in a different manner.

If the number of significant variables were compared to the 'normal' subject then there was a trend that suggests there was an increase in walking speed with the number of significant variables. For example, stance time was significantly positive for the 'normal' subject, so only the CMT subjects with a significantly negative value were included in the total number of significant variables. This essentially normalized the variables and those that were significant are shown in Table 3.7. Three variables that changed

significantly for most of the CMT subjects were all temporal parameters: time to the first peak (t_1), time to the braking peak (t_{yb}), and time to the propulsive peak (t_{yp}). All sixteen variables, including these three, are discussed next in this subsection; however graphs are only presented for those variables with major trends or significant changes. Graphs of all sixteen variables are included in Appendix C.

Table 3.7: GRF variables with significant changes as compared to the 'normal' subject (unbraced vs. braced conditions) Placed in order of increasing walking speed. Significant increases are highlighted in red. Significant decreases highlighted in blue.

		Subject, Foot															
		CMT1		CMT4		CMT7		CMT6		CMT3		CMT5		CMT8		CMT2	
		L	R	L	R	L	R	L	R	L	R	L	R	L	R	L	R
GRF Variable	Stance time									-	-	-	-	-	-		
	F_1																
	t_1	+	+				+	+	+	+		+	+	+		+	+
	F_{min}											-			-		
	t_{min}												+	+			
	F_2											-					
	t_2									+		+	+			+	+
	F_{yb}																
	t_{yb}	+	+	+	+	+	+	+	+	+	+	+	+	+	+	+	+
	F_{yp}													+			
	t_{yp}			+		+		+	+	+	+	+	+	+		+	+
	transition		+						+	+	+			+			+
	Number of GRF Variables with Significant Changes	2	3	2	1	2	2	3	4	6	4	7	6	7	3	4	5

All graphs show the average value of the variables including first and second standard deviation bars. As evident by most of the graphs, the CMT condition results in large standard deviation values. In general, the 'normal' subject had lower standard deviations than the CMT subjects which implies that the CMT condition results in higher variability.

The first variable to be discussed is stance time (time from HC to TO) which varied depending on the subject. The 'normal' subject had an increase in stance time which makes sense because the 'normal' subject's walking speed decreased. CMT1 also showed an increase in stance time while keeping the walking speed almost constant from the unbraced to braced condition. This implies that the swing phase for this subject became quicker. It might be possible that the brace assisted this individual in decreasing the time spent during swing. Subjects CMT3, CMT5, and CMT8 all showed a significant decrease in stance time which makes sense because these subjects showed an increase in walking speed.

In general, subjects with a significant increase in stance time had a lower walking speed whereas those subjects with a significant decrease in stance time had a higher walking speed. The anomaly in this case would be CMT2 since this subject did not show a significant decrease in stance time; however this subject had the largest increase in walking speed.

3.3.2.1 Ground Reaction Variables of Vertical Curve (F_z)

This section presents the forces and temporal variables of the vertical curve (F_z) ground reaction forces. The maximum vertical force during braking, F_1, is supposed to increase with an increase in velocity for normal subjects, but this was not seen with most of the CMT subjects. Only the 'normal' subject and CMT1 had a significant increase in

the F_1 peak in both legs which was not expected since walking velocity decreased for the 'normal' subject and walking velocity did not increase for CMT1. CMT2 and CMT4 were the only other two CMT subjects showing a significant increase in the F_1 peak, but only for one leg. CMT2 was the only subject that had an increase in the F_1 peak and an increase in walking velocity. These results indicate that the change in the F_1 peak was due to wearing the HELIOS brace.

The minimum vertical force, F_{min}, is supposed to decrease with increasing velocity. This was only true for CMT5 and CMT8 who showed a significant decrease in at least one leg. These two subjects had a larger increase in walking speed as compared to the other subjects. The 'normal' subject, CMT1, and CMT4 all had an increase in F_{min}. This would be expected in the 'normal' subject (decrease in walking speed) and CMT1 (no change in walking speed), but CMT2 had the largest increase in walking speed and still showed an increase in F_{min} in one leg.

The vertical force during propulsion (F_2) is supposed to remain unchanged with an increase in velocity but the 'normal' subject, CMT1, and CMT4 showed a significant increase in this peak for both feet. In addition, CMT2 showed a significant increase for one foot and CMT5 showed a significant decrease for one foot. Since this variable was supposed to remain constant regardless of walking speed, it can be stated that the HELIOS was creating this change. However, the three subjects showing a significant increase on both legs were also the three subjects with the lowest increase in walking speed.

All of the significant changes to the vertical GRF curve (increases to the F_1, F_{min}, and F_2 peaks) seen in the 'normal' subject, CMT1, and CMT4 would indicate that the brace

was altering the gait of these subjects without providing an increase in walking speed. CMT2 was the only subject showing an increase in these variables (in one leg) with an increase in walking speed.

Some of the subjects showed delays in the F_1, F_{min}, and F_2 peaks in the braced condition. The 'normal' subject did not show a delay in any of the peaks and in fact showed that for at least one leg, two of the peaks (F_1 and F_2) were faster to occur in the braced condition. Almost all of the CMT subjects showed a delay in the F_1 peak in at least one leg. CMT4 was the only CMT subject that did not show a delay in the F_1 peak in either leg. The F_{min} peak was delayed only in one leg for subjects CMT5 and CMT8 and was not significant for any of the other subjects. The F2 peak was delayed for CMT2, CMT5, and CMT8 whereas the F_2 peak was faster to occur for CMT1 and CMT8. Except for CMT8, a delay in the F_2 peak resulted in increased walking speed.

Most subjects had either a complete absence of the transient peak or had a significant decrease in the magnitude of the transient peak during the braced condition. The decreases were all calculated with respect to the F_1 peak since in some cases the F_1 peak and transient peak (F_{Tmax} and F_{Tmin}) were altered by the use of the brace. All subjects except CMT1, experienced a decrease in the number of occurrences a transient peak surfaced during the braced trials, as shown in Figure 3.12.

A typical transient peak is considered to be 10% BW [3]. "In barefoot walking the heel fat pad is responsible for minimizing the force at heel-strike by increasing the contact time and hence reducing the peak deceleration" [3]. By reducing this transient peak the brace was exhibiting shock-attenuating properties by absorbing the high-

frequency shock. The brace reduces the acceleration of the heel into the ground at heel strike.

The 'normal' subject only had one occurrence of a transient peak during the unbraced condition and none during the braced condition. When including the weight trials, the 'normal' subject had only three occurrences of a transient peak out of all 160 trials, one of these occurred during the braced condition.

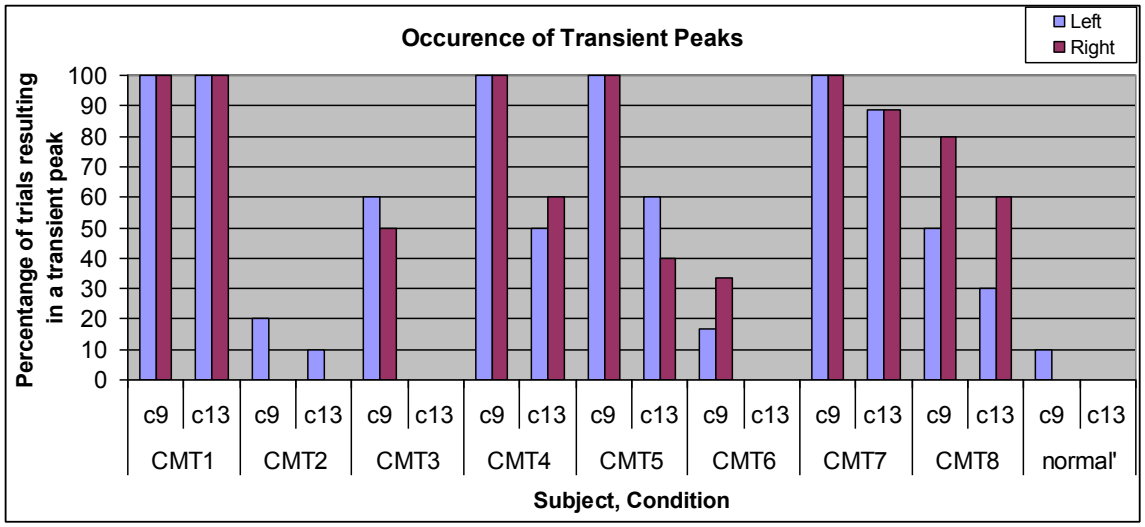

Figure 3.12: Occurrence of transient peaks

CMT1, CMT3, CMT5, and CMT7 all had a significant reduction in magnitude of the transient peaks. Subject CMT1 showed a high magnitude transient peak (average 97%BW) even though the transient peak did not diminish in magnitude while wearing the brace, it did decrease relative to the F_1 peak (see Figure 3.13). This subject had another orthotic brace that was tested and did not show a reduction in the transient peak. CMT3 showed low magnitude transient peaks during the unbraced condition that were completely eliminated during the braced condition with the HELIOS. This subject also

had another orthotic brace that was tested and showed a reduction in the transient peak, but did not eliminate it as did the HELIOS. CMT5 and CMT7 also showed a reduction in the occurrence of the transient peaks.

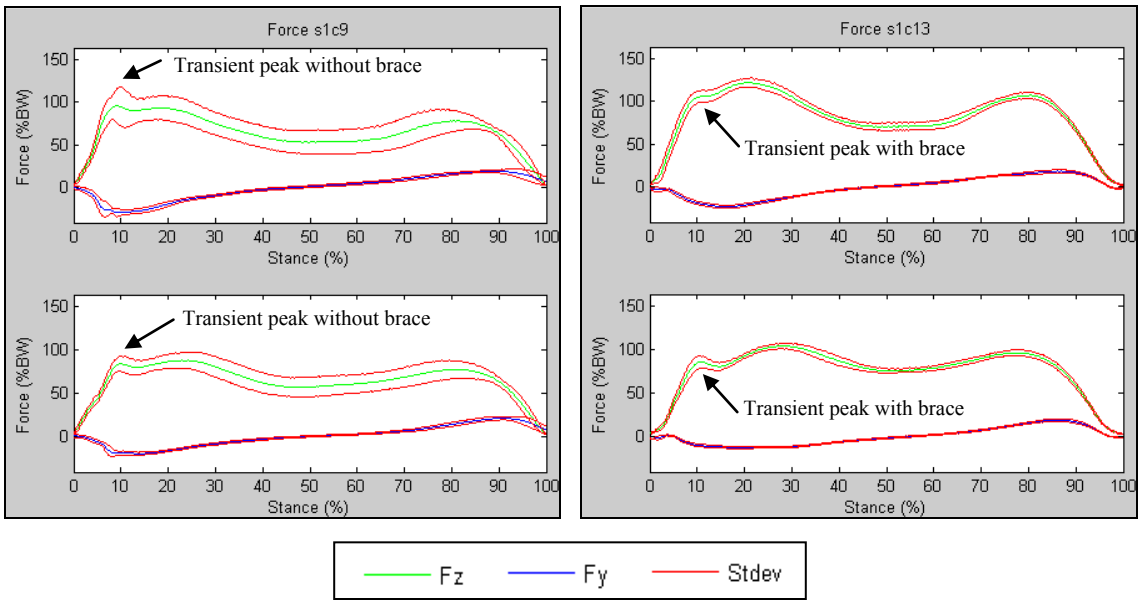

Figure 3.13: Transient peak reduction when HELIOS was worn by CMT1

The remaining CMT subjects, CMT2, CMT4, CMT6, and CMT8, did not show a significant reduction in magnitude of the transient peaks. CMT2 did not have a large occurrence of transient peaks during the unbraced condition, but no transient peaks occurred during walking with the HELIOS. CMT4 had a significant increase in magnitude of the minimum transient peak and a lower magnitude transient peak was eliminated both resulting in a smoother curve. CMT6 showed a few occurrences of transient peaks during the unbraced condition that were completely eliminated by wearing the HELIOS. For CMT8, the occurrence of transient peaks decreased on both feet.

3.3.2.2 Ground Reaction Variables of A/P Curve (F_y)

This section presents the forces and temporal variables of the anterior/posterior (A/P) curve (F_y) ground reaction forces. When walking speed is increased the braking force should increase in amplitude, instead it decreased in amplitude. The peak braking force peak (F_{yb}) significantly decreased for all subjects for at least one leg. Figure 3.14 shows the peak braking force for all subjects. The brace may be absorbing the posterior shear during heel strike too well, which results in the decreased braking force. In normal subjects, a decrease in braking force usually indicates a slower walking speed. The three subjects with the largest increase in walking speed (CMT2, CMT5, and CMT8) were also the three CMT subjects with a significant decrease in only one leg. It is possible that an increase in walking speed occurred when a significant decrease in the braking force was not seen, however the 'normal' subject also showed a significant decrease in only one leg and had a decrease in walking speed.

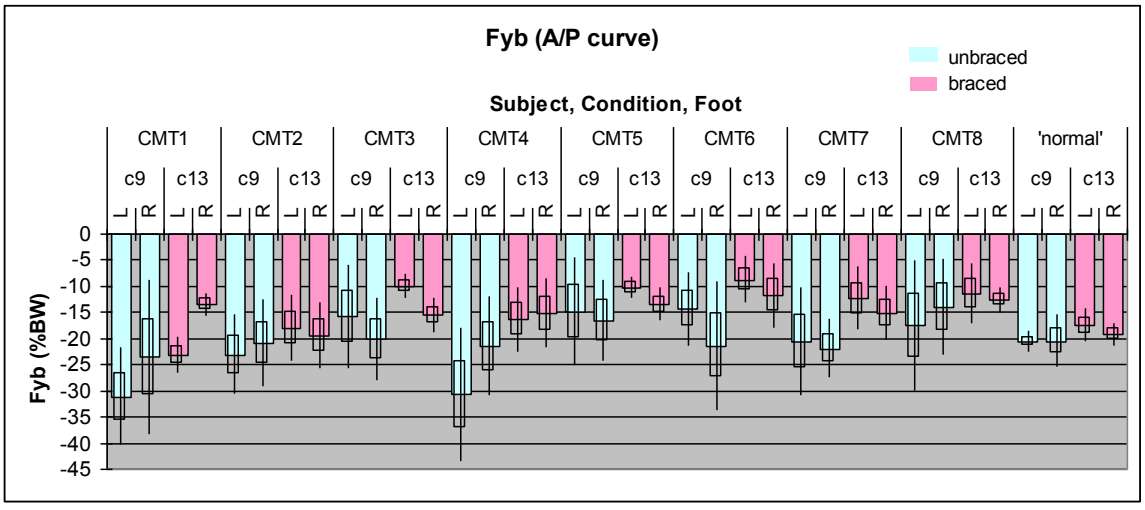

Figure 3.14: Peak braking force for all subjects

The propulsive force (F_{yp}), shown in Figure 3.15, significantly decreased in magnitude for CMT1, CMT2, CMT7, CMT8, and the 'normal' subject for at least one leg. The propulsive force should increase in magnitude as walking speed increases. CMT8 was the only subject showing a significant increase in this variable in at least one leg.

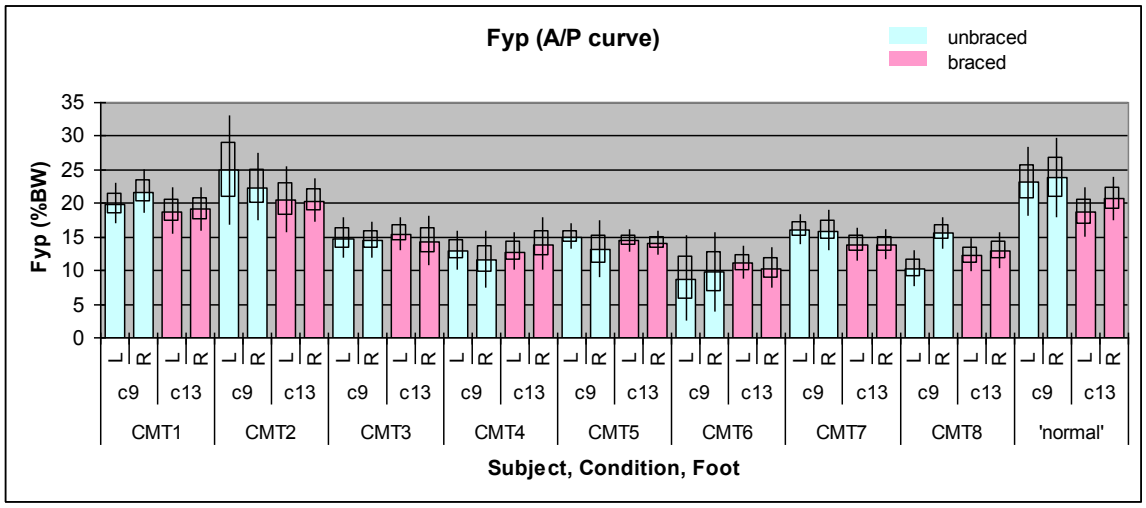

Figure 3.15 Peak propulsive force for all subjects

The one variable change that was common among all CMT subjects was the shifting of the braking force to occur later in stance (t_{yb}). Figure 3.16 shows the t_{yb} variable for all subjects in the unbraced and braced conditions. If the brace was acting as a shock-absorbing device at the beginning of stance it would make sense that the braking force would be delayed as the brace would absorb the impact and slow down the foot. The braking force time did not change significantly for the 'normal' subject. It is postulated that the brace did not act as a shock-absorbing device in this case since the 'normal'

subject was able to use the proper muscles to slow down after impact and was not relying on the brace.

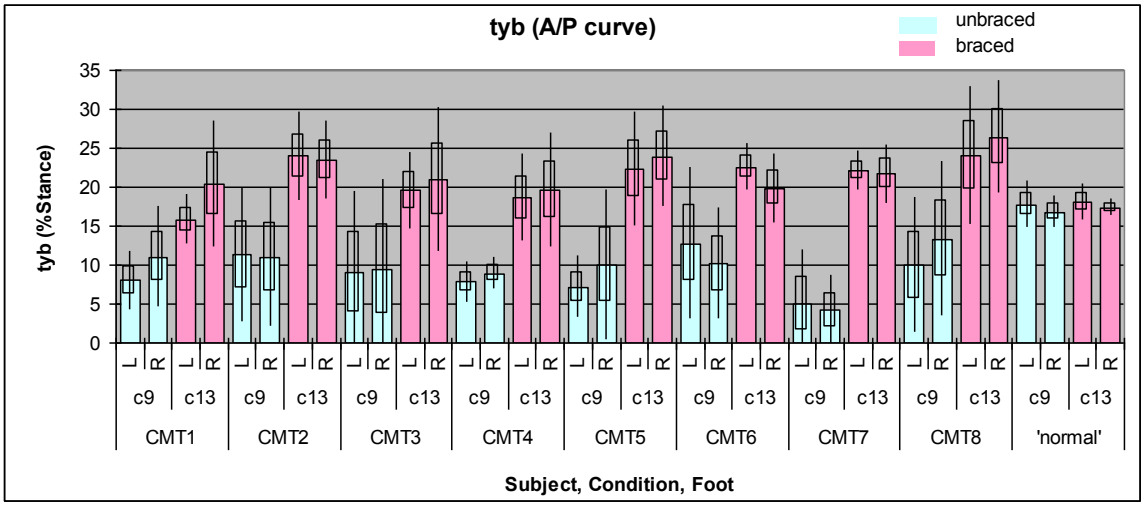

Figure 3.16: Time to reach peak braking force for all subjects

All the CMT subjects had a significant delay of the propulsive force during stance (t_{yp}) in at least one foot. Figure 3.17 shows this variable for all subjects. CMT8 and CMT1 were the two CMT subjects that showed the variable was significantly earlier to occur during stance in only one leg. The 'normal' subject also showed that the propulsive force was significantly earlier to occur but in both legs.

An increase in the variable, t_{yp}, means the propulsive force is delayed. It is possible that the brace was also acting as a shock-absorbing device as the brace was loaded at the pretibial shell after midstance. This would then delay the peak of the propulsive force. The 'normal' subject may show a decrease in this variable since the subject was not relying on the brace by leaning into the pretibial shell. This is perhaps why there was also a decrease in CMT1.

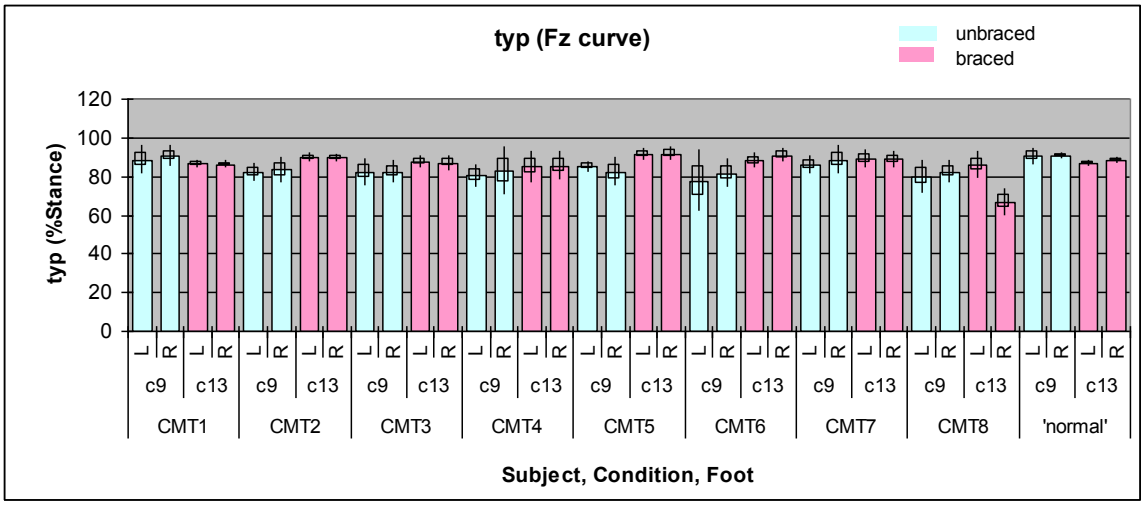

Figure 3.17: Time to reach peak propulsive force for all subjects

An odd case was presented by CMT8 where the right leg was presenting a plateau at the F_{yp} peak only in the braced condition, as shown in Figure 3.18. This was the only case where this plateau occurred among all of the subjects. This CMT subject also showed this plateau with another orthotic brace. It might be possible that the other orthotic brace (worn for 10 years) created this odd plateau by requiring the individual to walk with it in a certain manner, which then carried over to the new HELIOS brace. The left foot was not affected since the subject only had the left foot braced for less than a year with the old orthotic. This plateau was the reason why the peak propulsive force was not delayed and why the magnitude of the peak propulsive force decreased for this subject.

Even though the A/P propulsive and braking forces shifted, the transition time did not significantly increase for all of the subjects. Only one of the subjects, CMT3, showed a significant increase in the transition time in both legs. CMT1, CMT2, and CMT6 showed a significant increase in the right leg and CMT8 showed a significant increase in the left leg. Transition time for all subjects is shown in Figure 3.19.

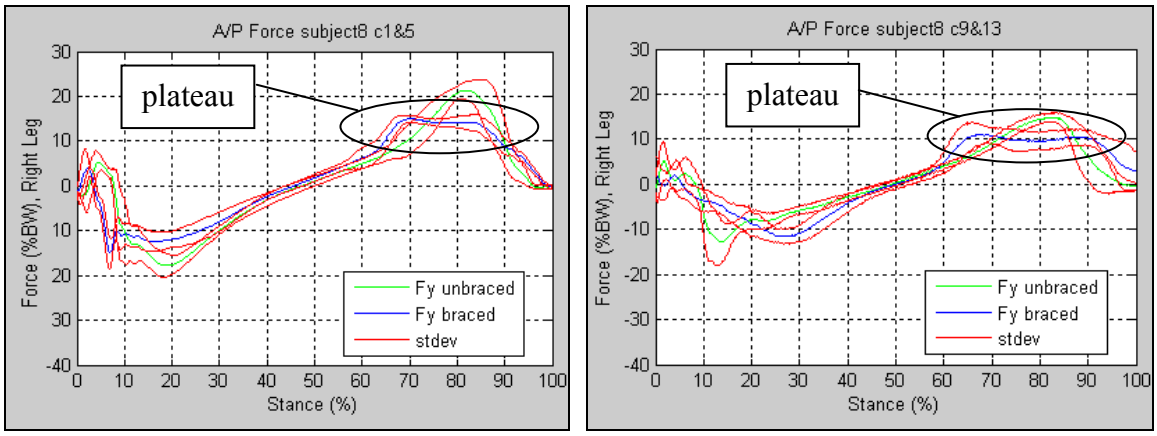

Figure 3.18: CMT8 right foot: (left) pre-test with current orthotic,

(right) post-test with HELIOS brace

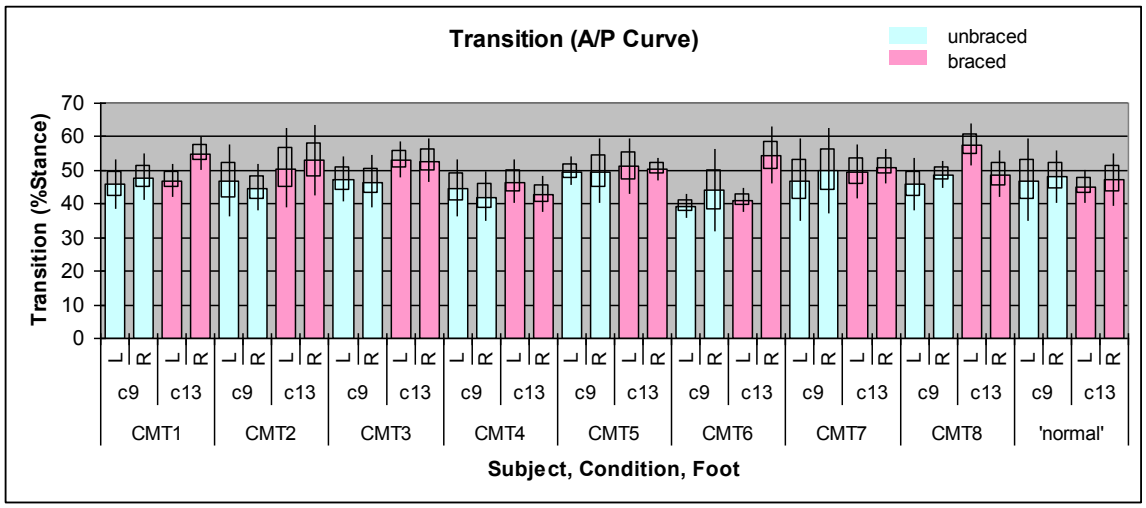

Figure 3.19: Transition for all subjects

3.3.2.3 Ground Reaction Forces Compared to Normative Ranges

All force and temporal variables were compared to the normative ranges from Chapter 2, Table 2.2. The average force and temporal variable values for all subjects are shown in Table 3.8 and Table 3.9, respectively. The variables highlighted in yellow were within one standard deviation of the normative range. One standard deviation (1SD)

statistically covers 67% of the normal population. Two standard deviations (2SD) cover 95%, shown in orange, and three standard deviations (3SD) cover 99.7%, shown in red. The values shown in white were outside the 3SD range.

The 'normal' subject showed values that were mostly within the 1SD range; however some variables were 2SD or 3SD. It is unclear why the 'normal' subject failed to be within these normal ranges. Perhaps it is because the subject is an athlete and this had altered their walking gait. The F_{min} peak was the only variable outside of the 3SD range. When the 'normal' subject wore the HELIOS brace some of the variables transferred to the 1SD range. One of the force variables, F_2, was below the normal range in the unbraced condition and then was above the normal range when the subject wore the HELIOS.

Since the 'normal' subject sometimes did not fit within the normal range of values it was only possible to compare the values of the CMT subjects relative to one another. Some of the variables were improved slightly and some were improved so well that they overshot the normative range. This phenomenon was shown for the braking force temporal variable, t_{yb}, which was consistently below the normative range for all CMT subjects during the unbraced condition and then was consistently above during the braced condition. This variable was within the normative range only for the 'normal' subject.

Table 3.8: Force variables

	F_1 (%BW) average	F_{min} (%BW) average	F_2 (%BW) average	F_{yb} (%BW) average	F_{yp} (%BW) average
CMT1 c9L	94.2	50.5	80.5	-31.2	19.9
CMT1 c9R	93.7	58.3	82.4	-23.6	21.7
CMT1 c13L	122.8	68.7	107.7	-23.3	18.8
CMT1 c13R	104.8	74.1	97.1	-13.5	19.1
CMT2 c9L	123.6	55.1	108.5	-23.2	24.9
CMT2 c9R	112.5	51.9	96.9	-20.9	22.4
CMT2 c13L	131.9	63.7	113.5	-18.0	20.4
CMT2 c13R	132.1	63.8	113.0	-19.5	20.4
CMT3 c9L	97.4	72.8	90.6	-15.9	14.7
CMT3 c9R	106.8	68.1	97.1	-20.2	14.6
CMT3 c13L	96.0	66.2	84.1	-10.0	15.5
CMT3 c13R	106.5	55.2	83.6	-15.5	14.3
CMT4 c9L	113.6	67.3	79.5	-30.7	13.0
CMT4 c9R	111.4	67.3	84.7	-21.6	11.6
CMT4 c13L	134.0	58.4	105.0	-16.4	12.8
CMT4 c13R	125.4	59.4	101.6	-15.2	13.9
CMT5 c9L	97.9	68.5	98.5	-15.0	15.0
CMT5 c9R	101.6	63.3	92.3	-16.7	13.1
CMT5 c13L	87.8	51.5	82.9	-10.3	14.4
CMT5 c13R	98.5	51.0	83.3	-13.5	14.1
CMT6 c9L	106.0	55.6	72.4	-14.4	8.8
CMT6 c9R	111.3	55.7	83.0	-21.4	9.7
CMT6 c13L	103.3	53.9	79.6	-8.8	11.1
CMT6 c13R	98.9	56.4	81.1	-11.8	10.3
CMT7 c9L	97.1	58.8	101.6	-20.6	16.0
CMT7 c9R	90.6	52.9	99.5	-21.9	15.9
CMT7 c13L	104.2	58.2	101.3	-12.4	13.9
CMT7 c13R	105.1	55.2	106.4	-15.2	13.8
CMT8 c9L	114.5	67.9	91.7	-17.6	10.3
CMT8 c9R	96.2	80.5	91.9	-14.1	15.5
CMT8 c13L	99.0	66.0	93.2	-11.5	12.2
CMT8 c13R	98.8	61.7	90.1	-12.7	12.9
'normal' c9L	99.4	40.0	100.7	-20.7	23.1
'normal' c9R	98.8	33.9	98.0	-20.6	23.8
'normal' c13L	124.9	70.0	115.6	-17.5	18.6
'normal' c13R	124.8	74.5	117.2	-19.3	20.7

Legend

- value is more than a 3 standard deviation difference
- value is within 3 standard deviation difference
- value is within 2 standard deviation difference
- value is within 1 standard deviation difference

Table 3.9: Temporal variables

	t_1 (%stance) average	t_{min} (%stance) average	t_2 (%stance) average	t_{yb} (%stance) average	t_{yp} (%stance) average	transition (%stance) average
CMT1 c9L	18.2	50.5	81.0	8.0	88.4	45.8
CMT1 c9R	22.4	48.2	80.1	11.0	90.7	47.9
CMT1 c13L	20.7	50.2	79.5	15.8	86.4	47.0
CMT1 c13R	27.8	51.7	77.7	20.4	86.0	54.9
CMT2 c9L	18.5	54.8	78.4	11.3	82.0	47.0
CMT2 c9R	18.7	55.7	78.5	11.0	83.4	44.7
CMT2 c13L	27.3	56.2	81.5	24.0	89.7	50.5
CMT2 c13R	26.9	55.6	81.3	23.5	89.5	52.9
CMT3 c9L	20.5	52.7	73.3	9.0	82.3	47.3
CMT3 c9R	21.4	50.7	77.8	9.5	82.4	46.5
CMT3 c13L	25.0	56.1	78.5	19.6	87.4	53.0
CMT3 c13R	24.0	54.7	79.3	21.0	86.8	52.7
CMT4 c9L	21.8	52.8	72.1	7.8	80.3	44.7
CMT4 c9R	23.8	49.2	67.8	8.9	82.7	42.1
CMT4 c13L	22.8	47.8	69.1	18.6	85.0	46.6
CMT4 c13R	24.5	44.4	62.2	19.7	85.4	42.8
CMT5 c9L	21.6	50.2	72.7	7.1	85.0	49.6
CMT5 c9R	20.0	42.6	72.4	9.9	82.2	49.5
CMT5 c13L	26.5	54.5	82.0	22.2	91.3	51.1
CMT5 c13R	26.8	52.3	80.9	23.9	91.7	50.3
CMT6 c9L	19.4	49.5	69.9	12.8	77.6	39.3
CMT6 c9R	21.4	50.3	77.0	10.1	81.6	43.9
CMT6 c13L	24.8	48.6	73.1	22.6	87.9	40.9
CMT6 c13R	25.9	55.0	80.0	19.8	90.9	54.2
CMT7 c9L	22.2	47.9	77.3	4.9	86.1	47.0
CMT7 c9R	20.3	56.2	78.5	4.2	88.6	49.8
CMT7 c13L	24.0	52.4	78.0	22.1	89.2	49.3
CMT7 c13R	23.9	50.4	78.1	21.7	88.8	50.9
CMT8 c9L	19.7	43.2	69.9	9.9	79.8	45.7
CMT8 c9R	27.3	56.3	75.3	13.3	82.4	48.7
CMT8 c13L	26.6	52.0	75.4	24.0	85.8	57.5
CMT8 c13R	27.8	49.8	70.9	26.4	66.7	48.7
'normal' c9L	25.1	50.8	81.4	17.7	90.3	47.0
'normal' c9R	25.0	49.6	80.3	16.8	90.6	48.1
'normal' c13L	25.0	49.5	78.0	18.1	86.8	45.1
'normal' c13R	23.1	47.1	79.3	17.3	87.9	47.2

Legend

- value is more than a 3 standard deviation difference
- value is within 3 standard deviation difference
- value is within 2 standard deviation difference
- value is within 1 standard deviation difference

3.3.2.4 Weight Trials of 'Normal' Subject

The 'normal' subject was the only participant that was tested in the unbraced and braced condition with the HELIOS during pre-test. All CMT subjects were only tested with the HELIOS during post-test. The 'normal' subject was also tested with different weights added during testing. When normalized for weight, there was not a significant difference in GRF variables between the unbraced and braced conditions when adding weight. Of course, there was a general increase or decrease in the amplitudes of the variables due to the weight increase but this was consistently seen for the braced and unbraced conditions and therefore, weight does not have an effect.

There was a significant difference in some GRF variables when comparing the unbraced and braced conditions in pre- and post-test. In pre-test the stance time decreased, whereas the stance time increased during post-test. The walking speed did not change significantly from pre- to post-test. This indicates that after adaptation with the brace, stance time increases during the braced condition without a change in walking speed. F_1, F_{min}, and F_2 were all significantly higher during post-test in the braced condition and the propulsive peak occurred significantly sooner during stance for post-test in the braced condition.

These changes suggest that after adaptation of the HELIOS the vertical force peaks (F_1, F_{min}, and F_2) increase and the propulsive peak will occur sooner in stance. During pre-test the braking peak (F_{yb}) amplitude significantly decreased in amplitude in the braced condition. This could indicate that before adaptation to the brace, the subject will have a significantly lower braking force. Also the propulsive peak (F_{yp}) was significantly higher in the pre-test unbraced condition than in the unbraced post-test condition. This is

interesting since the propulsive peak should increase with increasing walking speed and the pre- and post-test speeds were not significantly different. The data suggests that the 'normal' subject's propulsive peak during the unbraced condition was changed during post-test due to wearing the HELIOS.

3.3.3. Strain Gage Data

The braces of three CMT subjects (CMT1, CMT2, and CMT4) and one 'normal' subject were instrumented to provide strain data of the brace during human motion. All subjects were not instrumented due to limitations in the study. This was done to determine if the strain could be related to the GRF curves. The raw strain data of all ten walking trials for all eight strain gages are graphed for each instrumented subject and included in Appendix B. Graphs were broken down into left and right feet since each brace was unique.

Figure 3.20 shows the side profile of each instrumented brace. All of the HELIOS braces were hand fabricated and custom made for each individual subject. The braces for the CMT subjects look fairly uniform from the right brace to the left brace. The 'normal' subject braces had slightly different strut lengths. This was probably just manufacturing deviations and not intentional based on the normal subject's leg geometry. Appendix D shows the geometry of all braces at different orientations.

Shown in Figure 3.21 is the average strain data for CMT1, CMT2, CMT4, and the 'normal' subject. Each data line represents the average of all ten walking trials. All four graphs show a negative strain at the start of stance followed by a positive strain at the end of stance. The point at which the strain moves from negative to positive (crosses the x-axis) can be termed the strain transition point. At the beginning of stance the negative

strain corresponds to the struts being bent backwards; the outer surfaces of the struts are in compression. At the end of stance the positive strain corresponds to the struts being bent forward; the outer surfaces of the struts are in tension.

Maximum (tensile) strains and minimum (compressive) strains are graphed and shown in Appendix E for all subjects. Also included are the strains for the 'normal' subject under conditions 14 (5%BW), 15 (10%BW), and 16 (15%BW). Higher strains were seen in all three CMT subjects as compared to the 'normal' subject. This means the CMT subject braces had a larger change in displacement (bending was greater) as compared to the 'normal' subject braces. This could be due to the CMT subjects relying more on the brace during gait. During gait, the brace acts to absorb the impact during braking and prevents foot drop. The brace then supports the tibia during propulsion when the subject applies more pressure to the pretibial shell at the front of the brace before the swing phase. The struts experience both compression and tension to help absorb impact and stabilize the CMT subject during gait.

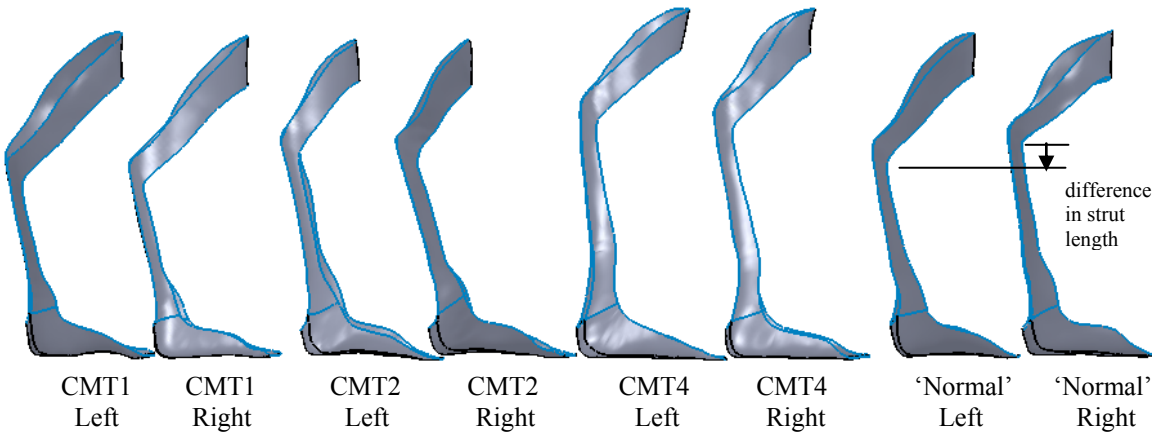

Figure 3.20: Brace geometry of instrumented braces

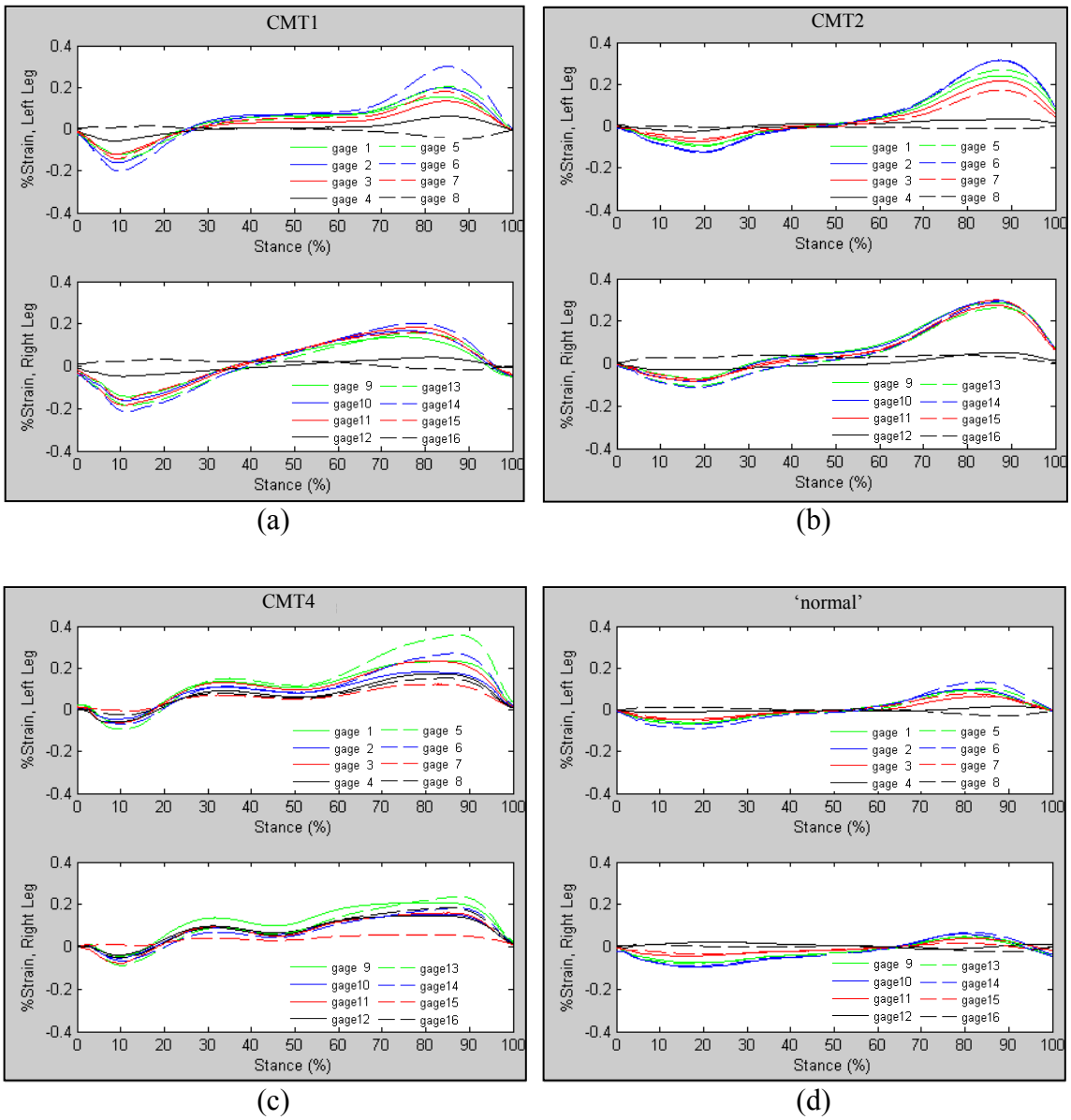

Figure 3.21: Average strain data during human testing

(a) CMT1, (b) CMT2, (c) CMT4, (d) 'normal'

Chu, et al., did extensive research on the stress measurement of a polypropylene brace using FEA and experimental testing. It was determined that the high stress location of a standard polypropylene brace would be in the middle-lower lateral neck region [41, 37]. This was not the case with the HELIOS brace, most likely due to differences in geometry.

The lowest strain area was the ankle location. This is perhaps because the brace includes extra layers of fabric at the ankle to ensure the brace did not fail at this location.

CMT1, CMT2, and the 'normal' subject showed similar results with the highest strain seen in the middle of the struts (gages 2, 6, 10, and 14). CMT4 showed a slightly different profile with the highest strain seen in the top of the struts (gages 1, 5, 9, and 13). All three CMT subjects also transition much sooner to a positive strain as compared to the 'normal' subject. Overall, results show that the highest strains are seen in the middle or top of the strut during stance followed by strain in the lower part of the strut. The lowest strain is usually seen at the ankle (gages 4, 8, 12, and 16).

The different strain profile of subject CMT4 was probably due to that subject's characteristic gait and not necessarily from the severity of CMT since subject CMT2 had the most severe CMT of all subjects. A slight decrease in strain was seen in CMT4 at around 50% stance that was not seen in the other subjects. It is possible that shortly after heel contact this subject falls into the brace hitting the tibia against the pretibial shell and then stabilizes before leaning into the pretibial shell again before toe off.

In most of the subjects, the medial side of the brace was strained more than the lateral side as shown in Figure 3.22. The subject with the most even distribution of maximum strain between medial and lateral was CMT2 who had the largest increase in walking speed. Perhaps the brace worked better for this individual because both struts were used evenly. It would be interesting to increase the strength of the medial side for subject CMT4, who had the largest difference between medial and lateral strains, to see if evening out these strain levels would improve walking speed.

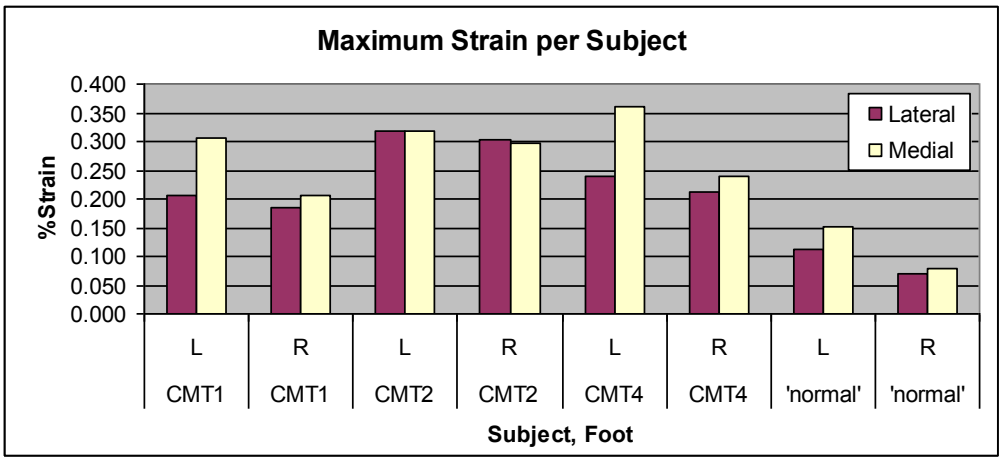

Figure 3.22: Maximum strain values for all subjects

The trials of the 'normal' subject with extra added weight showed that maximum and minimum strains generally increase as weight increases. The exception to this is the 15 %BW condition. In this case, the left brace maximum strain increased more but the right leg decreased. An example of this is shown in Figure 3.23., where the lateral maximum strains are shown for the left and right brace. This sudden change could be due to differences in the brace geometry as discussed earlier for the 'normal' subject. It is possible that the additional 15 %BW requires the 'normal' subject to walk differently and rely more on the left foot (more dominant) than the right foot.

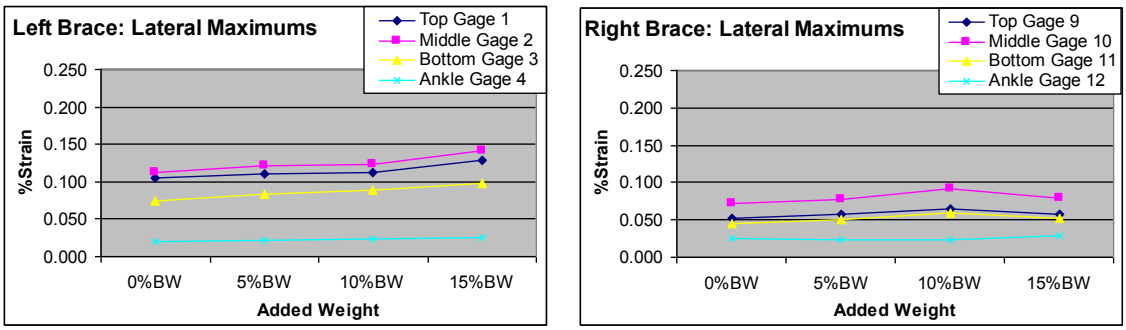

Figure 3.23 Lateral maximum strains for 'normal' subject with added weight

3.4 Linking Gage Strain and A/P Curves

Figures 3.24 - 3.27 show the strain curves and the A/P curves graphed side by side. It is evident that during the braking peak of the A/P curve, the brace struts were in compression and during the propulsive peak of the A/P curve, the brace struts were in tension. This section compares the temporal variables of the strain curves to the temporal variables of the A/P curve to determine the connection between brace strain and A/P force. Appendix F shows graphs of when the temporal variables occur for each subject during stance.

Most subjects had maximum compressive strain at the medial ankle toward the end of stance except for CMT2 (right leg only) and CMT4 where the medial ankle was strained at the beginning of stance. All subjects showed the maximum compressive strain for all other gages occurred before the braking force (F_{yb}). This was the only temporal variable that occurred similarly for all instrumented subjects.

Strain transition occurs just after F_1 and before A/P transition for CMT1 and CMT2 while CMT4 strain transition occurs just before F_1 and during the braking peak (F_{yb}). The normal subject strain transition occurs just after the A/P transition. It makes sense that the normal subject would have a delayed strain transition because the normal subject had full use of the leg muscles and did not need the pretibial shell to support the tibia before A/P transition. CMT4 flexes the brace even sooner than the other two CMT subjects. It is hypothesized that CMT4 was prematurely leaning into the pretibial shell during braking and then leaned into the pretibial shell again near the A/P transition. This individual may be purposefully doing this to increase speed, but since the walking velocities of this subject do not increase considerably, this technique does not work.

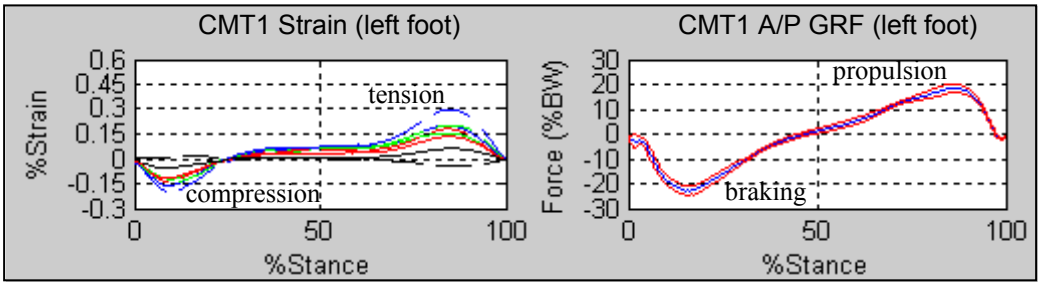

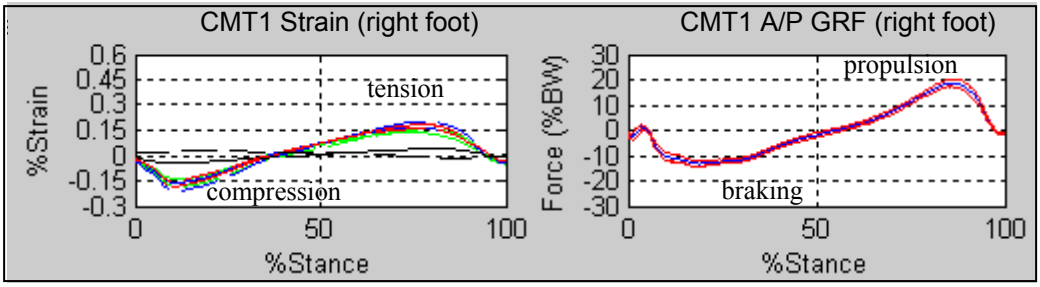

Figure 3.24: Strain and A/P curves for CMT1 (top) left foot, (bottom) right foot

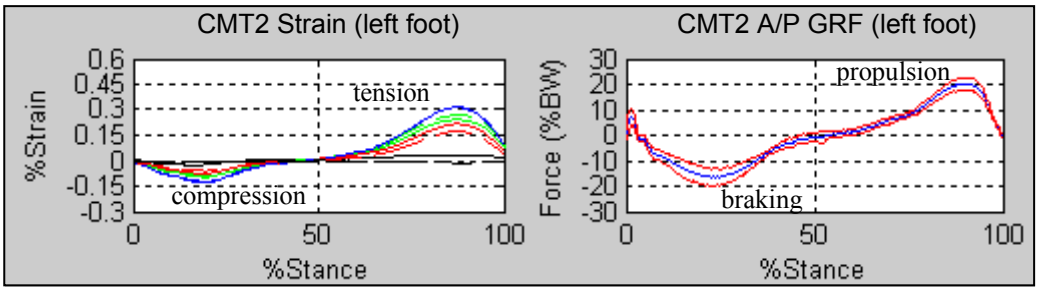

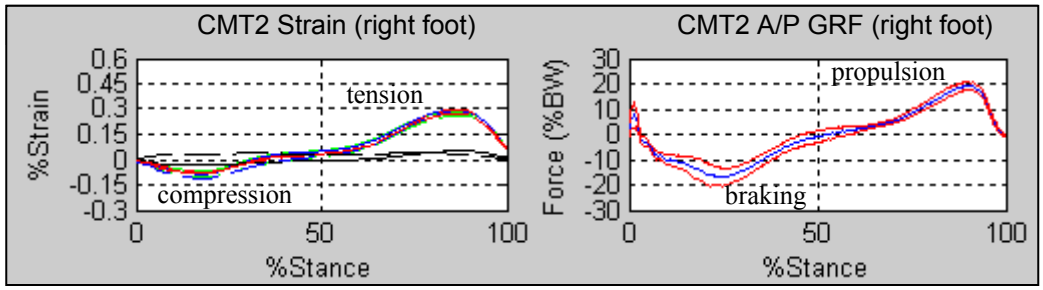

Figure 3.25: Strain and A/P curves for CMT2 (top) left foot, (bottom) right foot

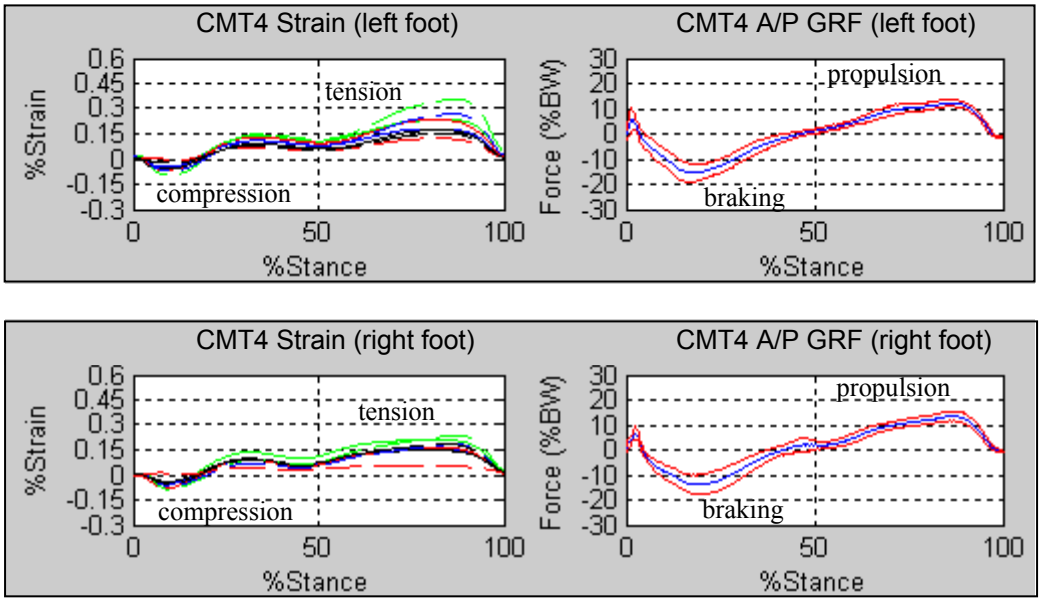

Figure 3.26: Strain and A/P curves for CMT4 (top) left foot, (bottom) right foot

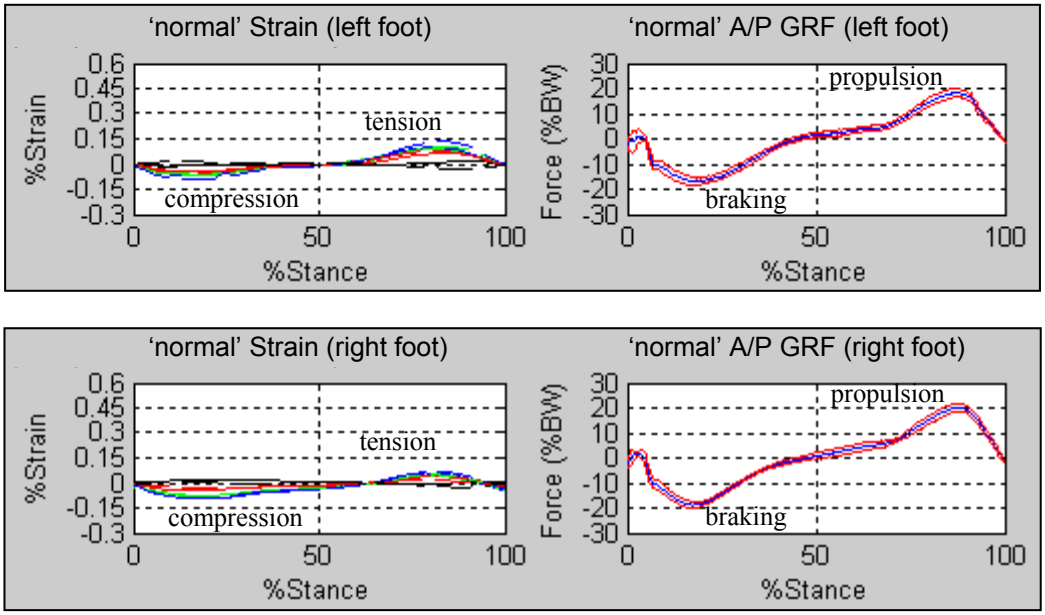

Figure 3.27: Strain and A/P curves for 'normal' subject (top) left foot, (bottom) right foot

The medial ankle tends to show maximum tensile strain values at the beginning of stance before strain transition. CMT4 was the only subject that had maximum stress at the medial ankle near the propulsion peak (F_{yp}). CMT1, CMT2, and the normal subject showed the remaining maximum tensile strains occur near the F_2 peak and before the propulsion peak (F_{yp}). CMT4 was the only subject that showed maximum strains closer to the propulsion peak (F_{yp}) and even occurred after the peak (F_{yp}). This would indicate that CMT4 was stressing the brace by leaning into the pretibial shell while the propulsion peak (F_{yp}) was occurring and therefore, was probably not benefiting from the energy release of the brace during propulsion. If the brace was stressed to the maximum before the propulsion peak it would allow time for the brace to spring back and assist the subject during propulsion just as the peak (F_{yp}) was occurring. The maximum strains could be delayed for CMT4 because this subject was leaning into the brace prematurely before A/P transition and was probably not able to rebound quick enough to lean into the brace again before the propulsion peak (F_{yp}).

CMT2 was the only subject with a nonzero strain at toe off (100%Stance). This subject was also the only subject of the four instrumented subjects with a substantial increase in walking speed. Perhaps, CMT2 had an increase in walking speed because this subject leaned into the pretibial shell enough so that the brace was still recovering from maximum strain even after the foot left the ground.

CHAPTER 4

EXPERIMENTAL MECHANICAL TESTING

4.1 Mechanical Test Setup

An MTS Axial/Torsion Material Test System was used with a 500 lb DSM-500 dual stud mount load cell. The National Instruments data acquisition system was used to collect data from the load cell, strain gages, and deflectometer (Epsilon Model 3540 Displacement Gage).

The HELIOS brace resembles a quarter-elliptic or simple cantilever flat spring so the goal of mechanical testing was to record the spring properties and not the individual material properties. Therefore two experimental setups were used to determine the relationship between force, strain, and displacement.

The HELIOS foot plate is well reinforced and is not meant to flex during gait. No incidents of failure have been observed in this area. It was determined the force plate could be fixed during a mechanical AFO test without affecting results. This allowed the remainder of the brace to be left free to deform due to the applied force. It was deemed more important to look at the deformation of the struts of the HELIOS than of the footplate due to the location of the strain gages used during the walking trials.

The first test was a horizontal cantilever flexure configuration which is shown in Figure 4.1. This test closely replicates the normal force applied to the pretibial shell during toe off. The bending of the brace creates tension in the strain gages on the strut. This horizontal flexure test should replicate the strain seen at the F_{yp} peak on the GRF curve and provide the applied pretibial shell force.

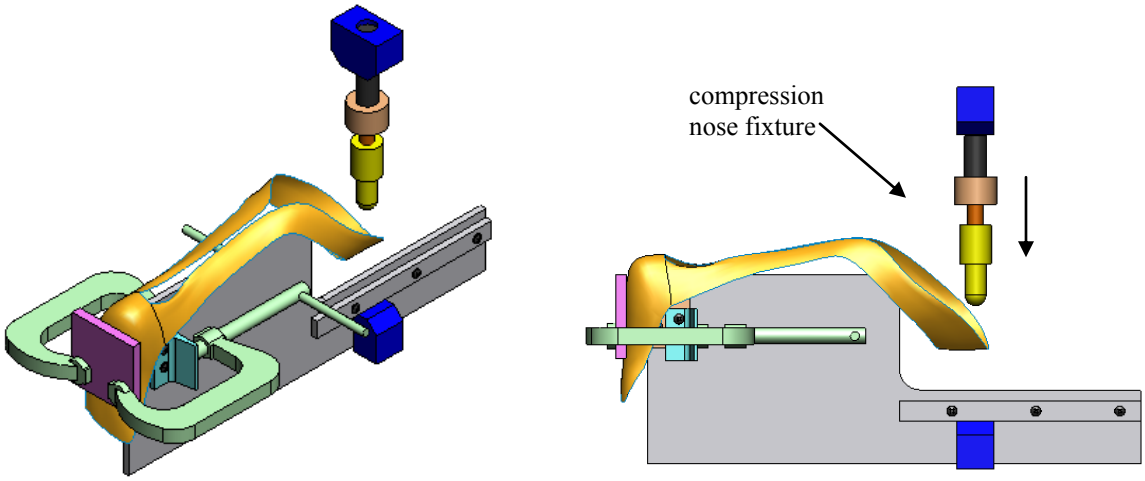

Figure 4.1: Horizontal cantilever flexure test (strain gages in tension)

The second test is shown in Figure 4.2 and is a vertical compression test that provides the response of the brace when a force is applied vertically. These results will be compared with the horizontal cantilever flexure test to determine differences in strain along the struts. The brace was clamped at the toe and heel to the lower platen and then compressed with an upper platen which enabled the brace to move forward at the top. This was expected and is considered to be the natural movement of the brace. The maximum horizontal distance traveled by the top of the brace was recorded using a dial gage.

Each brace was clamped into the fixtures a little differently to achieve proper alignment with the test fixtures. Figure 4.3 and Figure 4.4 show the actual test setups for the horizontal cantilever flexure test and the vertical compression test, respectively. The brace was mounted in the horizontal cantilever flexure fixture so the compression nose hit the pretibial shell at the lowest point of the curve. The struts of the brace were lined up to split center when looking down on the brace from above the brace. To achieve this

alignment, the back plate needed to be adjusted down or up and this caused movement of the brace at the 'ankle' during testing. For the vertical compression test, the brace was placed flat on the lower platen and then clamped at the heel and toe to minimize the foot plate loosing contact with the lower platen.

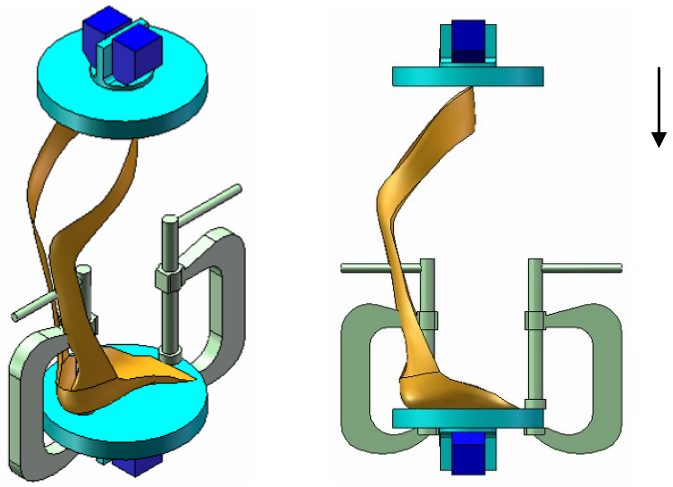

Figure 4.2: Vertical compression test (strain gages in tension)

The experimental setups were performed under quasi-static loading conditions in addition to dynamic loading conditions. Each condition was tested four times and then averaged. The quasi-static rate was chosen as 1.016 cm/min (0.4 in/min) and the dynamic rate was chosen as 609.6 cm/min (4 in/sec). The dynamic rate should have been based on half the stance time for the horizontal tests since these tests replicate loading and unloading during stance, but the limitations of the test equipment did not allow such a high rate. Shown later in the results section, the chosen 609.6 cm/min (4 in/sec) rate was too high of a rate for the test equipment and a slower rater was eventually used for the dynamic tests. The NI equipment recorded measurements at 15 Hz for the quasi-static

tests and at 1080 Hz for the dynamic tests. Data were collected while the brace was being loaded and unloaded.

Figure 4.3: Actual test setup for horizontal cantilever flexure test

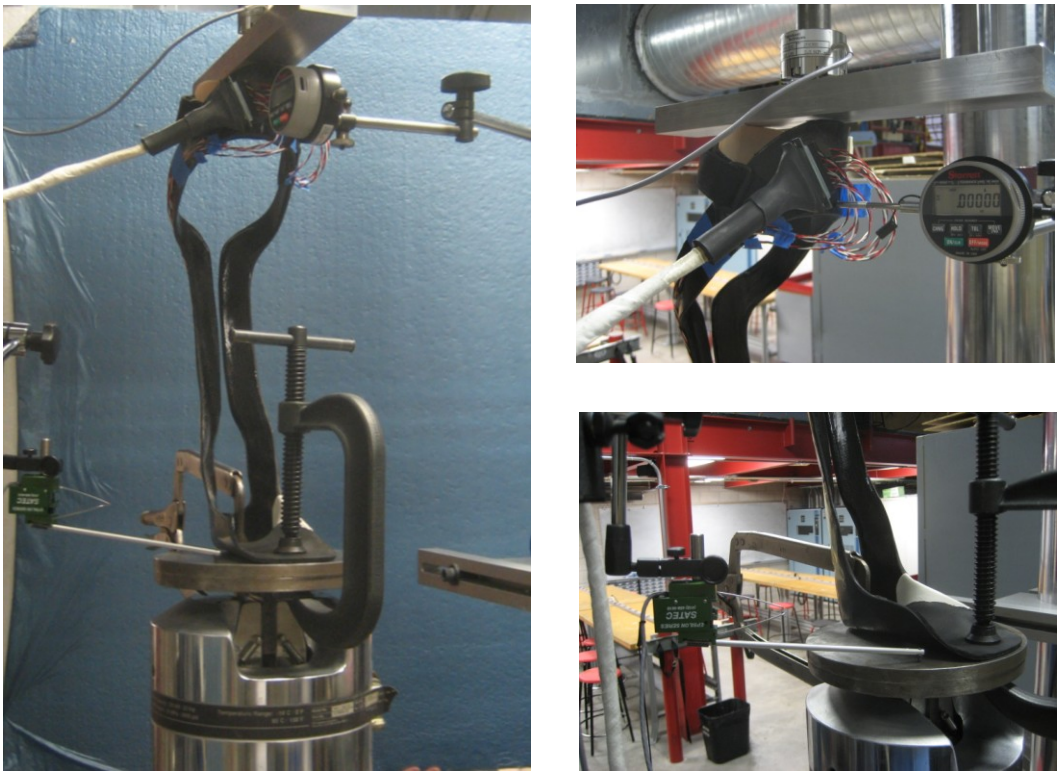

Figure 4.4: Actual test setup for vertical compression test

4.1.1. Data Reduction

The mechanical testing yielded the relationship between the force being applied to the pretibial shell and the strain seen in the struts of the brace. The mechanical tests also yielded the associated displacement at the pretibial shell. This provided a relationship between strain, pretibial force, and pretibial displacement. Since the gage strain was collected during human motion tests, it was possible to know what the pretibial force and displacements were during those tests. This can then be related to the GRF curves since all three will be in terms of %stance. Figure 4.5 shows the four variables that can be combined in order to establish this relationship.

Data reduction was performed using a combination of Matlab and Excel. The loading and unloading portions of the data were separated from one another by graphing the displacement vs. time curve. Figure 4.6 shows an example of this curve for the static and dynamic tests, respectively. The loading portion is defined as the data to the left of the peak and the unloading portion is defined as the data to the right of the peak. A displacement of 0.05 cm was used as the cutoff to remove noise from the beginning and end of the raw data.

It was necessary for some of the tests, to take the maximum displacement past the capabilities of the 2.54 cm deflectometer maximum. In these cases, the load and unload curves of the raw data were fit to linear regressions and a theoretical peak point based on the intersection of these two regressions was used to divide the raw data into a load portion and an unload portion. Examples of this for three cases is shown in Figure 4.7.

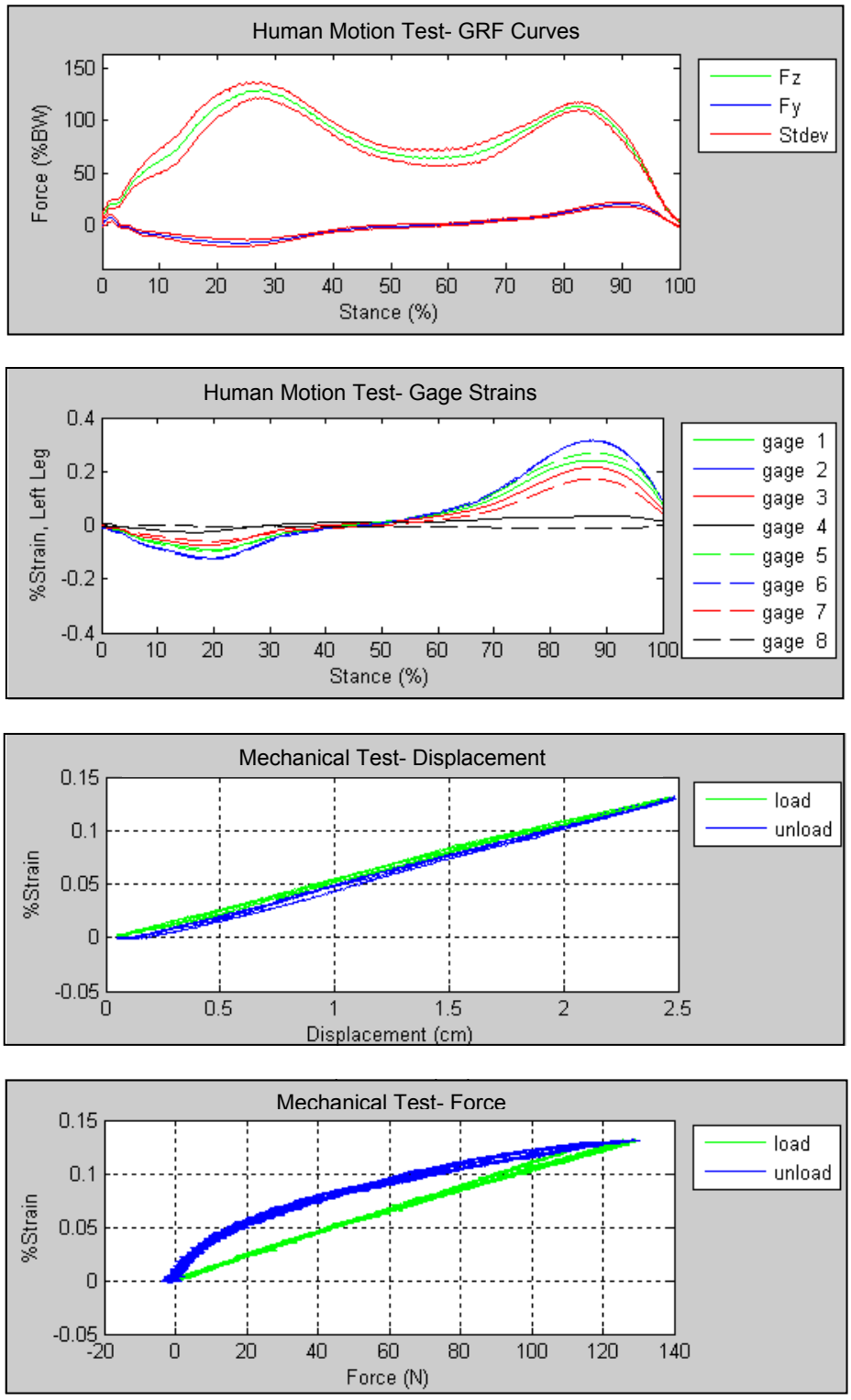

Figure 4.5: Relating GRF-strain-pretibial force-pretibial displacement

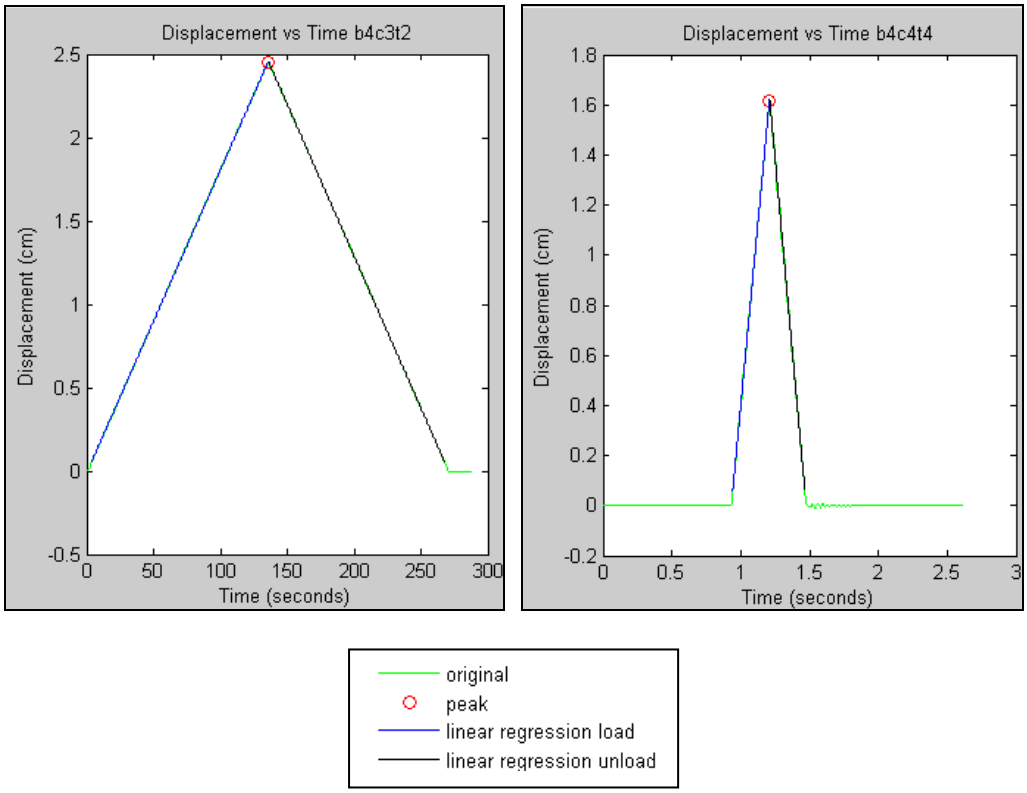

Figure 4.6: Displacement vs. time (left) static test, (right) dynamic test

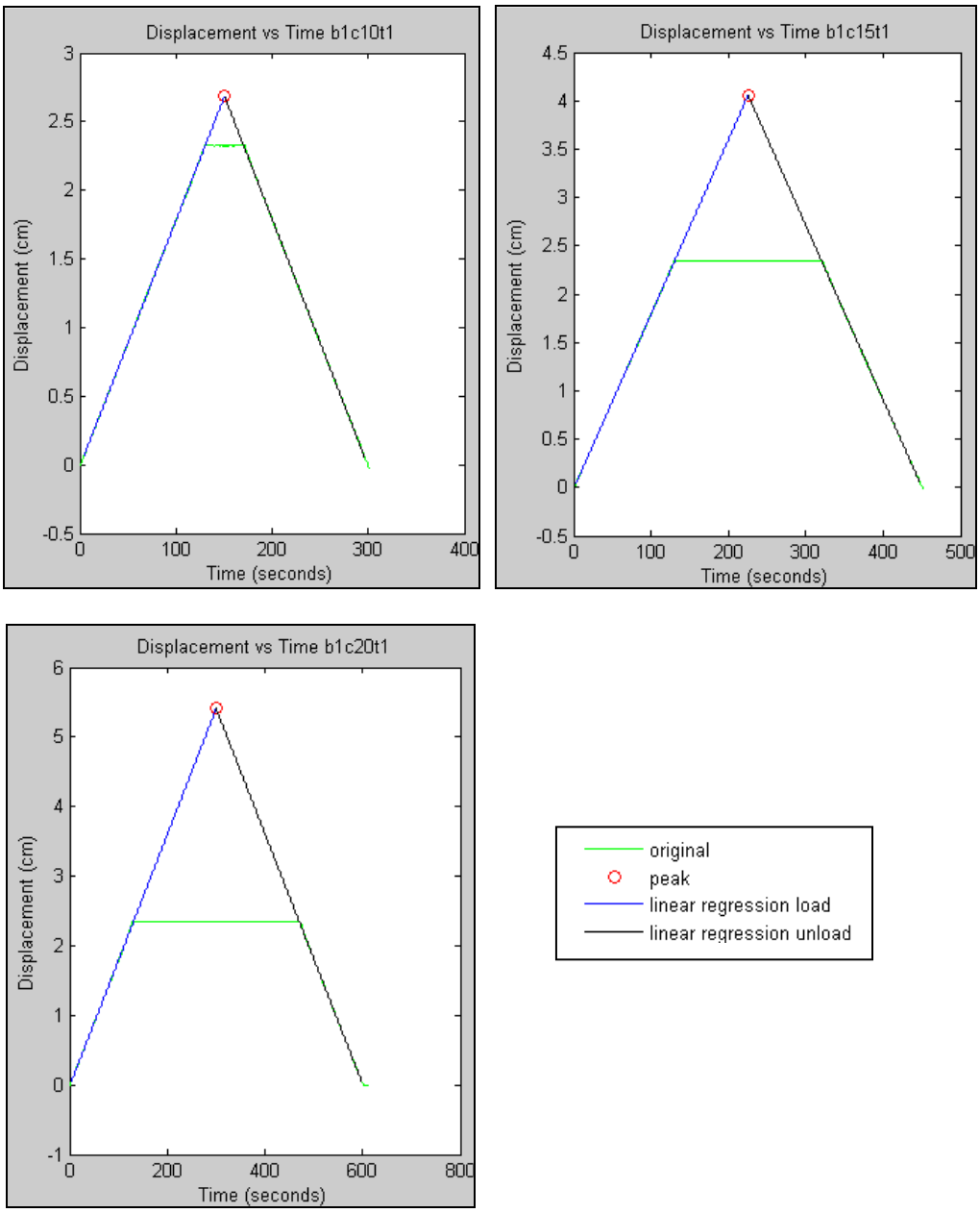

Figure 4.7: Displacement vs. time (a) 2.54 cm max, (b) 3.81 cm max, (c) 5.08 cm max

4.2 Results of Experimental Mechanical Testing

Experimental mechanical testing was performed to accomplish two goals. The first was to determine the force vs. displacement relationship of each brace to validate FEA results. The second was to relate the strain of the brace struts seen in the mechanical tests

to the strain of the brace struts seen in the human motion tests. This relationship allowed the force and displacement at the pretibial shell to be determined. Therefore, graphs are presented as force vs. displacement (for FEA), in addition to strain vs. force and strain vs. displacement (for human motion). The force and displacement data always represent the data taken from the load cell and deflectometer. The strain is always the measured strain from the gages located on the brace struts.

All eight instrumented braces were tested and are labeled as shown in Table 4.1. Four test conditions based on the configuration and the loading rate are defined in Table 4.2. Each test condition was performed four times to eliminate the possibility of error and to prove repeatability. All subsequent data are labeled by the brace number and condition number. For example, a graph of data for brace 1, condition 3 is labeled ‘b1c3’.

Table 4.1: Tested braces

Brace Number	Foot	Subject
1	Left	'normal'
2	Right	'normal'
3	Left	CMT4
4	Right	CMT4
5	Left	CMT2
6	Right	CMT2
7	Left	CMT1
8	Right	CMT1

Table 4.2: Conditions

Condition	Configuration	Loading Rate
1	vertical compression	static
2	vertical compression	dynamic
3	horizontal cantilever flexure	static
4	horizontal cantilever flexure	dynamic

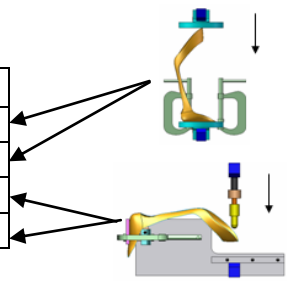

4.2.1 Loading and Unloading Characteristics

Loading and unloading data were collected for the mechanical tests and are graphed with respect to gage strain, pretibial force, and pretibial displacement. All graphs show the loading portion of the curve in green whereas the unloading portion is shown in blue. Also, all braces were tested four times in the same loading configuration, so all trials are included in each graph.

Shown in Figure 4.8 are curves of force vs. displacement for all eight braces. The graphs show that the brace loaded and unloaded in a different manner. The load and unload curves for all the braces resemble a bow shape, where the loading is fairly linear and the unloading is nonlinear. The HELIOS was fabricated from material that can be assumed to be linear-elastic. However, when tested in a horizontal cantilever fashion, it acts as a nonlinear spring and resembles a viscoelastic material, just like human tissues.

The load-deflection curve also resembles a hyperelastic material but only on first loading. Unlike a hyperelastic material, the HELIOS does not show the Mullins effect. When reloaded the brace would retrace the load line, not the unload line as seen with hyperelastic materials. No softening was seen during the four different tests; there were slight variations (no more than 3%) but not a definite decline in force at the peak displacement. The braces were tested after considerable use and perhaps the brace was able to reach a cyclic stability point. Since loading was consistent, this would indicate loading was occurring before the yield point and that the fiber/matrix was not delaminating, not permanently deforming, or undergoing any microtearing/cracking.

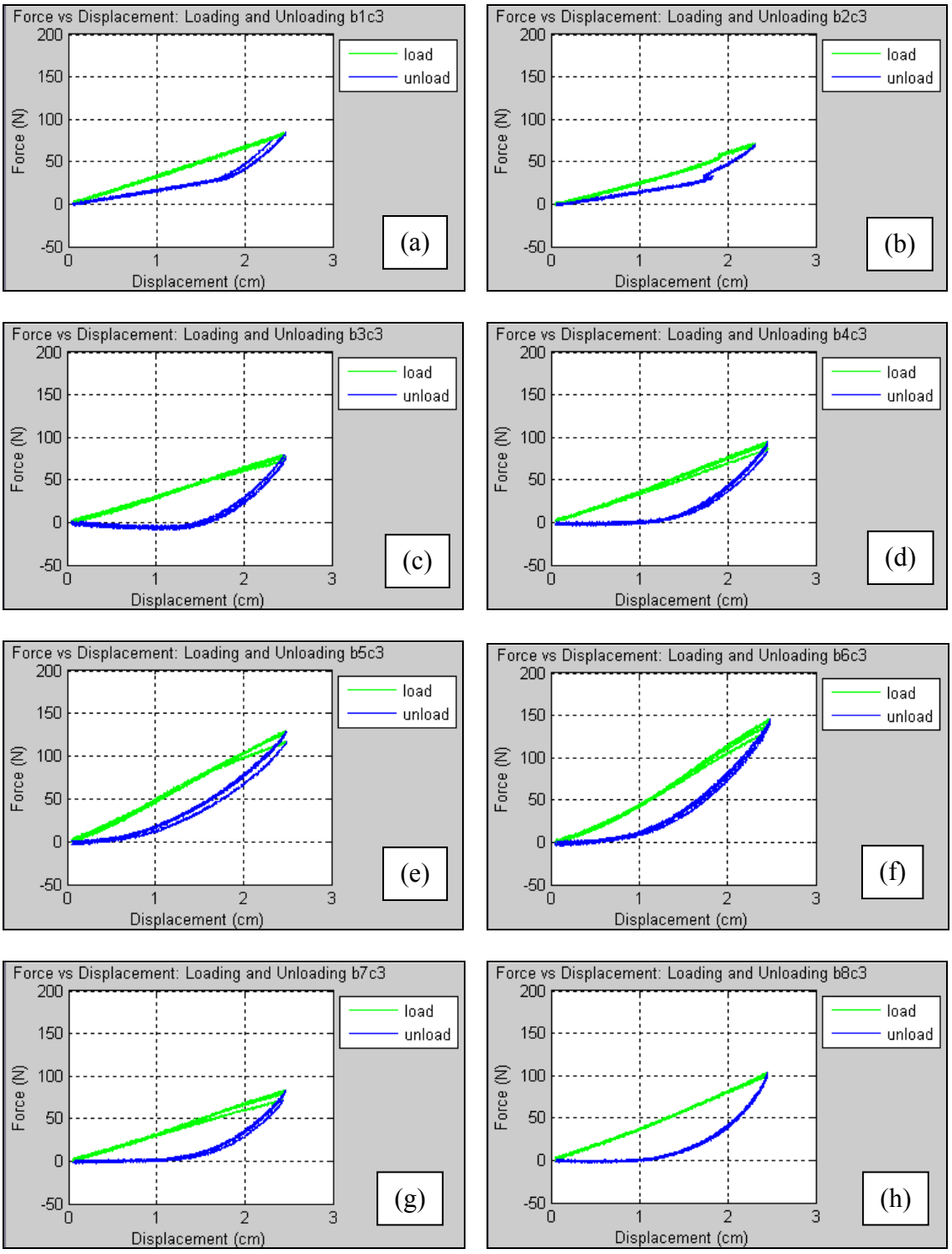

Figure 4.8: Force vs. displacement curve for all braces tested in configuration 3 (horizontal cantilever flexure) (a) brace 1, (b) brace 2, (c) brace 3, (d) brace 4, (e) brace 5, (f) brace 6, (g) brace 7, (h) brace 8

The unloading curves can be broken into two sections to adequately describe unloading. Figure 4.9 defines the two unloading sections as “initial unload” and “terminal unload”, which are defined on either side of the break point. Initial unload is the section where the brace begins to unload from the maximum displacement point and terminates at the break point. Terminal unload is the section that begins at the break point and then terminates at the point where the brace returns to the original start position.

All of the braces had a distinct break point for conditions 1 and 2 (vertical compression) most likely because the load was applied vertically to the braces causing the struts to buckle. However, for conditions 3 and 4 (horizontal flexure) only braces 1 and 2 for the ‘normal’ subject had distinct break points. Figure 4.10 shows an example of a curve where the break point is more difficult to define. In this case the break point was chosen where the slope of the initial unload line begins to change significantly. In the next subsection a more in-depth analysis is undertaken to determine the break point.

The break point indicates that during unloading the brace acts as a series of springs with different stiffness values. In some cases where the break point was distinct, there are just two different spring stiffness values. In this case, one spring releases first and the second spring follows after the break point has been reached. However, when the unload portion is a curve without distinct straight sections, there are multiple spring stiffness values releasing at different times during unloading.

The energy stored by the brace is the area under the load curve. The energy being released during unloading can be described as the area under the unload curve. The area between the load and unload curves is dissipated energy due to internal energy, friction, heat, or sound.

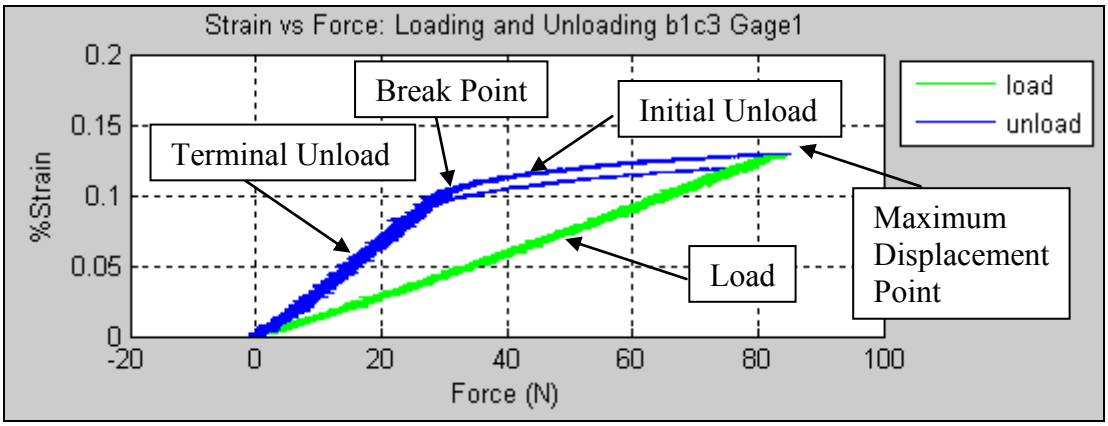

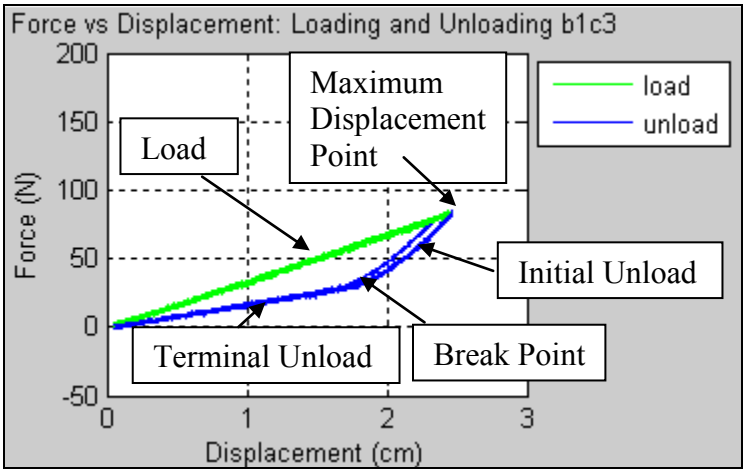

Figure 4.9: Curve characteristics

It is interesting to note that the subjects with the smallest increase in walking speed show the same force vs. displacement profile. At approximately 1.0 cm the force goes to zero. After the break point for CMT1 and CMT4 no energy was released but for CMT2 and the 'normal' subject, energy was still being released. This could potentially be one of the possible reasons why CMT1 and CMT4 show a smaller increase in walking speed as compared to CMT2.

Shown in Figures 4.11 - 4.13 are graphs for the 'normal' subject left brace tested under condition 3 (static horizontal cantilever flexure test). Figure 4.11 shows that force and displacement decreased equally until the break point was reached. After the break

point, the force decreased slowly as compared to the faster decreasing rate of the displacement. Figure 4.12 shows the strain of each individual strain gage vs. displacement and Figure 4.13 shows the strain of each individual strain gage vs. force. The strut gages (1, 2, 3, 5, 6, and 7) for brace 1 retained a higher strain value with respect to force during unloading until the break point.

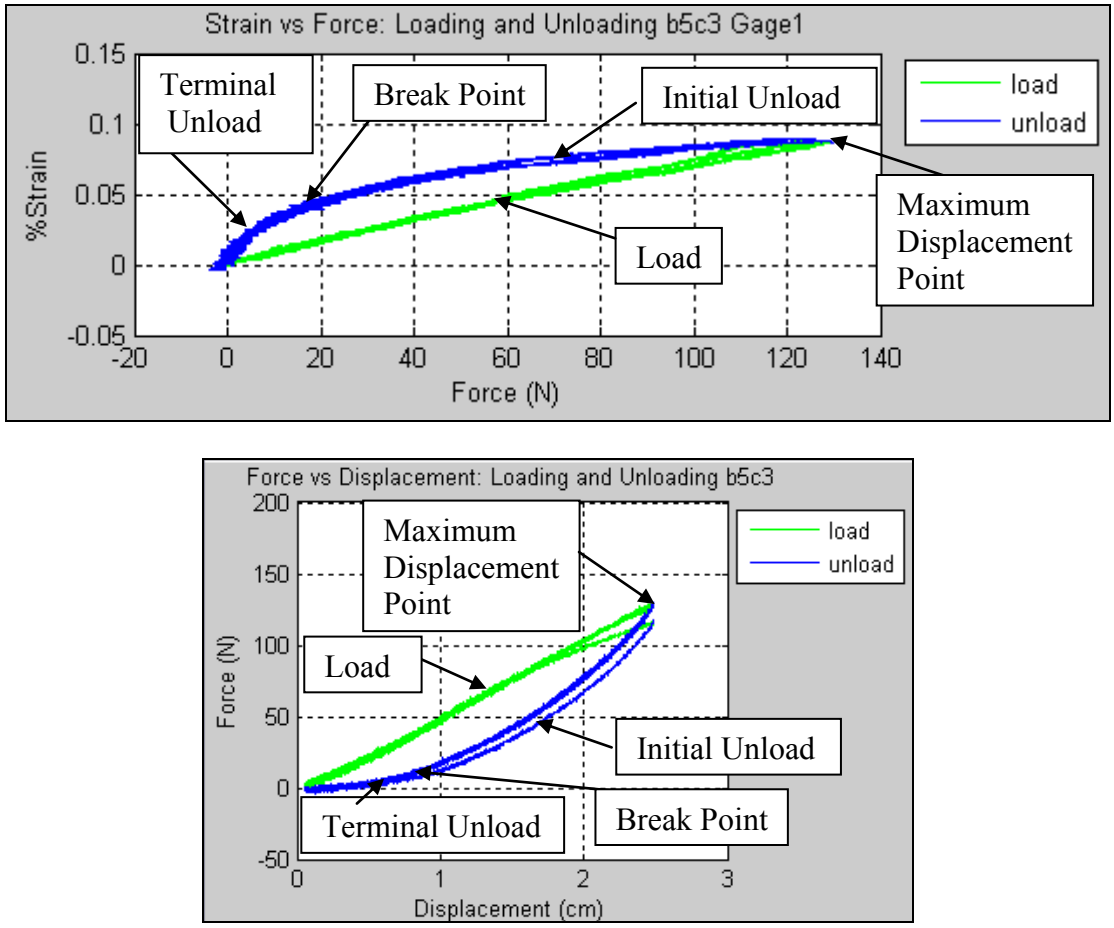

Figure 4.10: Unclear break point

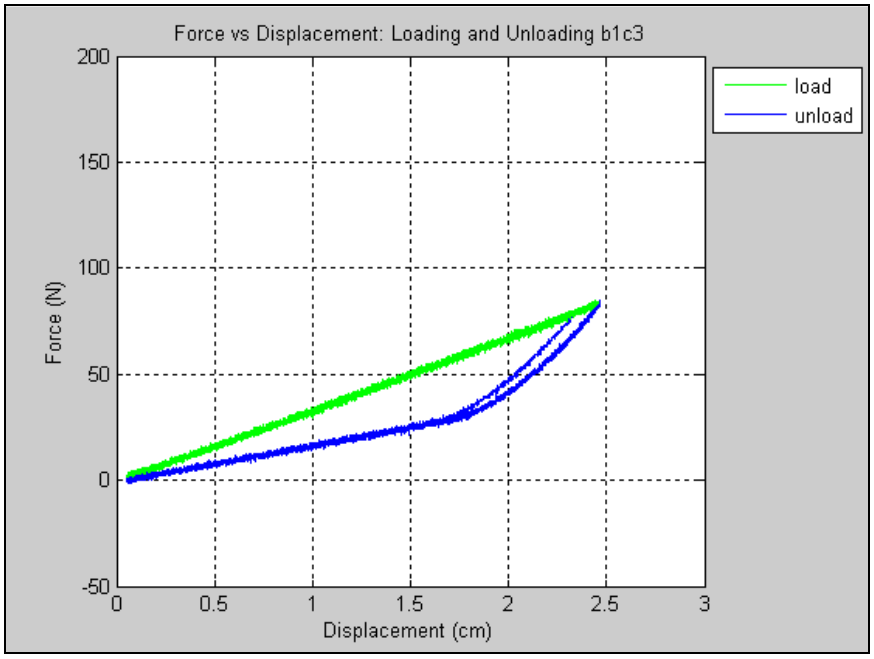

Figure 4.11: Loading and unloading of 'normal' left brace in configuration 3 force vs. displacement

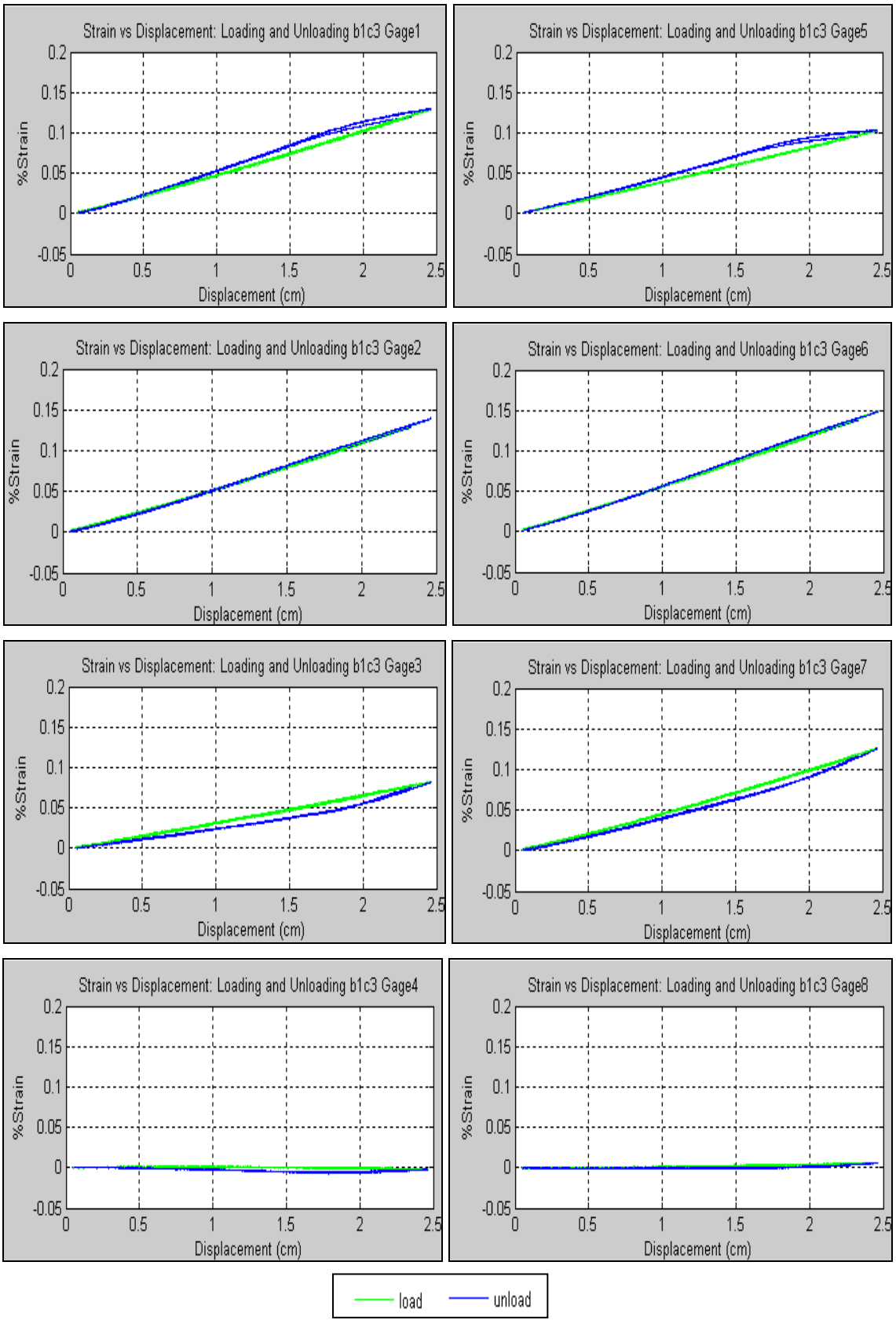

Figure 4.12: Gage strain vs. pretibial displacement ('normal' left brace, configuration 3)

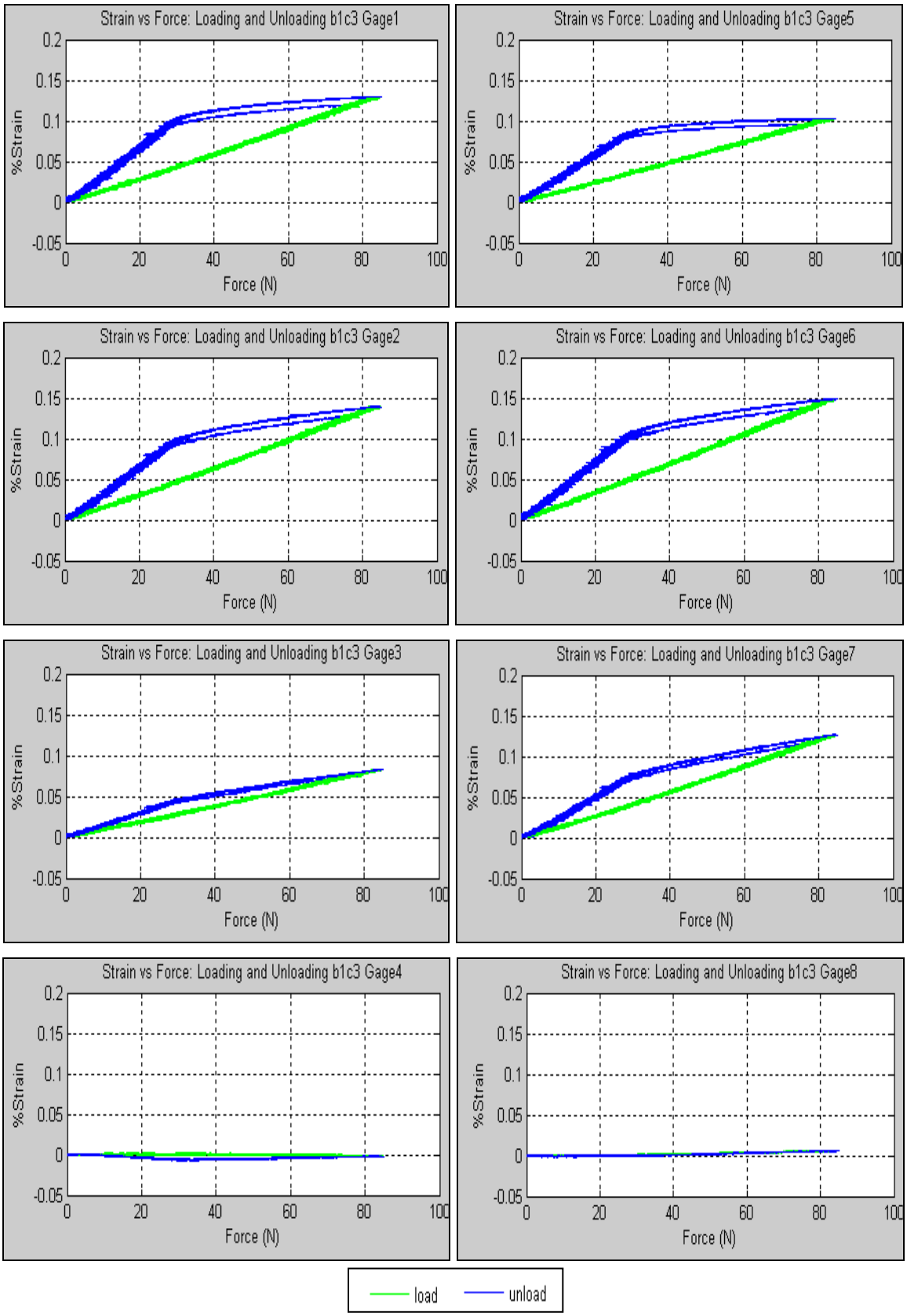

Figure 4.13: Gage strain vs. pretibial force ('normal' left brace, configuration 3)

4.2.2 Loading to Different Maximum Displacements

Most of the braces presented different characteristics in loading vs. unloading. It was necessary to perform tests at different maximum displacements to see what effect the maximum displacement would have on the force, displacement, and brace strut strain. Four maximum loading displacements were chosen: 1.27 cm (0.5 in), 2.54 cm (1.0 in), 3.81 cm (1.5 in), and 5.08 cm (2.0 in). Two braces were chosen to highlight the characteristic loading since each had slightly different unloading profiles. Shown in Figures 4.14 - 4.17 are all eight gages presented in separate graphs with each graph showing all four trials. Shown in Figure 4.18 are the force vs. displacement curves of brace 1 ('normal' subject's left brace) and brace 3 (left brace of CMT4). The geometry of brace 3 limited the last maximum from 5.08 cm (2.0 in) to 4.45 cm (1.75 in).

The loading portion of the curve was fairly linear and did not deviate more than 3% between the four trials for each loading condition (under 1% when comparing the second trial to the fourth trial). However, the slope did vary 15% between the 1.27 cm test and 5.08 cm test and is shown graphically in Figure 4.19. This can be explained by the small differences between the trials being added up to produce a larger difference overall. Essentially, the slope of the line decreased for each test condition once a certain maximum displacement was reached. A comparison was made between two sets of 2.54 cm tests performed on two separate days. The slopes were nearly identical with only a 0.3% difference between the average slope values. This indicates that over time the brace returned to its original state. This finding shows that with use, the brace will adjust to the highest maximum displacement of the user and produce the same force vs. displacement curve for that maximum displacement. A fatigue study would need to be conducted to

assess if the brace lost strength over an extended period of time, which is beyond the scope of this paper.

The unloading portion was nonlinear for most cases but acts in a scaled manner with respect to the maximum displacement tested. For those graphs showing a definite break point, the break point did not occur at any particular displacement or force. In all cases, after the break point the curves followed the same linear path to zero load.

As stated previously, these two braces were chosen because of the differences in the unloading profiles. Originally, all of the braces were tested to a maximum displacement of 2.54 cm. At this displacement, brace 1 and brace 3 match the profiles of Figure 4.9 and 4.11, respectively. It was much more evident where the break point existed for brace 3 when the brace was loaded to a higher maximum displacement.

Brace 1 and brace 2 (‘normal’ subject) were the only braces that showed a definite break point for condition 3 and 4 (horizontal flexure) when tested to 2.54 cm. All braces showed a definite break point for condition 1 and 2, most likely because the braces were tested to higher brace strut strains. The reason for the break point being more evident at smaller brace strut strains for brace 1 and brace 2 is probably because these braces were designed for the ‘normal’ subject and therefore did not need to have as much force applied to show a definite break point.

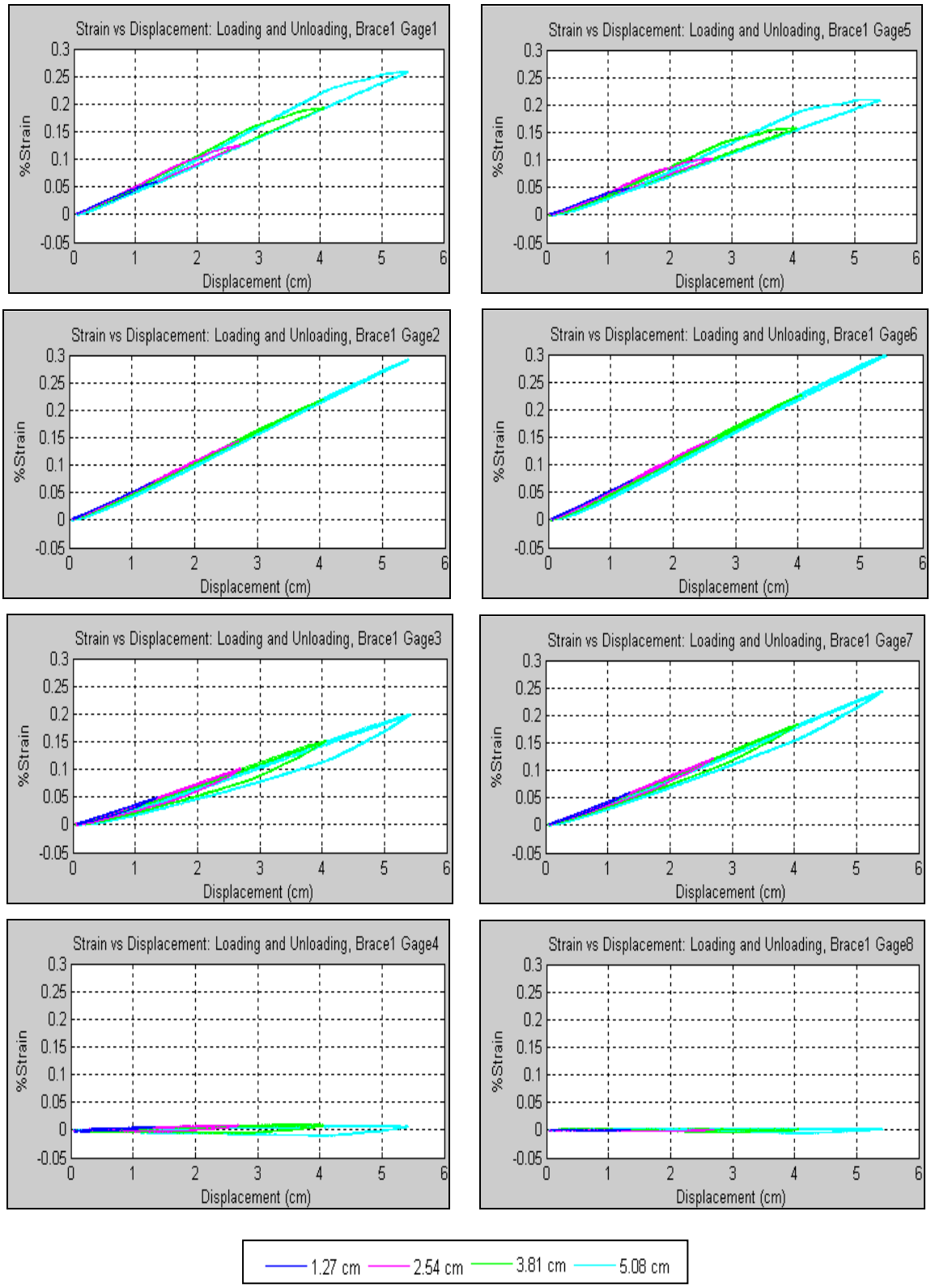

Figure 4.14: Gage strain vs. pretibial displacement for multiple maximum displacements ('normal' left brace, configuration 3)

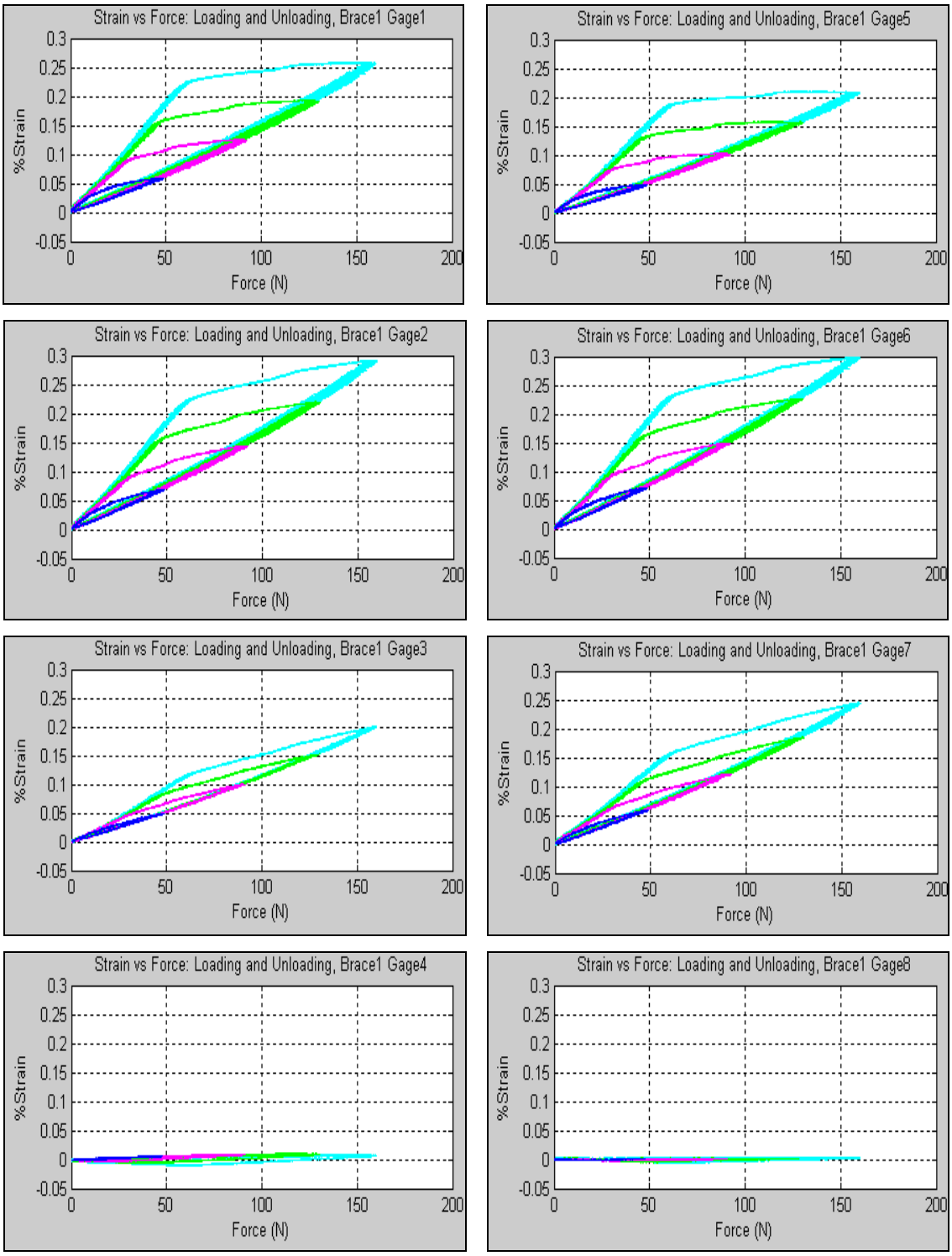

Figure 4.15: Gage strain vs. pretibial force for multiple maximum displacements

(‘normal’ left brace, configuration 3)

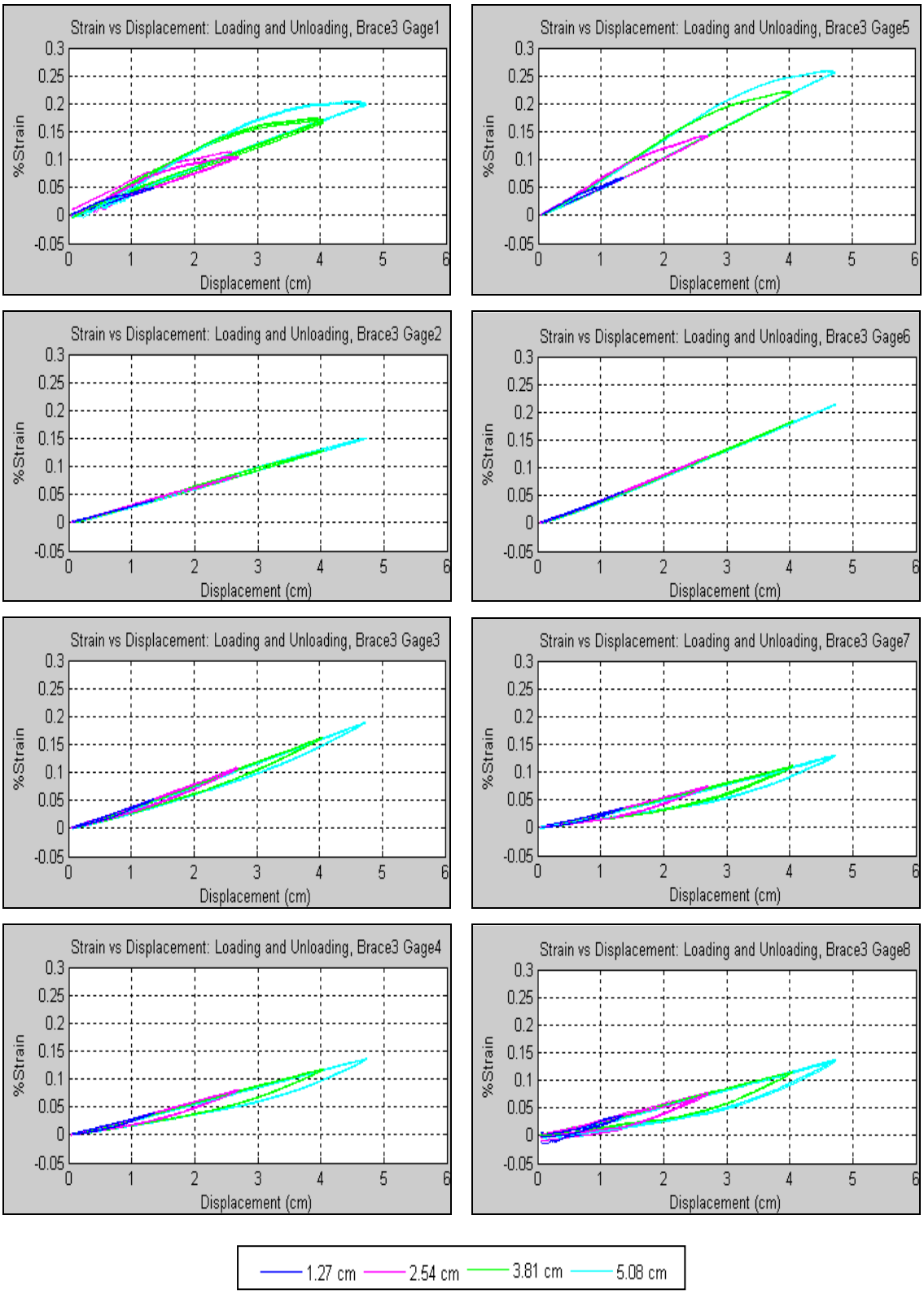

Figure 4.16: Gage strain vs. pretibial displacement for multiple maximum displacements

(CMT4 left brace, configuration 3)

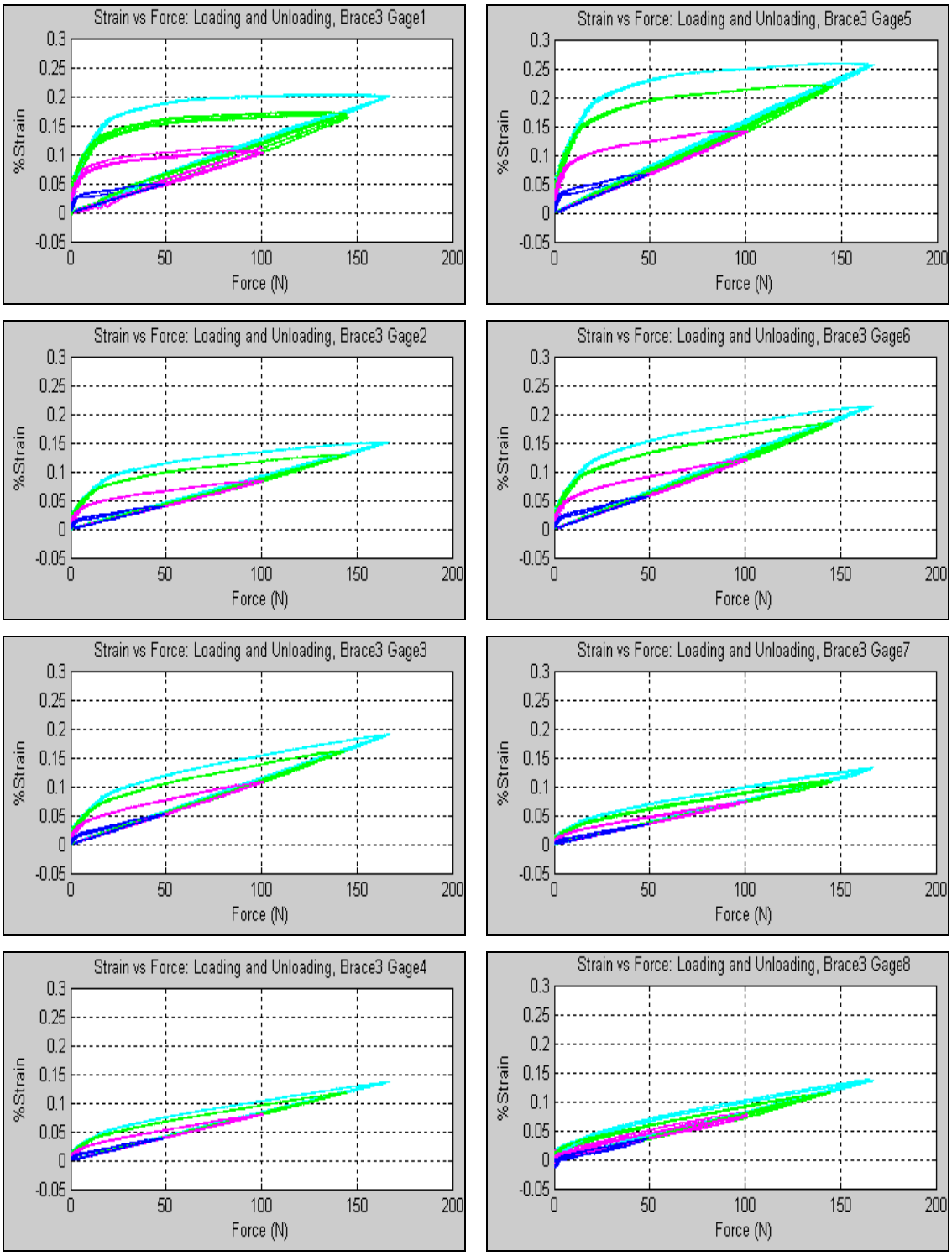

Figure 4.17: Gage strain vs. pretibial force for multiple maximum displacements

(CMT4 left brace, configuration 3)

Figure 4.18 proves that the break point exists in the brace developed for a CMT subject, although less defined. By looking at the area under the unloading curve, the 'normal' subject brace 1 had more energy release than the CMT4 subject's brace 3. More of the CMT4 brace energy was being dissipated as shown by the large hysteresis envelope between the load and unload curves. The 'normal' subject brace released energy almost consistently during unloading (the area under the initial unload line is only a little larger than the area under the terminal unload line). The CMT subject brace released the majority of energy before the break point (the area under the initial unload line). This means that for CMT4, energy is released to assist the subject in propelling the foot and leg forward only until the break point. The break point should occur sooner providing a higher sloped terminal unload line in the CMT subject since the CMT subject will be depending on the brace to propel the foot and leg forward.

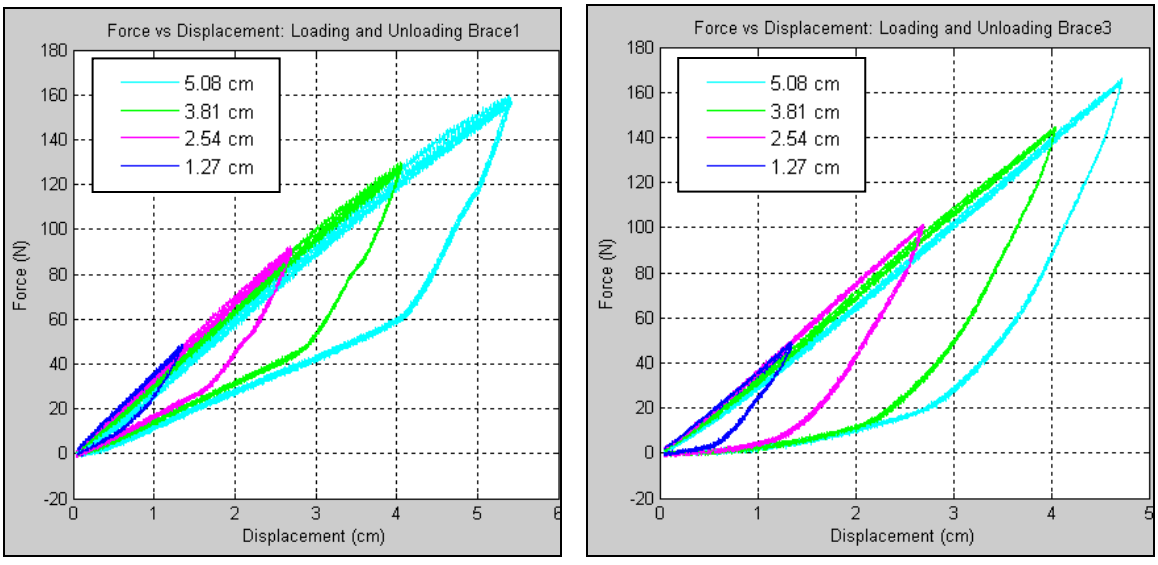

Figure 4.18: Force vs. displacement: (left) 'normal' left brace, (right) CMT4 left brace

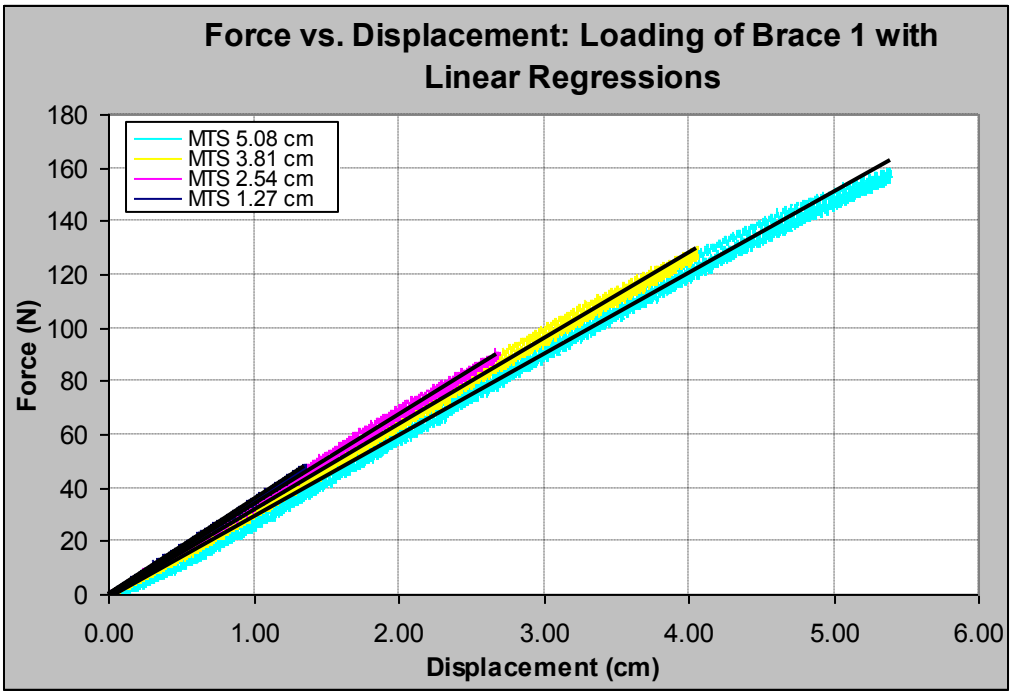

Figure 4.19: Loading portion of curve for 'normal' left brace with linear regressions

4.2.3. Static vs. Dynamic

Performing quasi-static and dynamic tests determined how the load curves changed as the testing rate increased. Final analysis showed that the actual loading rate for the quasi-static and dynamic tests differed from the set values of 1.016 cm/min and 609.6 cm/min, respectively. The actual values and the standard deviations are shown in Table 4.3. The dynamic rate deviated significantly from the set value because of limitations of the MTS.

Table 4.3: Loading and unloading rates for quasi-static and dynamic tests

		Set Rate cm/min	Loading (cm/min)	Unloading (cm/min)
Quasi-static	Average	1.02	1.0978	-1.1006
	Std Dev	-	0.0069	0.0060
Dynamic	Average	609.6	346.8	-364.7
	Std Dev	-	6.006	3.378

As stated in the previous subsection, the maximum displacement had an effect on the unloading portion of the curve. The dynamic tests yielded a different maximum displacement than the static tests since the dynamic rate tested the limits of the MTS, therefore the curves will be scaled based upon the maximum displacement as discussed in the previous subsection. Figure 4.20 shows the four static and four dynamic trials of all the braces during the vertical compression tests. The load curve for these tests was not as linear as the curves for the horizontal cantilever flexure tests. This might be due to the slippage of the brace on the upper fixture during loading. Results indicate that the rate of testing does not have an effect on the curves tested in this configuration. The same cannot be said for the horizontal cantilever flexure tests which are shown in Figure 4.21.

Brace 1 and 2 show a similar loading slope up to the maximum loading point, whereas all other braces had a larger slope for the dynamic tests in comparison to the static tests. Some of the braces exhibited an increase in force as the brace was beginning to unload. It is possible that this could be caused from the brace loosing contact with the compression nose fixture at maximum displacement and due to inertia the brace continues to deform in the loading direction. However, in all the cases where this was seen, the brace strut strain remained constant as the force increased as shown in Figure 4.22.

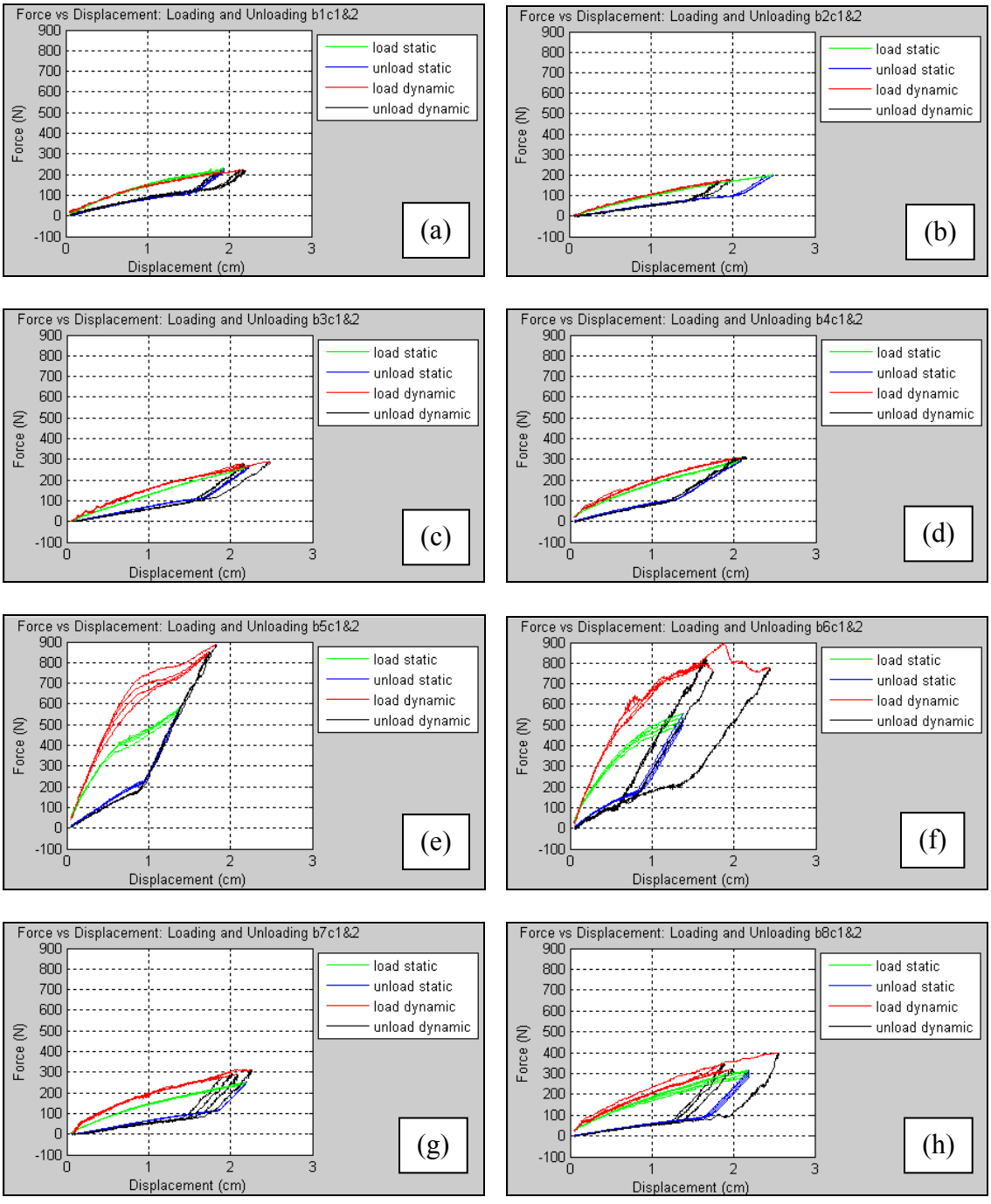

Figure 4.20: Static and dynamic loading and unloading of all braces in vertical compression test (a) brace 1, (b) brace 2, (c) brace 3, (d) brace 4, (e) brace 5, (f) brace 6, (g) brace 7, (h) brace 8

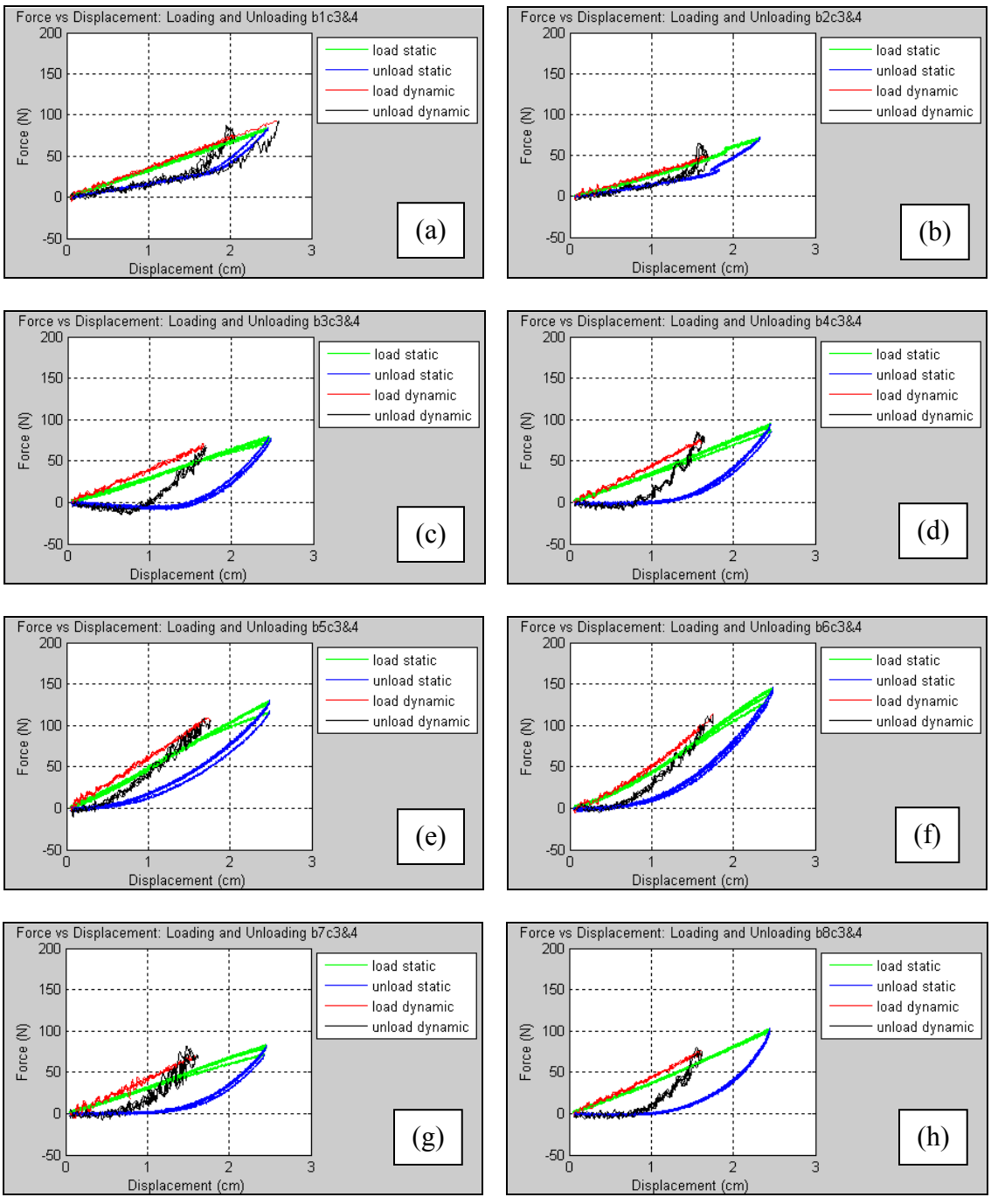

Figure 4.21: Static and dynamic loading and unloading of all braces in horizontal cantilever flexure test (a) brace 1, (b) brace 2, (c) brace 3, (d) brace 4, (e) brace 5, (f) brace 6, (g) brace 7, (h) brace 8,

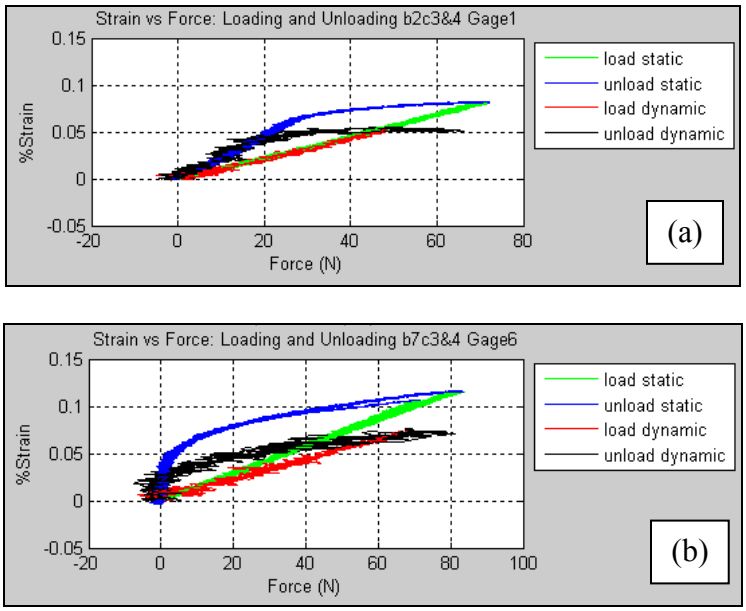

Figure 4.22: Examples of brace strut strain curves showing differences in dynamic loading: (a) brace 2, (b) brace 7

4.2.4. Clamping Effects

Each brace had to be clamped into the horizontal cantilever flexure fixture a little differently to achieve proper alignment with the test fixtures. It was thought that the clamping might have an effect on the results of the test. Two braces, brace 1 and brace 3, were clamped on two separate days of testing, so it was possible to see if clamping had an affect on these two braces. Force vs. displacement curves are shown in Figure 4.23. Brace 1 had a similar load curve for both clamping positions, but brace 3 showed slight differences in the load curves. Surprisingly, both braces showed differences in the brace strut strain curves based on the clamping. An example of a gage from each brace is shown in Figure 4.24 to illustrate the differences. Take note of how the strain at the end of unloading brace 3 has changed. This implies that clamping had more of an affect on the strut gage strain than on the force and displacement of the pretibial shell.

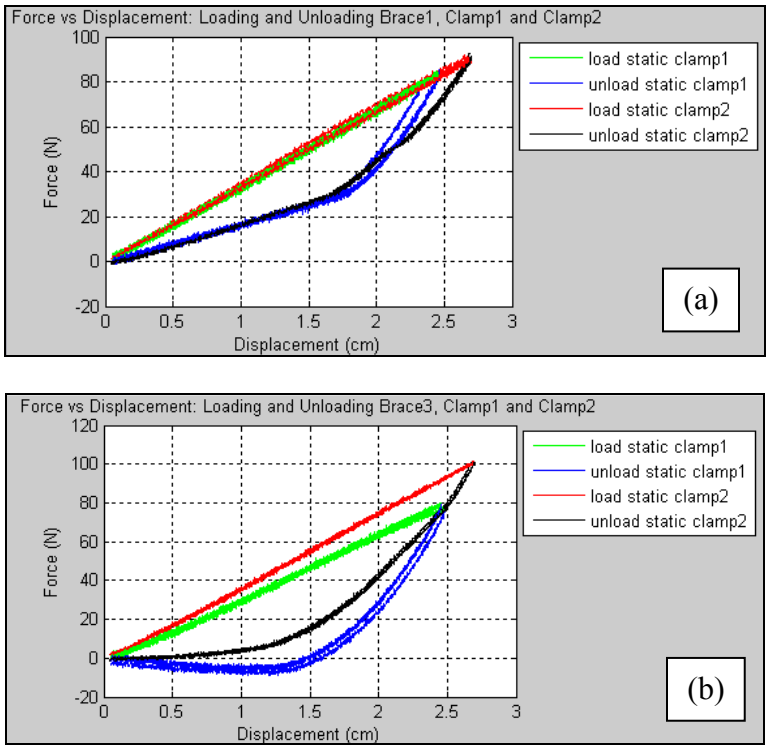

Figure 4.23: Force vs. displacement curves with different clamping

(a) brace 1, (b) brace 3

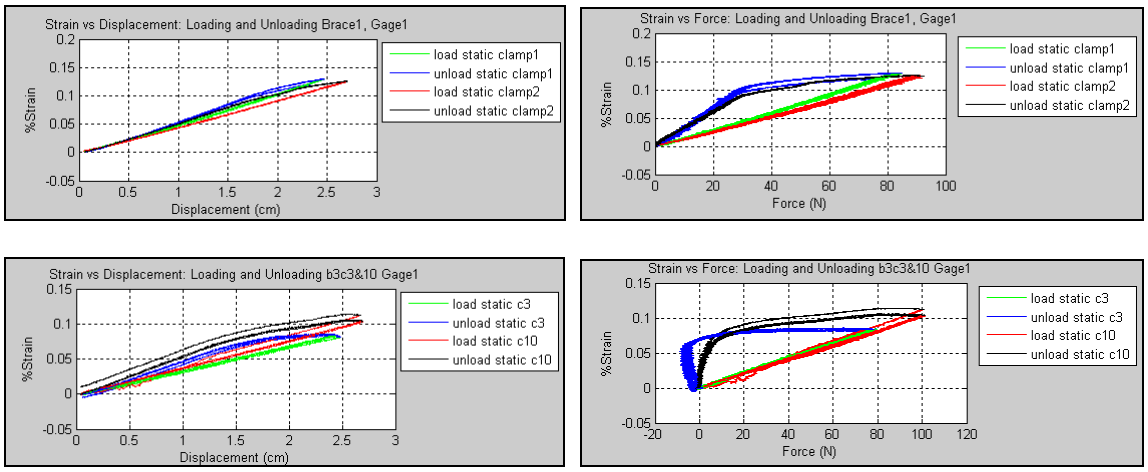

Figure 4.24: Strain vs. displacement and strain vs. force curves with different clamping

(top) brace 1, (bottom) brace 3

4.2.5. Maximum Strain Profiles

The vertical compression and horizontal flexure test setups load the braces in two distinct ways. This is shown by graphing the maximum strain values from each of the eight brace gages (Figures 4.26 through 4.29). The vertical compression tests loaded the braces at the top of the struts (gages 1 and 5) to a much higher strain than did the horizontal flexure tests. All but one of the braces (brace 4) had the same profile type for the vertical compression tests as shown by Figure 4.25.

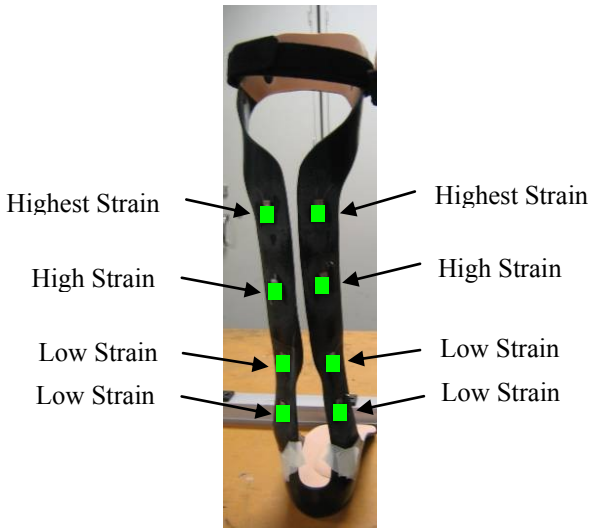

Figure 4.25: General strain profile of vertical compression tests

The horizontal flexure test results had a wider range of variation compared to the vertical compression tests. Brace 4 was the only one with a maximum at the ankle of the brace (gage 8); all other braces had the maximum strain reading in the top three gage positions on the brace. The maximum value did vary within these three gage positions depending on the brace tested.

When compared to the gage readings recorded during human motion tests, the strain values of the horizontal flexure tests matched the human motion profiles much better than the vertical compression tests. This is to be expected since the brace was being loaded in the horizontal flexure test in a similar manner to the loading performed by the human subject. Small deviations could exist in the profile due to the positioning and clamping of the brace in the testing machine. Also, the experimental tests clamped and loaded the braces in a uni-axial direction, whereas the human subject moved from the outside of the heel to the big toe during a step which would load the brace in a slightly different manner.

Comparing the human motion and horizontal flexure maximum strain data it is possible to conclude that the geometry of the brace had a greater effect on the maximum strain profile of the brace rather than the human subject. Brace 3 and brace 4 were two of the eight braces that showed unique maximum strain profiles from the other braces. These two braces had an extra piece of composite fabric located in the middle of the struts, most likely causing the strain in the middle of the struts to be lower. Coincidently these two braces belonged to subject CMT4 who also showed a unique strain vs. stance profile from the other instrumented brace subjects. It is possible that the differences in that subject's braces required the subject to alter gait to compensate.

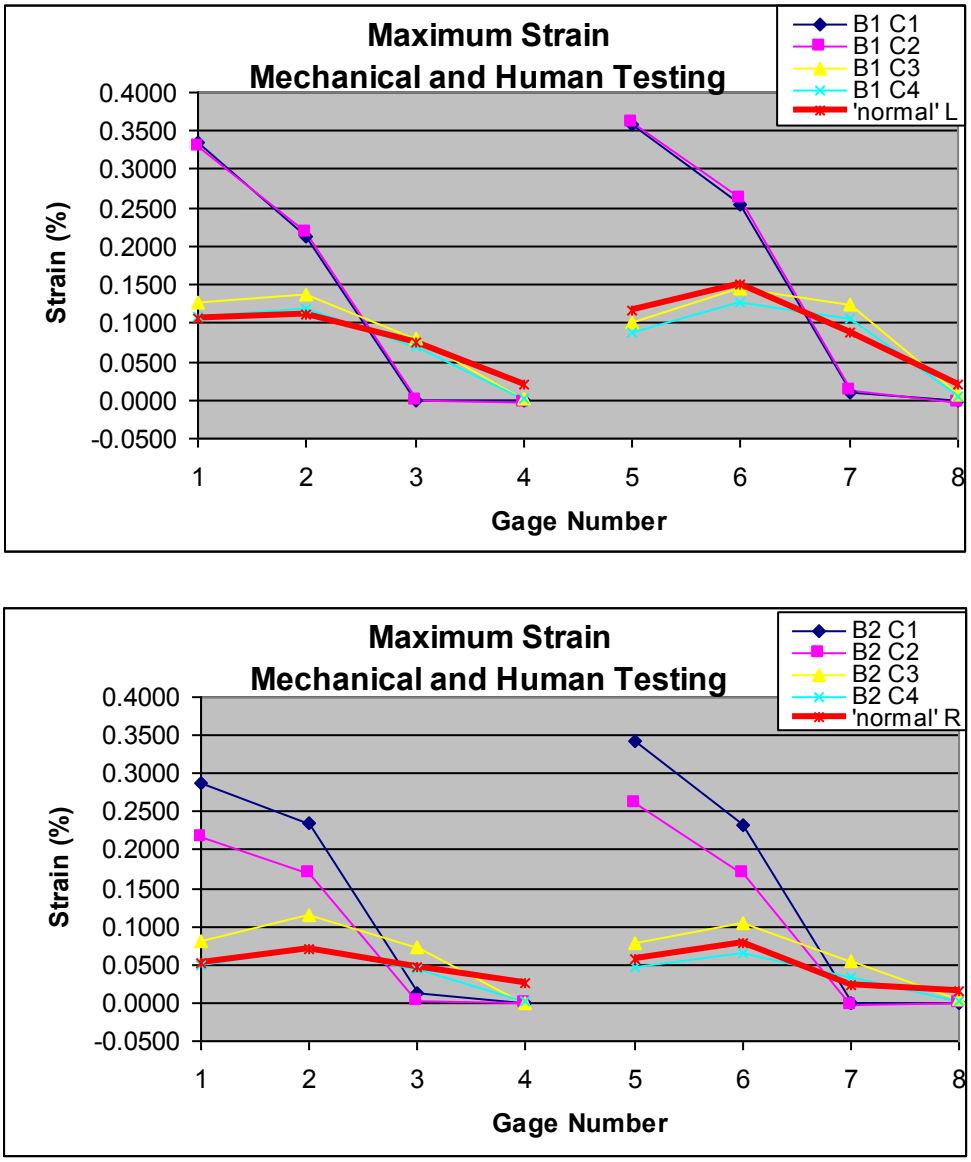

Figure 4.26: Maximum strain profiles (brace 1, brace 2, 'normal' subject) (top) mechanical testing of brace 1 graphed with human motion testing of 'normal' subject left foot, (bottom) mechanical testing of brace 2 graphed with human motion testing of 'normal' subject right foot

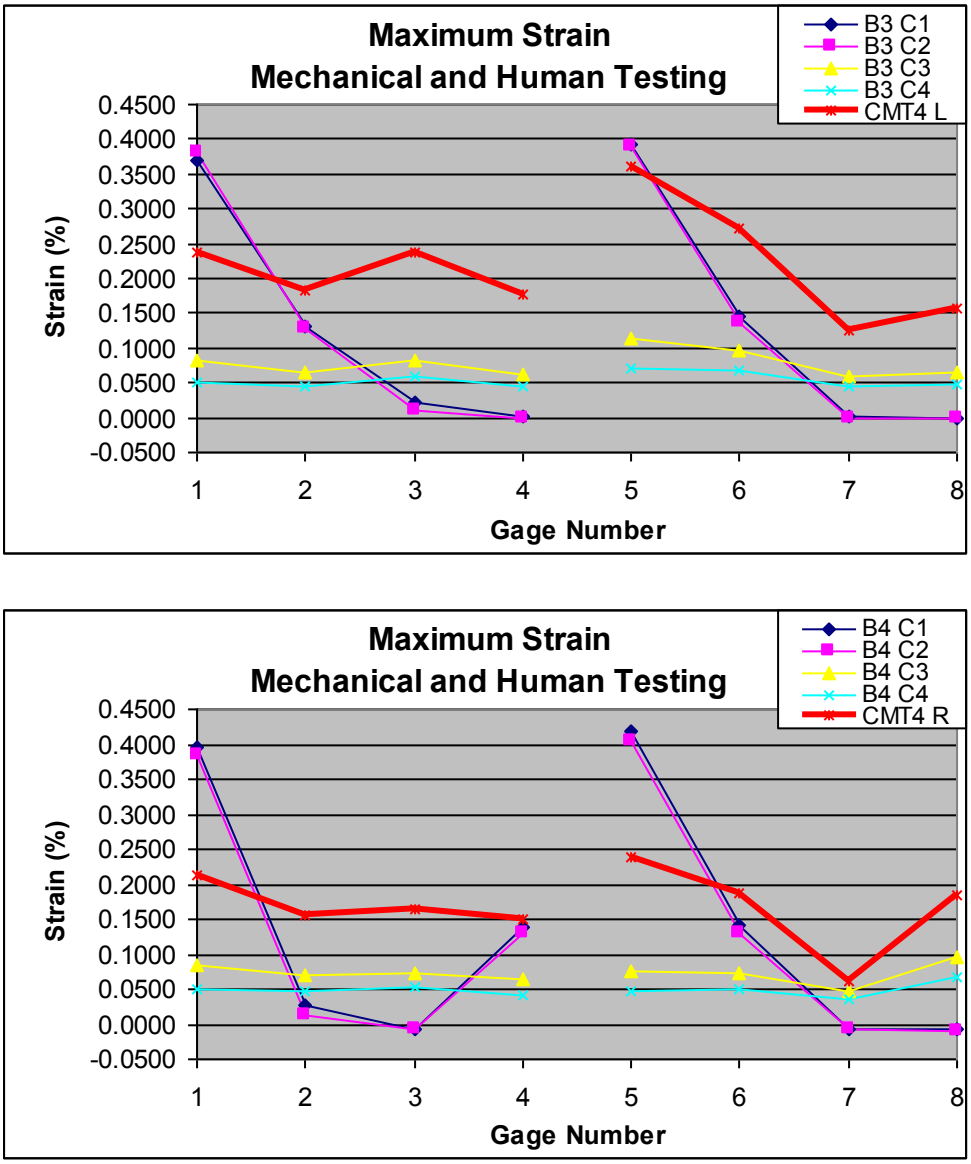

Figure 4.27: Maximum strain profiles (brace 3, brace 4, CMT4 subject) (top) mechanical testing of brace 3 graphed with human motion testing of 'CMT4' subject left foot, (bottom) mechanical testing of brace 4 graphed with human motion testing of 'CMT4' subject right foot

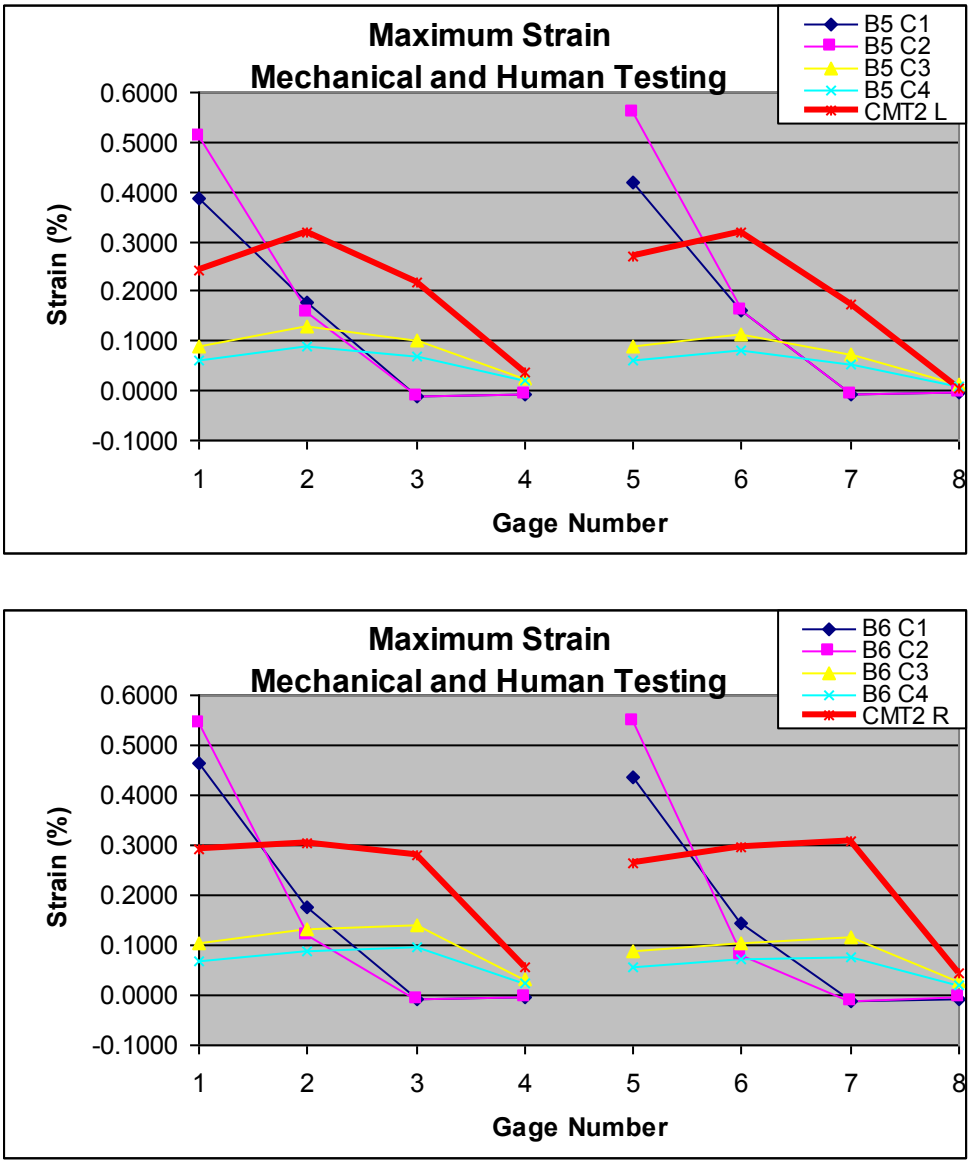

Figure 4.28: Maximum strain profiles (brace 5, brace 6, CMT2 subject) (top) mechanical testing of brace 5 graphed with human motion testing of 'CMT2' subject left foot, (bottom) mechanical testing of brace 6 graphed with human motion testing of 'CMT2' subject right foot

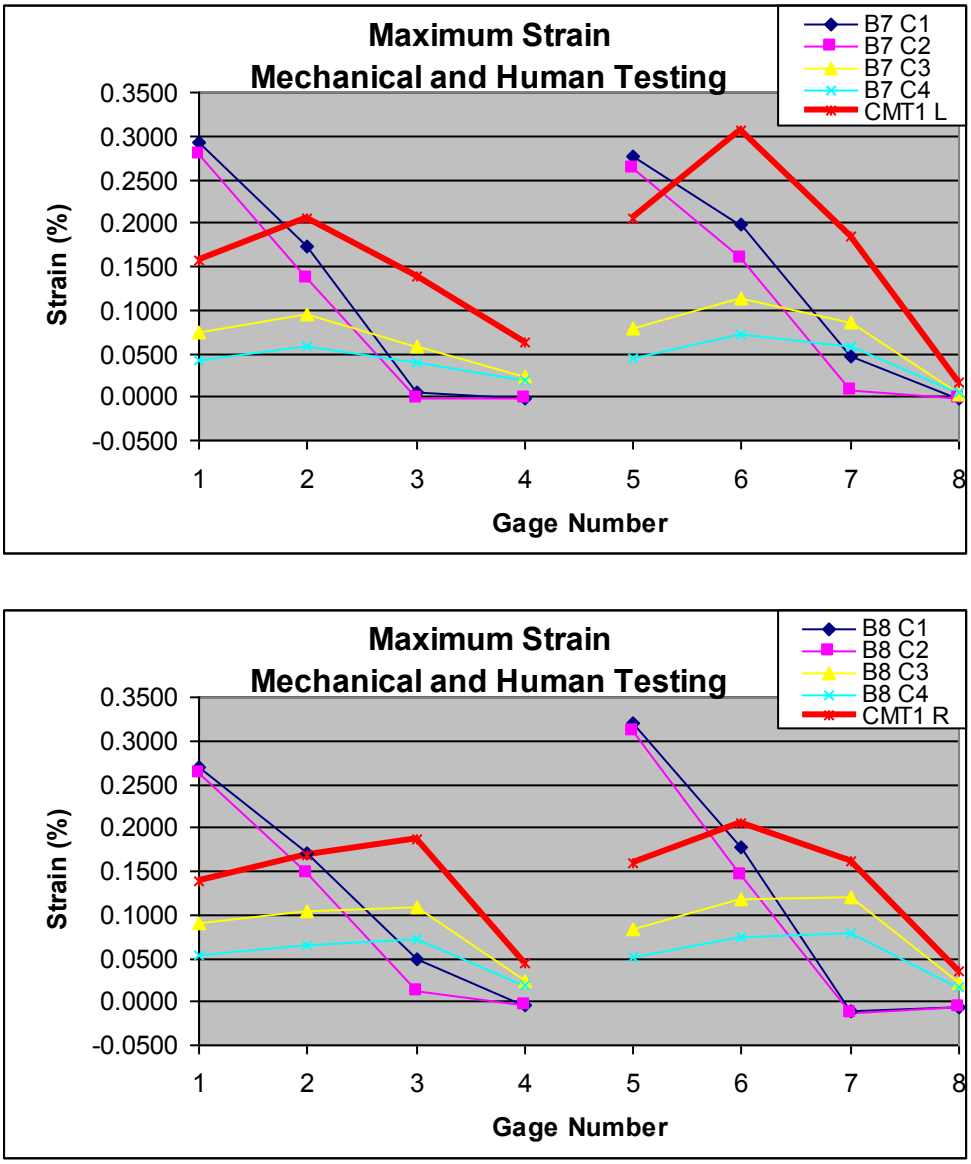

Figure 4.29: Maximum strain profiles (brace 7, brace 8, CMT1 subject) (top) mechanical testing of brace 7 graphed with human motion testing of 'CMT1' subject left foot, (bottom) mechanical testing of brace 8 graphed with human motion testing of 'CMT1' subject right foot

4.2.6. Pretibial Force and Displacement during Human Motion

The data gathered from the horizontal cantilever flexure test were used to calculate the force and displacement at the pretibial shell applied by the human subject during human motion testing. For purposes of this discussion, the gage strain, force, and displacement collected during the mechanical testing are called the MTS gage strain, MTS force, and MTS displacement.

The MTS gage strain is graphed with respect to the MTS displacement and MTS force. Linear regressions were used to create the relationship between pretibial MTS force and MTS gage strain as well as pretibial MTS displacement and MTS gage strain. Each of the four trials from mechanical testing was individually fitted to a linear regression as shown in Figure 4.30. This allowed the four trials to be averaged together and a single regression to be calculated. Figure 4.31 shows all four trials (load and unload are shown as green lines) with the final regressions of the load curve (shown in black), and unload curve (shown in black and red). The blue and red lines have been extended for graphical clarity.

The linear regressions, now in equation form, are presented as Eq 5.1 and Eq 5.2. These equations allowed the gage strain from the human motion tests to be inserted and then solved for the associated displacement or force that occurred at the pretibial shell during human motion testing.

$$\text{gage strain} = \text{slope} \cdot \text{displacement} + \text{intercept} \qquad \text{(Eq 5.1)}$$

$$\text{gage strain} = \text{slope} \cdot \text{force} + \text{intercept} \qquad \text{(Eq 5.2)}$$

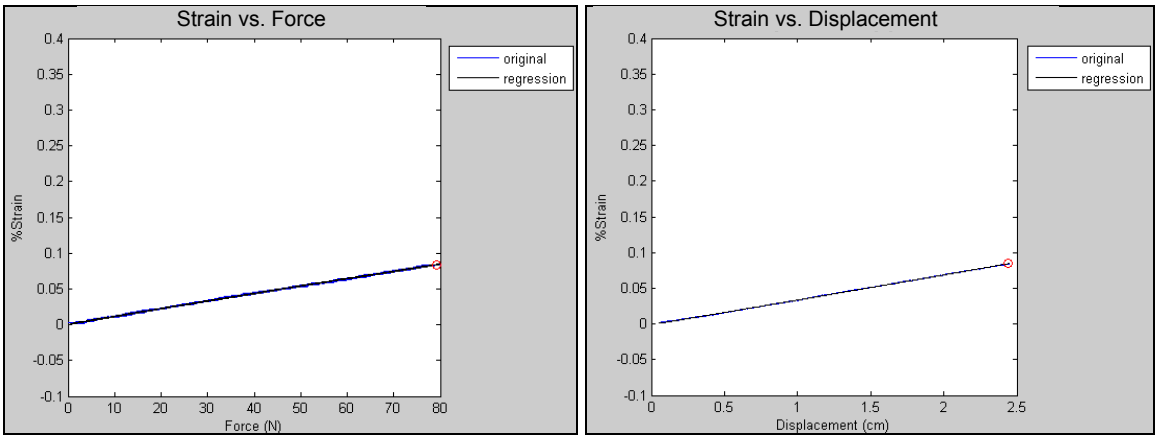

Figure 4.30: Example of regression performed on strain vs. force and strain vs. displacement graphs

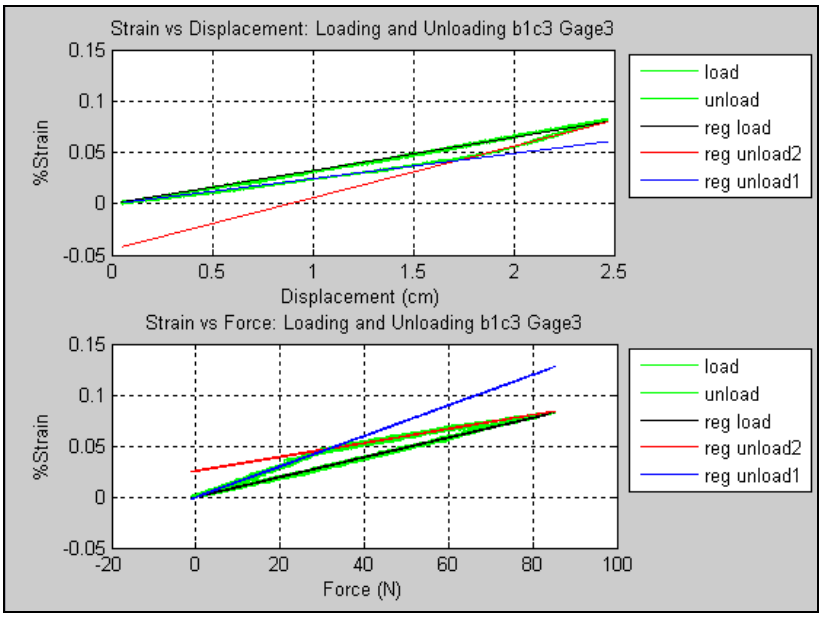

Figure 4.31: Four trials with associated final regressions

Once the pretibial force and displacement were calculated using the human motion gage strain in Eq 5.1 and Eq 5.2, these values could be graphed with respect to %stance as shown in Figure 4.32 (Note: the displacement and force have only been calculated for

the gages while in tension). The maximum pretibial displacement and force could be calculated in this manner and are shown by the peaks on the graphs in Figure 4.32. The displacement and force were shown to follow the same profile as the gage strain. This indicated that as maximum gage strain was achieved, so too were the maximum force and displacement at the pretibial shell. The force curves show how the break point impacts the force profile. This is where the energy release of the brace begins to change during the stance phase of gait. As discussed in the previous section, the peak A/P braking force for the 'normal' subject occurred at around 87% stance and coincides with the break force.

The maximum displacement and force at the pretibial shell during human motion can be calculated using the linear regression equations (Eq 5.1 and Eq 5.2) and the mechanical test data gathered during loading. These equations were applied to each of the strut gages, excluding the gages at the ankle (gages 4 and 8). The ankle gages were not included in this analysis since the strain values were significantly lower than the other gages and because they did not follow the same profile during gait. Each of the six gages produced a slightly different value for the maximum force and displacement at the pretibial shell. This is due to many factors including how the brace was clamped and loaded during mechanical testing in addition to the unique loading of the human subject. Since there was variation, all values from one brace were averaged and a standard deviation was calculated. Figure 4.33 and Figure 4.34 show the averages and first and second standard deviation bars of maximum pretibial displacement and force, respectively, for each subject.

The ‘normal’ subject had the lowest displacement and the lowest force at the pretibial shell. The highest force is seen by CMT2 which was the subject with more advanced CMT characteristics. In fact, the maximum force applied to the pretibial shell seemed to increase with more advanced CMT characteristics since the ‘normal’ subject had no CMT symptoms, CMT1 had the mildest case of CMT, CMT4 showed more symptoms than CMT1, and CMT2 showed the most CMT symptoms.

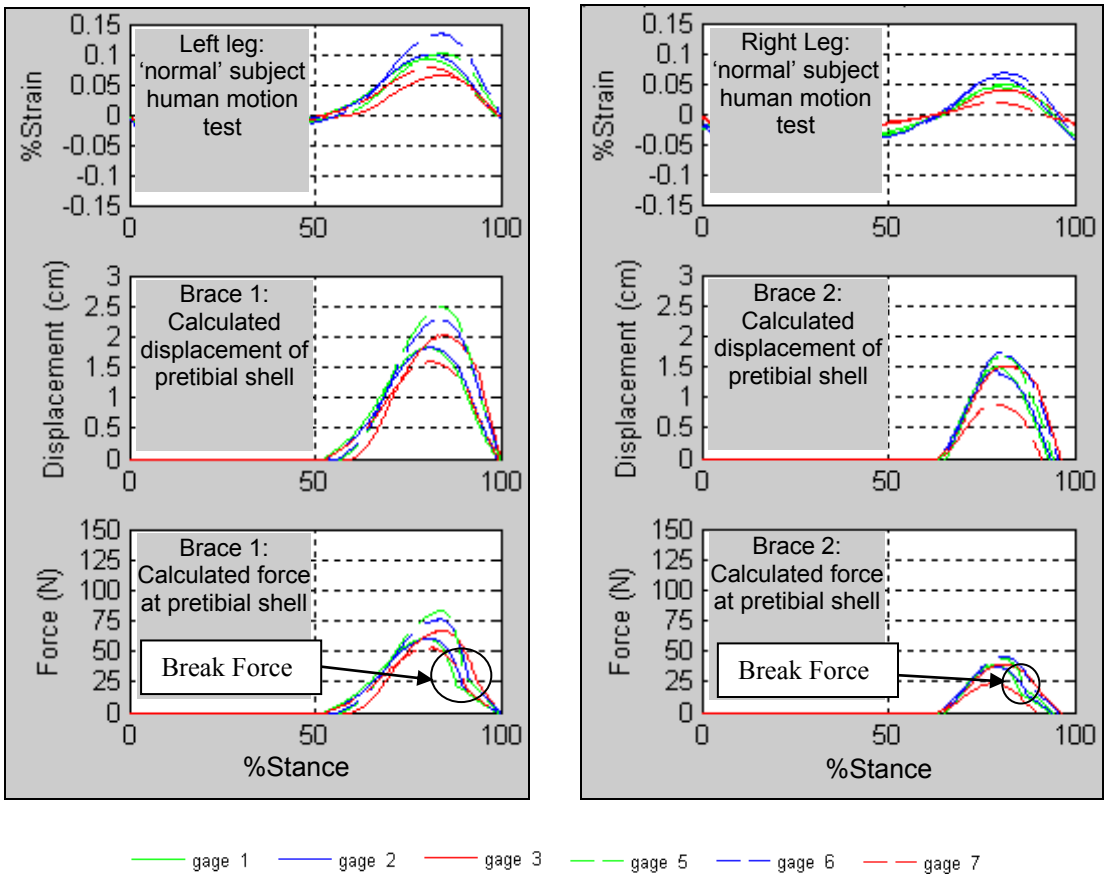

Figure 4.32: %Gage strain from human motion testing, calculated displacement based on mechanical testing strain vs. displacement curve, and calculated force based on mechanical testing strain vs. force curve

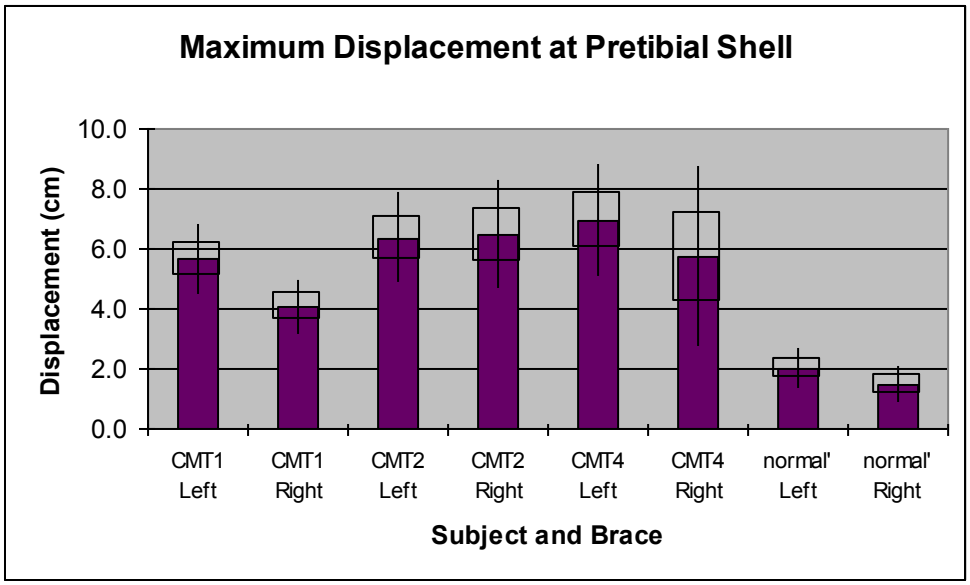

Figure 4.33: Calculated maximum displacement at pretibial shell for all subjects

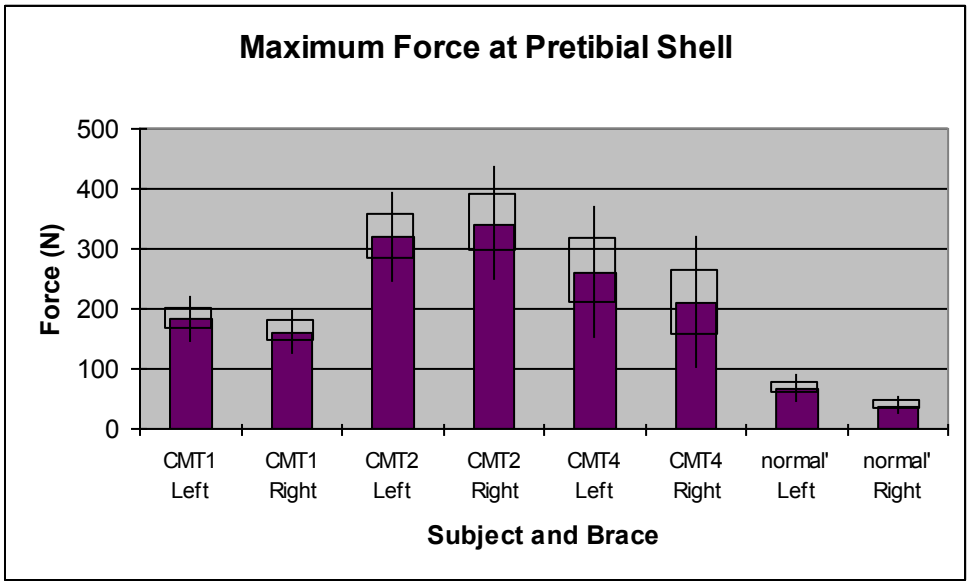

Figure 4.34: Calculated maximum force at pretibial shell for all subjects

Table 4.4 provides the numerical averages of the calculated maximum pretibial force and displacement. Also provided are the individual subject's weights and the force

normalized as a percentage of body weight (%BW). The force was normalized to rule out differences in body weight. Again, the amount of force applied to the pretibial shell was related to CMT severity for that individual, regardless of the individual's weight. Interestingly, the highest strain seen during the human testing was for CMT4, but the highest calculated maximum pretibial force was seen in CMT2, and both CMT4 and CMT2 have approximately the same calculated maximum pretibial displacement.

Table 4.4: Calculated maximum pretibial force and displacement

	Ave Displacement (cm)	Weight (N)	Ave Force (N)	Ave Force (%BW)
CMT1 Left	5.64	1036.46	181.94	17.55
CMT1 Right	4.05	1036.46	160.86	15.52
CMT2 Left	6.35	604.97	318.78	52.69
CMT2 Right	6.45	604.97	341.55	56.46
CMT4 Left	6.91	911.92	260.60	28.58
CMT4 Right	5.71	911.92	209.11	22.93
'normal' Left	2.01	511.51	66.89	13.08
'normal' Right	1.46	511.51	38.20	7.47

Based on the average maximum displacements presented in Table 4.4 it was possible to calculate the percentage of deflection relative to the brace length and strut length. Obviously, percentages will be larger when considering strut length, but this was done to emphasize a worst case scenario. These percentages are presented in Table 4.5 and results indicate that the maximum deflection at the pretibial shell is less than 30% when based on strut length and therefore, based on beam theory, significant changes in geometry are unlikely for all braces. CMT2 showed the highest deflections as a percentage of brace length and strut length.

Table 4.5: Maximum displacement as a percentage of brace and strut length

	Maximum displacement as a percentage of	
	Brace Length	Strut Length
CMT1 Left	13%	26%
CMT1 Right	9%	19%
CMT2 Left	15%	24%
CMT2 Right	15%	24%
CMT4 Left	14%	23%
CMT4 Right	12%	19%
‘normal' Left	5%	8%
‘normal' Right	3%	5%

4.3 Energy Storage and Return

Human motion testing yielded the GRF and the brace strain for CMT subjects and a ‘normal’ subject. The human motion testing provided a better understanding of how the brace alters the GRF. The most significant finding from the human motion testing was the delay of the propulsive and braking peaks during the braced condition. The brace was acting as a shock absorber at the beginning of stance, slowing the impact of the foot during heel contact and thereby, delaying the braking peak. The brace was again acting as a shock absorbing device at the end of stance by delaying the propulsive peak.

It is proposed that the HELIOS stores and releases energy during propulsion as well as during braking. A brace strain curve is shown in Figure 4.35 with the energy storage and return sections defined. The brace was storing energy when the brace struts bent to the maximum compressive strain and maximum tensile strain. The energy was then released as the brace returned to zero strain. This energy release in the beginning of stance is perhaps why the A/P transition point was not significantly delayed even though

the braking peak was delayed. The energy release at the end of stance could also be allowing toe off to occur soon after the delayed propulsive peak.

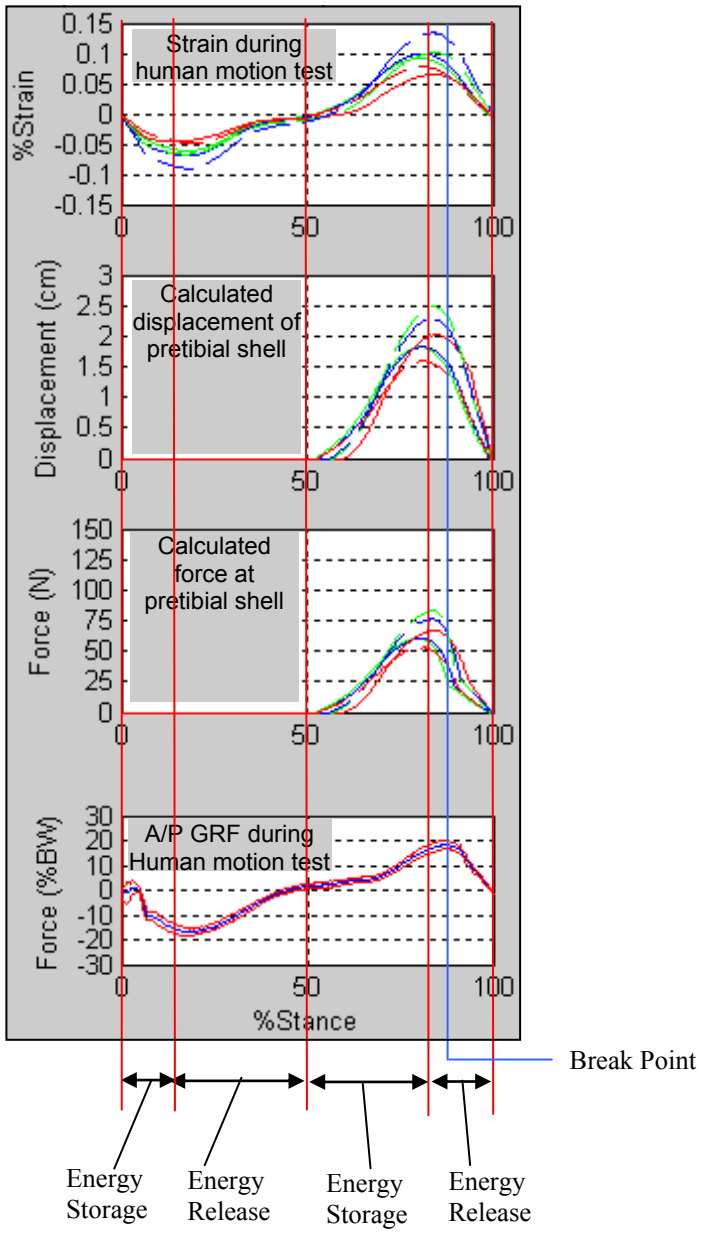

Figure 4.35: Phases of energy storage and release during one stance cycle

Mechanical testing showed that the HELIOS braces loaded and unloaded differently. During the unloading portion there was a break point where the slope of the unloading curve changed. This was seen more clearly with the 'normal' subject brace and is shown in Figure 4.35. Coincidently, this break point occurred at about the same time as the propulsive peak.

The HELIOS resembles a quarter-elliptic beam spring or simple cantilever flat spring as shown in Figure 4.36. The length can be defined from the base of the brace to the top of the pretibial shell, and the force F can be applied to the pretibial shell to deflect the brace a distance d. The struts were created from layering different lengths of fibers, but the lengths all terminate well beyond the strut (i.e. at the pretibial shell or foot plate). The only exceptions to this are the braces for CMT4. An extra piece of fabric was used on the middle of the struts. This is perhaps why the strain seen in these braces was lower for the middle gages. All of the braces did not have constant stress along the length of the struts since the geometry was fairly consistent and did not taper significantly. The braces are similar to a leaf spring in that they can both hold structural and spring loads. The HELIOS can carry a full load in either direction because of the epoxy that is holding the fibers together. The fibers provide the necessary strength in tension and compression whereas the epoxy prevents the fibers from buckling during compression. During bending, the struts will experience tension on one side and compression on the other.

The HELIOS can be thought of as a spring and damper system where the spring is deflected by the force and the damping elements resist the deflection by absorbing and dissipating. This is similar to the Maxwell model, however damage did not occur to the springs in the HELIOS and therefore did not change with repeated loading (i.e. show

Mullins effect or stress softening). The springs would help to release energy while the dampers would help to absorb energy, therefore the HELIOS acts as a shock absorber in addition to an energy release mechanism.

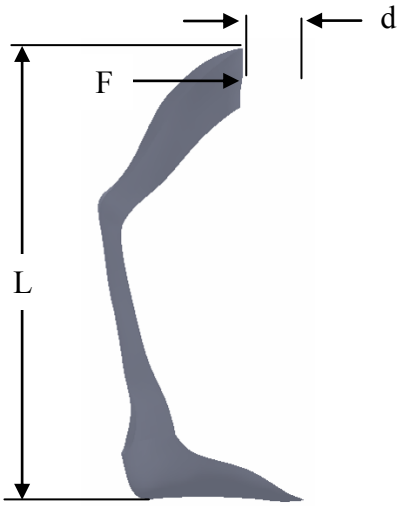

Figure 4.36: HELIOS brace defined as a beam spring

The work performed by the subject, applying force at the pretibial shell, creates potential energy that is stored by the HELIOS. Once the subject released the applied force, the HELIOS was unloaded releasing some of this potential energy which can be used to propel the subject during the propulsive stage of gait. However, not all of the potential energy was transferred as shown by the load-displacement curves. Since the load and unload curves create a hysteresis area, some of the potential energy was dissipated due to internal energy, friction, heat, or sound. The braces were not monitored during testing to indicate differences in temperature. Through normal use of the brace, subjects indicated no noticeable difference in brace temperature during use.

An analysis was performed to determine the brace stiffness values in addition to the energy storage and release of the eight instrumented braces. The brace spring stiffness coefficient was calculated as the slope of the force-displacement curve. Shown in Figure 4.37 are the spring coefficients calculated from the static and dynamic vertical compression tests (condition 1 and condition 2). Shown in Figure 4.38 are the spring coefficients calculated from the static and dynamic horizontal cantilever tests (condition 3 and condition 4).

Most of the braces showed an increase in the spring coefficient during the dynamic tests. A higher stiffness coefficient indicates a harder spring whereas a lower stiffness coefficient indicates a softer spring. This means that most braces act as a harder spring in the dynamic tests. All of the braces also had a much higher stiffness coefficient in the vertical tests as compared to the horizontal cantilever tests; therefore the braces were much more pliable when the force was applied to the pretibial shell during normal gait.

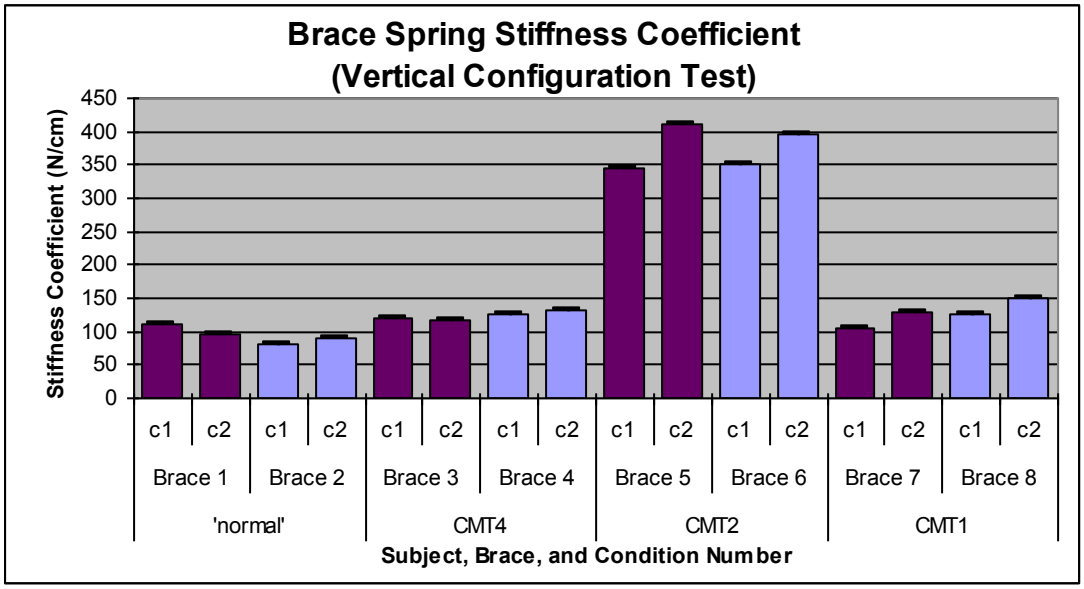

Figure 4.37: Brace spring stiffness coefficients for vertical compression tests

Brace 5 and brace 6, belonging to CMT2, both had the highest stiffness coefficient of all the braces. This increase was seen in the vertical tests more so than in the horizontal tests. Perhaps the braces were able to increase this subject's speed the most simply because the spring coefficient was higher. It does imply that the spring stiffness could be a major factor in the effectiveness of the brace. Since these brace had the same number of layers and type of fabric as the other braces (except brace 3 and brace 4), one could conclude that the difference in spring stiffness for these braces was due to geometry. Brace 1 and 2, belonging to the 'normal' subject showed the lowest spring stiffness. This was intentionally done during fabrication and is understandable since the 'normal' subject was not depending on the brace for support during gait.

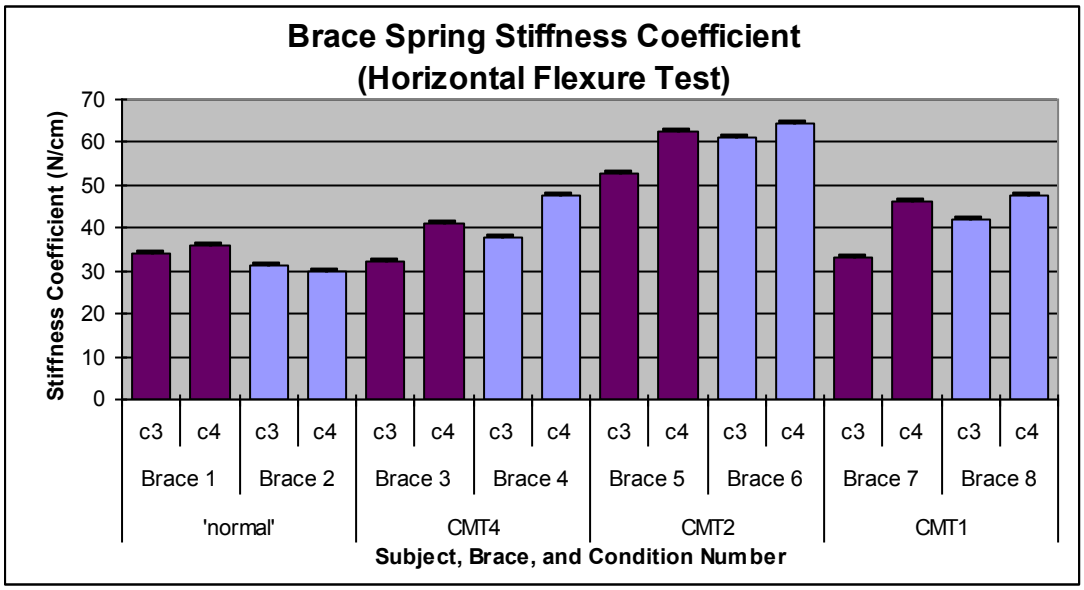

Figure 4.38: Brace spring stiffness coefficients for horizontal cantilever tests

All of the braces were tested up to a maximum displacement of 2.54 cm. Only two braces, brace 1 and brace 3, were tested to different maximum displacements to

determine differences in spring stiffness due to maximum displacement. Shown in Figure 4.39 are the results of these tests. Interestingly, brace 1 has a decrease in stiffness as maximum displacement increases, and brace 3 remaines relatively stable. This could be due to geometry differences or from extra fabric that was added to brace 3.

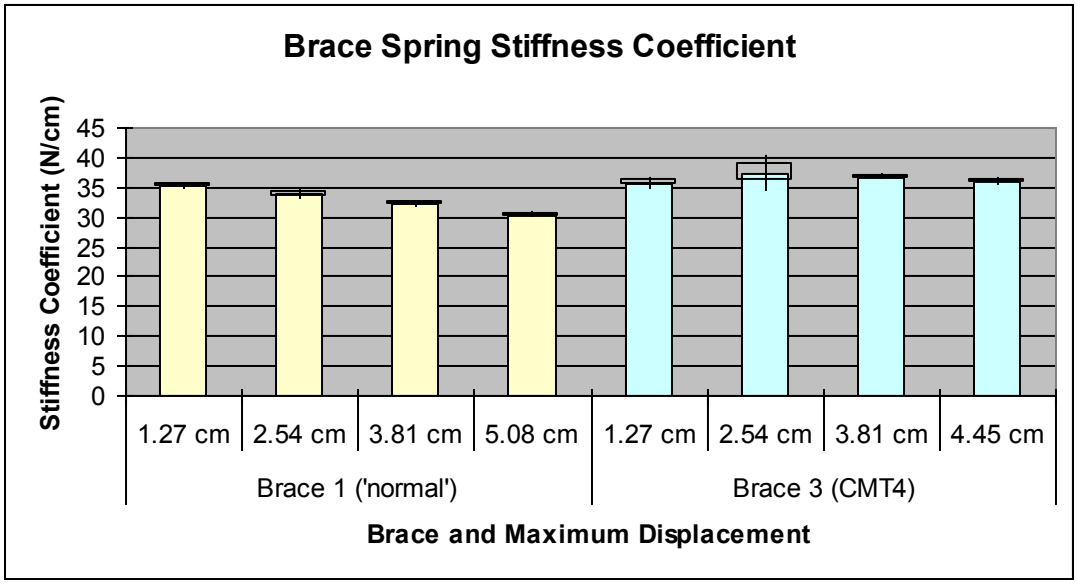

Figure 4.39: Brace 1 and brace 3 spring stiffness coefficients for horizontal cantilever tests

The work done by the subject to move the pretibial shell of the HELIOS brace can be defined as the force applied to the pretibial shell multiplied by the pretibial displacement as shown by Eq 5.3. The energy to perform this work (strain energy) can be calculated as shown in Eq 5.4. Alternatively, the energy can be calculated as the area under the load-displacement curve.

$$\text{Work done by the subject} = \text{pretibial force} \cdot \text{pretibial displacement} \qquad \text{(Eq 5.3)}$$

$$\text{Energy to perform work (strain energy)} = \tfrac{1}{2} \cdot F \cdot d = \tfrac{1}{2} \cdot k \cdot d^2 \qquad \text{(Eq 5.4)}$$

The energy stored by the brace is the area under the load curve. The energy being released during unloading can be described as the area under the unload curve. The area between the load and unload curves is dissipated energy due to internal energy, friction, heat, or sound. All energy variables were calculated using trapezoidal numerical integration in Matlab.

Figure 4.40 shows the amount of energy stored, released, and dissipated for all instrumented braces. Similar to the brace stiffness results, brace 5 and brace 6 have the greatest amount of energy storage capacity of all the braces for the vertical compression and horizontal cantilever mechanical tests. All other braces show similar energy storage capacity.

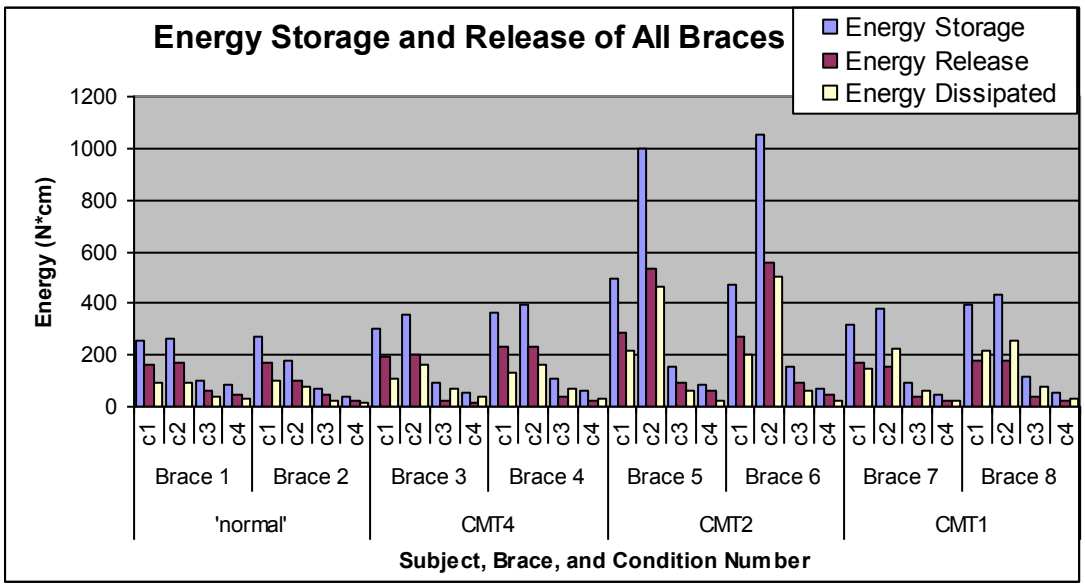

Figure 4.40: Energy storage and release of all instrumented braces

To understand how the braces use the maximum energy storage capacity, another way to look at the data was through percentages of the energy released and dissipated, as shown in Figure 4.41. A brace that used the energy most efficiently would have a smaller percentage of that energy dissipated.

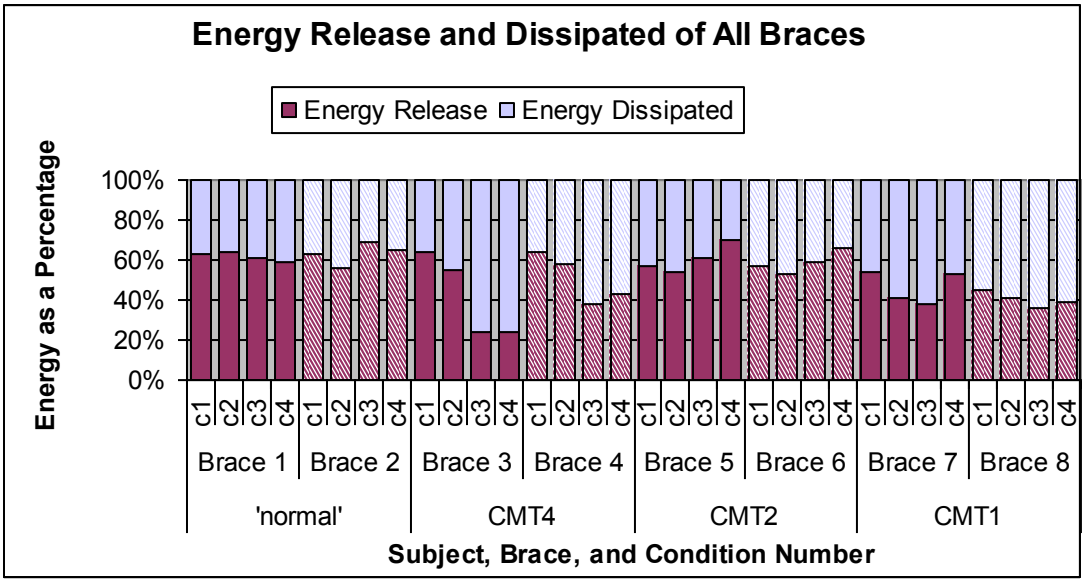

Figure 4.41: Energy percentages of release and dissipation of all instrumented braces

The braces tested in the horizontal cantilever configuration with the highest percentage of dissipated energy were brace 3 and brace 4, used by CMT4. In this case, only 20% to 40% of the energy stored by the brace was released. Perhaps this lack of energy release was the reason why this particular subject had a different gait than the other subjects. The brace required this subject to push or lean into the pretibial shell more to yield the necessary amount of energy during toe off. Brace 7 and brace 8 worn by CMT1 also showed a low amount of energy release compared to dissipated energy. Only 35% to 55% of the energy stored in these two braces is released. The 'normal' subject

and CMT2 had similar energy release values, 50% to 70%. CMT2 had the largest increase in walking speed and it is possible that this occurred due to the better energy storage capacity and better energy release properties.

Only two braces, brace 1 and brace 3, were tested to determine differences in energy due to maximum displacement. Shown in Figure 4.42 are the results of these tests. Both braces showed that with an increase in maximum displacement, the energy stored, released, and dissipated also increased fairly linearly. Note that brace 3 was only tested up to 4.45 cm due to limits in testing equipment.

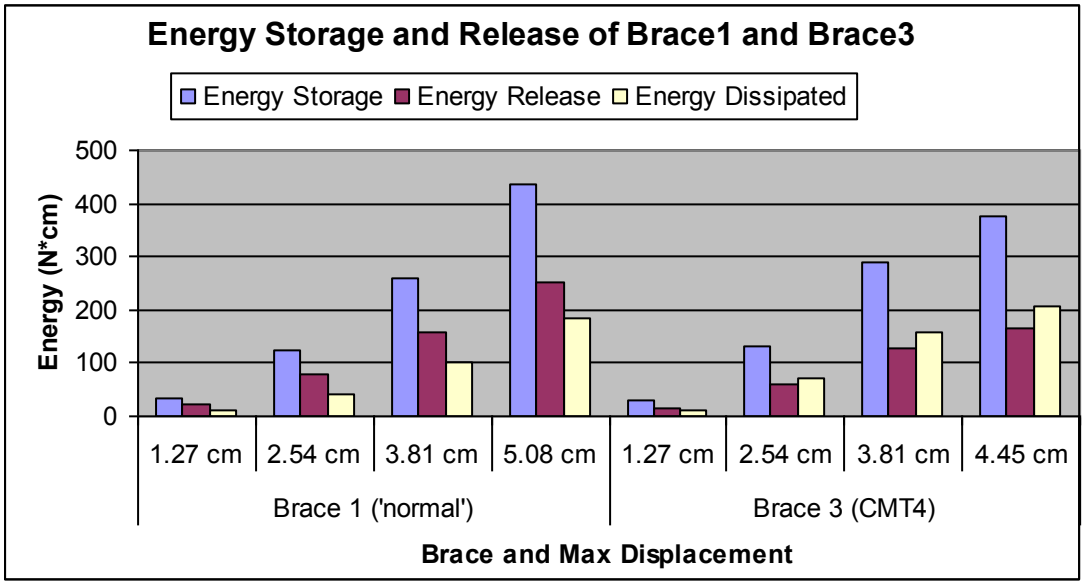

Figure 4.42: Energy storage and release of brace 1 and brace 3

The percentages of the energy released and dissipated for brace 1 and brace 3 are shown in Figure 4.43. Results show that the amount of energy dissipated increases with increasing maximum displacement of the pretibial shell. However, it does appear that the dissipated energy begins to level off at the higher maximum displacements.

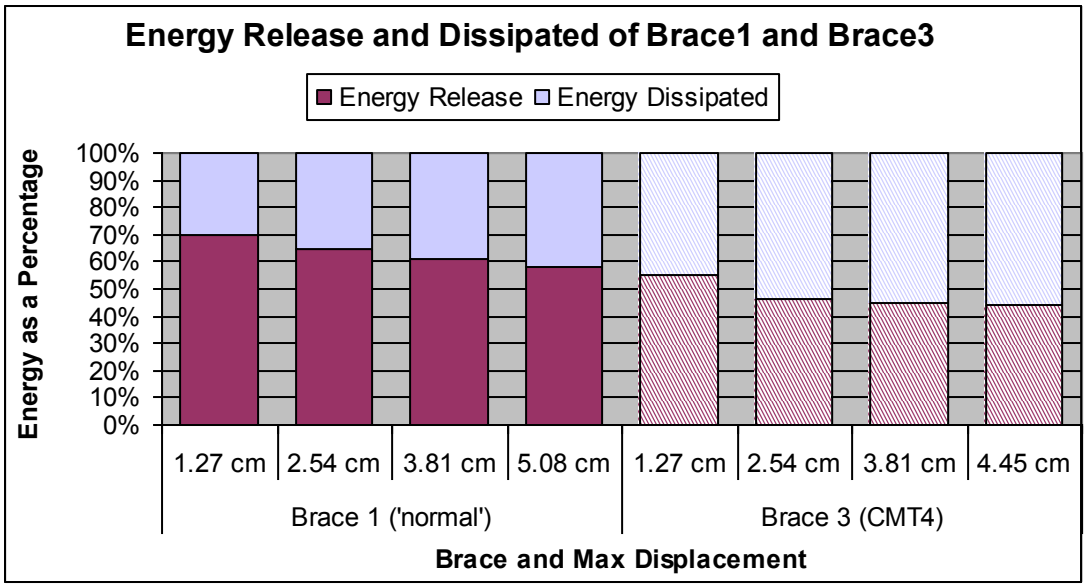

Figure 4.43: Energy percentages of release and dissipation of brace 1 and brace 3

CHAPTER 5

FINITE ELEMENT MODELING AND ANALYSIS

5.1 System and Software

Finite Element Analysis (FEA) provided an efficient way to change the AFO variables and determine the effect on overall performance. It can be used to determine if the performance is a function of the material or the geometry. It also allowed calculation of the brace energy storage properties.

A replication of the 'normal' subject left brace was analyzed to verify the model based on experimental test data from the previous chapter. The model was analyzed in the horizontal cantilever configuration using different ply angles to determine brace stiffness and gage strain. A nonlinear analysis was also used to attempt to replicate the nonlinear unload line seen during experimental testing.

The model was analyzed by a Xeon CPU 3.00GHz dual processor computer with 2.00GB of RAM. The software used was Altair HyperMesh, a high-performance finite element pre- and post-processor, OptiStruct a static solver, and LS-DYNA, a dynamic finite element program. The material of the brace was altered to determine differences in the model due to ply orientation. The model was compared to human motion data and experimental data to determine the accuracy of the force vs. displacement curves and the gage strain.

5.2 Capturing Surface Geometry of the HELIOS

The outer surface of each brace was digitized into the computer using a Polhemus FastSCAN Scorpion 3D scanner. The scanner wand shown in Figure 5.1 had a non-

contact range finder and used a laser to produce scans relative to the position of the stationary transmitter. The setup shown in Figure 5.1 was used to allow full scanning of a brace without the need to reorient it during scanning. Since the surface of the brace was black and therefore difficult for the scanner to see, tape was applied to the surface to be scanned. The tape adds a negligible thickness to the surface being scanned. Many sweeps were performed to digitize the entire brace. The Polhemus software was used to combine the overlapping sweeps and delete redundant points. The RBF surface was exported as a cloud of points (Figure 5.2 (a)) and then imported into SolidWorks for further processing. The SolidWorks add-in option ScanTo3D was used and further processing was performed to delete points. The cloud of points was made into a 3D surface by creating a series of 3D sketches with splines (Figure 5.2 (b) and (c)) and then lofting the splines together. This created a fairly accurate surface of the brace as shown in Figure 5.2(d).

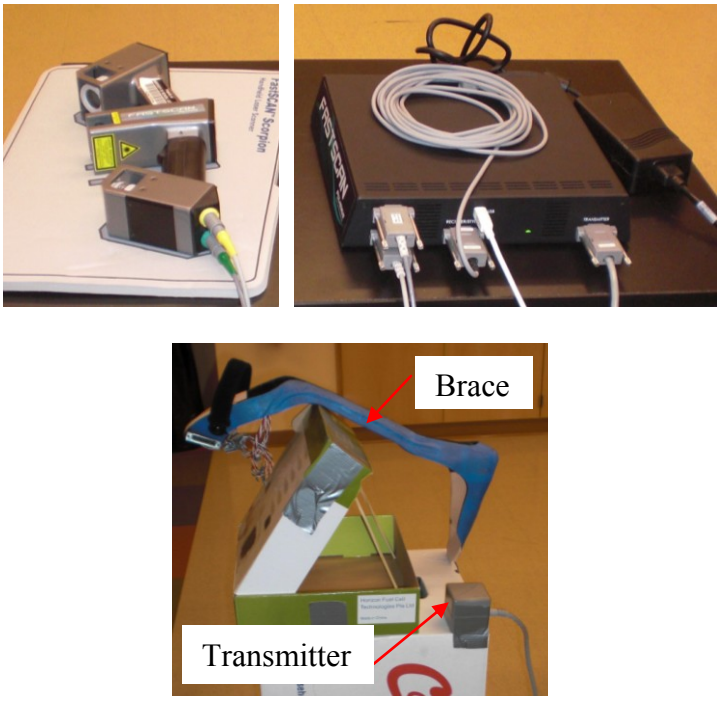

Figure 5.1: 3D scanner wand, processing unit, and scanning setup

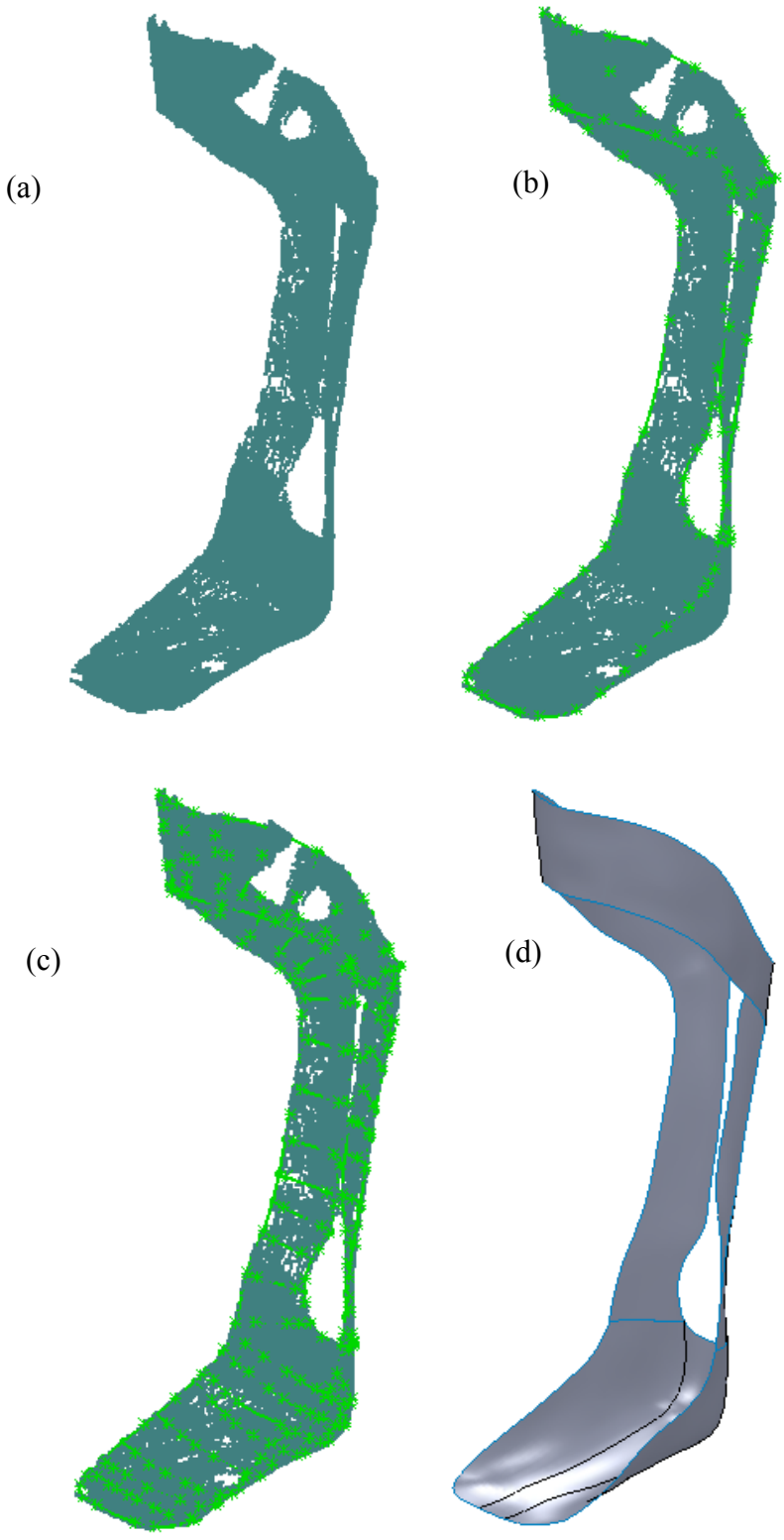

Figure 5.2: 3D brace (a) cloud of points, (b) exterior splines,

(c) interior splines, (d) surface loft

5.3 Selection of Mesh in HyperMesh

The 3D surface of the brace was imported into Altair HyperMesh and meshed with 4-node quadratic shell elements (Figure 5.3) where variable thicknesses could be defined to create a 3D body. The thicknesses of the shell elements were based on manual measurements of the composite fabric as discussed in the next section.

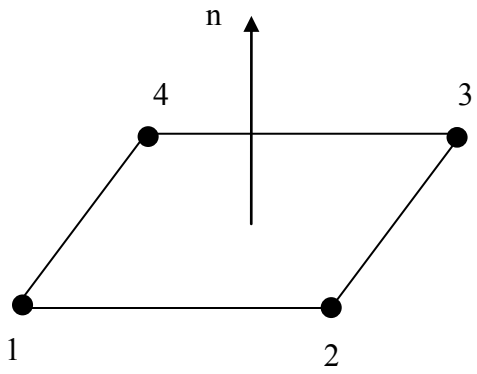

Figure 5.3: 4-node quadratic shell element

Shell elements were chosen since this type of element conforms well to surface contours and can be deformed in all 6 degrees of freedom at each node (three components of translation in the nodal x, y, and z directions and three components of rotation about the x, y, and z axes). The shell element also permits the use of HyperLaminate, a tool in HyperMesh that allows composite laminates to be defined, when the MAT8 card is chosen. The MAT8 card defines orthotropic material properties. The number of integration points defined in HyperLaminate was 1 since the thickness of the individual plies was small and multiple plies were used to create the laminate.

5.4 Material Properties

Each HELIOS brace was made from multiple layers of bidirectional carbon, bidirectional carbon-Kevlar, and was vacuum formed with an epoxy matrix. The brace also contained stretch nylon which is located in the pretibial shell. Two types of carbon were used on the brace and are designated as “narrow carbon” and “wide carbon”. The narrow carbon had a standard width of 3.81 cm whereas the wide carbon had a standard width of 12.7 cm. The carbon-Kevlar had a standard width of 1.91 cm.

During fabrication of the brace, the carbon and carbon-Kevlar were stretched and the original angle and thicknesses of the fabric were altered. These fabrics were measured to determine the angle and thicknesses of the original fabric, the fabric stretched longitudinally, and the fabric stretched transversely. Ply angles were measured with a protractor and thicknesses were measured with calipers. The stretch nylon did not retain its shape when stretched longitudinally or transversely so, this fabric was only measured for thickness and angle in the original unaltered state. All of these results are shown in Table 5.1.

The reported angles are with respect to the vertical axis as shown by Figure 5.4 which shows the change in angles of the carbon-Kevlar bidirectional material. When the material was stretched longitudinally a small angle was produced, whereas a large angle was produced when the material was stretched transversely. In the remainder of the text “small angle” will refer to the longitudinally stretched material and “large angle” will refer to the transversely stretched material.

Table 5.1: Material angles and thicknesses

		Material			
		carbon-Kevlar	narrow carbon	wide carbon	nylon
Original (OA)	width (cm)	1.91	3.81	12.70	12.70
	angle (deg)	30	30	30	30
	thickness (mm)	0.80	0.49	0.55	0.28
longitudinally stretched (SA)	width (cm)	1.52	3.49	7.62	n/a
	angle (deg)	20	24	17.5	n/a
	thickness (mm)	0.86	0.51	0.60	n/a
transversely stretched (LA)	width (cm)	2.67	6.35	22.86	n/a
	angle (deg)	40	47	56	n/a
	thickness (mm)	0.74	0.42	0.47	n/a

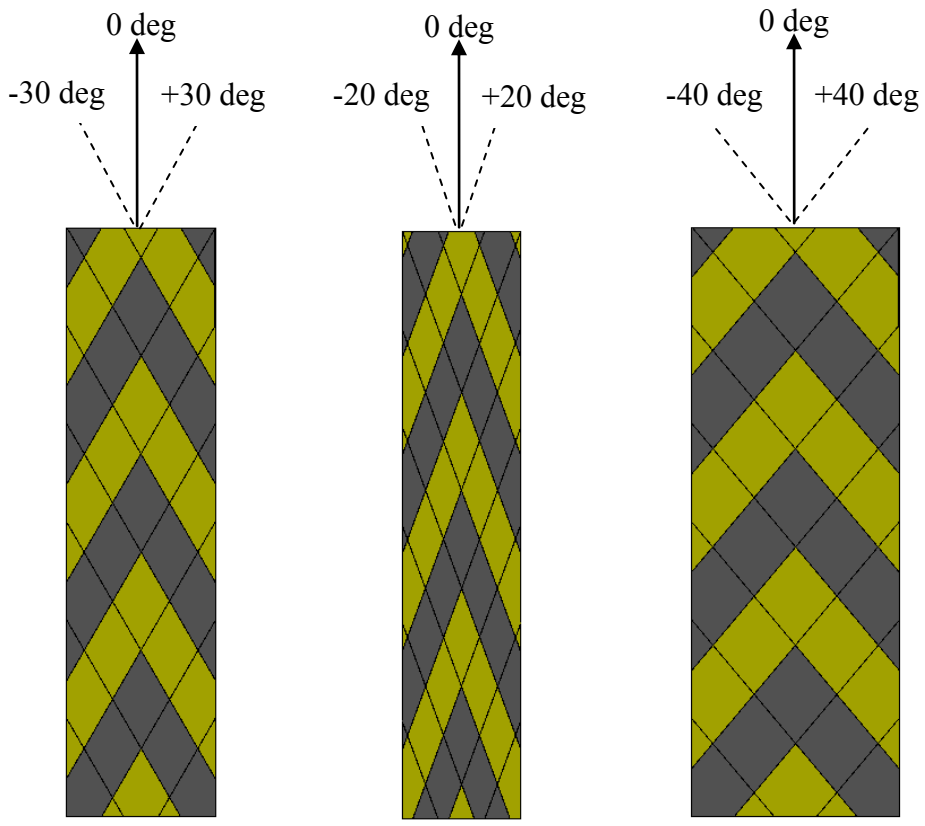

Figure 5.4: The effect of stretching the braided carbon-Kevlar performs: (a) original fabric "original angles (OA)", (b) longitudinally stretched fabric "small angles (SA)", (c) transversely stretched fabric "large angles (LA)"

Properties were calculated for the bidirectional plies using classic plate theory as discussed by Mallick [16] using the properties of unidirectional high strength carbon-epoxy, unidirectional Kevlar-49-epoxy, and unidirectional nylon-epoxy as shown in Table 5.2. The nylon-epoxy properties were calculated from material properties of nylon and epoxy, as shown in Table 5.3. All material properties were calculated assuming a 50% volume fraction.

Table 5.2: Material properties for unidirectional Kevlar-49-epoxy, unidirectional high strength carbon-epoxy, and unidirectional nylon-epoxy *[16] **[calculated]

	Unidirectional Kevlar 49-epoxy*	Unidirectional AS carbon-epoxy*	Unidirectional Nylon-epoxy**
Modulus along fiber, E_1 (GPa)	76	127.5	3.2
Modulus across fiber, E_2 (GPa)	5.5	9	3.2
Shear modulus, G_{12} (GPa)	2.1	5.7	2.0
Poisson's ratio, υ_{12} (-)	0.34	0.25	0.33
Density, ρ (kg/m^3)	1380	1540	1195

Table 5.3: Material properties for nylon and epoxy *[54, 55] **[16]

	Nylon*	Epoxy**
Tensile modulus, E (GPa)	3	3.425
Shear modulus, G_{12} (GPa)	4.1	1.354
Poisson's ratio, υ_{12} (-)	0.392	0.265
Density, ρ (kg/m^3)	1140	1250

Figure 5.5 illustrates the difference between a unidirectional ply and a bidirectional ply. For a unidirectional ply, the properties in the direction of the fiber orientation are denoted with a '1' and the properties transverse to the fiber orientation are denoted with a

‘2’. To distinguish different directions for a bidirectional material ‘x’ and ‘y’ are used in place of ‘1’ and ‘2’.

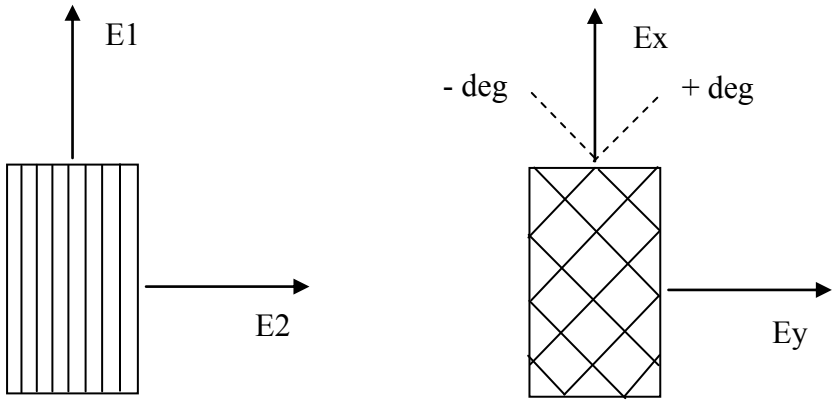

Figure 5.5: (left) Unidirectional, (right) Bidirectional

Eight layers were used to define the carbon-Kevlar material as a symmetric laminate with the following stacking sequence $[\pm 30C/\pm 30K]_s$. This is the minimum number of layers to adequately describe the bidirectional ply since it contains two material types (carbon and Kevlar) and two angles (±30 deg). The narrow and wide carbon materials were defined as four layers to create a symmetric ply with two angles $[\pm 30]_s$. The plies were layered as shown in Figure 5.6 for the carbon-Kevlar and Figure 5.7 for the carbon and nylon.

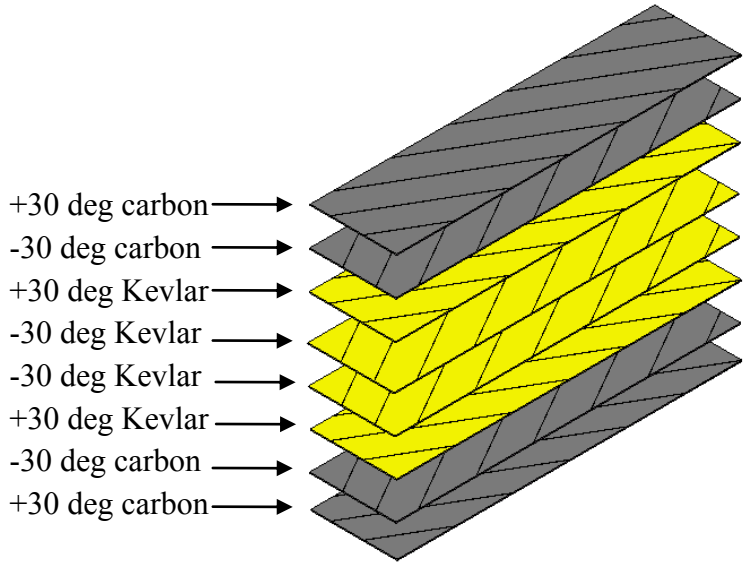

Figure 5.6: Unidirectional layered plies for carbon-Kevlar laminate

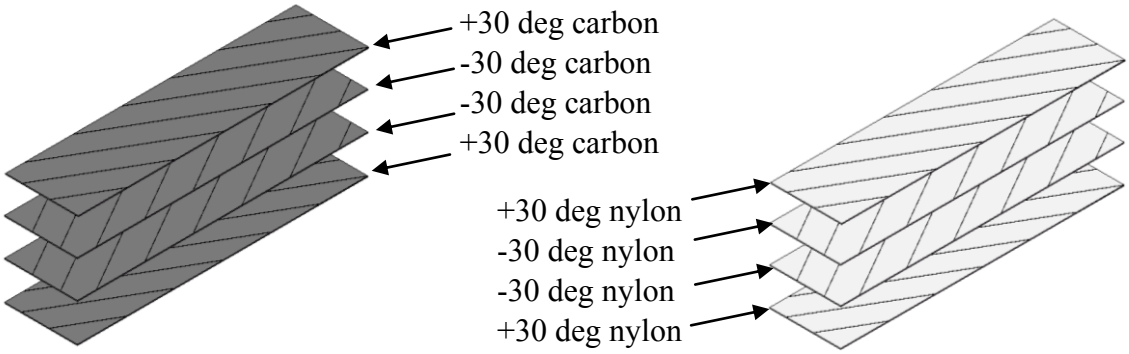

Figure 5.7: Unidirectional layered plies for (left) carbon laminate (right) nylon laminate

Table 5.4 shows the calculated material properties for the bidirectional carbon-Kevlar-epoxy and bidirectional carbon-epoxy with respect to the different fiber angles. There was no difference in the calculated combined properties of the materials if the stacking sequence was changed, as long as the ply was symmetric. The calculated material properties for carbon-epoxy were compared to values determined by experimental tests found in the literature (citations not included due to confidentiality

agreement). The properties compared were E_x, E_y, and ν_{xy}, at ply angles of 25°, 30°, and 60°. The calculated properties were approximately 15% higher for E_x and E_y, as shown in Figure 5.8, and 15% higher for ν_{xy}, as shown in Figure 5.9. The moduli could be lower than the Classical Laminate Theory (CLT) calculations due to the interlacing tows which create a complicated loading path and decrease properties. The Poisson's ratio could be higher due to the interlaced material scissoring during loading. The calculated properties of all materials were adjusted to reflect the differences between the calculated and experimental properties and are shown in Table-5.5.

Table 5.4: Unadjusted material properties for bidirectional nylon-epoxy, bidirectional carbon-Kevlar-epoxy, and bidirectional carbon-epoxy

	nylon-epoxy	carbon-Kevlar-epoxy			narrow-carbon-epoxy			wide-carbon-epoxy		
	OA	SA	OA	LA	SA	OA	LA	SA	OA	LA
	±30°	±20°	±30°	±40°	±24°	±30°	±47°	±7.5°	±30°	±56°
Modulus along x-axis, E_x (GPa)	4.1	67.7	36.5	18.3	70.7	49.0	17.8	96.1	49.0	12.7
Modulus along y-axis, E_y (GPa)	4.1	7.6	8.4	11.0	10.3	11.5	21.8	9.6	11.5	37.7
Shear modulus, G_{xy} (GPa)	1.4	13.2	20.7	25.6	20.8	26.2	32.9	14.7	26.2	29.2
Poisson's ratio, υ_{xy} (-)	0.14	1.24	1.33	0.96	1.28	1.25	0.65	1.05	1.25	0.38
Density, ρ (kg/m^3)	1195	1460	1460	1460	1540	1540	1540	1540	1540	1540
Ply thickness, t (mm)	0.278	0.865	0.804	0.739	0.511	0.493	0.424	0.602	0.546	0.466

Note: OA = "original angles", SA = "small angles", LA = "large angles"

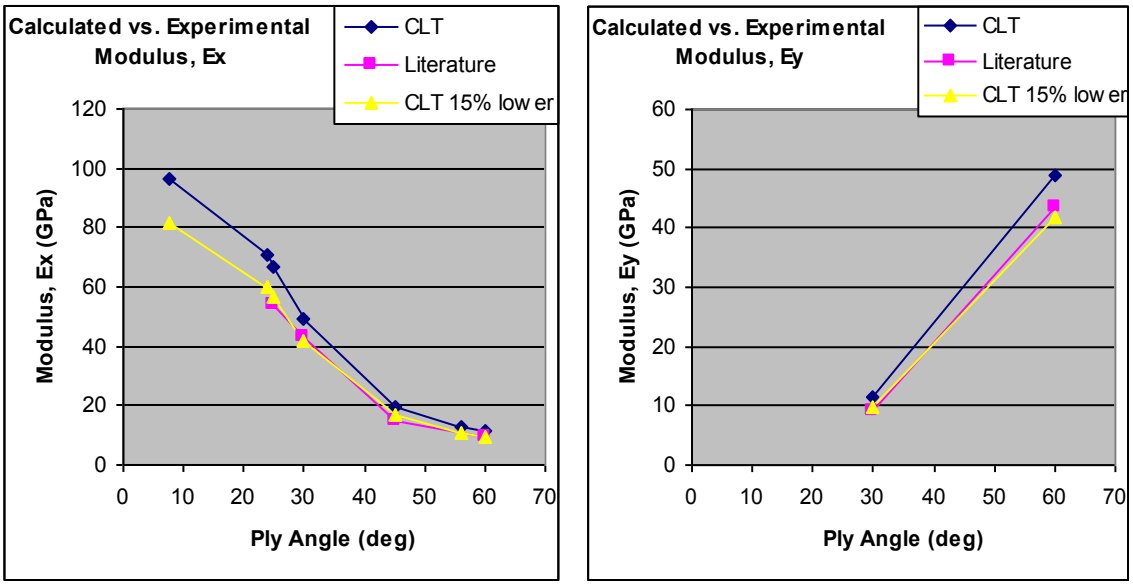

Figure 5.8: Differences in calculated Modulus using Classical Laminate Theory (CLT) and experimental values from the literature

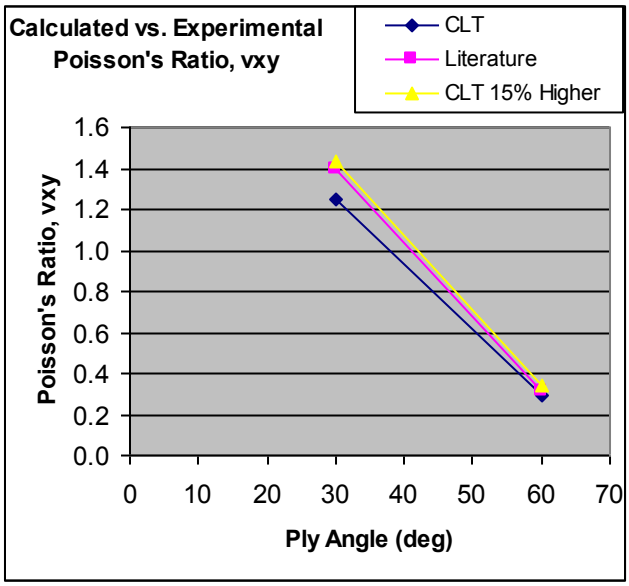

Figure 5.9: Differences in calculated Poisson's Ratio using Classical Laminate Theory (CLT) and experimental values from the literature

Table 5.5: Adjusted material properties for bidirectional nylon-epoxy, bidirectional carbon-Kevlar-epoxy, and bidirectional carbon-epoxy

	nylon-epoxy	carbon-Kevlar-epoxy			narrow-carbon-epoxy			wide-carbon-epoxy		
	OA	SA	OA	LA	SA	OA	LA	SA	OA	LA
	±30°	±20°	±30°	±40°	±24°	±30°	±47°	±7.5°	±30°	±56°
Modulus along x-axis, E_x (GPa)	3.5	57.5	31.0	15.5	60.1	41.6	15.1	81.7	41.6	10.8
Modulus along y-axis, E_y (GPa)	3.5	6.4	7.1	9.3	8.8	9.8	18.5	8.2	9.8	32.0
Shear modulus, G_{xy} (GPa)	1.2	11.2	17.6	21.8	17.7	22.3	28.0	12.5	22.3	24.8
Poisson's ratio, υ_{xy} (-)	0.16	1.43	1.53	1.11	1.47	1.44	0.75	1.20	1.44	0.44
Density, ρ (kg/m^3)	1195	1460	1460	1460	1540	1540	1540	1540	1540	1540
Ply thickness, t (mm)	0.278	0.865	0.804	0.739	0.511	0.493	0.424	0.602	0.546	0.466

5.5 Meshed FE Model

Material properties calculated in the previous section were applied to the shell elements for bidirectional carbon fiber-epoxy and bidirectional carbon-Kevlar-epoxy. Since the properties were dependant upon the angle of the fibers and the narrow carbon angles differ from the wide carbon angles, there were actually three different material types which made up the brace: 1) narrow carbon, 2) wide carbon, and 3) carbon-Kevlar. There was also a fourth material which was a piece of stretch nylon located in the pretibial shell. The brace was broken into eight different material sections because not all of the materials were combined in each area of the brace. These sections are shown in Figure 5.10. The model was comprised of 4154 shell elements. A model comprised of

16454 elements was evaluated as well and the response only varied an average of 1.2% from the response of the model comprised of 4154 shell elements.

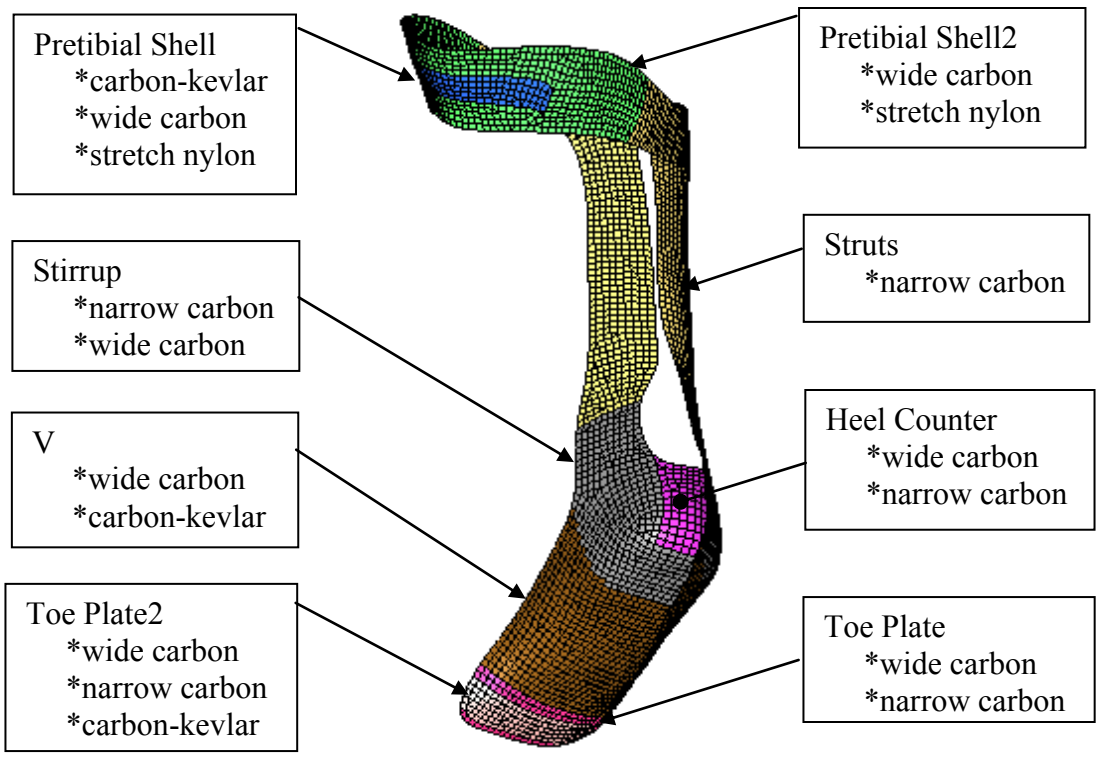

Figure 5.10: HELIOS brace divided into material sections

HyperLaminate was used to define material properties: E_x (modulus along x-axis), E_y (modulus along y-axis), G_{xy} (shear modulus), υ_{xy} (Poisson's ratio), and ρ (density). The material properties used assumed a linear stress-strain relationship, so the material model was only valid for the elastic region. This limited the FE model to small deformations within the linear-elastic region.

Local coordinate systems were individually defined for each section. This was done to align the ply directions properly. Four different methods were utilized to properly

define the coordinate systems as shown in Table 5.6. Figure 5.11 through Figure 5.14 graphically shows the defined coordinate systems for each of the eight sections. The struts are of particular interest because the fabric moves in the direction of the contour.

Table 5.6: Methods to properly define local coordinate systems

coordinate system defined by	section name
system axis (local 2-axis, select XYZ global axis)	pretibial shell 2
	heel counter
angle (90 deg)	struts
vector	prebibial shell
system ID (select XYZ global axis)	toe plate
	toe plate 2
	stirrup
	sole

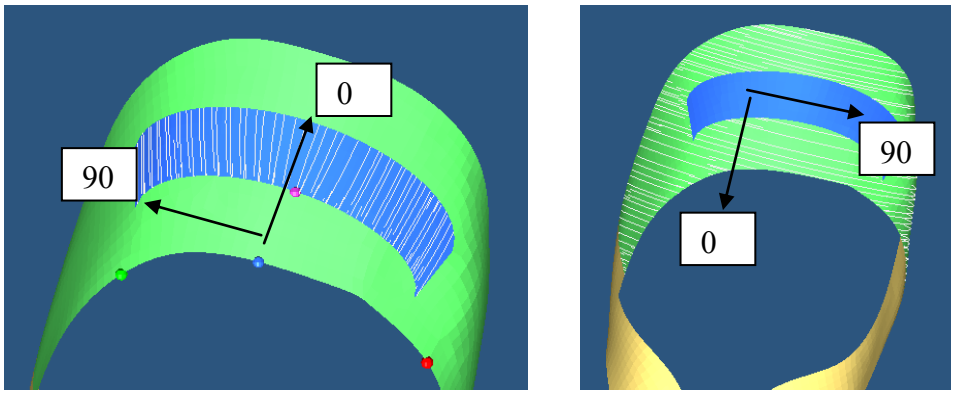

Figure 5.11: (left) Pretibial shell, (right) Pretibial shell2

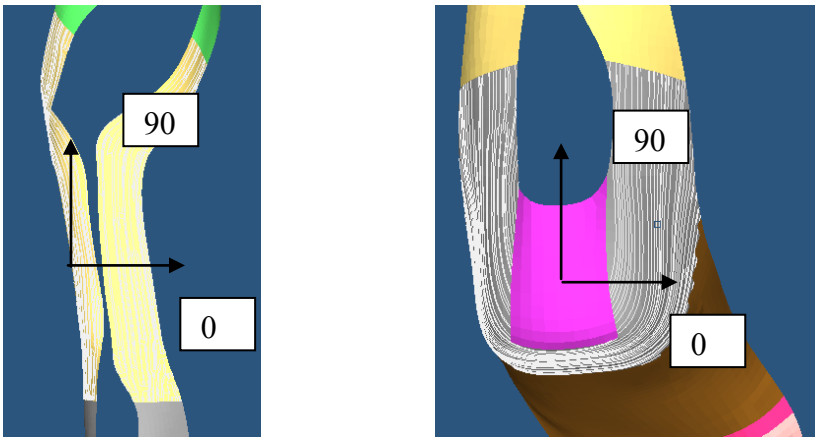

Figure 5.12: (left) Struts, (right) Stirrup

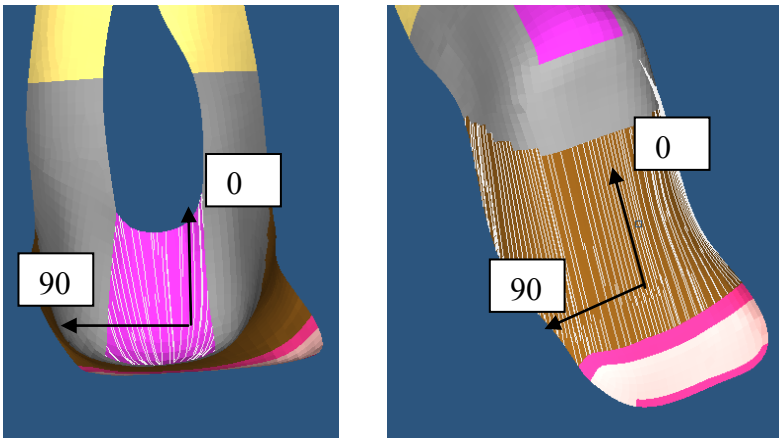

Figure 5.13: (left) Heel counter, (right) Sole

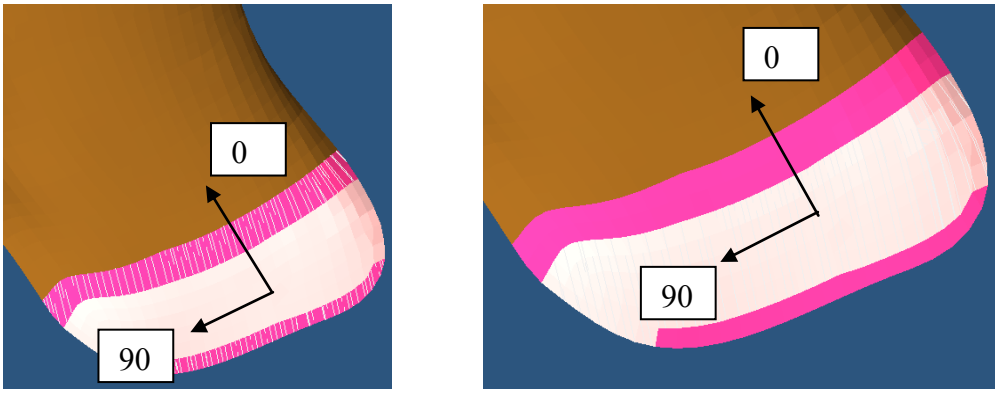

Figure 5.14: (left) Toe plate, (right) Toe plate 2

Once the local coordinate systems were defined, HyperLaminate could be used to change the direction of the plies. Since the material properties were calculated based on the bidirectional angles, the plies only needed to be oriented in reference to the 0 degree axis or 90 degree axis. For example, Figure 5.15 shows a ply defined with respect to the 0 degree axis and the 90 degree axis. In addition, since material properties were calculated and entered for the bidirectional ply, each layer was considered to be one ply. This made the FE model more accurate (rather than modeling eight plies) since there truly was only one ply.

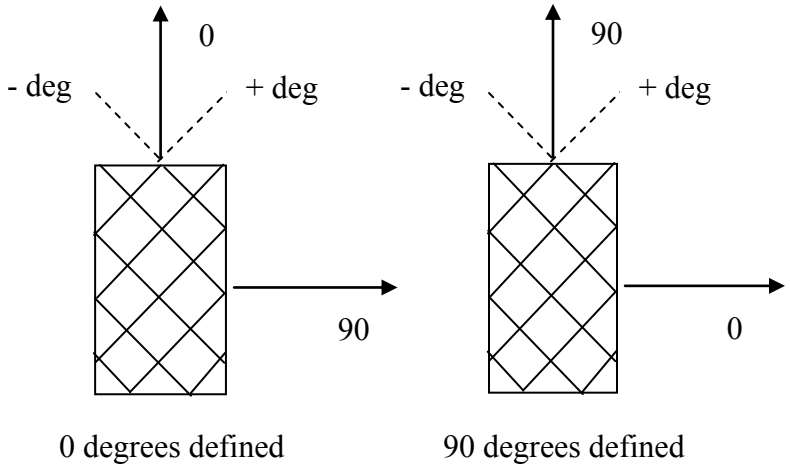

Figure 5.15: (left) Ply oriented on 0 degree axis, (right) Ply oriented on 90 degree axis

5.6 Boundary Conditions

The boundary conditions included an applied force at the pretibial shell and single point constraints at the base of the brace as shown in Figure 5.16. The input to the model was the pretibial force as determined by experimental mechanical tests. A total of 46 nodes were chosen to define the area where the 2.54 cm diameter nose applied force

during experimental testing. The model was constrained at the foot corresponding to where the brace was fixed during experimental mechanical tests. A total of 177 nodes were rigidly constrained. These nodes encompassed a 3.18 cm x 6.35 cm area corresponding to the clamping marks left on the brace from experimental testing.

It is important to note that the brace had a low density foam placed on the pretibial shell and foot area for optimum comfort of the user and was left on during experimental mechanical testing. This made the brace suitable to clamping and assured the load was applied evenly to the surface of the brace. The foam was not included in the model since the strength of the composite materials is significantly greater than the foam. The foam will only have an effect on the beginning of the load curve.

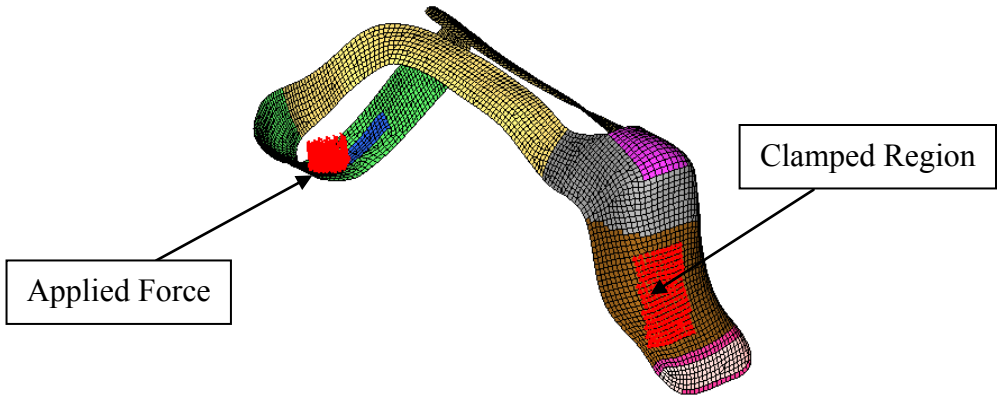

Figure 5.16: Forces and constraints, isometric view

5.7 Static Linear Analysis

A static analysis using Altair OptiStruct was performed first to validate the model using the results of the experimental mechanical tests. Five conditions were analyzed to show the effect of the ply angle and thickness on the displacement of the pretibial shell.

Table 5.7 shows the five conditions with the material properties and ply thicknesses used for the analysis corresponding to those listed in Table 5.5.

Table 5.7: Conditions used for static analysis

Condition	Material Properties	Ply Thickness
1	small angle values	small angle values
2	small angle values	original angle values
3	original angle values	original angle values
4	large angle values	original angle values
5	large angle values	large angle values

The measured thicknesses of the individual plies, shown in Table 5.5, were input into HyperLaminate and added together to calculate the total thickness of each section. These total thicknesses and the measured thicknesses of the physical brace for each section are shown in Table 5.8. Most sections showed smaller values for the FE calculated thicknesses than for the measurements of the physical brace. Two sections with the largest difference were the 'Pretibial Shell 2' and 'Toe Plate'. Both of these sections occurred next to another section with a larger thickness of fabric. It is concluded that these two sections might harbor extra epoxy to provide a smooth transition (taper) from a section with a larger thickness to another section with a smaller thickness, the smaller thickness area having extra epoxy.

Two of the sections showed larger calculated thicknesses than the measurements of the physical brace, 'Pretibial Shell' and 'Sole'. The 'Pretibial Shell' section may be squeezed and flattened out more so than the other sections due to it having extra layers of fabric. The 'Sole' section had several overlapping pieces of material and due to limitations of the digital micrometer, measurements of the entire section could not be

made. The remaining sections were all slightly smaller in thickness when calculated by the FE model. It is possible that this error was most likely due to extra epoxy thickening up the entire brace. It could also be caused from inaccurate measurements of the physical brace itself. Since the brace contains complex contours it was difficult to measure the thicknesses even though a digital micrometer with a ball end attachment was used and could be a source of error.

Table 5.8: Brace thicknesses

	Thicknesses of brace according to section					
	FE condition 1	FE condition 2	FE condition 3	FE condition 4	FE condition 5	Physical brace measured
	(mm)	(mm)	(mm)	(mm)	(mm)	(mm)
Pretibial Shell2	1.76	1.65	1.65	1.65	1.49	2.47
Pretibial Shell	3.49	3.26	3.26	3.26	2.97	3.20
Struts	3.07	2.96	2.96	2.96	2.54	3.29
Heel Counter	2.23	2.08	2.08	2.08	1.78	2.29
Stirrup	5.29	5.04	5.04	5.04	4.32	5.84
Toe Plate2	3.96	3.69	3.69	3.69	3.26	4.60
Toe Plate	2.23	2.08	2.08	2.08	1.78	3.85
Sole	3.54	3.25	3.25	3.25	2.88	3.17

The brace mass was also calculated by HyperMesh for all of the five conditions based on the input material densities and thicknesses. The physical brace weighed in at 0.302 kg whereas HyperMesh calculated the brace to be between 0.23 kg and 0.283 kg. This weight difference could be from excess epoxy attributing to the higher mass. The brace mass for all five FE conditions are included in Table 5.9.

Table 5.9: Brace mass

	FE condition 1	FE condition 2	FE condition 3	FE condition 4	FE condition 5	Physical brace measured
overall mass (kg)	0.283	0.268	0.268	0.268	0.233	0.302

As stated previously, the input to the model was the pretibial force. The outputs of the model were the strains and stresses on the brace struts in addition to the pretibial displacement. All five conditions were analyzed and all simulations would completely run in just a few seconds. Brace contours of displacement and deformation for condition 1 are shown in Figures 5.17 and 5.18. Brace contours for all five conditions are provided in Appendix G.

Figure 5.19 shows the pretibial force and associated pretibial displacement of all five conditions. The relationship was linear and expected since a linear analysis was performed on the FE model. Conditions 1, 2, and 3 are grouped closely together whereas conditions 4 and 5 are grouped together. This indicates that the material properties of the small angles and original angles were similar and as the angle was increased considerably, the brace decreased its ability to hold the same load. The graph also shows that the thickness of the plies had less of an effect on the material than the angle of the ply fibers.

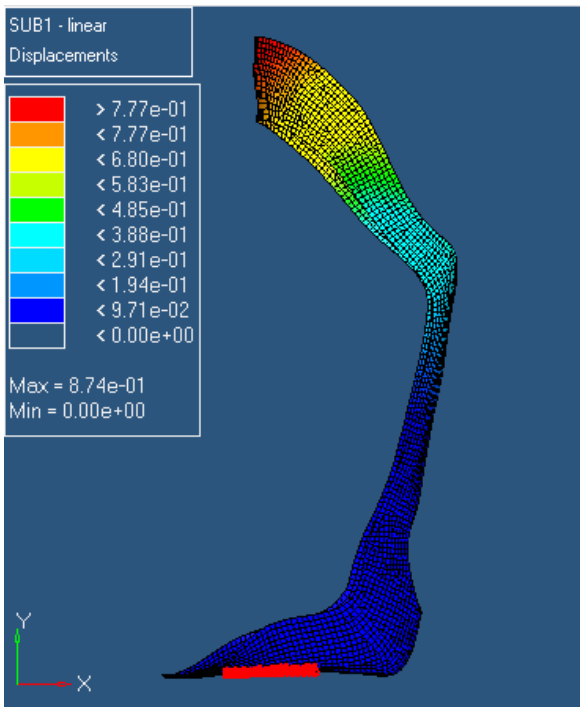

Figure 5.17: Displacement contour of condition 1, small angle thickness and properties

(units are shown in inches)

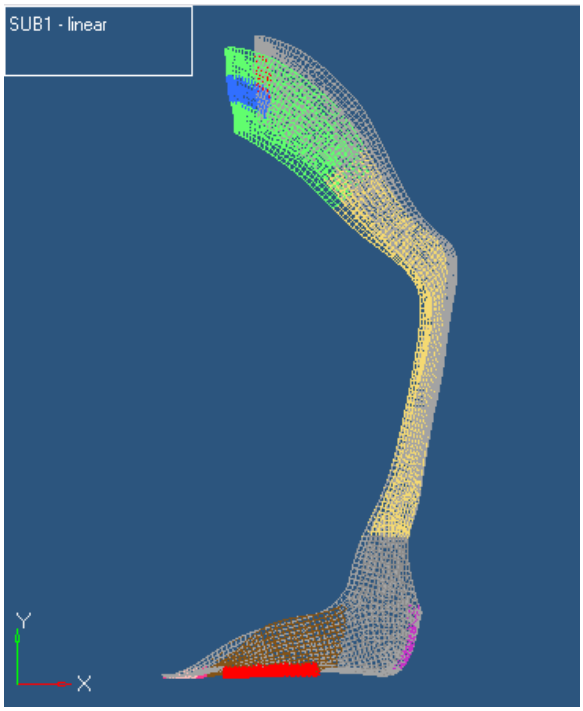

Figure 5.18: Deformation of condition 1, small angle thickness and properties

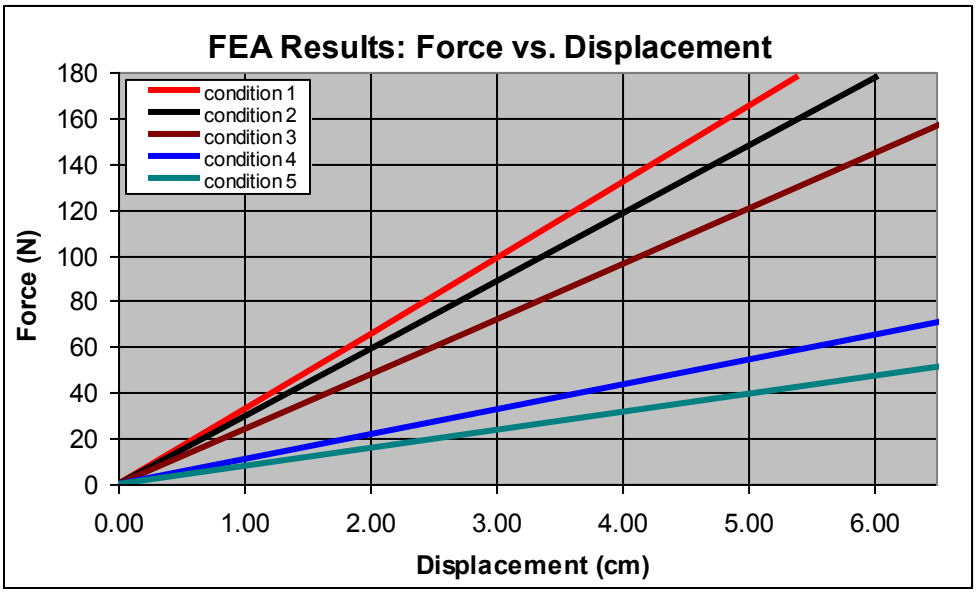

Figure 5.19: Pretibial force and displacement

Figure 5.20 shows a graph of the FE forces and displacements with the MTS experimental forces and displacements. Results show a good match of the FE model with the MTS testing data. Condition 1 (small angle material values with small angle ply thickness values) and condition 2 (small angle material values with original angle ply thickness values) matched the best to the MTS data. This is highly encouraging since during fabrication the materials were stretched so that smaller angles were created as compared to the original fabric. This indicates that the FE model is accurately predicting the pretibial displacement. As discussed in the previous chapter, the experimental results showed a decrease in slope with an increase in maximum displacement. Since the FE model was analyzed as a linear case, it should match best with MTS 1.27 cm which lines up well with condition 1.

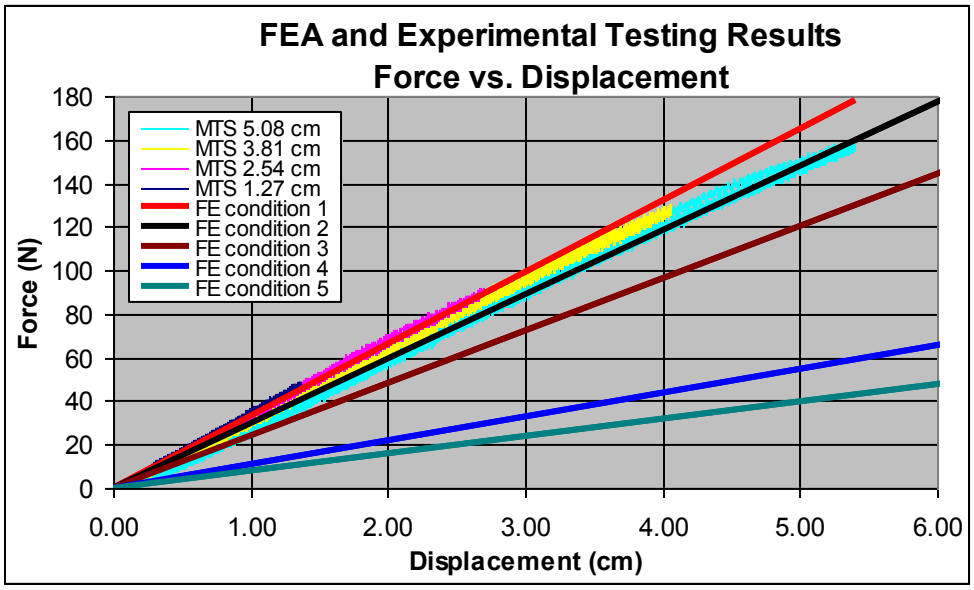

Figure 5.20: FEA and MTS experimental pretibial force and pretibial displacement

The maximum pretibial displacement of the brace during human motion testing was approximately 2.01 cm, as calculated in the previous chapter. This value was based on the maximum strain gage readings of the human test and related to the strain gage readings of the MTS experimental tests where the pretibial force was known. To accurately compare the strain of the brace struts of the FE model to the human testing and MTS testing, the FE model was analyzed for all five conditions using a 66.7 N applied force at the pretibial shell which corresponded to the 2.01 cm displacement. The FE calculated strains can now be compared directly to the human testing maximum strain values and the MTS strain values at the 66.7 N applied force. Figure 5.21 shows the P1 (major) strain contour for condition 1.

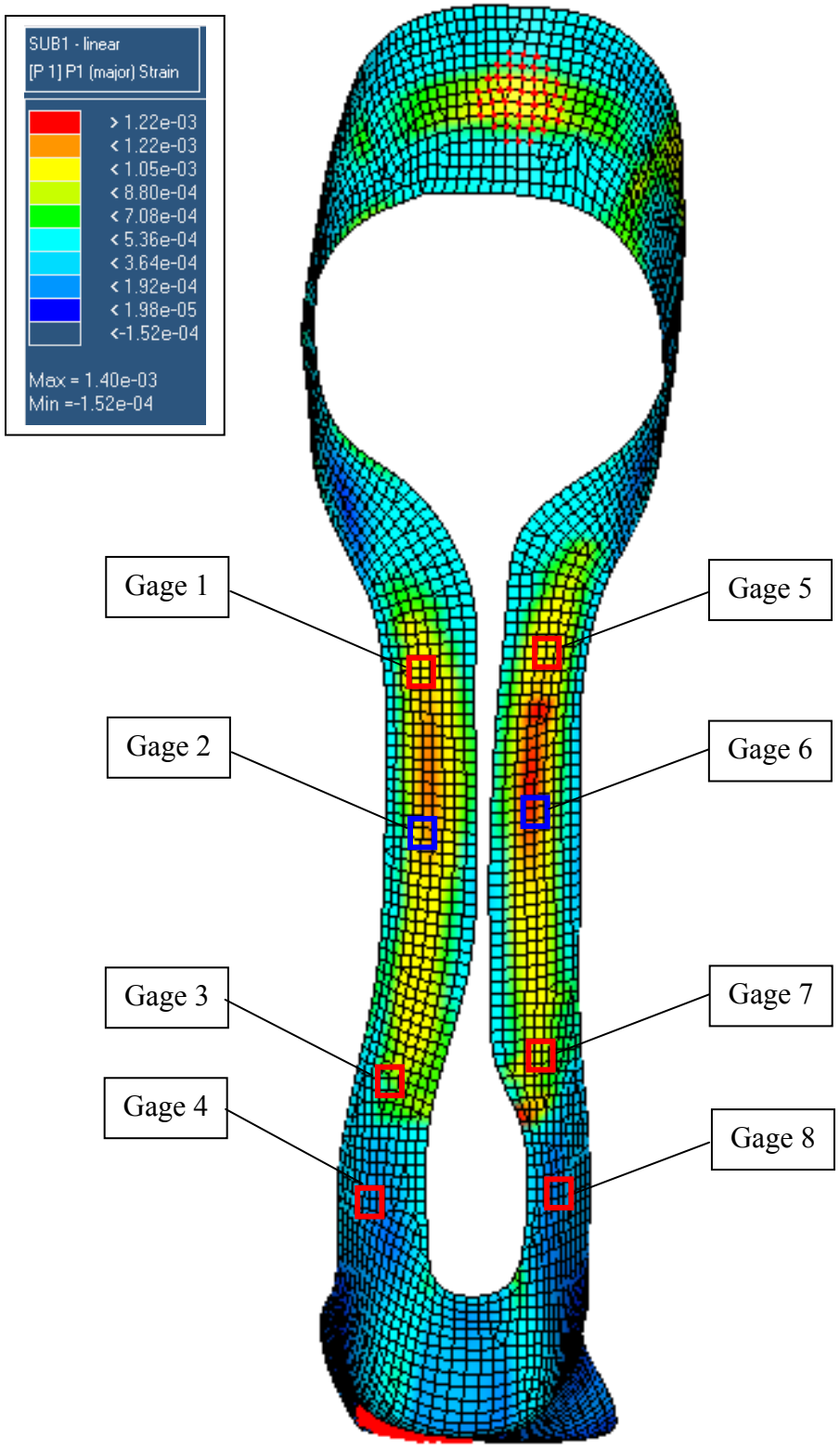

Figure 5.21: Strain contour of condition 1, small angle thickness and properties

The physical brace was measured to locate the position of each of the strain gages and then correlated to an element located on the FE model. Figure 5.22 shows the strain of these elements corresponding to the gage number for all five evaluated conditions. HyperMesh allowed the selection of several types of strain, in this instance "P1 major strain" was chosen. This is the principal major strain located on the outermost ply of the brace which was also the ply on which the strain gages recorded strain. There is a slight error in that the strain calculated by HyperMesh was the strain located on the midplane of the ply and not on the exterior of the brace surface as measured experimentally. Depending on the condition, the midplane of the outermost ply was located approximately 0.25 mm away from the ply surface.

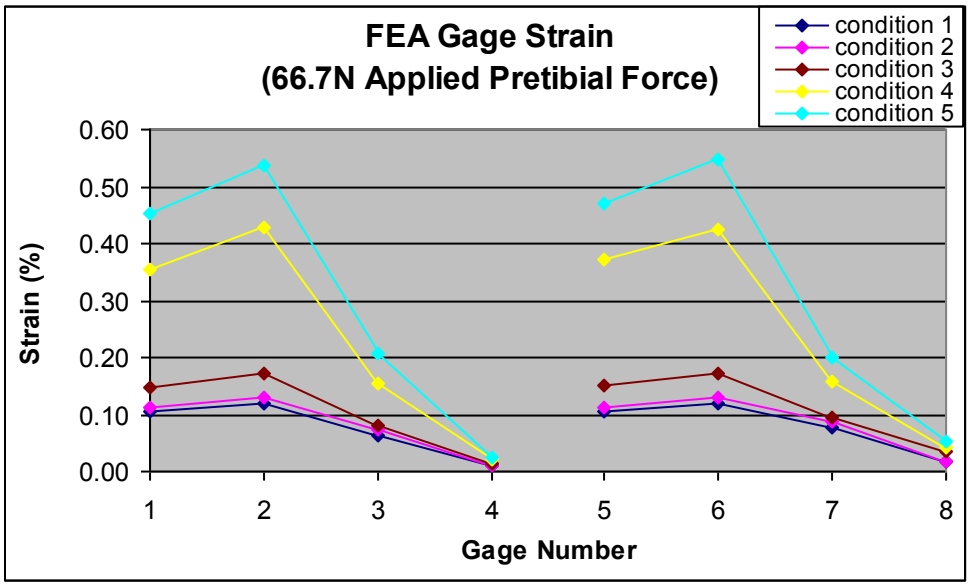

Figure 5.22: FE model strain with an applied pretibial force of 66.7 N

As shown by the graph, the strain on the brace increased with increasing ply angle and again, similar to the force vs. displacement curves, the first three conditions were

grouped closely together. It should be noted that the strain values seen were well within the failure strain of the material which is about 1.85 %strain as determined by mechanical testing of the bidirectional material (citation not included due to confidentiality agreement).

Figure 5.23 shows the FE model strain with the measured gage strain during MTS experimental testing and human motion testing. Only the first three FE conditions are shown graphically since these were the conditions that match better with the measured strain values from the experimental and human testing. The MTS tests and FE conditions 1 and 2 (small angles) matched the best. Table 5.10 shows the %Strain values of all the tests shown in the figure in addition to the %difference values of the FE conditions that matched best with the MTS and human motion tests. The static MTS test matched best with FE condition 1.

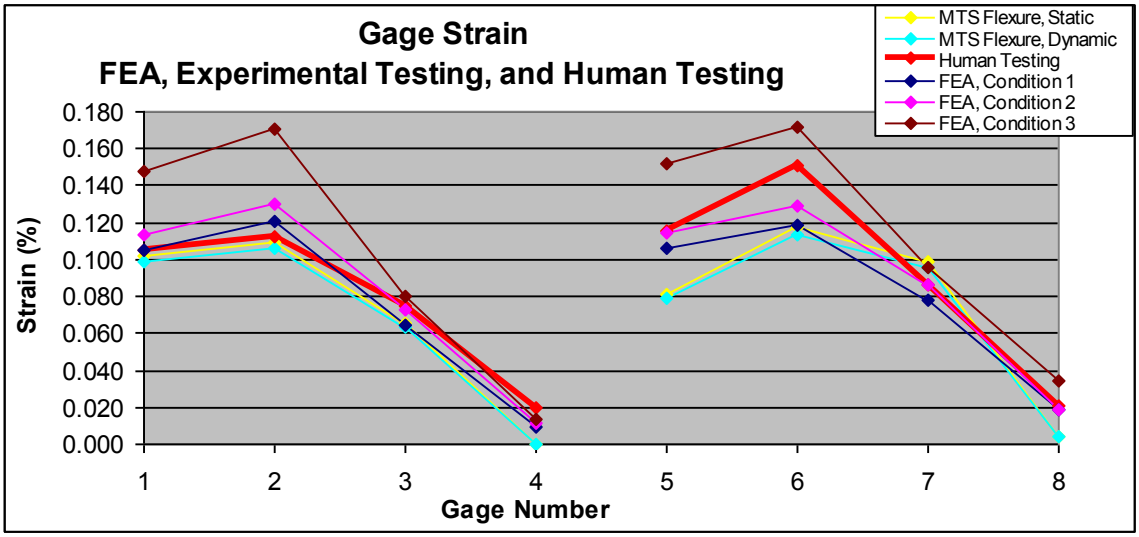

Figure 5.23: Strain from FEA, MTS experimental testing, and human testing with an applied force of 66.7 N

Table 5.10: Strain values and percent differences of MTS, Human, and FE tests

	% Strain						% Difference	
Gage Number	MTS Static	MTS Dynamic	Human Motion	FE Cond. 1	FE Cond. 2	FE Cond. 3	MTS Static vs. FE Cond. 1	Human Motion vs. FE Cond. 2
1	0.1017	0.0985	0.1056	0.1052	0.1132	0.1481	3.4	7.0
2	0.1092	0.1061	0.1122	0.1203	0.1296	0.1702	9.7	14.4
3	0.0653	0.0632	0.0744	0.0642	0.0724	0.0800	1.7	2.7
4	-0.0003	-0.0005	0.0200	0.0095	0.0111	0.0131	214.3	57.6
5	0.0811	0.0789	0.1156	0.1063	0.1140	0.1520	26.9	1.4
6	0.1176	0.1139	0.1511	0.1191	0.1287	0.1715	1.3	16.0
7	0.0987	0.0953	0.0867	0.0781	0.0863	0.0958	23.3	0.4
8	0.0043	0.0037	0.0211	0.0187	0.0191	0.0345	125.7	10.3

The largest differences seen were at the ankle gage locations. It is possible that these large percent differences were seen because the strain gage values were small and minute differences created large differences. Previous research showed the highest strains were located in the ankle of standard polypropylene braces [32,37,41]. This was not the case for the HELIOS brace probably due to the unique strut design of the brace.

Interestingly, the gage strain at the 66.7 N load does not differ significantly from the static MTS tests to the dynamic MTS tests. This could indicate that either the dynamic rate was not fast enough or that this brace operates similarly under static and dynamic rates. In addition, it could also be that the applied force was too low to create a large difference between the static and dynamic rates.

The human data matched better with FE conditions 1 and 2 (small angles). Only gage 6 for the human data tended to be much higher than all of the other gage data. The FE condition 3 (original angles) values for gage 1, 2, 5, and 6 were also much larger than the

values for all other conditions. This indicates that the ply angle had a larger effect on gages 1, 2, 5, and 6. These were the gages located at the top curve of the strut and on the middle of the struts. Applying this same logic to the human tests could indicate that fabric located at the gage 6 spot might have slightly larger ply angles than at the other gage locations. This is possible since the brace was handmade and variations in fabrication may exist.

One explanation for the differences seen between the human data, MTS tests, and FE model may be from the different loading of the brace under the three different testing methods. The human subject will load the brace in a different manner than the MTS tests since during normal gait the subject will roll from the lateral part of the heel to the medial side of the ball of the foot. This type of action was not replicated in the MTS tests since a simple fixturing design was chosen. The MTS tests and FE conditions might not match due to modeling the brace which may include geometric differences, applied force placement, constraint placement, material properties, and ply angles and to name a few.

The stresses of the brace were calculated using HyperMesh, which allowed the selection of several types of stress. The principal major stress "P1 major stress" is the stress located on the outermost ply of the brace. Just as the strain values are located on the midplane of the ply, so too are the stress values. Figure 5.24 shows the P1 (major) stress contour of the brace for condition 1 and Figure 5.25 shows the stress of the selected strain gage locations. The stress values were fairly close together for all conditions except condition 5.

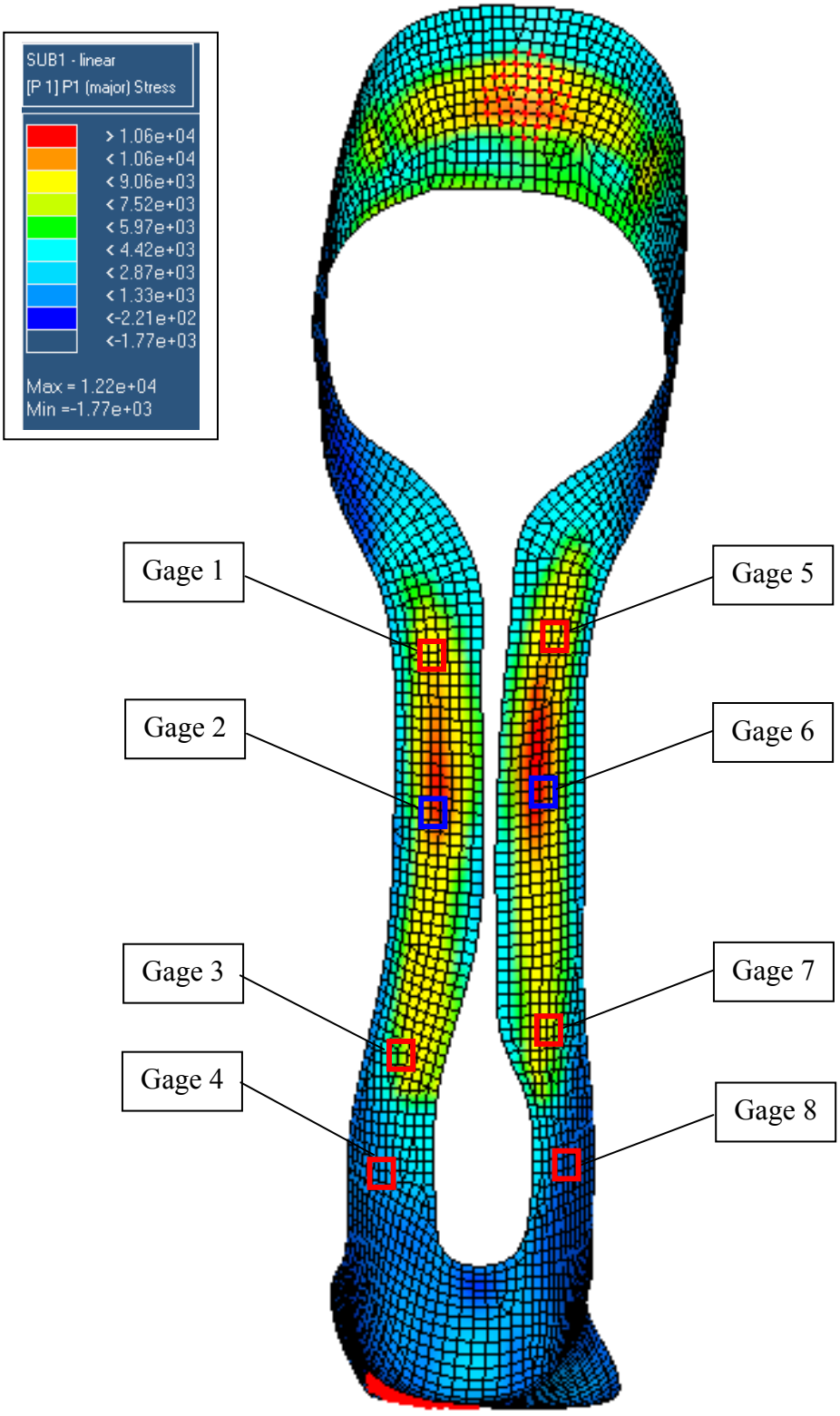

Figure 5.24: Stress contour of condition 1, small angle thickness and properties

(units are shown in psi)

While keeping the thickness of the brace constant, small ply angles (condition 2) tended to increase the amount of stress whereas large ply angles (condition 4) decreased the amount of stress. When taking into account the natural decrease in ply thickness with an increase in ply angle, the stresses increased with the larger ply angles.

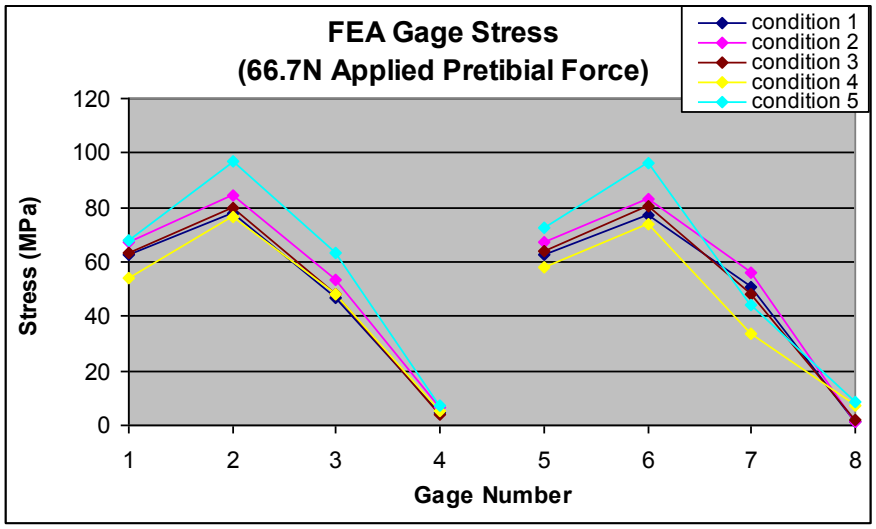

Figure 5.25: FEA calculated stress at strain gage locations

5.7.1 Ply Angle Effects

It was hypothesized that the struts would impact the displacement, strain, and stress results the most. This was tested by running the model using condition 3 properties for all sections except the strut section. This allowed the struts to be changed to small angle and large angle properties to determine if this was indeed the case. Figure 5.26 shows the results of this analysis including condition 2, 3, and 4 as the comparisons.

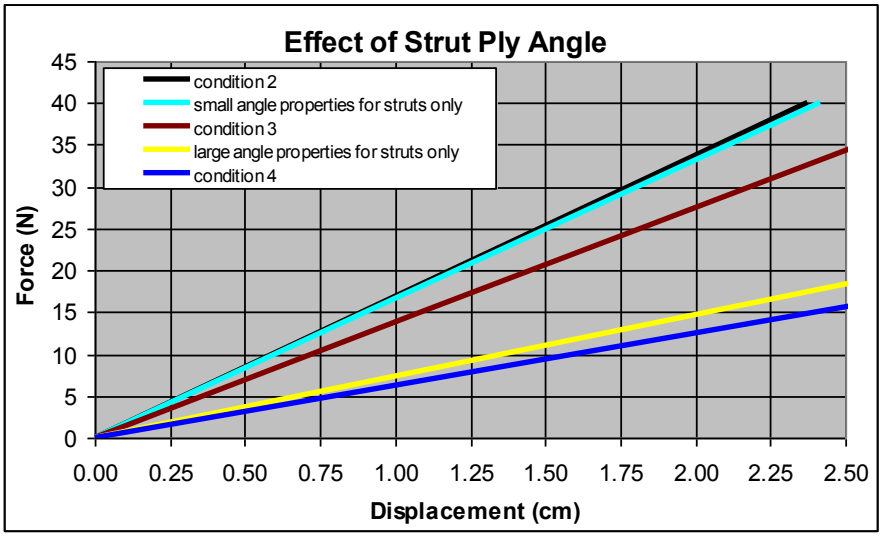

Figure 5.26: Effect of strut ply angle on the pretibial force and pretibial displacement

The original condition 3 with the struts changed to small angle properties yielded a similar result to condition 2 (all sections with small angle properties). Similarly, the original condition 3 with the struts changed to large angle properties yielded a similar result to condition 4 (all sections with large angle properties). This proves that the struts highly influence the force vs. displacement relationship. The same was true for the gage strain as shown in Figure 5.27. The stress of the struts changed when the large angle properties were used for the struts as shown in Figure 5.28. This is perhaps due to the way in which the brace deforms since gage 3 and 7 were located just before the section changes into original angle ply material.

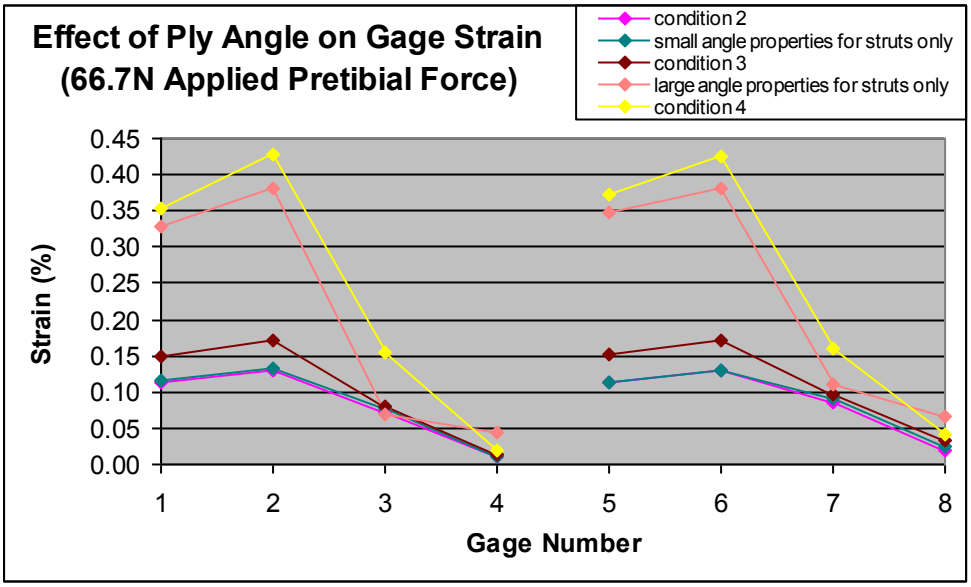

Figure 5.27: Effect of strut ply angle on strain

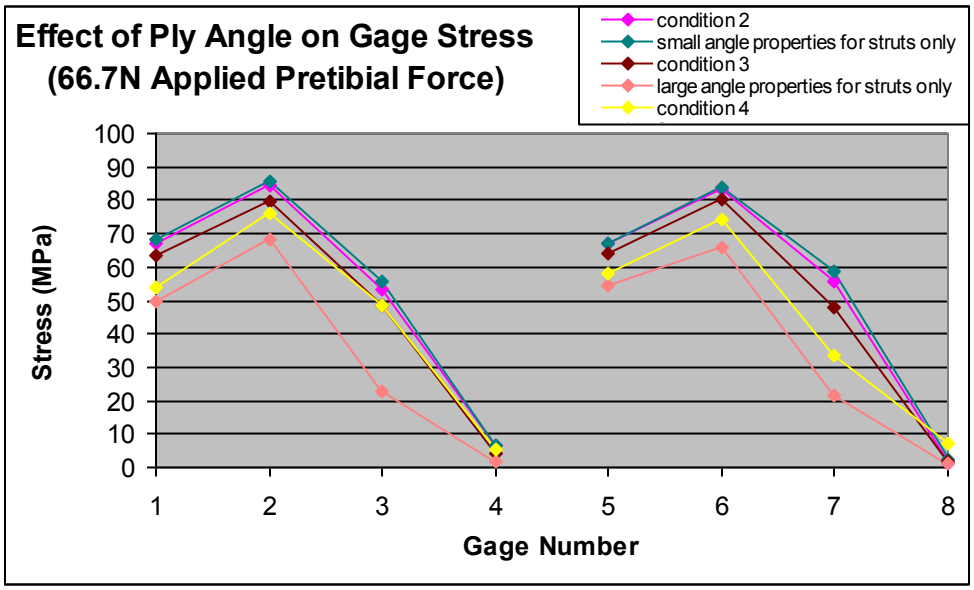

Figure 5.28: Effect of strut ply angle on stress

5.7.2 Maximum Displacement Effects

The condition 1 model was analyzed to see the differences in the strut deformations when a different maximum displacement was applied. Figures 5.29 through 5.32 show the condition 1 model with displacements of 1.27 cm (41.8 N), 2.54 cm (85.6 N), 3.81 cm (125.4 N), and 5.08 cm (167.2 N). The figures show that as the applied maximum displacement increased, the gap between the struts began to decrease. At around 3.81 cm the struts began to touch and by 5.08 cm the struts were overlapping.

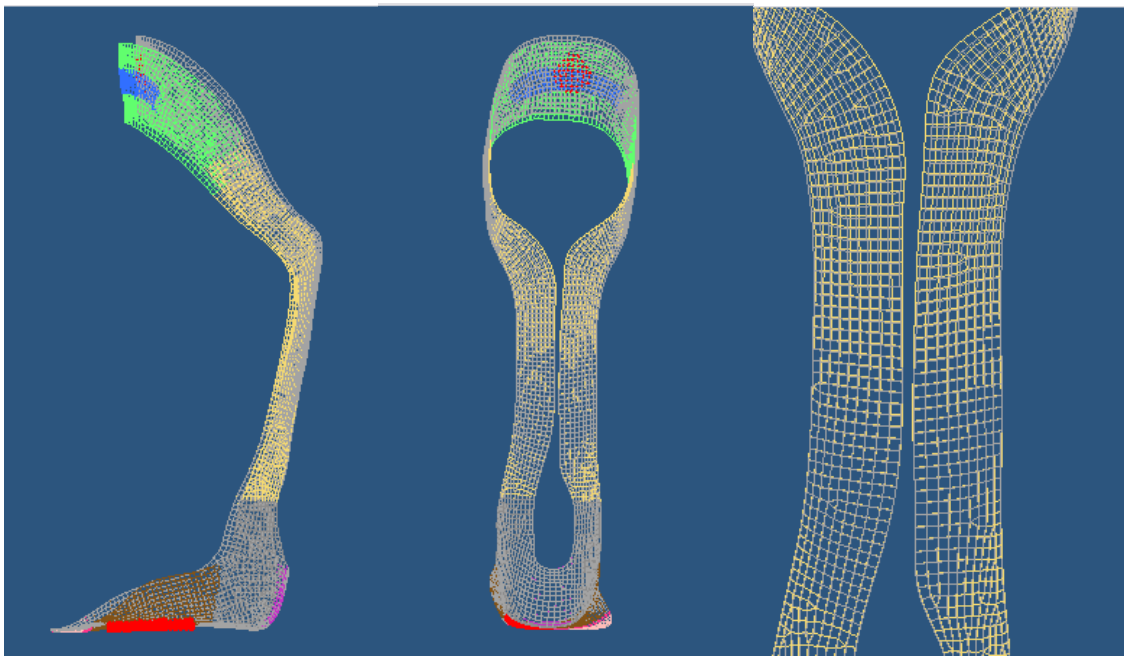

Figure 5.29: Condition 1 deformation at 41.8 N and 1.27 cm

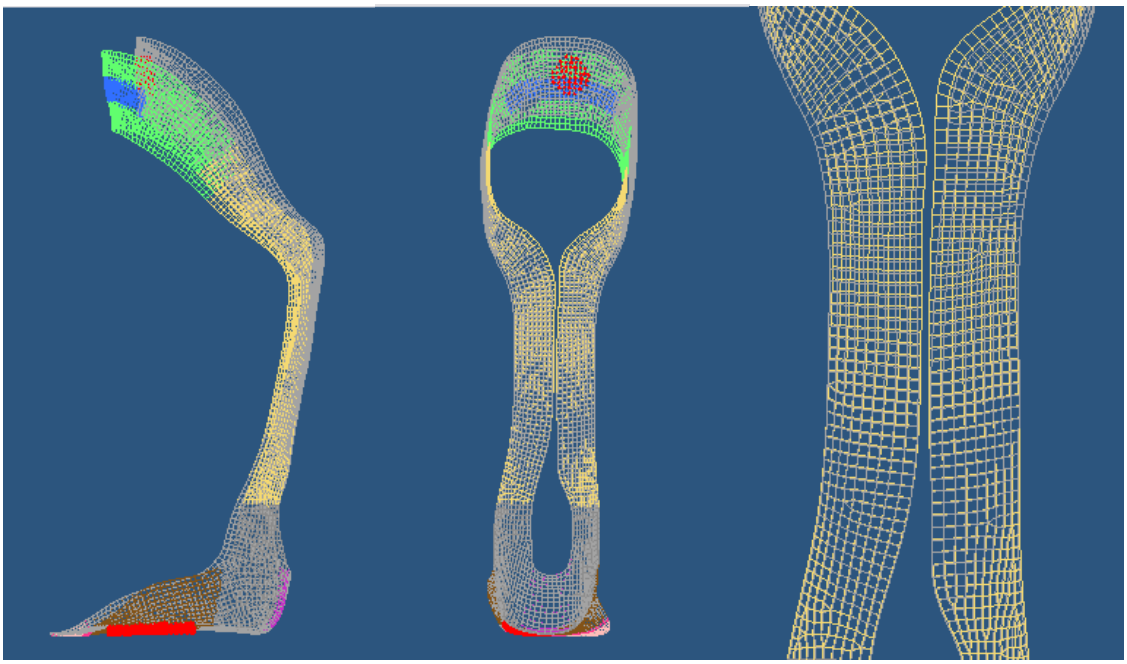

Figure 5.30: Condition 1 deformation at 85.6 N and 2.54 cm

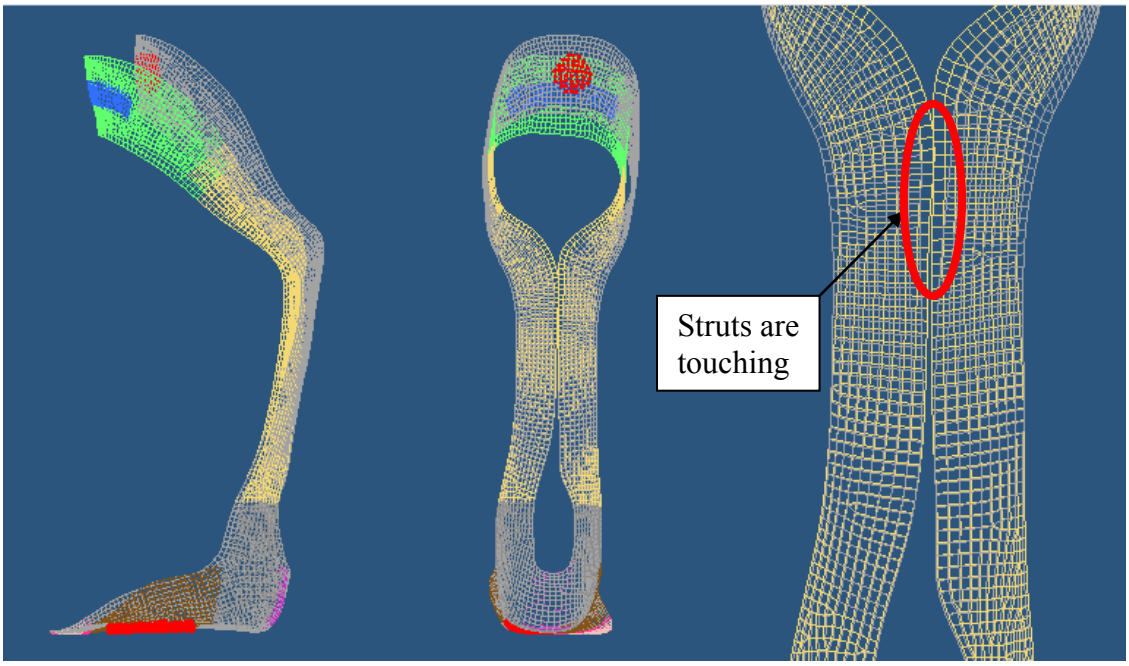

Figure 5.31: Condition 1 deformation at 125.4 N and 3.81 cm

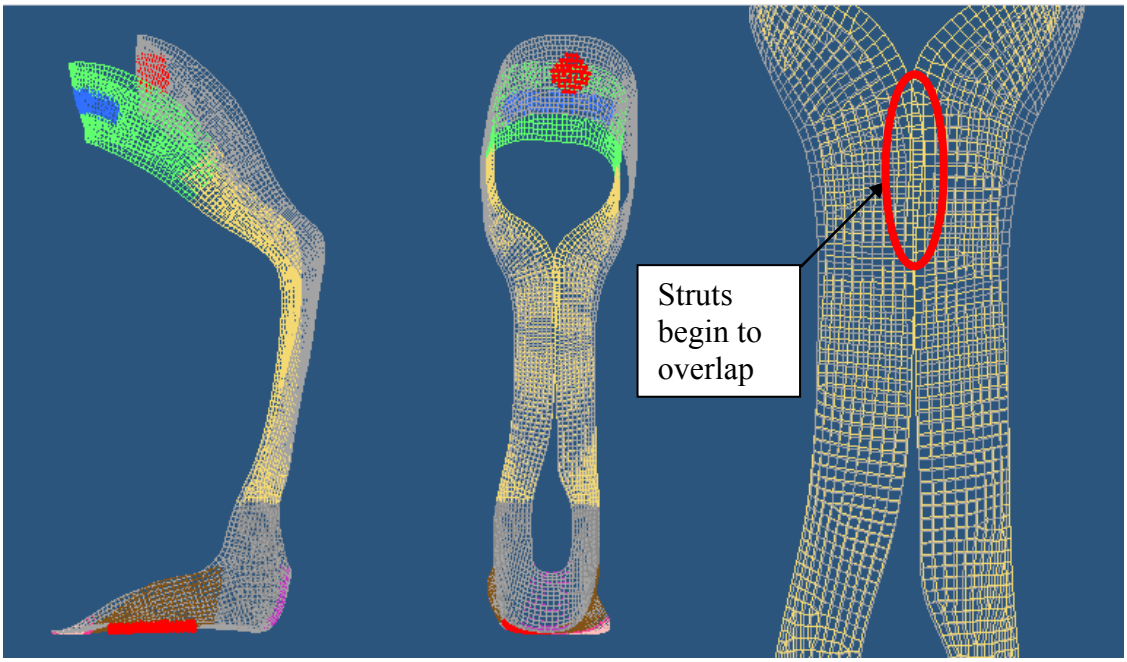

Figure 5.32: Condition 1 deformation at 167.2 N and 5.08 cm

The struts were not observed to touch during experimental testing, so an extra piece of carbon narrow fabric was added to the pretibial2 section shown in green in Figure 5.33. The deformation of the struts with this extra fabric matched better with the deformation of the struts seen during experimental testing. The struts contained overlapping pieces of narrow carbon fiber and it is possible that the definition of the start of the pretibial2 section could be defined a little too low on the brace. If this is indeed the case, the deformation and strains would be a little lower than what was calculated. Shown in the figure is a displacement of 7.62 cm with an applied force of 250.7 N.

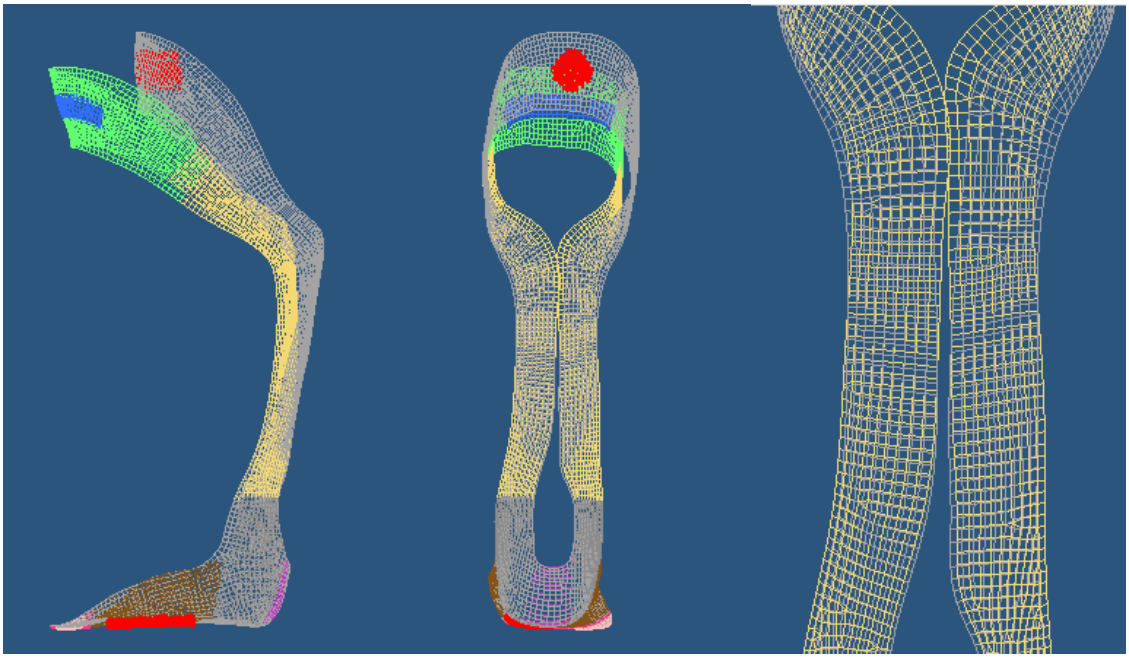

Figure 5.33: Deformation of condition 1 with an extra layer of fabric

(250.7 N and 7.62 cm)

5.8 Static Nonlinear Analysis

LS-DYNA, a dynamic finite-element solver, was used to perform a nonlinear analysis on the HELIOS brace to produce the loading and unloading curves seen during experimental mechanical testing. It was not possible to calculate the unloading curve using static linear analysis since time can not be used as a factor. The nonlinear model using LS-DYNA allowed the analysis to be completed with respect to time. The same meshed model that was used for the static linear analysis was also used for the nonlinear model.

5.8.1 Poisson's Ratio

A Poisson's ratio of 0.3 was used for the carbon and carbon-Kevlar combined material properties to perform the analysis in LS-DYNA. As discussed earlier, the

Poisson's ratios of these combined materials was over 0.5 since they are both orthotic materials. Lemprier proves that an orthotic material does not conform to the $-1<\nu<0.5$ range. Since a bi-directional composite ply is a structure instead of a material it can have a Poisson's ratio larger than 0.5. Lempriere shows that for an orthotropic material, $-1< \nu < 1 - 2\nu'^{2} (E/E')$ [56].

LS-DYNA will not run the analysis with a Poisson's ratio greater than 0.5, so a Poisson's ratio of 0.3 was chosen since the Poisson's ratio of unidirectional carbon-epoxy is 0.3 [16]. The static analysis using OptiStruct was able to run with the calculated Poisson's ratios shown in Table 5.5. The Poisson's ratios were changed to determine the difference in pretibial displacement and strain.

Shown in Figure 5.34 are the values of pretibial displacement when the Poisson's ratio of both composite materials was changed. The Poisson's ratio of nylon was left as is since it was under 0.5. As shown by the figure, the Poisson's ratio did not have a large effect on the outcome. There was a difference of 0.128 cm (6%) in the pretibial displacement when using $\nu=1.5$ as compared to using $\nu=0.15$. There was a similar change in the %strain values as shown by Figure 5.35. There was a difference of 0.008 %strain when using $\nu=1.5$ as compared to using $\nu=0.15$. This equated to less than a 7% change for the top and middle gages (1, 2, 5, and 6), a 17%-19% change for the bottom gages (3 and 7), and a 27% and 45% change for the ankle gages (4 and 8).

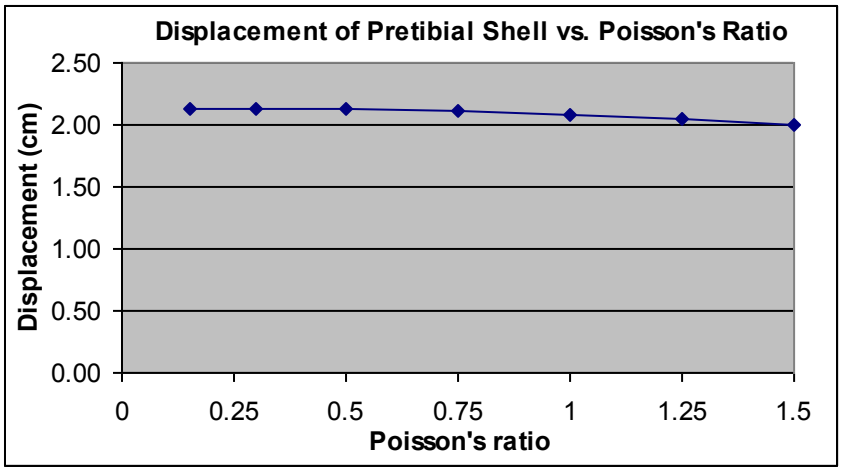

Figure 5.34: Displacement of pretibial shell (condition 1) when different Poisson's ratios are used

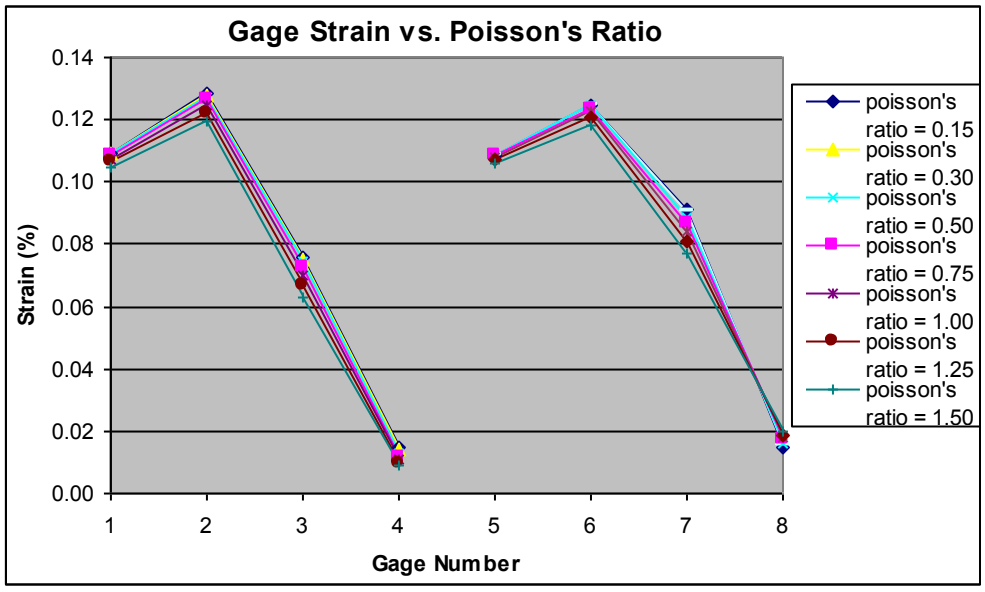

Figure 5.35: Gage strain (condition 1) when different Poisson's ratios are used

5.8.2 Explicit Analysis

Initially an explicit analysis was undertaken since this type of analysis calculates the dependent variables directly from the independent variables. Explicit analysis is generally

used for dynamic simulations but can also be used for static simulations with large deformations. In the case of static simulations, time scaling or mass scaling can be implemented to reduce run time.

A static time curve was used to run the analysis and is shown in Figure 5.36. LS-DYNA calculated the time step to be 6.58e-8 seconds based on this time curve of 600 seconds. The curve was chosen to replicate the quasi-static testing of the brace in loading and unloading with a maximum displacement of 5.08 cm. Using this time step, the analysis would have taken over four weeks to complete. It was decided that mass scaling would be used to decrease the run time of the model. A time step of 8e-6 seconds was chosen which provided a run time of 64 hours.

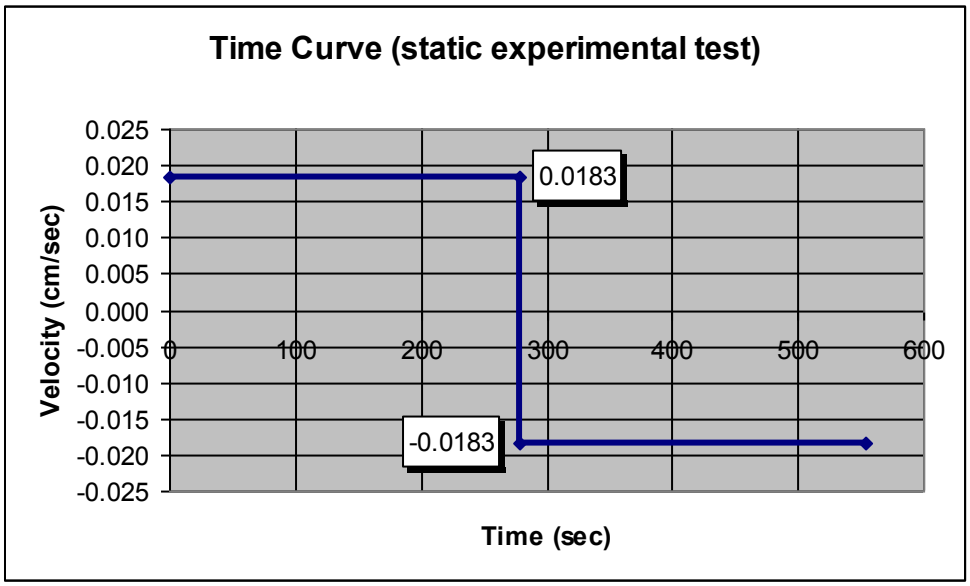

Figure 5.36: Static time curve

Unfavorable results were seen with the brace using the explicit analysis. The force and displacement (138.3 N and 5.08 cm) matched fairly well (15% difference) with the

static HyperMesh analysis (160.1 N and 5.08 cm), but the struts deformed considerably more than the static HyperMesh analysis as shown in Figure 5.37. A contact was not defined so the struts were shown to be overlapping. In addition, a plot of the force vs. displacement (Figure 5.38) for the brace did not yield a nonlinear unload curve, both the loading and unloading curve were linear. It is unclear if the mass scaling used to speed up the analysis was to blame for these errors.

It may be possible that the mass scaling was having a dynamic effect on the brace model and could explain why the load curve was nonlinear. It is also possible that the struts were being deformed drastically and had created a nonlinear loading curve after 4 cm of displacement. The dynamic experimental test did not show a nonlinear load line, but perhaps the experimental loading rate was not large enough to produce the nonlinear loading effect.

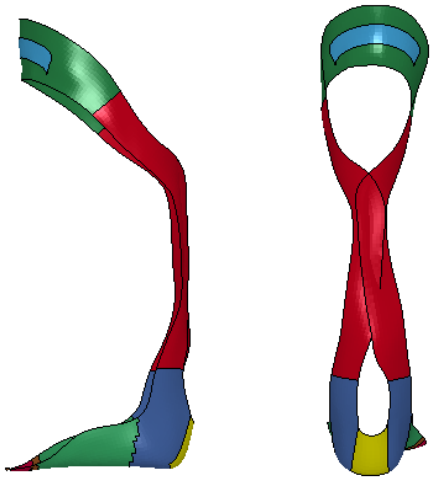

Figure 5.37: Deformation of brace at 5.08 cm pretibial displacement in LS-DYNA using explicit analysis

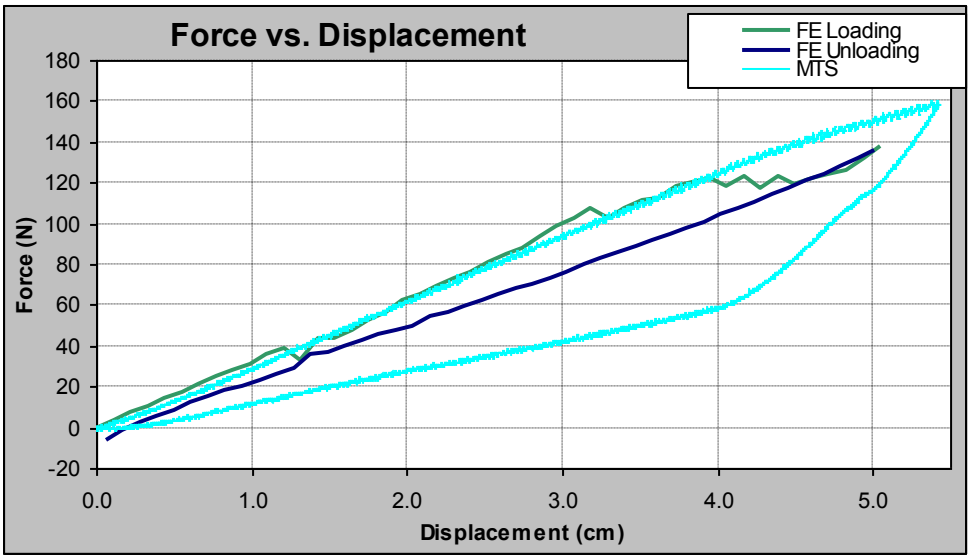

Figure 5.38: Load vs. displacement of brace in LS-DYNA using explicit analysis

5.8.3 Implicit Analysis

It was decided that an implicit analysis would be performed with the hopes that the analysis would yield a nonlinear unloading curve. An implicit analysis uses an iterative technique to solve for the dependent variables and can be used for quasi-static simulations. This method requires the solution to converge on the calculated answer and can be performed in LS-DYNA but requires the use of more control cards. Appendix H includes the control cards used for the explicit and implicit analyses. Further explanation of LS-DYNA cards can be found in the LS-DYNA keyword user's manual [57].

The load function used for the implicit model was displacement control which is more stable than using force control. The analysis showed a much better match of the strut deformations to the HyperMesh model, unlike the explicit analysis. The deformation of the brace struts shown at four different maximum displacements is shown in Figure

5.39. The struts touch at around 3.81 cm displacement and overlap slightly at 5.08 cm displacement.

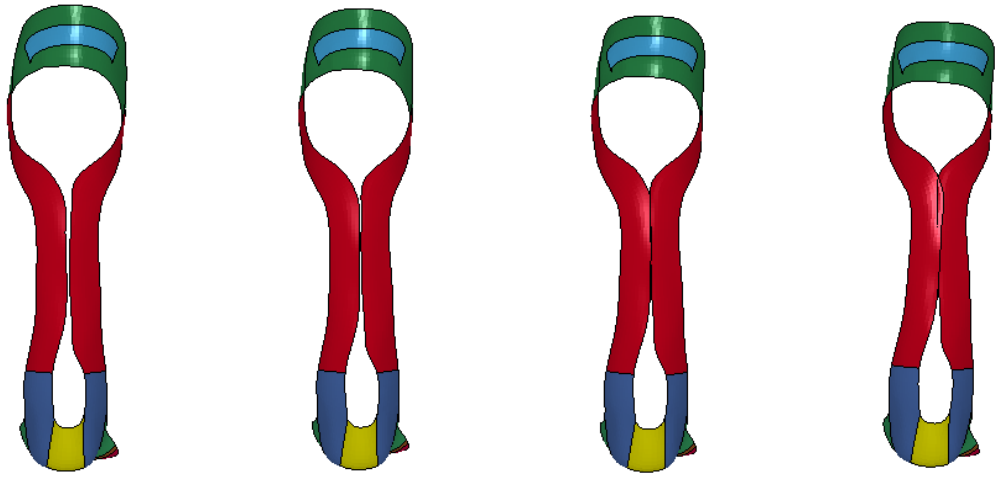

Figure 5.39: Deformation of brace in LS-DYNA using implicit analysis (a) 1.27 cm maximum displacement, (b) 2.54 cm maximum displacement, (c) 3.81 cm maximum displacement, (d) 5.08 cm maximum displacement

The load and unload curves for force vs. displacement are shown in Figure 5.40 for two maximum displacements. The 5.08 cm maximum displacement was chosen to compare the force vs. displacement curve to the experimental tests. The 2.01 cm maximum displacement was chosen to compare the strain values of the model to the human motion testing. The resulting pretibial force with the 2.01 cm applied displacement was 68.24 N which equates to a 2.3 %difference between the LS-DYNA model and HyperMesh model. As shown in the figure, the loading and unloading lines are linear for both maximum displacements. This is unfortunate since it was hoped the implicit model may be able to replicate the nonlinear unloading curve.

It is thought that the nonlinear curve could be caused by the composite material and not the geometry. If this was the case then perhaps a more detailed material model (i.e. more nonlinear terms) would need to be used in the FE model. Several types of material models were used that yielded similar results (i.e. MAT116 Composite Layup and MAT002 Orthotropic Elastic). Some material models could not be used for an implicit analysis (i.e. MAT040 Nonlinear Orthotropic, MAT058 Laminated Composite Fabric). If the nonlinear unload curve was due to the material properties, geometry would still be an important factor for the brace since it acts to impart the applied force to the brace. This means that if a side stay brace was made from the same composite materials, it most likely would not perform the same simply because the applied force was being applied differently. The geometry might also influence the overall stiffness of the brace.

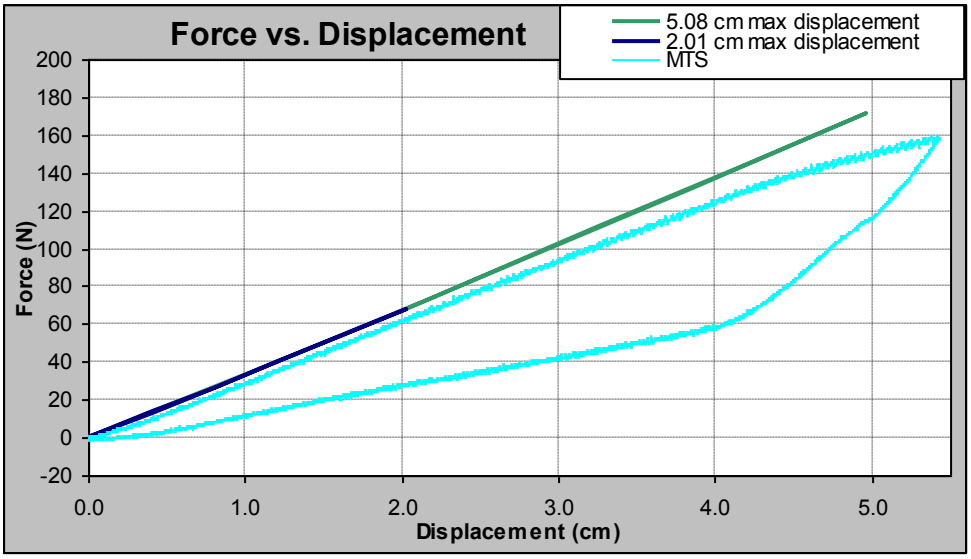

Figure 5.40: Load vs. displacement of brace in LS-DYNA using implicit analysis

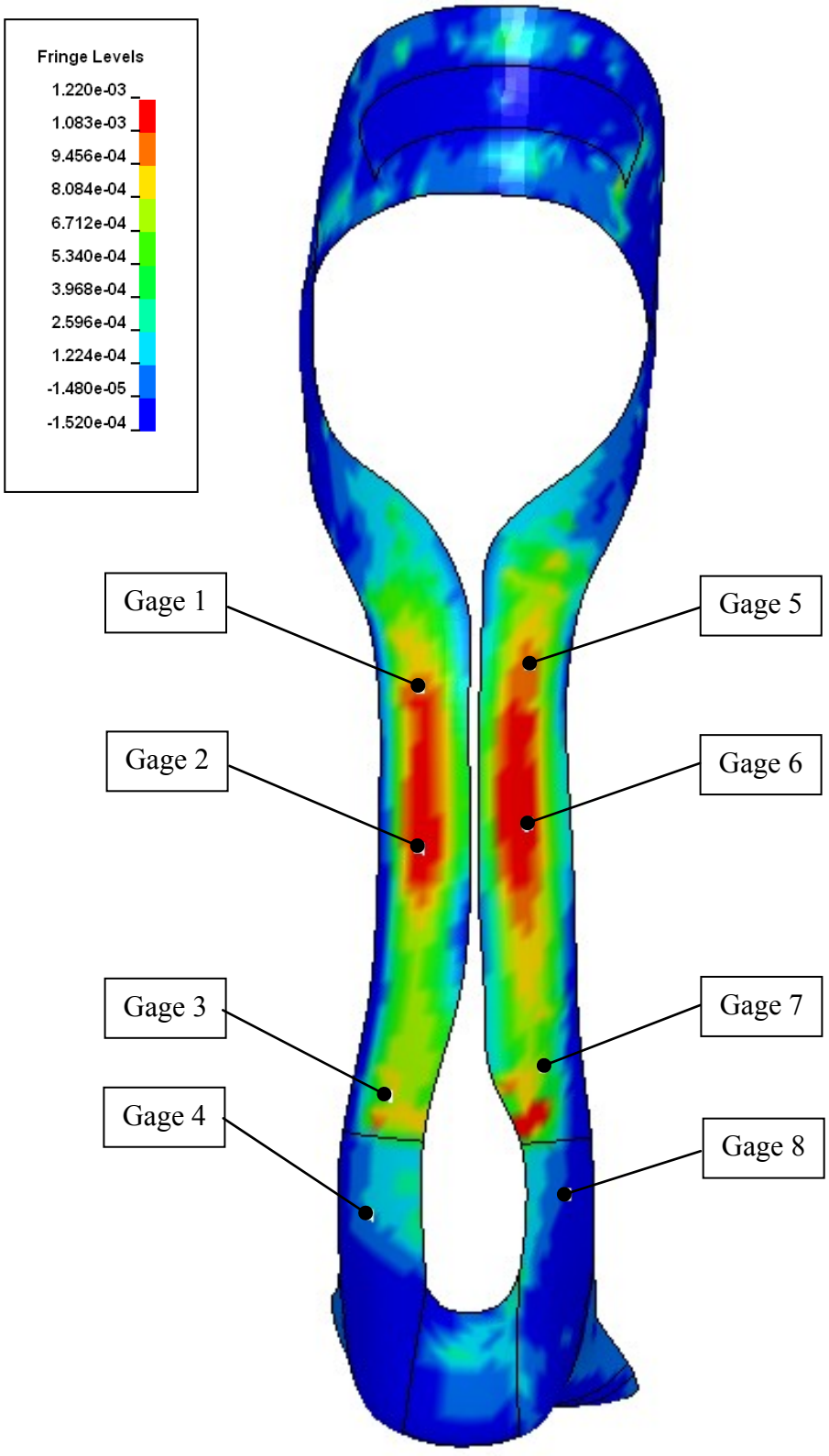

Figure 5.41: Strain contour of condition 1, small angle thickness and properties

Shown in Figure 5.41 is the strain contour of the 2.01 cm maximum pretibial displacement model. The high strain areas match the OptiStruct linear model. There was a high concentration of strain located on the medial strut near the heel counter that was not seen in the HyperMesh model. Experimental testing would need to be performed to verify this high strain area.

Figure 5.42 shows the gage strain of the OptiStruct and LS-DYNA models for the same pretibial displacement (2.01 cm). The lateral strut matches well for both models but the bottom two gages on the medial strut did not match as well. The HyperMesh Gage 8 matched best to the human testing whereas the LS-DYNA gage 8 matched best to the MTS static test.

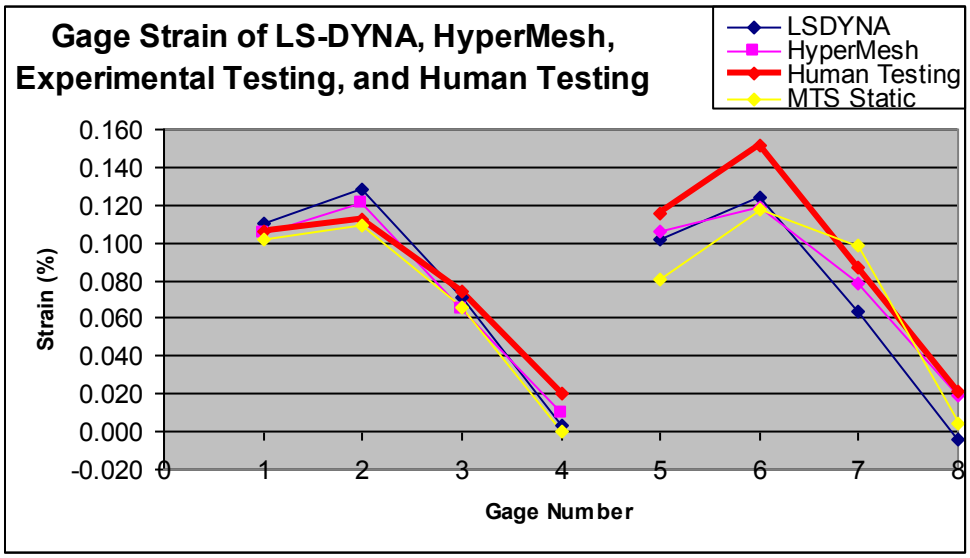

Figure 5.42: Gage strain of LS-DYNA, HyperMesh, and Experimental Testing, and Human Testing

5.9 Predicting Energy Storage Properties using FEA

The load vs. displacement curves of the OptiStruct and LS-DYNA models (condition 1) matched well with experimental testing. It is therefore, possible to accurately calculate the energy storage of the brace using FEA by calculating the area under the load vs. displacement curve. It is also possible to accurately calculate the brace stiffness from FEA using the slope of the load vs. displacement curve.

The FE models produced strain gage profiles similar to the profiles seen in the experimental and human tests. Therefore, FEA can provide an accurate representation of where the highest and lowest strains will be seen in the struts of the brace. In addition, it was shown by the strain contours that the higher strains were seen at and between the top and middle of the struts.

Analyzing the brace with five different ply angle orientations showed that the brace stiffness and energy storage properties were dependent on the angle of the plies. A small angle ply was shown to yield a stiffer brace (hard spring) and a large angle ply was shown to yield a weaker brace (soft spring). It was also shown that the struts provide much of the stiffness of the brace.

Unfortunately, the FE model could not replicate the nonlinear unload curve seen during experimental testing. This nonlinear curve allows for the calculation of the amount of energy released and the energy dissipated. Since the analysis was unable to provide the nonlinear unload curve as seen in experimental testing, additional analyses were not performed. Originally the effect of the dynamic rate was going to be analyzed, in addition to the effect of different ply angles (conditions 1 through 5). The implicit analysis

performed was for static options only and could not be used to perform a dynamic analysis.

The FEA could be producing a linear unload curve different from the MTS testing for many reasons. There could be problems with the FE material model since the brace acts more like a plastic being deformed (viscoelastic) and therefore the material model may need to include more higher order terms. There could be hysteresis in the carbon fiber material that needs to be defined to accurately predict a nonlinear unload line. The brace was also modeled with combined ply properties; perhaps modeling with unidirectional plies would yield different results. An even more accurate analysis would be to model the entire brace with the actual weave structure.

There might also be problems associated with the testing apparatus. During testing the brace naturally moves forward. A stopper could be implemented to limit this forward motion but this would require a different fixture and would also impart a moment arm on the grips. In addition, testing the brace while limiting the forward motion would not accurately represent the brace while being used for gait since the forward motion would not be limited in its use.

It is possible that an FE analysis could be altered to more accurately model the testing setup. The current model uses a point load located at several nodes on the pretibial shell. Perhaps modeling the nose fixture as a rigid body and defining contacts between the rigid body and pretibial shell would replicate the nonlinear unloading line.

Shown in Figure 5.43 are graphs of force vs. time and displacement vs. time for the four different maximum displacement tests performed on brace 1. The force vs. time curves show that the unloading force was nonlinear while the displacement vs. time

curves show that the displacement was linear during unloading. This indicates that as the brace was unloaded, less force was required to displace it the same distance. This indicates that the brace was retaining its shape and not deforming as quickly during unloading as compared with loading. Since the displacement was recorded on the fixture this is why a linear unload line is seen in the graph. However, if the brace was retaining its shape thereby requiring less force, then the displacement of the brace should also be nonlinear retaining a higher displacement than that shown by the linear line. If this was the case than an even more pronounced nonlinear unloading line would be produced on the force vs. displacement graph. This would mean that more energy would be dissipated by the brace during unloading.

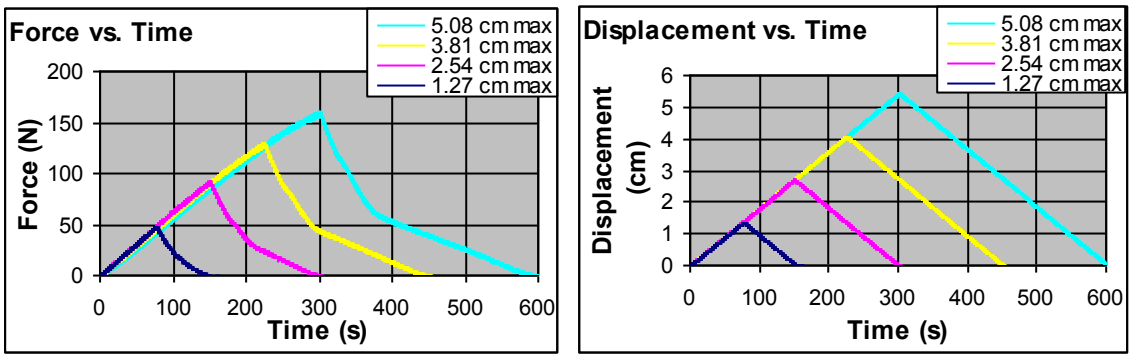

Figure 5.43: MTS experimental testing of brace 1 (left) force vs. time, (right) displacement vs. time

Since the brace is a passive energy storage device it is expected that the unloading of the brace occurs with a smaller force. Optimally, a brace that provides more force than used to displace it initially would provide better energy release properties. This would however, only be achievable in an active energy storage device.

Hansen et al. analyze the moment of the human ankle and determine that a clockwise hysteresis loop was seen at slow walking speeds and a counterclockwise hysteresis loop was seen at fast waking speeds whereas at normal walking speeds the hysteresis loop was nearly absent [58]. The ankle dissipates energy at the slower walking speeds just as the HELIOS brace dissipates energy as seen by the load vs. deflection curves. This is perhaps why the HELIOS helps to improve gait; it mimics the same hysteresis loop as the ankle. However, at faster walking speeds the brace is not able to replicate the ankle by producing more force than the force applied to the pretibial shell. Ultimately, for faster walking an active energy storage device would need to be developed.

CHAPTER 6

CONCLUSIONS

The HELIOS, an orthotic brace, was analyzed through human motion testing, experimental testing, and finite element modeling to characterize the effect on gait and to examine the energy storage properties. Human motion testing yielded ground reaction force data in addition to strain gage data of four instrumented braces. Experimental testing yielded force vs. displacement curves of the instrumented braces which can be used to calculate the brace stiffness in addition to the energy stored, released, and dissipated. The FE model showed that the angle of the ply had a larger effect on the brace stiffness and energy storage properties than the ply thickness.

The subjects showed differences in the analyzed ground reaction force variables between the unbraced and braced conditions. In fact, most of the CMT subjects had delays in the temporal parameters: time to the first peak (t1), time to the braking peak (tyb), and time to the propulsive peak (typ). In addition, the peak braking force (Fyb) significantly decreased for all subjects for at least one leg. Most subjects had either a complete absence of the transient peak or had a significant decrease in the magnitude of the transient peak during the braced condition.

The brace may be absorbing the posterior shear during heel strike resulting in a decreased braking force. If the brace is acting as a shock-absorbing device at the beginning of stance it would make sense that the braking force would be delayed as the brace would absorb the impact and slow down the foot. The brace is also exhibiting shock-attenuating properties by absorbing the high-frequency shock of the transient peaks. The brace is essentially reducing the acceleration of the heel into the ground at

heel strike. In addition, the delay of the propulsive force signifies that the brace is also acting as a shock-absorbing device when loaded at the pretibial shell after midstance.

The HELIOS brace resembles a quarter-elliptic or simple cantilever flat spring so a horizontal cantilever flexure configuration was used to replicate the normal force applied to the pretibial shell during toe off and to replicate the strain seen at the F_{yp} peak on the GRF curve. The force vs. displacement relationship for all braces presented a linear load line with a nonlinear unload line. The unload portion for most braces was a curve without distinct straight sections which means there are multiple spring stiffness values releasing at different times during unloading. The HELIOS is fabricated from material that can be assumed to be linear-elastic. However, when tested in a horizontal cantilever fashion, it acts as a nonlinear spring and resembles a viscoelastic material, just like human tissues.

Subjects with the smallest increase in walking speed had braces that showed no energy being released when the brace was displaced less than 1 cm, whereas the subject with the largest increase in walking speed had braces that showed energy being released throughout. This could indicate why the CMT2 subject's strain readings during human motion testing did not go back to zero strain at toe off. Ideally, the brace should be providing energy release through to toe off to assist the subject in propelling the foot and leg forward. CMT2 had the largest increase in walking speed and it is possible that this occurred due to the better energy storage capacity and better energy release of this subject's braces as compared to the other tested braces.

Comparing the human motion and horizontal flexure maximum strain data it is possible to conclude that the geometry of the brace has a greater effect on the maximum strain profile of the brace rather than the human subject. Results of human testing and

experimental mechanical testing show that the highest strains are seen in the middle or top of the strut during stance with the lowest strain usually seen at the ankle. The highest strain was not seen at the ankle most likely due to the double strut geometry of the HELIOS.

Finite element analysis can be used to determine the brace stiffness and energy storage capacity of an AFO. A static analysis using Altair OptiStruct validated the FE model using the results of the experimental mechanical tests. Five conditions were analyzed to show the effect of the ply angle and thickness on the displacement of the pretibial shell. It was shown that the material properties of the small angle ply and original angle ply were similar and as the ply angle was increased considerably, the brace decreased its ability to hold the same load. It was also shown that the thickness of the plies had less of an effect on the material than the angle of the ply fibers. The ply angles of the struts highly influenced the strain and the force vs. displacement relationship.

A nonlinear FE model was analyzed using LS-DYNA to allow for the selection of a time curve to produce the unloading curve. An implicit model was analyzed but unfortunately the nonlinear unloading force vs. displacement curve was not replicated (FE and experimental data did not match for unloading). It is thought that the nonlinear curve might be caused by the composite material and that perhaps a more detailed material model would need to be defined.

It is possible to accurately calculate the energy storage of the brace using FEA by calculating the area under the load vs. displacement curve. It is also possible to accurately calculate the brace stiffness from FEA using the slope of the load vs. displacement curve. FEA can provide an accurate representation of where the highest and lowest strains will

be seen in the struts of the brace. Stiffness and energy storage may be a function of geometry as seen by differences between braces as well as the ply angle as seen by the FE model.

Not all subjects showed the same amount of speed increase between the unbraced and braced conditions. This may be from differences in the CMT subject from one individual to another. Don et al. discuss how there may be two different types of gait strategies depending on the type of muscle impairment present (i.e. plantar flexor weakness) [59]. The brace may not produce the same increase in walking speed but it may decrease the amount of energy used by the subjects to walk. A study documenting the energy expenditure of the subjects in the braced and unbraced condition by monitoring the subject's oxygen consumption may prove that this is indeed the case.

The ground reaction forces were normalized for %stance and it was shown that the some of the temporal parameters were delayed. It might be beneficial to look at the impulses instead of peak forces to get a more accurate assessment of the changes to the A/P curve.

The focus of analyzing the brace has been on the energy storage properties. The damping action may be as important and contribute to gait as much as energy release. Perhaps, analyzing the brace in terms of its shock absorption during the first part of stance may be beneficial. Since significant changes were seen in the GRF of the A/P curve during the first part of gait, the brace may be acting as a shock absorbing device. Performing experimental mechanical testing on the brace for this first section of stance might provide some insight into what is occurring. However, the force being applied to the brace during this part of stance would be applied through the strap and would be

much smaller that the force seen on the pretibial shell. This is evident by the much lower strains seen during human testing.

An in-depth analysis of the composite materials during loading and unloading may prove to be beneficial. Creating a material model that would accurately describe the composite for a simple structure (i.e. cantilever) could be performed to determine if nonlinearity exists during unloading. A fatigue study would also be beneficial to assess if the brace loses strength over an extended period of time. If the brace fabric was modeled it would provide a more accurate picture of how the brace is behaving and might provide the necessary nonlinear unload curve to calculate energy release properties.

Ideally, FEA could be used to optimize the brace geometry and ply angles for maximum energy storage and release. The brace geometry, i.e. strut length, strut curve diameter, etc. could be altered to determine changes in stiffness and energy storage properties. FEA could also be used to examine the effect of different dynamic rates, i.e. the response of the brace when an individual is walking as compared to running. It might also be beneficial to use FEA as a design tool where the goal is a given stiffness and the geometry, fiber orientation, and number of plies would need to be determined. In order to analyze the brace energy storage properties in FEA an accurate nonlinear unload line would need to be produced.

It is advised that standard off the shelf polypropylene braces be analyzed similar to the HELIOS to gain a better understanding of how the braces differ. It is hypothesized that the HELIOS will provide much better stiffness and energy storage properties than a polypropylene due to material property and geometry differences. This would allow a

definitive answer as to how and why the HELIOS braces are better than COTS polypropylene braces at improving the gait of individuals with CMT.

It might also be beneficial to evaluate the effect of brace stiffness on the gait of a CMT subject. This could be done with one CMT subject and several different braces of varying stiffness. It might also be interesting to determine how the energy release properties change as the stiffness changes.

The HELIOS is considered a custom designed AFO brace since it is specifically fabricated for one individual based on that individual's geometry and physical needs. It would be ideal to be able to mass produce the HELIOS as closely to a COTS model as possible to benefit more patients in need of an AFO brace. If a HELIOS brace was developed based on average leg diameters, leg lengths, and foot lengths would it perform as well as the custom designed HELIOS? Perhaps a HELIOS COTS model could be developed and a study documenting the stiffness, energy storage properties, and changes of gait could be completed to show how different a non-custom model would be to the custom HELIOS.

It can be concluded that the HELIOS is an energy storage device and may be well suited for slow walking as well as preventing foot drop. It also acts to absorb the impact during braking and then supports the tibia during propulsion when the subject applies more pressure to the pretibial shell at the front of the brace before the swing phase. The work performed by the subject, applying force at the pretibial shell, creates potential energy that is stored by the HELIOS. Once the subject releases the applied force, the HELIOS is unloaded releasing some of this potential energy which can be used to propel the subject during the propulsive stage of gait. However, not all of the potential energy is

transferred and is instead dissipated. Since the brace has a large amount of energy dissipation, only the development of an active energy storage device that would provide more force to the subject than the force applied would assist with fast walking.

APPENDIX A

HUMAN MOTION GROUND REACTION FORCE CURVES

All Subjects (Conditions 1, 5, 9, and 13)

Shown in this section are graphs of GRFs (F_x and F_y) broken into left and right feet. The graphs on the left show the GRFs for each individual trial. The graphs on the right show the average GRFs and the standard deviations. Condition 1 is pre-test unbraced and condition 5 is pre-test braced with the subject's current brace. Condition 9 is post-test unbraced and condition 13 is post-test braced with the HELIOS.

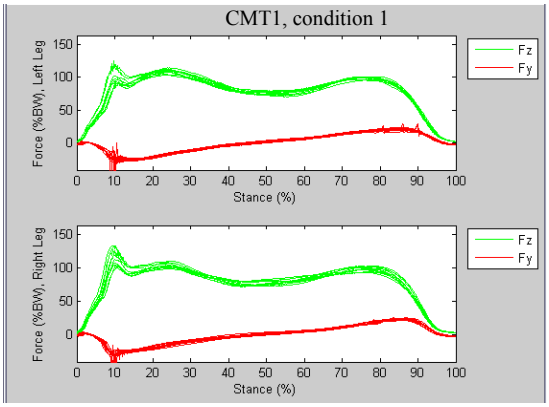

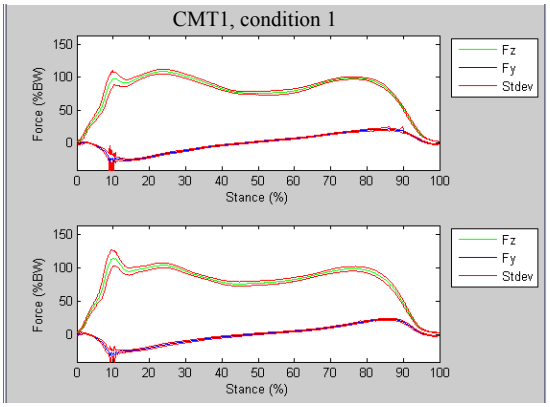

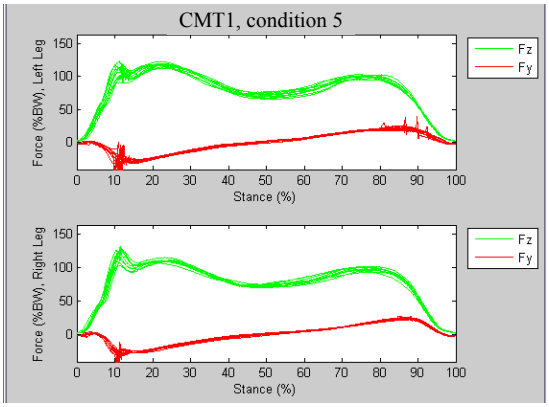

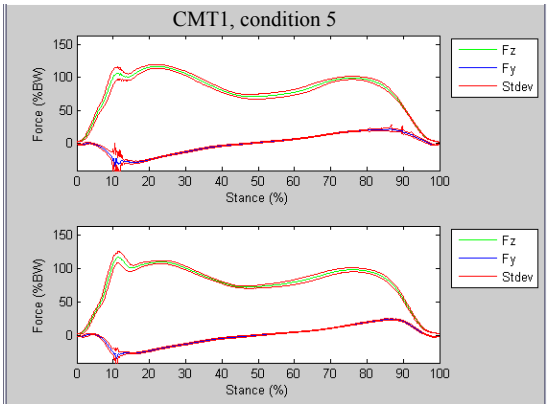

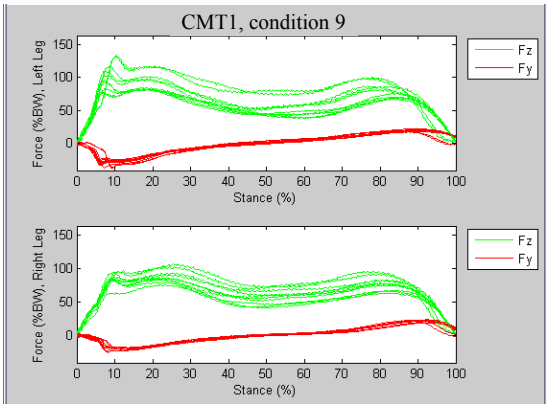
CMT1, condition 9
Force (%BW), Left Leg
Force (%BW), Right Leg
Stance (%)
Fz
Fy

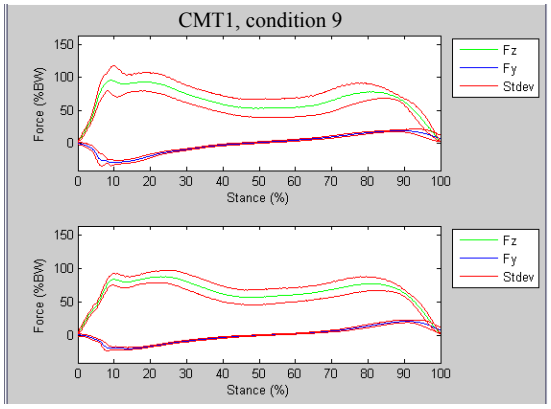
CMT1, condition 9
Force (%BW)
Stance (%)
Fz
Fy
Stdev

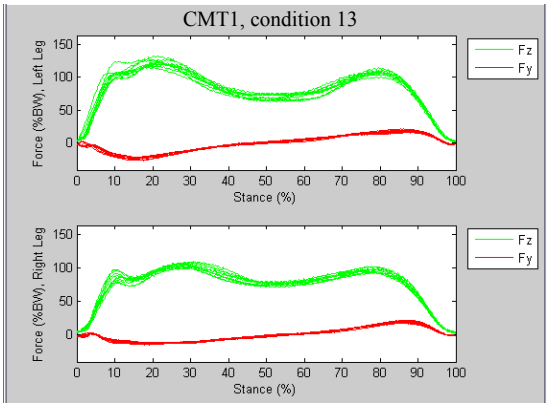
CMT1, condition 13
Force (%BW), Left Leg
Force (%BW), Right Leg
Stance (%)
Fz
Fy

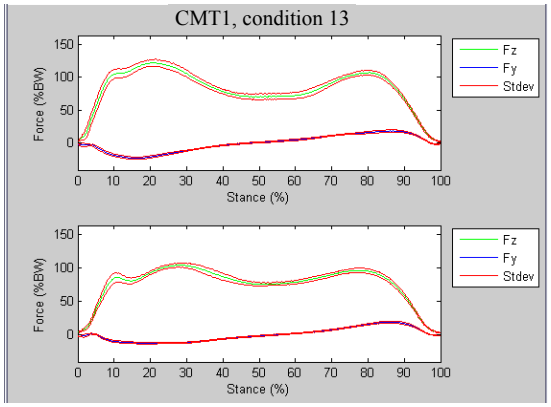
CMT1, condition 13
Force (%BW)
Stance (%)
Fz
Fy
Stdev

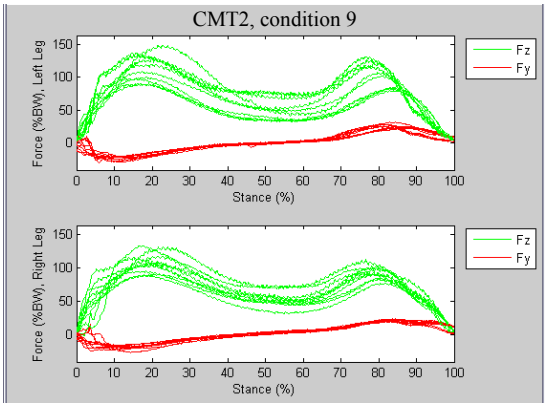
CMT2, condition 9
Force (%BW), Left Leg
Force (%BW), Right Leg
Stance (%)
Fz
Fy

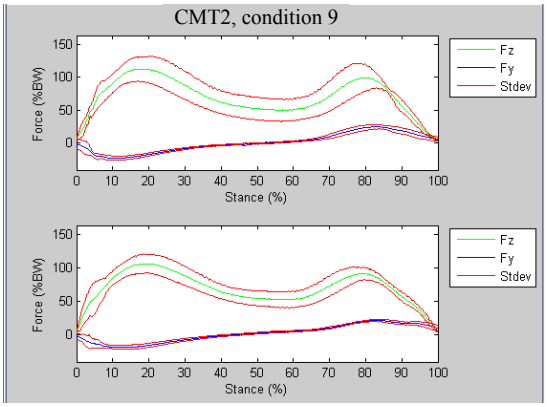
CMT2, condition 9
Force (%BW)
Stance (%)
Fz
Fy
Stdev

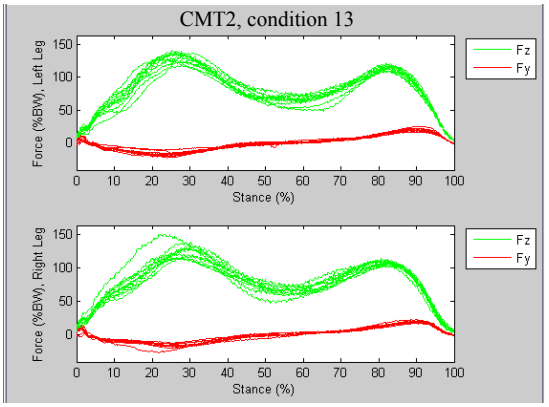
CMT2, condition 13
Force (%BW), Left Leg
Force (%BW), Right Leg
Stance (%)
Fz
Fy

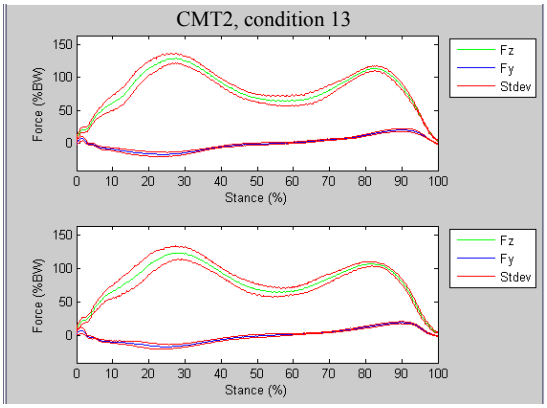
CMT2, condition 13
Force (%BW)
Stance (%)
Fz
Fy
Stdev

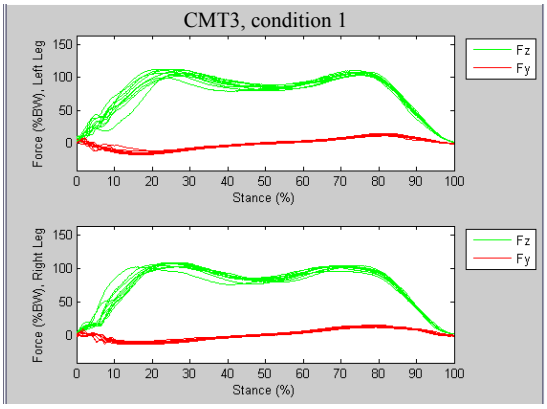
CMT3, condition 1
Force (%BW), Left Leg
Force (%BW), Right Leg
Stance (%)
Fz
Fy

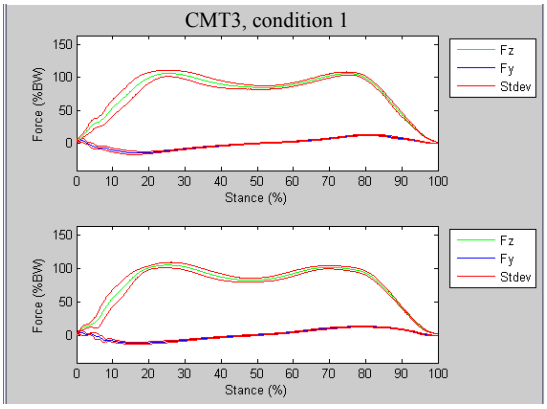
CMT3, condition 1
Force (%BW)
Stance (%)
Fz
Fy
Stdev

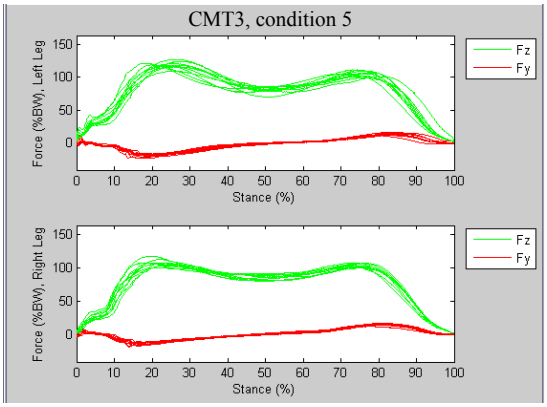
CMT3, condition 5
Force (%BW), Left Leg
Force (%BW), Right Leg
Stance (%)
Fz
Fy

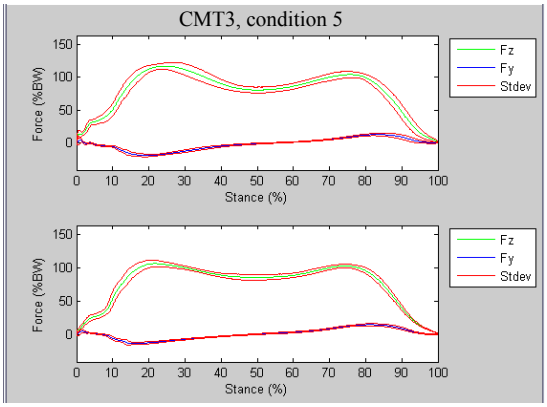
CMT3, condition 5
Force (%BW)
Stance (%)
Fz
Fy
Stdev

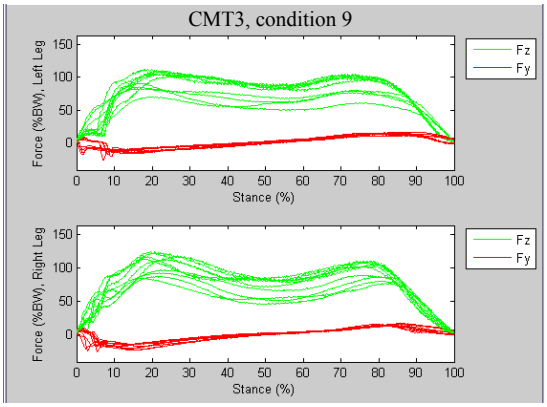
CMT3, condition 9
Force (%BW), Left Leg
Force (%BW), Right Leg
Stance (%)
Fz
Fy

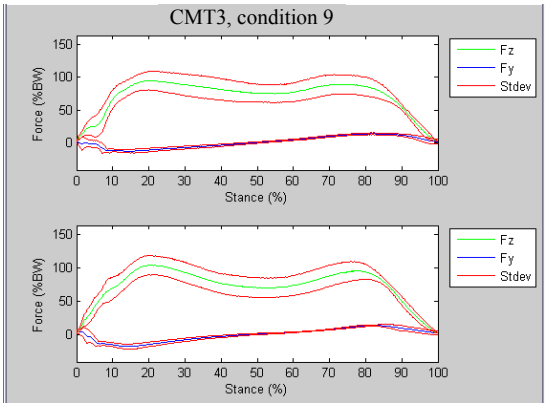
CMT3, condition 9
Force (%BW)
Stance (%)
Fz
Fy
Stdev

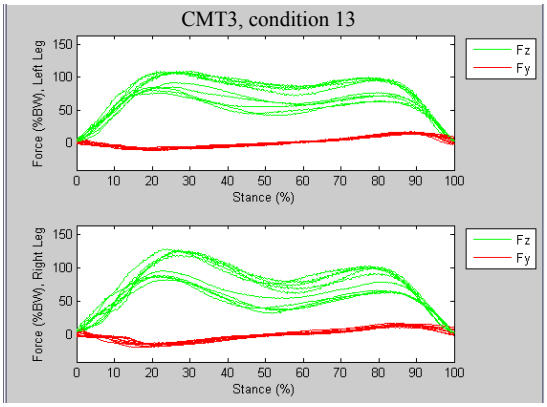
CMT3, condition 13
Force (%BW), Left Leg
Force (%BW), Right Leg
Stance (%)
Fz
Fy

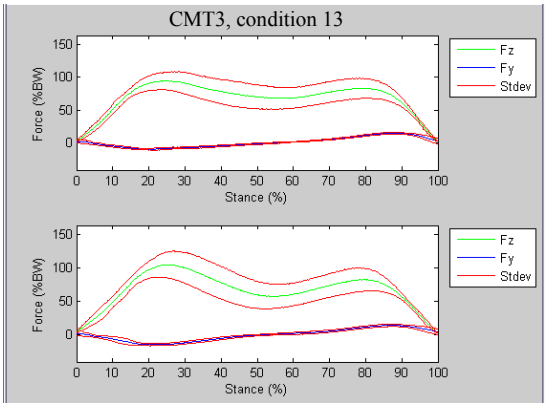
CMT3, condition 13
Force (%BW)
Stance (%)
Fz
Fy
Stdev

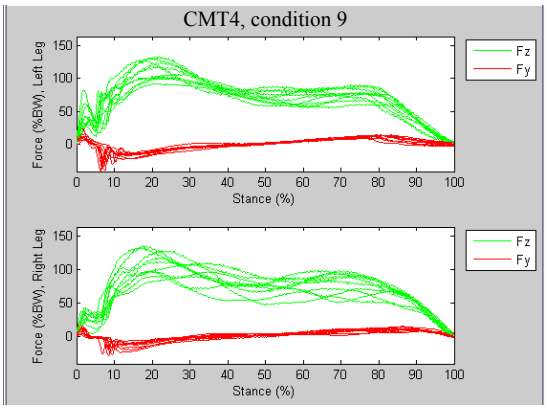
CMT4, condition 9
Force (%BW), Left Leg
Force (%BW), Right Leg
Stance (%)
Fz
Fy

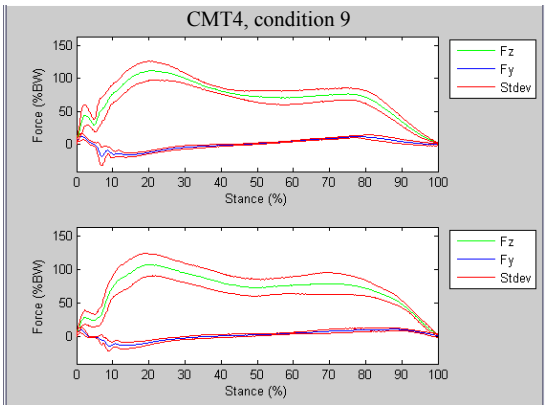
CMT4, condition 9
Force (%BW)
Stance (%)
Fz
Fy
Stdev

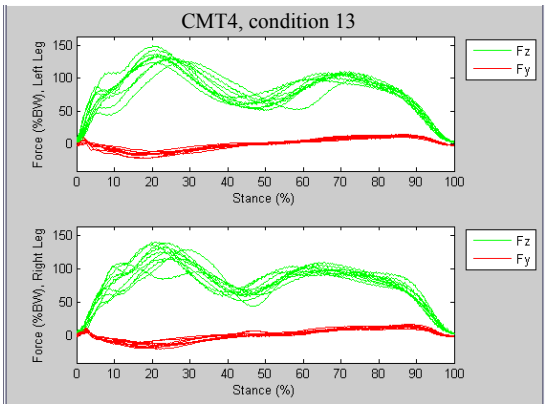
CMT4, condition 13
Force (%BW), Left Leg
Force (%BW), Right Leg
Stance (%)
Fz
Fy

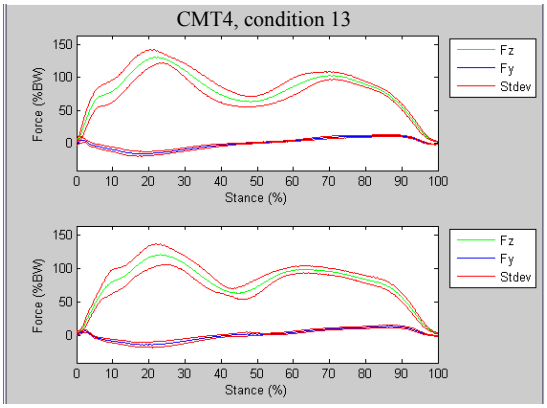
CMT4, condition 13
Force (%BW)
Stance (%)
Fz
Fy
Stdev

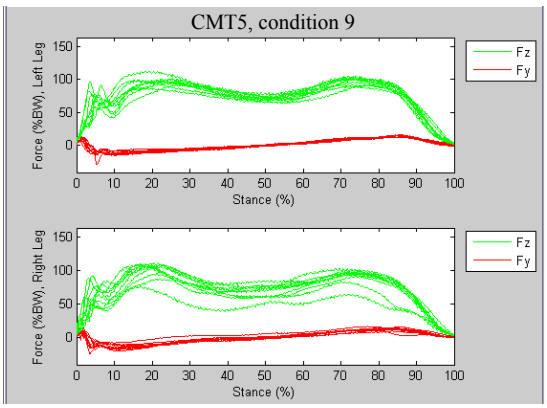
CMT5, condition 9
Force (%BW), Left Leg
Force (%BW), Right Leg
Stance (%)
Fz
Fy

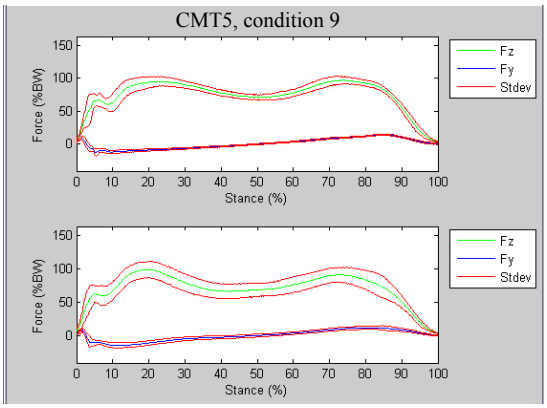
CMT5, condition 9
Force (%BW)
Stance (%)
Fz
Fy
Stdev

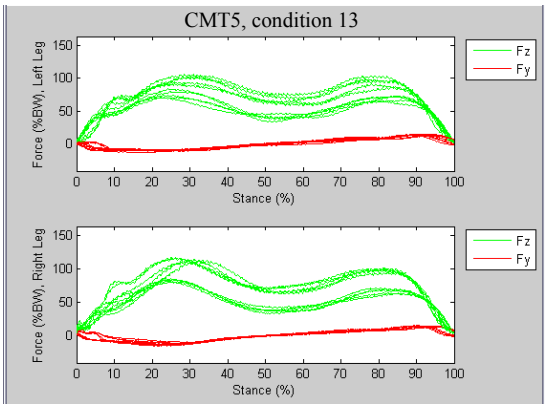
CMT5, condition 13
Force (%BW), Left Leg
Force (%BW), Right Leg
Stance (%)
Fz
Fy

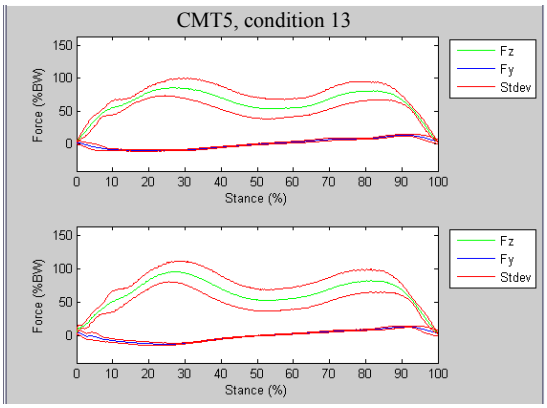
CMT5, condition 13
Force (%BW)
Stance (%)
Fz
Fy
Stdev

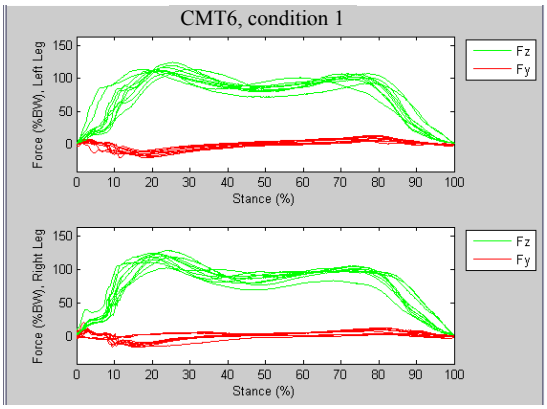
CMT6, condition 1
Force (%BW), Left Leg
Force (%BW), Right Leg
Stance (%)
Fz
Fy

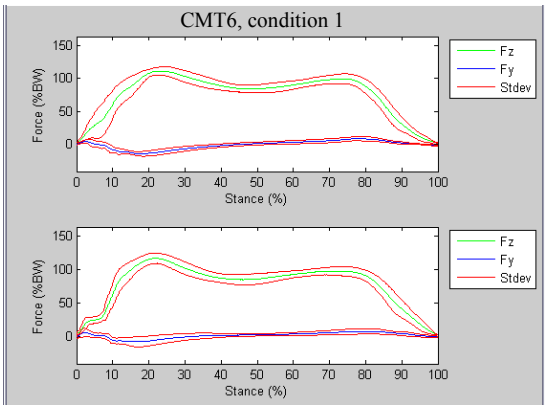
CMT6, condition 1
Force (%BW)
Stance (%)
Fz
Fy
Stdev

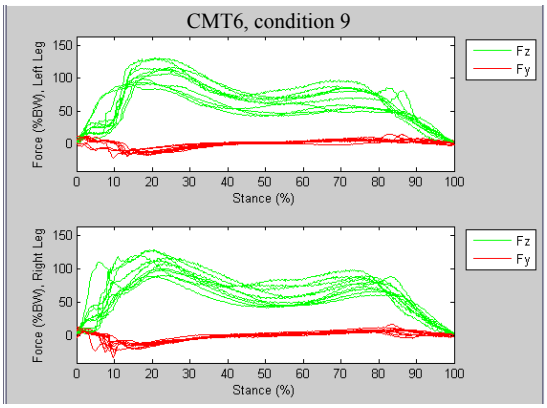
CMT6, condition 9
Force (%BW), Left Leg
Force (%BW), Right Leg
Stance (%)
Fz
Fy

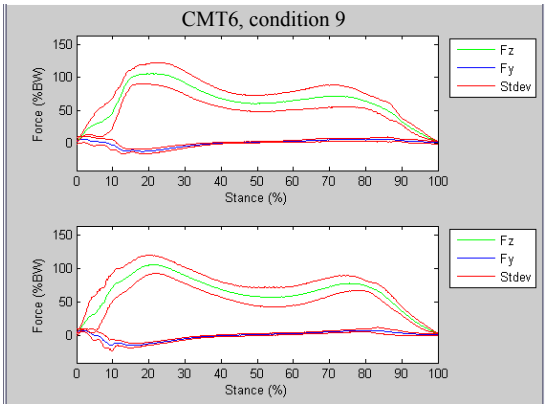
CMT6, condition 9
Force (%BW)
Stance (%)
Fz
Fy
Stdev

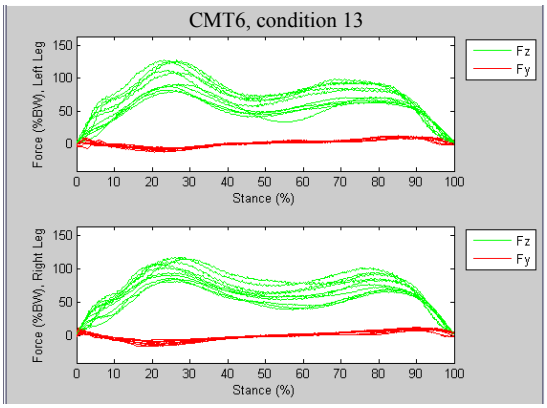
CMT6, condition 13
Force (%BW), Left Leg
Force (%BW), Right Leg
Stance (%)
Fz
Fy

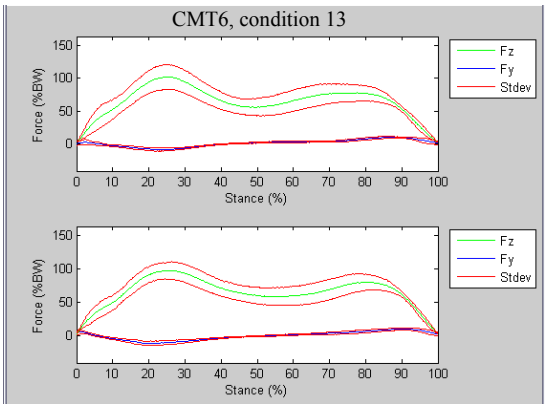
CMT6, condition 13
Force (%BW)
Stance (%)
Fz
Fy
Stdev

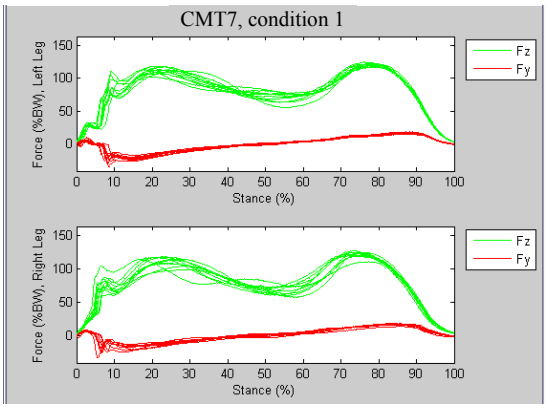
CMT7, condition 1
Force (%BW), Left Leg
Force (%BW), Right Leg
Stance (%)
Fz
Fy

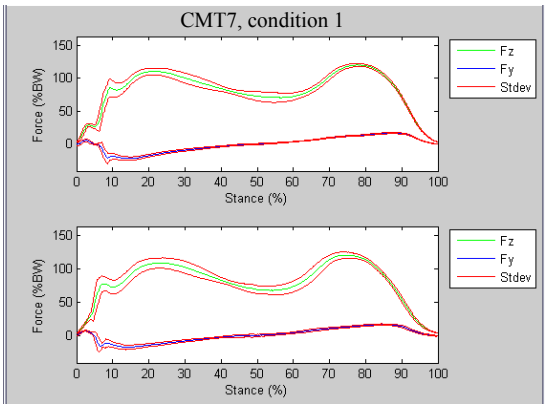
CMT7, condition 1
Force (%BW)
Stance (%)
Fz
Fy
Stdev

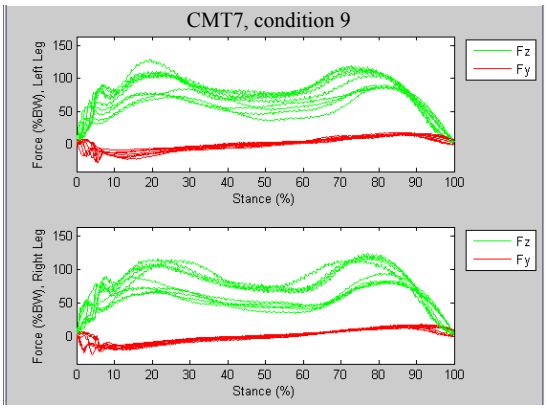
CMT7, condition 9
Force (%BW), Left Leg
Force (%BW), Right Leg
Stance (%)
Fz
Fy

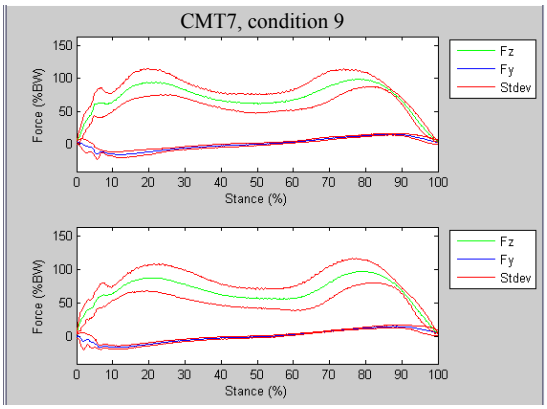
CMT7, condition 9
Force (%BW)
Stance (%)
Fz
Fy
Stdev

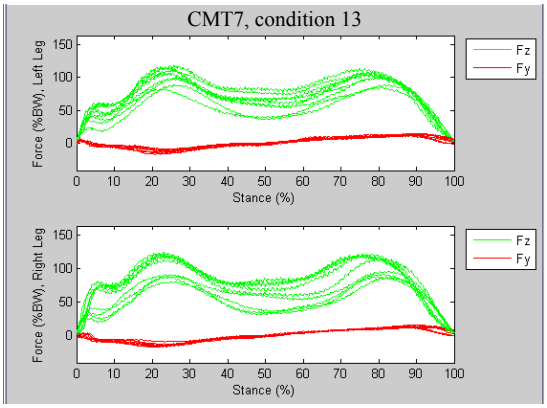
CMT7, condition 13
Force (%BW), Left Leg
Force (%BW), Right Leg
Stance (%)
Fz
Fy

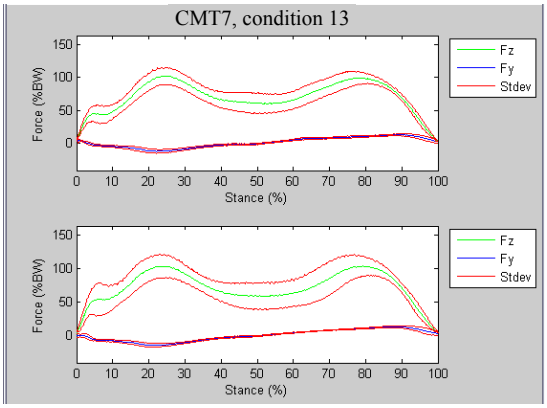
CMT7, condition 13
Force (%BW)
Stance (%)
Fz
Fy
Stdev

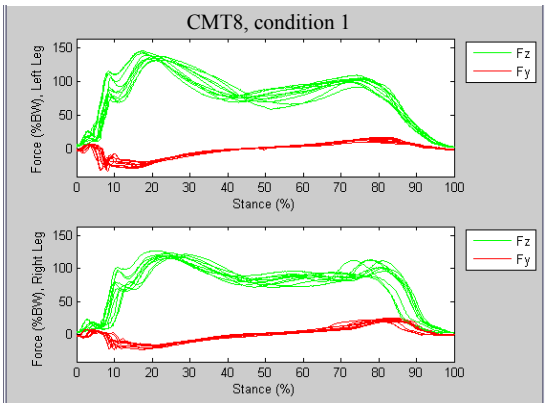
CMT8, condition 1
Force (%BW), Left Leg
Force (%BW), Right Leg
Stance (%)
Fz
Fy

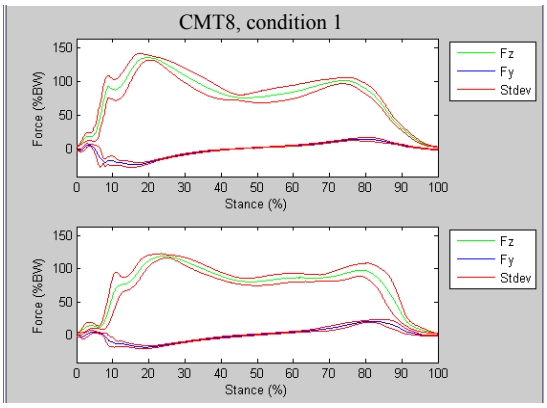
CMT8, condition 1
Force (%BW)
Stance (%)
Fz
Fy
Stdev

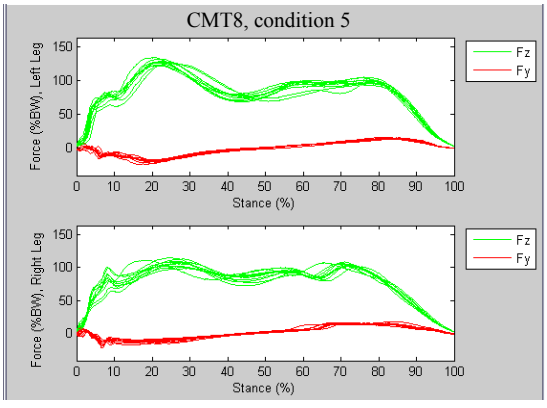
CMT8, condition 5
Force (%BW), Left Leg
Force (%BW), Right Leg
Stance (%)
Fz
Fy

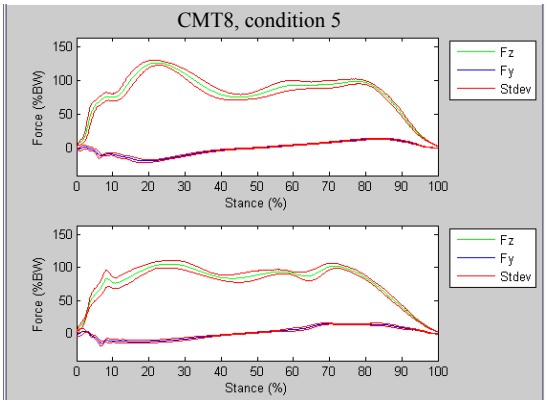
CMT8, condition 5
Force (%BW)
Stance (%)
Fz
Fy
Stdev

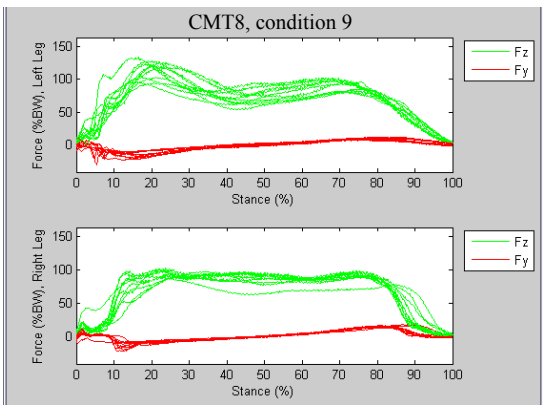
CMT8, condition 9
Force (%BW), Left Leg
Force (%BW), Right Leg
Stance (%)
Fz
Fy

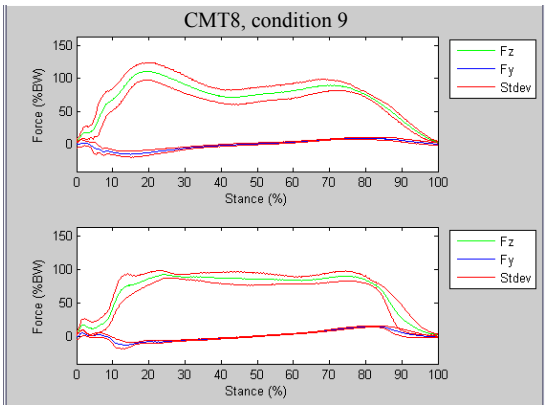
CMT8, condition 9
Force (%BW)
Stance (%)
Fz
Fy
Stdev

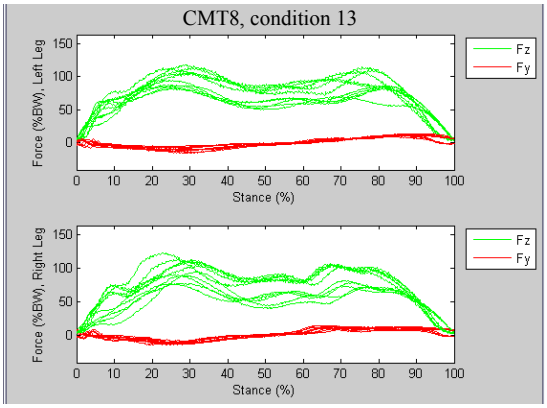
CMT8, condition 13
Force (%BW), Left Leg
Force (%BW), Right Leg
Stance (%)
Fz
Fy

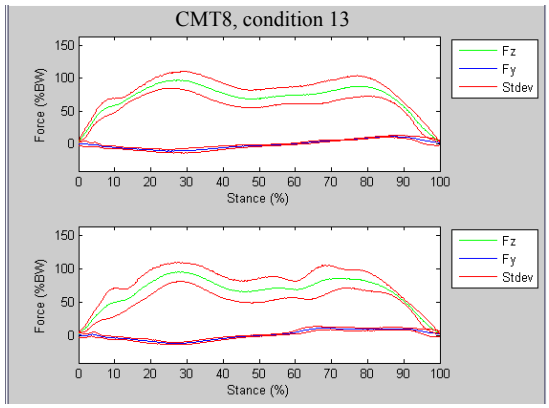
CMT8, condition 13
Force (%BW)
Stance (%)
Fz
Fy
Stdev

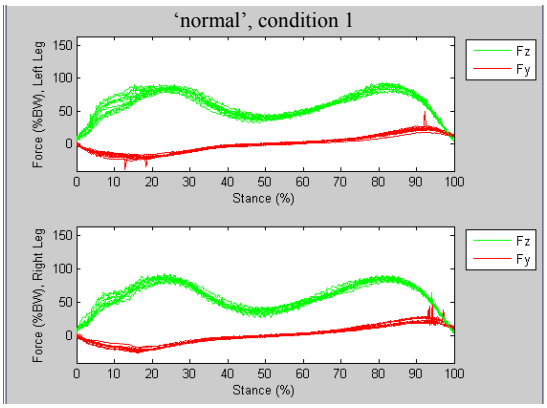
‘normal’, condition 1
Force (%BW), Left Leg
Force (%BW), Right Leg
Stance (%)
Fz
Fy

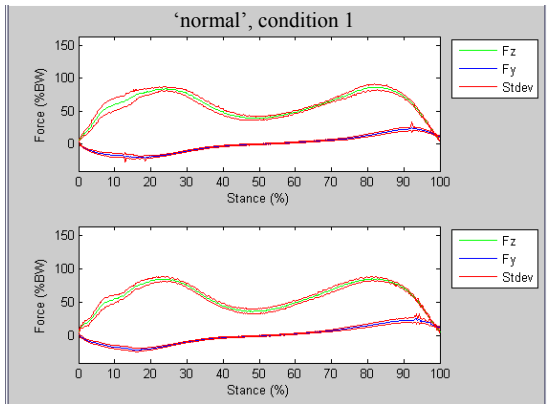
‘normal’, condition 1
Force (%BW)
Stance (%)
Fz
Fy
Stdev

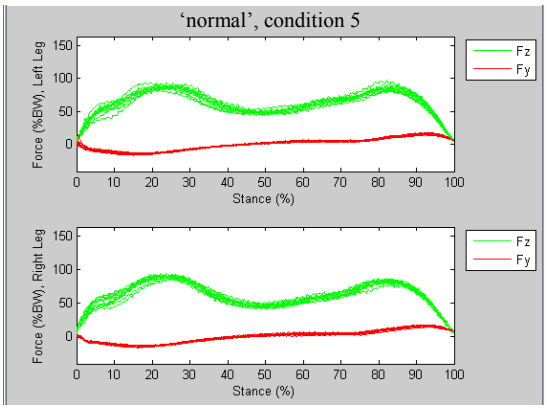
‘normal’, condition 5
Force (%BW), Left Leg
Force (%BW), Right Leg
Stance (%)
Fz
Fy

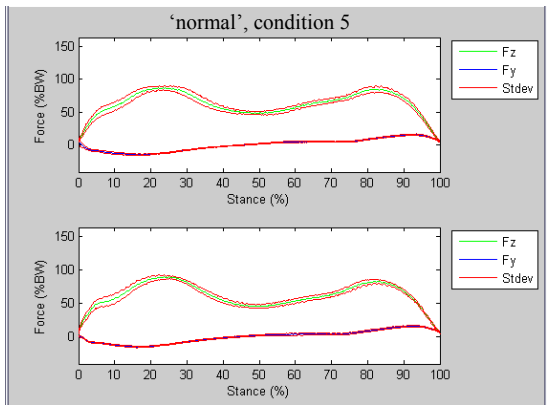
‘normal’, condition 5
Force (%BW)
Stance (%)
Fz
Fy
Stdev

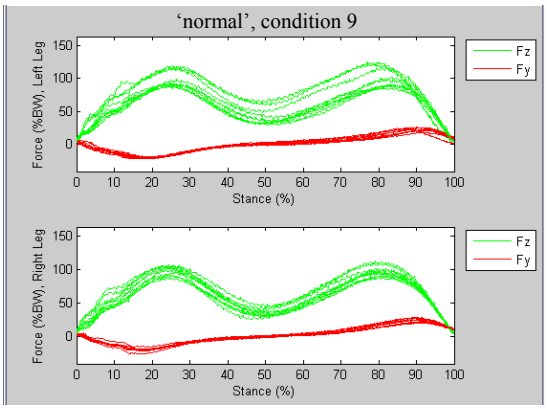
'normal', condition 9
Force (%BW), Left Leg
Force (%BW), Right Leg
Stance (%)
Fz
Fy

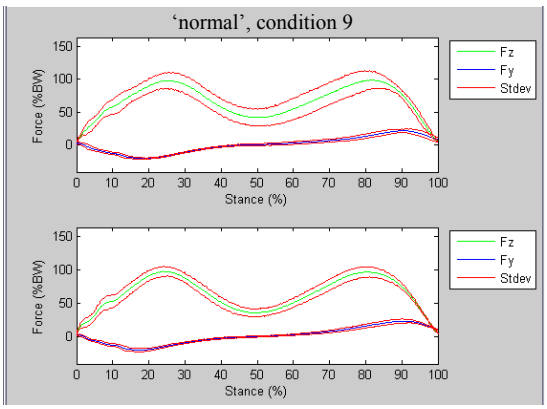
'normal', condition 9
Force (%BW)
Stance (%)
Fz
Fy
Stdev

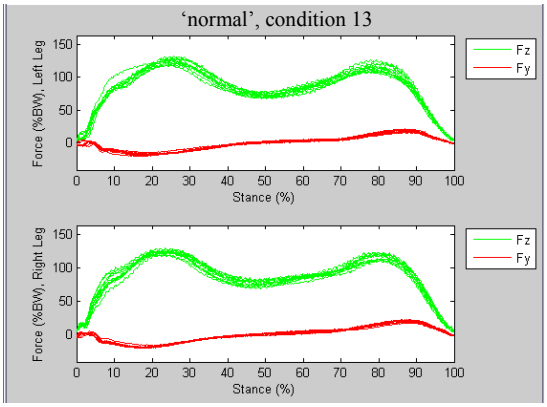
'normal', condition 13
Force (%BW), Left Leg
Force (%BW), Right Leg
Stance (%)
Fz
Fy

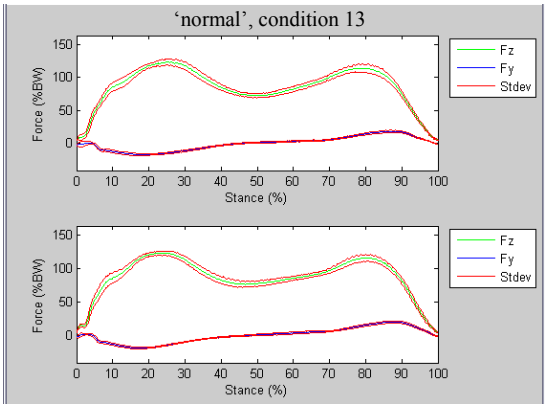
'normal', condition 13
Force (%BW)
Stance (%)
Fz
Fy
Stdev

All Subjects (Conditions 9, and 13)

Shown in this section are graphs of the average GRFs (F_x and F_y) with standard deviations broken into left and right feet. The graphs show condition 9 and condition 13 overlaid to highlight differences between the unbraced and braced conditions.

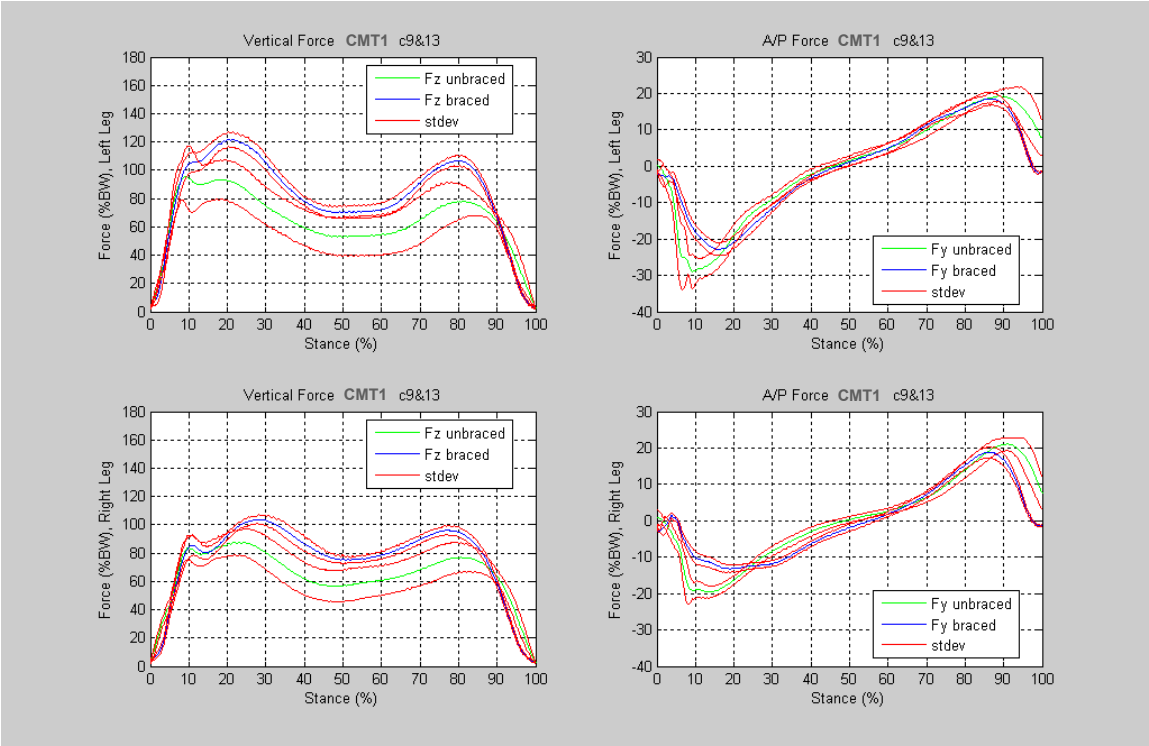

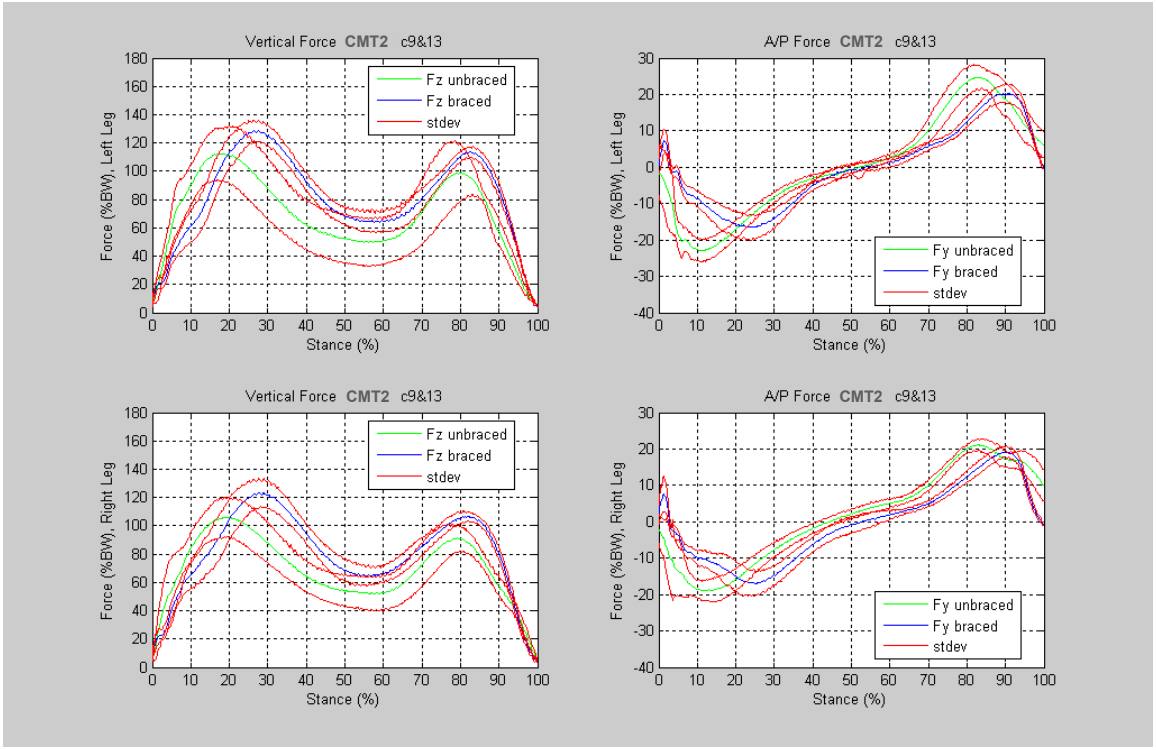
Vertical Force CMT2 c9&13
Force (%BW), Left Leg
Stance (%)
Fz unbraced
Fz braced
stdev
A/P Force CMT2 c9&13
Force (%BW), Left Leg
Stance (%)
Fy unbraced
Fy braced
stdev
Vertical Force CMT2 c9&13
Force (%BW), Right Leg
Stance (%)
Fz unbraced
Fz braced
stdev
A/P Force CMT2 c9&13
Force (%BW), Right Leg
Stance (%)
Fy unbraced
Fy braced
stdev

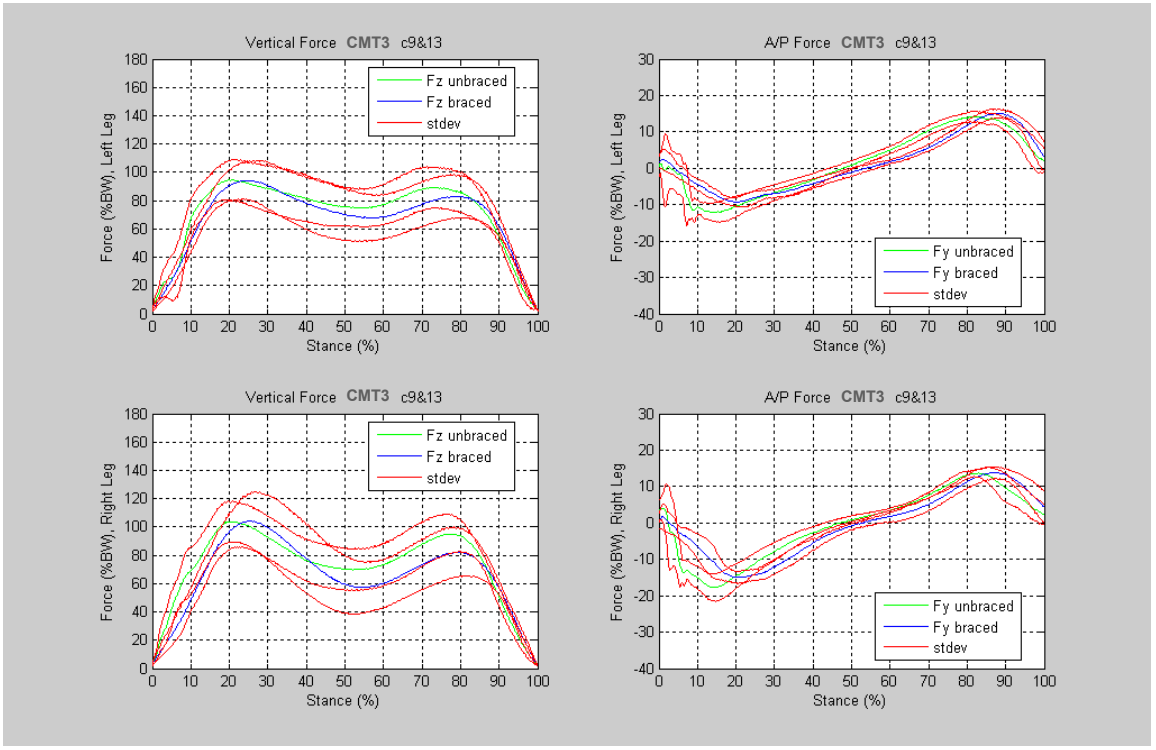
Vertical Force CMT3 c9&13
Force (%BW), Left Leg
Stance (%)
Fz unbraced
Fz braced
stdev
A/P Force CMT3 c9&13
Force (%BW), Left Leg
Stance (%)
Fy unbraced
Fy braced
stdev
Vertical Force CMT3 c9&13
Force (%BW), Right Leg
Stance (%)
Fz unbraced
Fz braced
stdev
A/P Force CMT3 c9&13
Force (%BW), Right Leg
Stance (%)
Fy unbraced
Fy braced
stdev

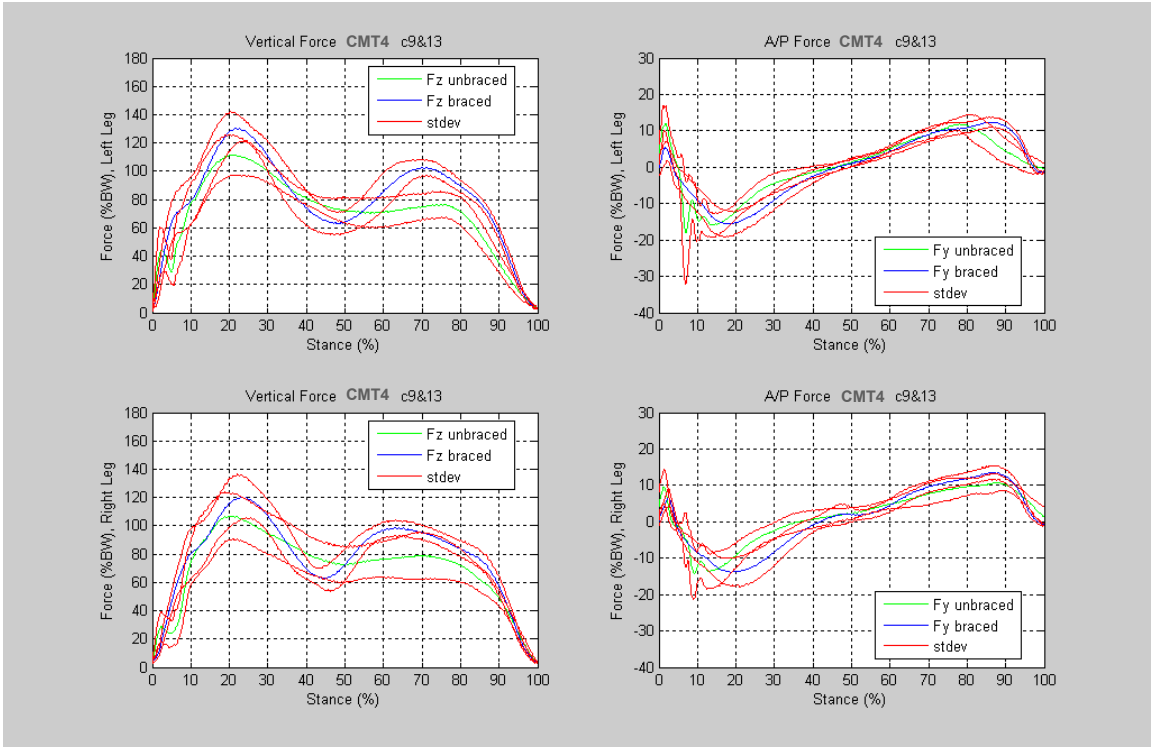
Vertical Force CMT4 c9&13
Force (%BW), Left Leg
Stance (%)
Fz unbraced
Fz braced
stdev
A/P Force CMT4 c9&13
Force (%BW), Left Leg
Stance (%)
Fy unbraced
Fy braced
stdev
Vertical Force CMT4 c9&13
Force (%BW), Right Leg
Stance (%)
Fz unbraced
Fz braced
stdev
A/P Force CMT4 c9&13
Force (%BW), Right Leg
Stance (%)
Fy unbraced
Fy braced
stdev

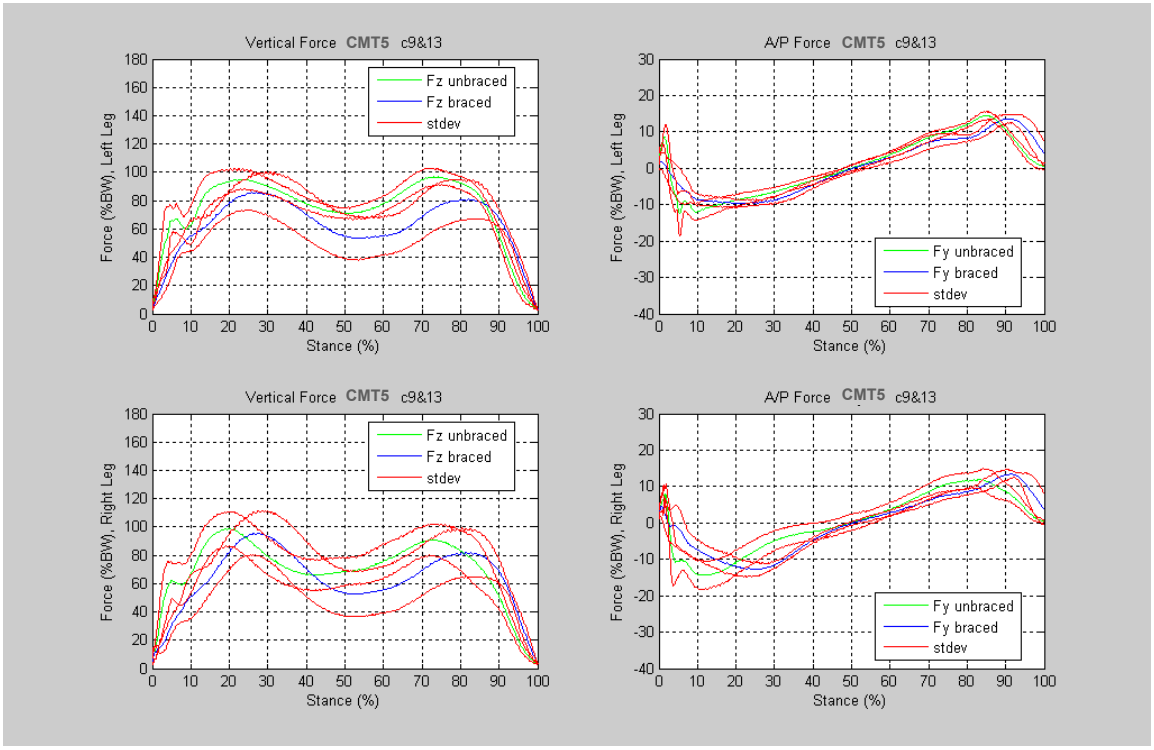
Vertical Force CMT5 c9&13
Force (%BW), Left Leg
Stance (%)
Fz unbraced
Fz braced
stdev
A/P Force CMT5 c9&13
Force (%BW), Left Leg
Stance (%)
Fy unbraced
Fy braced
stdev
Vertical Force CMT5 c9&13
Force (%BW), Right Leg
Stance (%)
Fz unbraced
Fz braced
stdev
A/P Force CMT5 c9&13
Force (%BW), Right Leg
Stance (%)
Fy unbraced
Fy braced
stdev

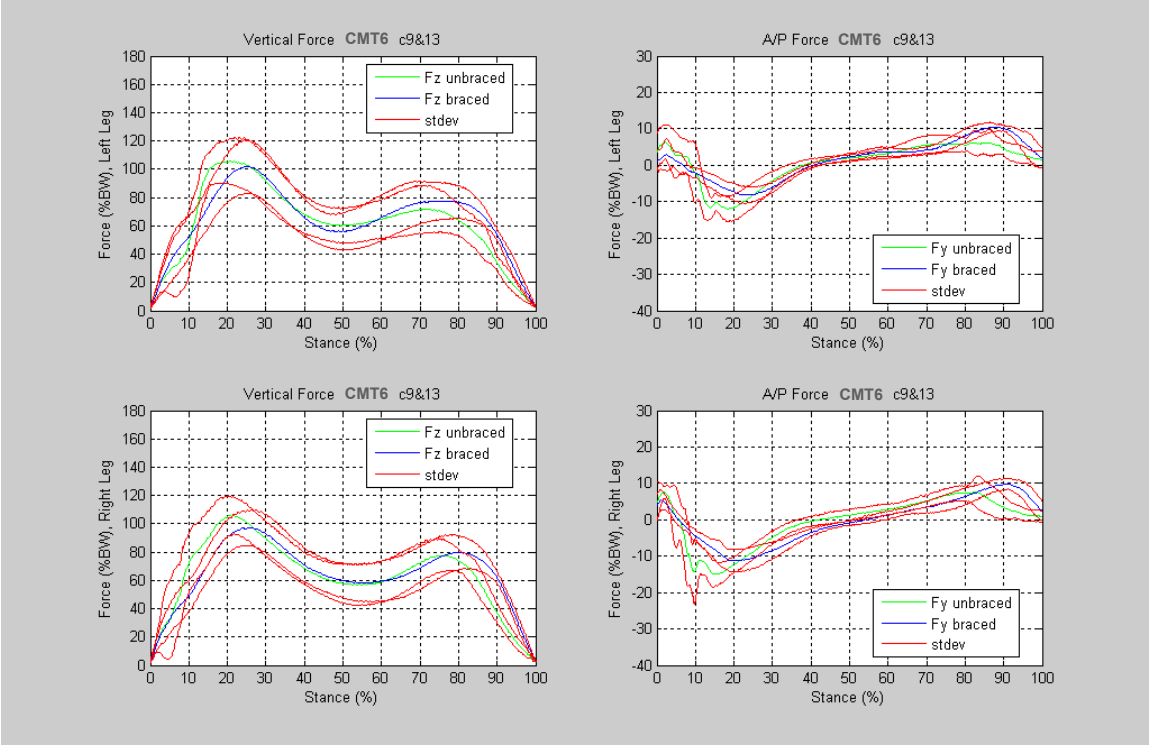
Vertical Force CMT6 c9&13
Fz unbraced
Fz braced
stdev
Force (%BW), Left Leg
Stance (%)
A/P Force CMT6 c9&13
Fy unbraced
Fy braced
stdev
Force (%BW), Left Leg
Stance (%)
Vertical Force CMT6 c9&13
Fz unbraced
Fz braced
stdev
Force (%BW), Right Leg
Stance (%)
A/P Force CMT6 c9&13
Fy unbraced
Fy braced
stdev
Force (%BW), Right Leg
Stance (%)

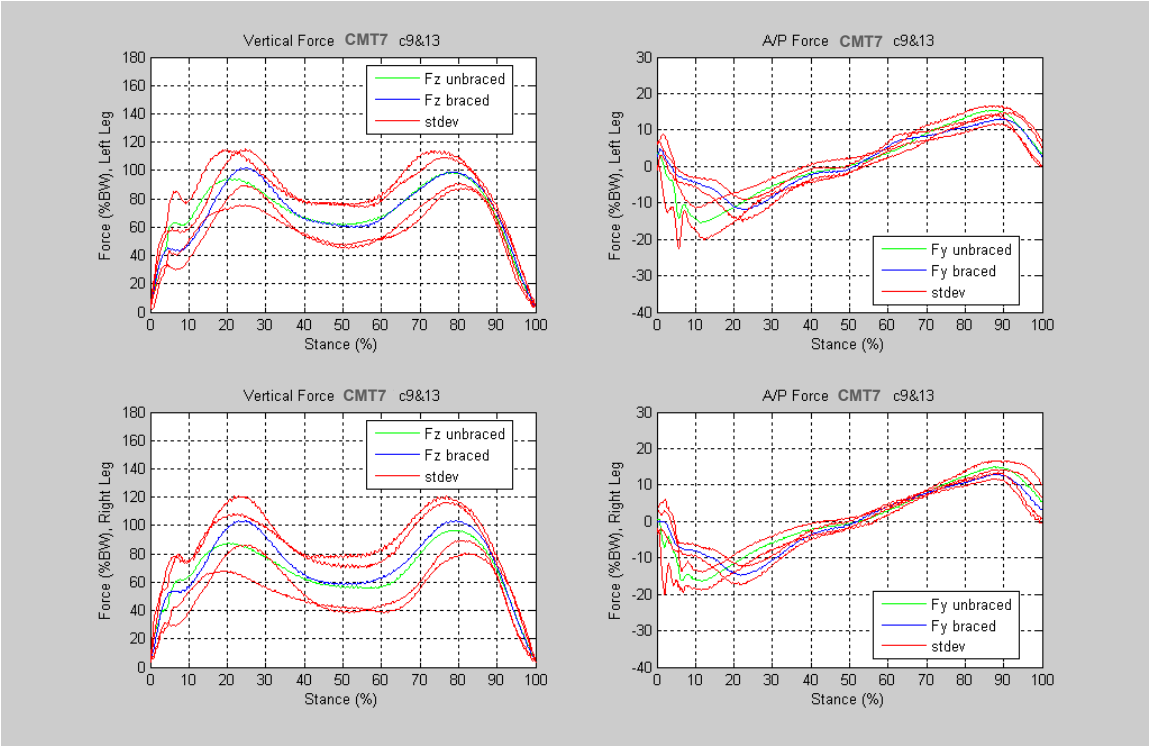
Vertical Force CMT7 c9&13
Fz unbraced
Fz braced
stdev
Force (%BW), Left Leg
Stance (%)
A/P Force CMT7 c9&13
Fy unbraced
Fy braced
stdev
Force (%BW), Left Leg
Stance (%)
Vertical Force CMT7 c9&13
Fz unbraced
Fz braced
stdev
Force (%BW), Right Leg
Stance (%)
A/P Force CMT7 c9&13
Fy unbraced
Fy braced
stdev
Force (%BW), Right Leg
Stance (%)

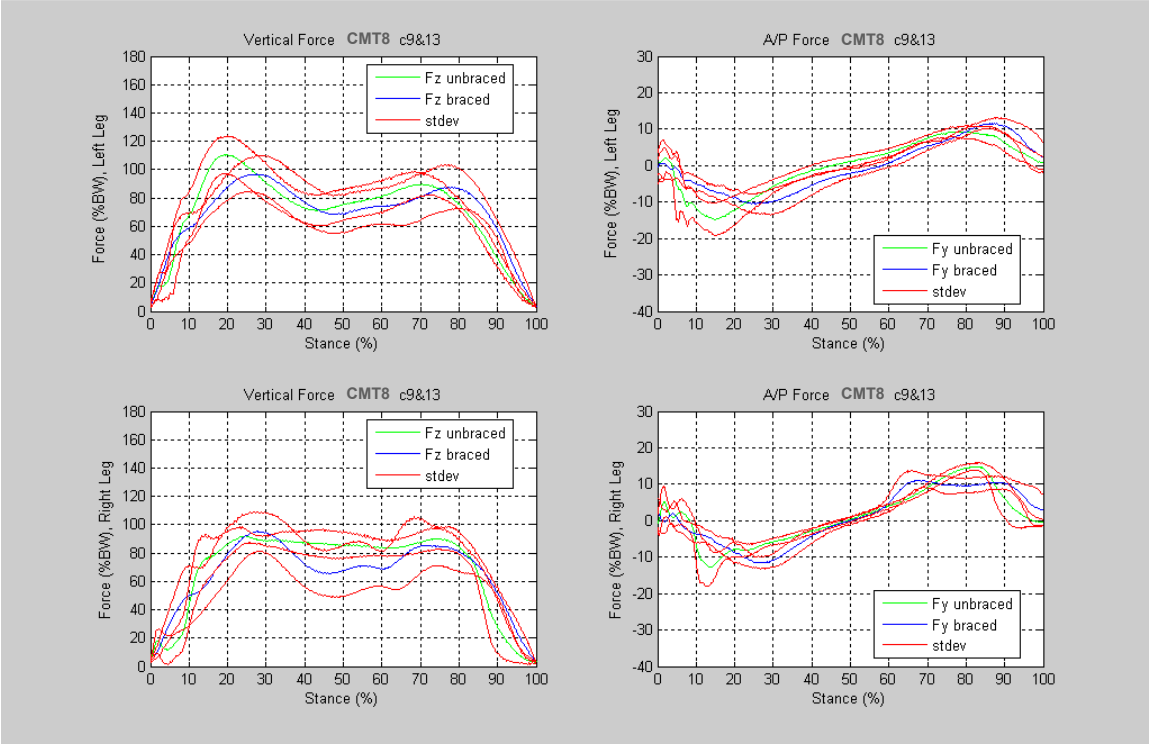
Vertical Force CMT8 c9&13
Force (%BW), Left Leg
Stance (%)
Fz unbraced
Fz braced
stdev
A/P Force CMT8 c9&13
Force (%BW), Left Leg
Stance (%)
Fy unbraced
Fy braced
stdev
Vertical Force CMT8 c9&13
Force (%BW), Right Leg
Stance (%)
Fz unbraced
Fz braced
stdev
A/P Force CMT8 c9&13
Force (%BW), Right Leg
Stance (%)
Fy unbraced
Fy braced
stdev

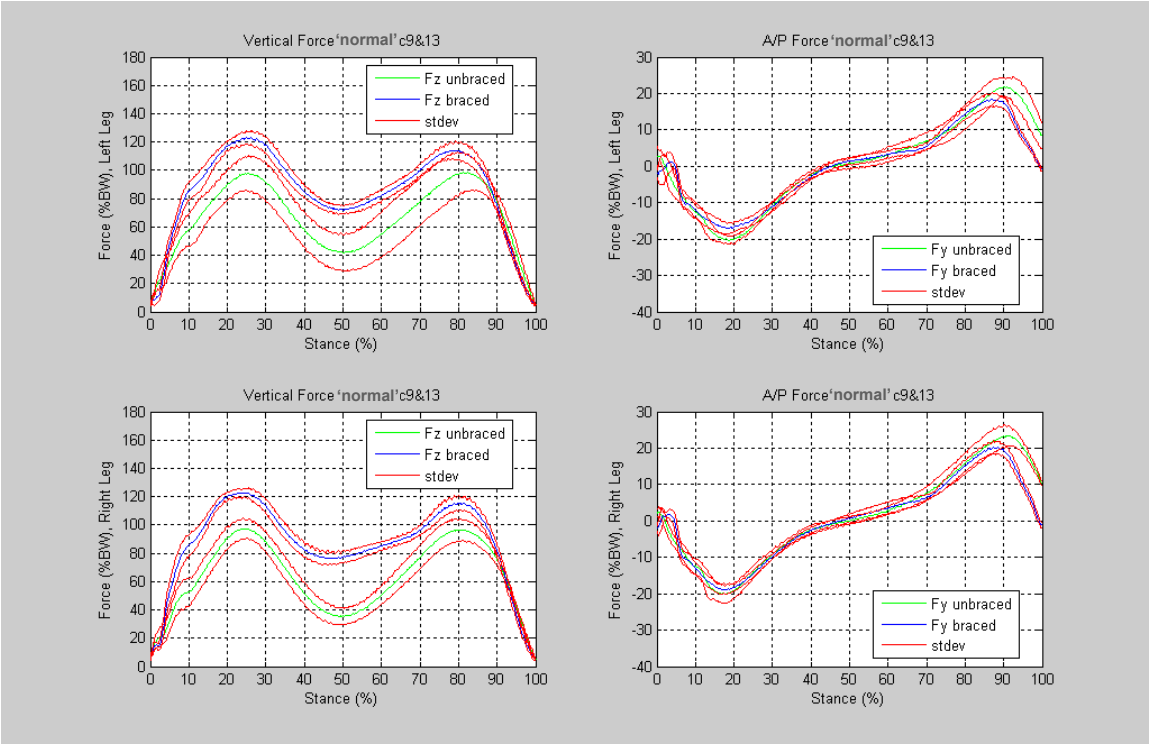
Vertical Force 'normal' c9&13
Force (%BW), Left Leg
Stance (%)
Fz unbraced
Fz braced
stdev
A/P Force 'normal' c9&13
Force (%BW), Left Leg
Stance (%)
Fy unbraced
Fy braced
stdev
Vertical Force 'normal' c9&13
Force (%BW), Right Leg
Stance (%)
Fz unbraced
Fz braced
stdev
A/P Force 'normal' c9&13
Force (%BW), Right Leg
Stance (%)
Fy unbraced
Fy braced
stdev

Selected Subjects (Conditions 1 and 5)

Shown in this section are graphs of the average GRFs (F_x and F_y) with standard deviations broken into left and right feet. For subjects who had a current brace, conditions 1 and condition 5 are overlaid to highlight differences between the unbraced and braced conditions.

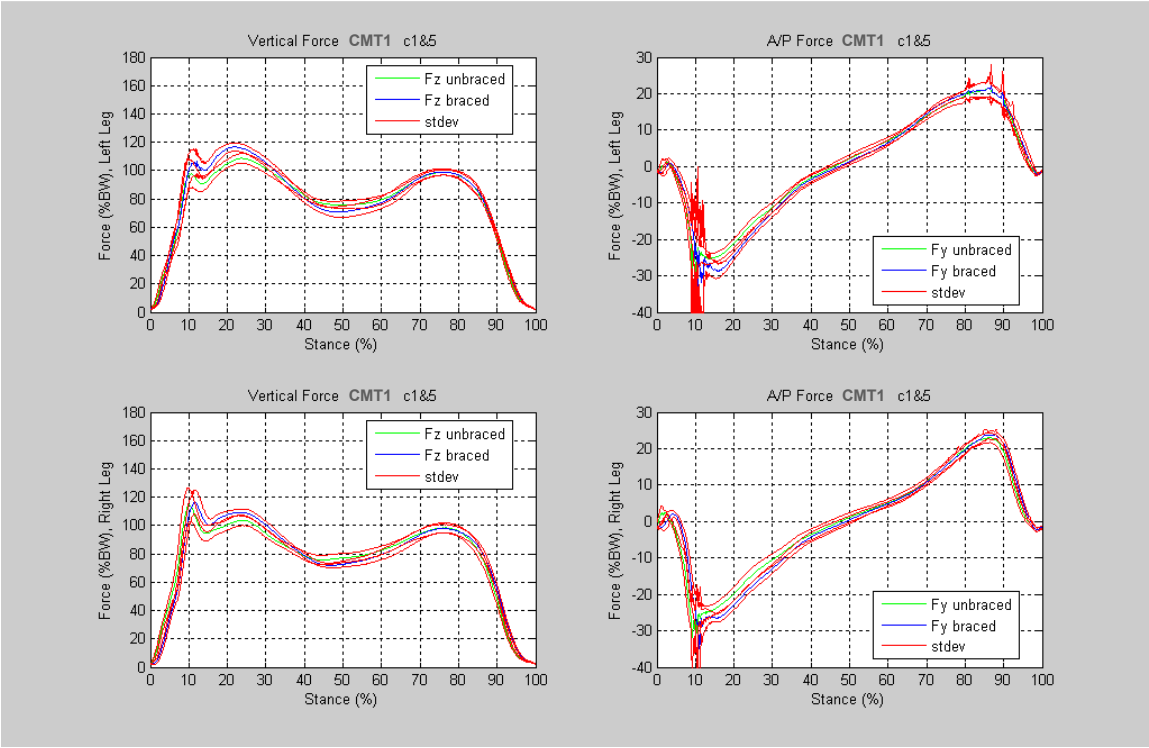

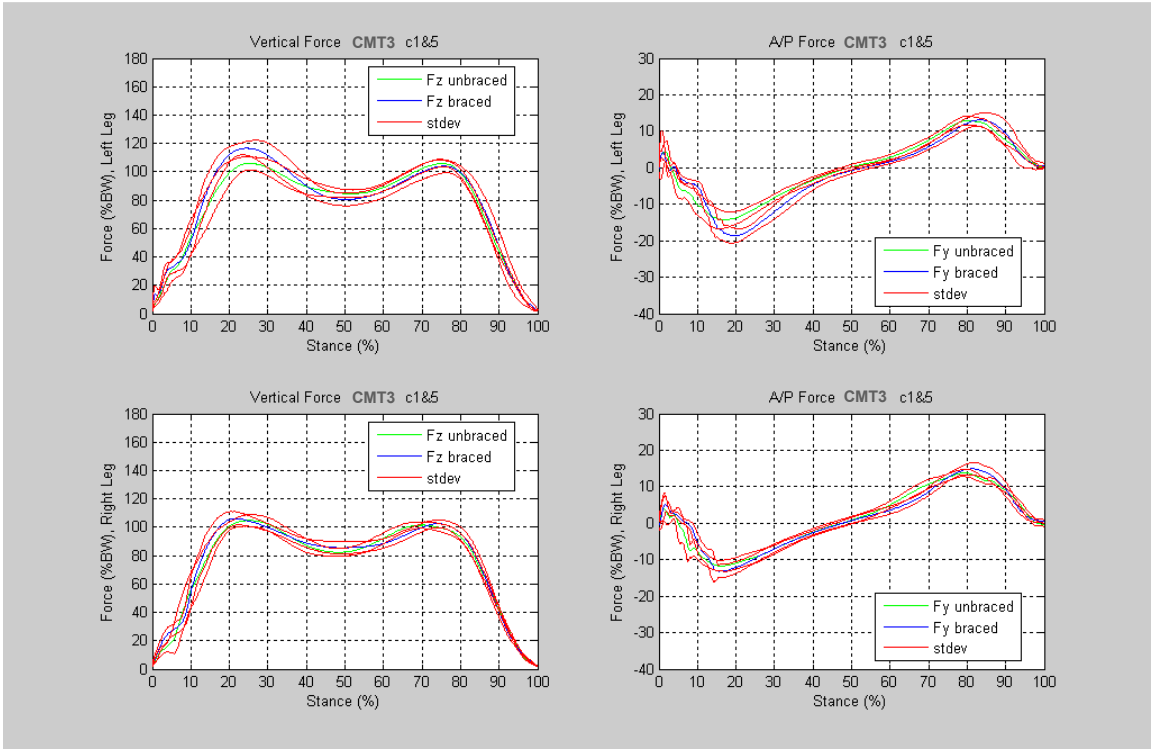
Vertical Force CMT3 c1&5
Force (%BW), Left Leg
Stance (%)
Fz unbraced
Fz braced
stdev
A/P Force CMT3 c1&5
Force (%BW), Left Leg
Stance (%)
Fy unbraced
Fy braced
stdev
Vertical Force CMT3 c1&5
Force (%BW), Right Leg
Stance (%)
Fz unbraced
Fz braced
stdev
A/P Force CMT3 c1&5
Force (%BW), Right Leg
Stance (%)
Fy unbraced
Fy braced
stdev

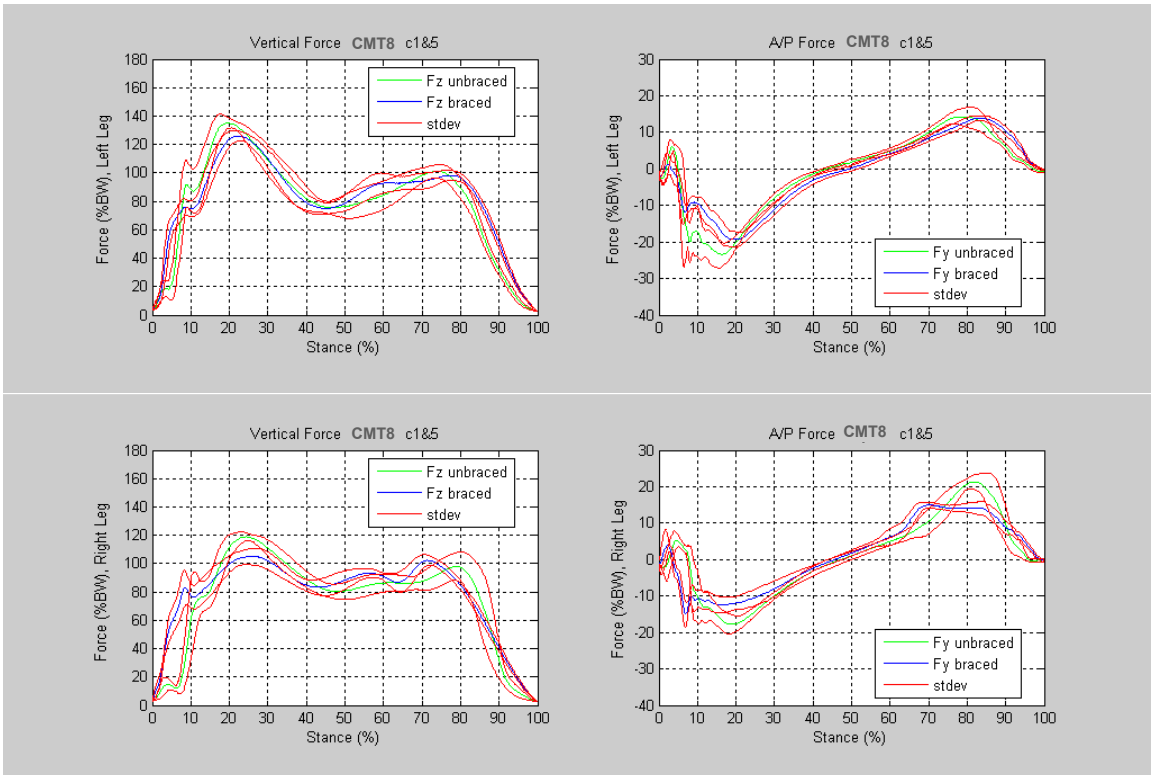
Vertical Force CMT8 c1&5
Force (%BW), Left Leg
Stance (%)
Fz unbraced
Fz braced
stdev
A/P Force CMT8 c1&5
Force (%BW), Left Leg
Stance (%)
Fy unbraced
Fy braced
stdev
Vertical Force CMT8 c1&5
Force (%BW), Right Leg
Stance (%)
Fz unbraced
Fz braced
stdev
A/P Force CMT8 c1&5
Force (%BW), Right Leg
Stance (%)
Fy unbraced
Fy braced
stdev

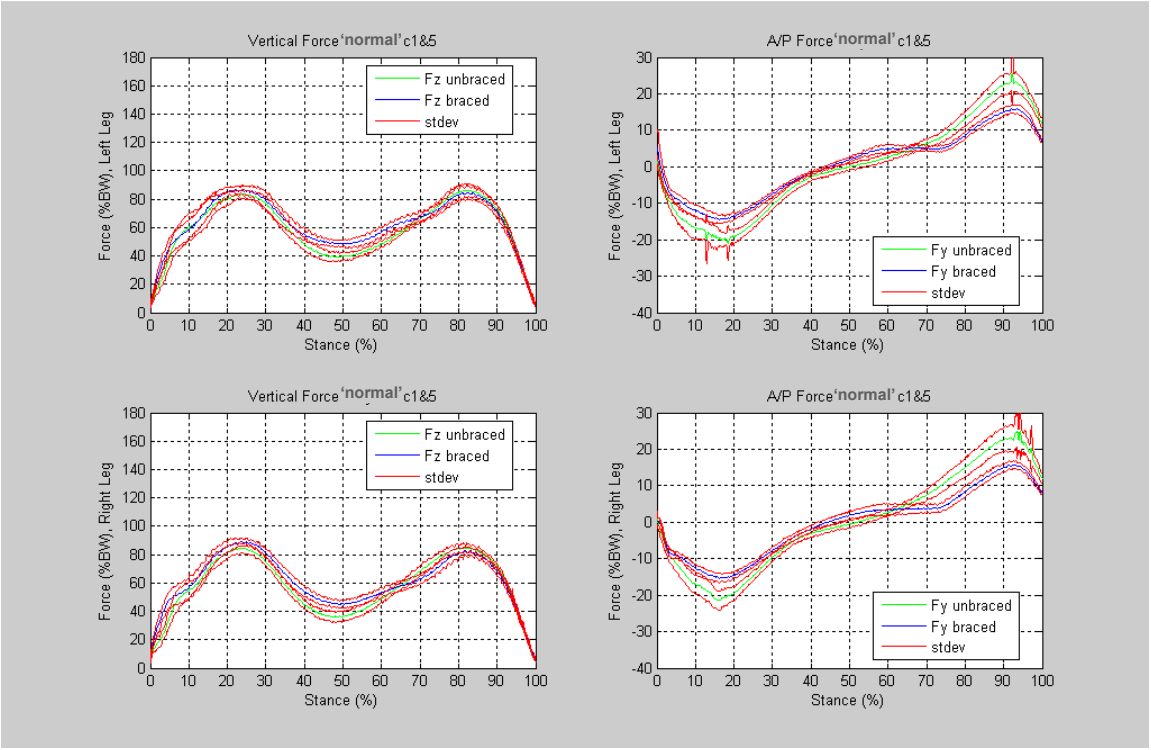
Vertical Force 'normal' c1&5
Force (%BW), Left Leg
Stance (%)
Fz unbraced
Fz braced
stdev
A/P Force 'normal' c1&5
Force (%BW), Left Leg
Stance (%)
Fy unbraced
Fy braced
stdev
Vertical Force 'normal' c1&5
Force (%BW), Right Leg
Stance (%)
Fz unbraced
Fz braced
stdev
A/P Force 'normal' c1&5
Force (%BW), Right Leg
Stance (%)
Fy unbraced
Fy braced
stdev

APPENDIX B

HUMAN MOTION STRAIN DATA

Shown in this section are graphs of the gage strain data during human motion testing broken into left and right feet. The graphs on the left show the gage strains for each individual trial. The graphs on the right show the average gage strains.

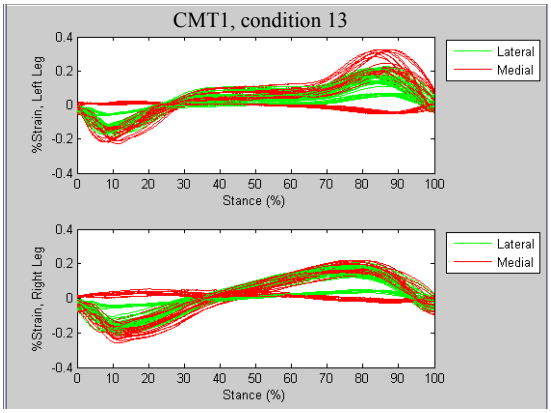

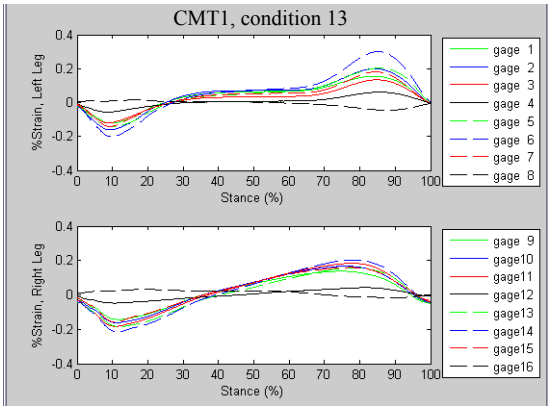

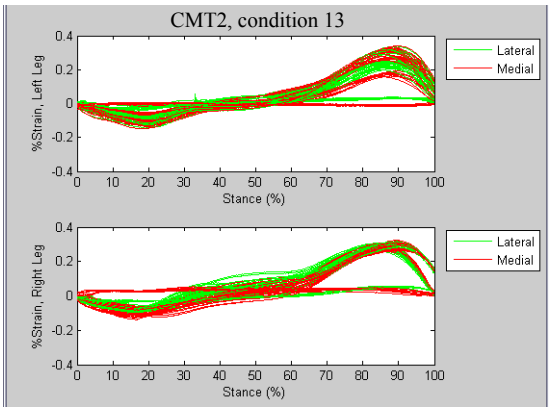

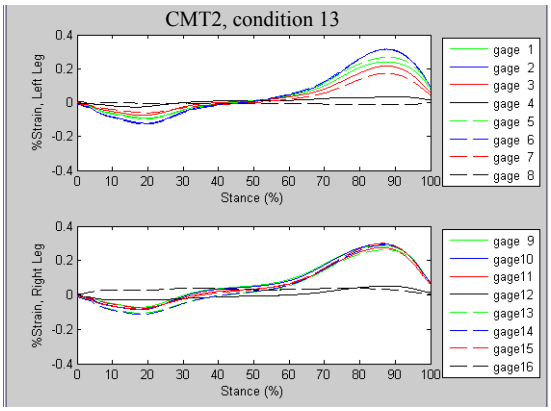

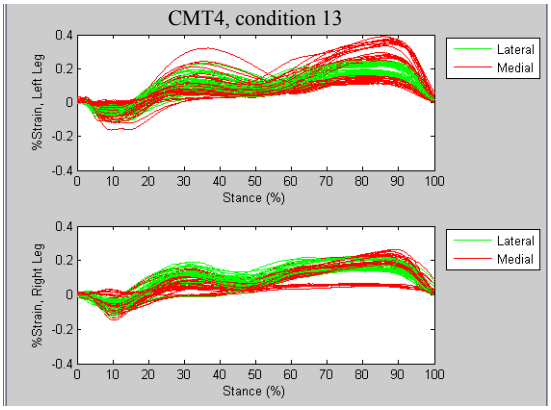

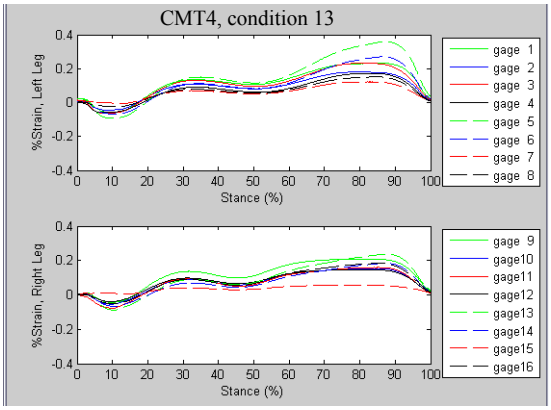

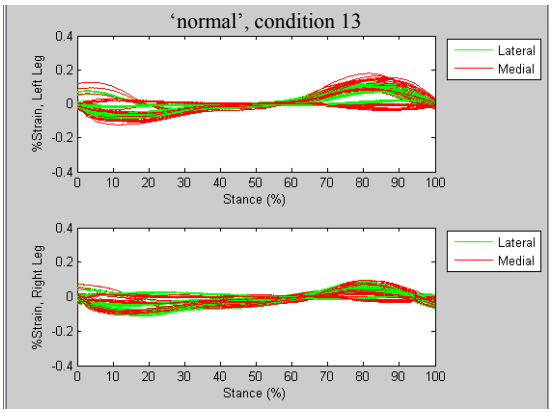
‘normal’, condition 13
%Strain, Left Leg
%Strain, Right Leg
Stance (%)
Lateral
Medial

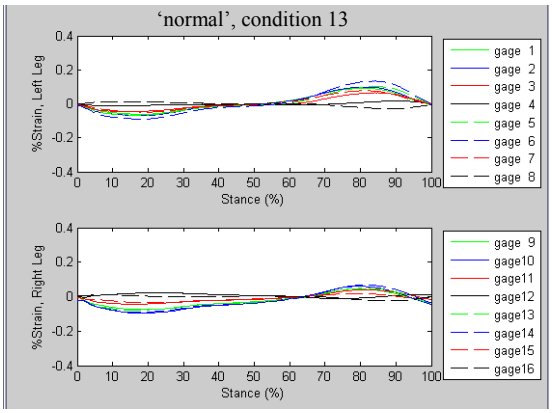
‘normal’, condition 13
%Strain, Left Leg
%Strain, Right Leg
Stance (%)
gage 1
gage 2
gage 3
gage 4
gage 5
gage 6
gage 7
gage 8
gage 9
gage10
gage11
gage12
gage13
gage14
gage15
gage16

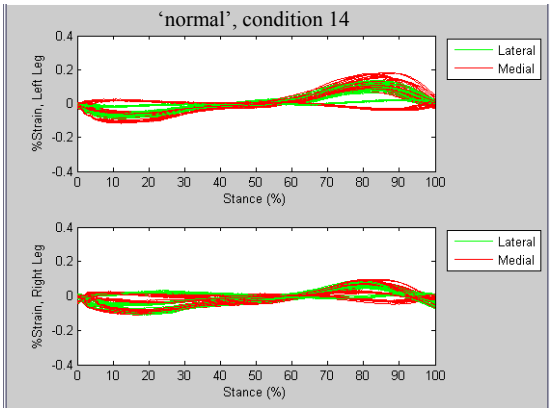
‘normal’, condition 14
%Strain, Left Leg
%Strain, Right Leg
Stance (%)
Lateral
Medial

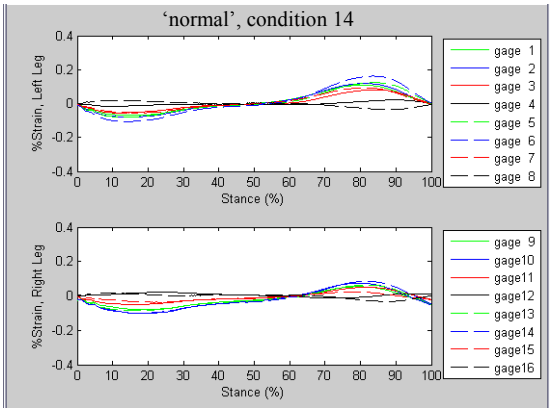
‘normal’, condition 14
%Strain, Left Leg
%Strain, Right Leg
Stance (%)
gage 1
gage 2
gage 3
gage 4
gage 5
gage 6
gage 7
gage 8
gage 9
gage10
gage11
gage12
gage13
gage14
gage15
gage16

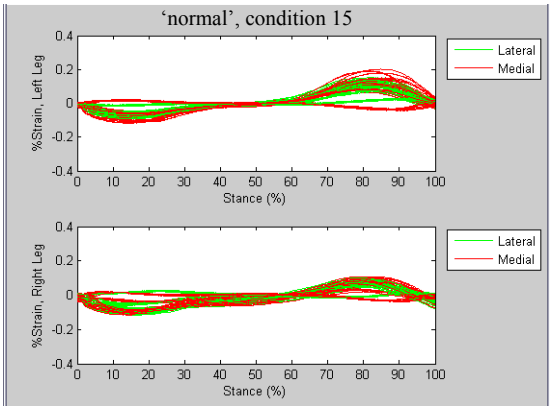
‘normal’, condition 15
%Strain, Left Leg
%Strain, Right Leg
Stance (%)
Lateral
Medial

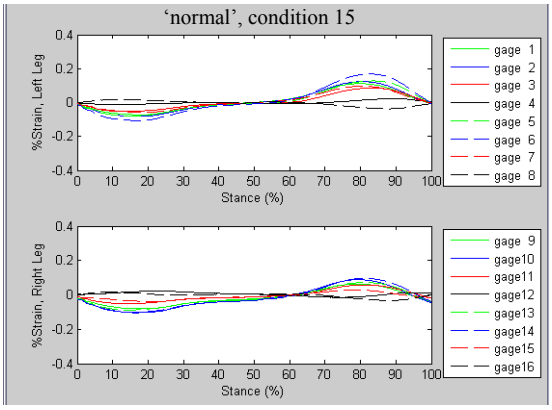
‘normal’, condition 15
%Strain, Left Leg
%Strain, Right Leg
Stance (%)
gage 1
gage 2
gage 3
gage 4
gage 5
gage 6
gage 7
gage 8
gage 9
gage10
gage11
gage12
gage13
gage14
gage15
gage16

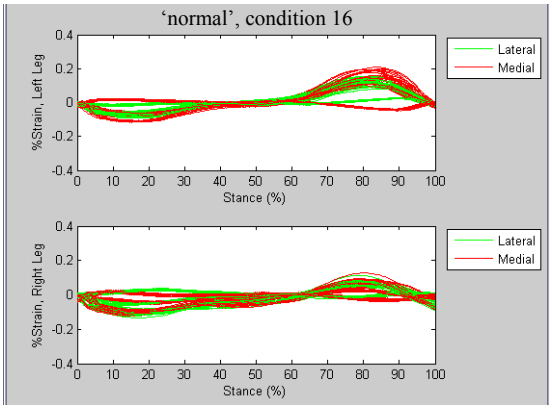
‘normal’, condition 16
%Strain, Left Leg
%Strain, Right Leg
Stance (%)
Lateral
Medial

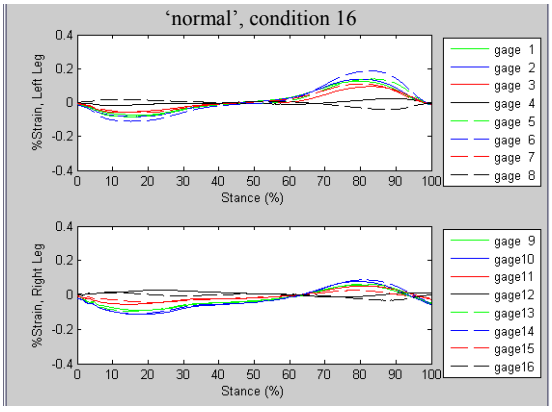
‘normal’, condition 16
%Strain, Left Leg
%Strain, Right Leg
Stance (%)
gage 1
gage 2
gage 3
gage 4
gage 5
gage 6
gage 7
gage 8
gage 9
gage10
gage11
gage12
gage13
gage14
gage15
gage16

APPENDIX C

HUMAN MOTION FORCE AND TEMPORAL PARAMETER COMPARISONS

All Subjects (Conditions 9, and 13)

Shown in this section are graphs of the averages and standard deviations for the force (F_y and F_z) and temporal parameters for all subjects. Condition 9 is post-test unbraced and condition 13 is post-test braced with the HELIOS.

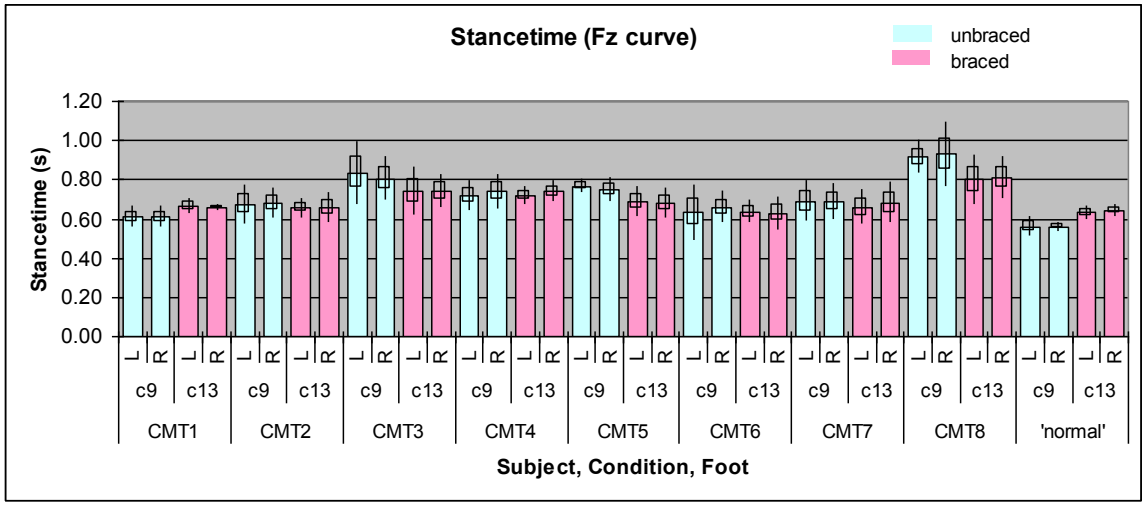

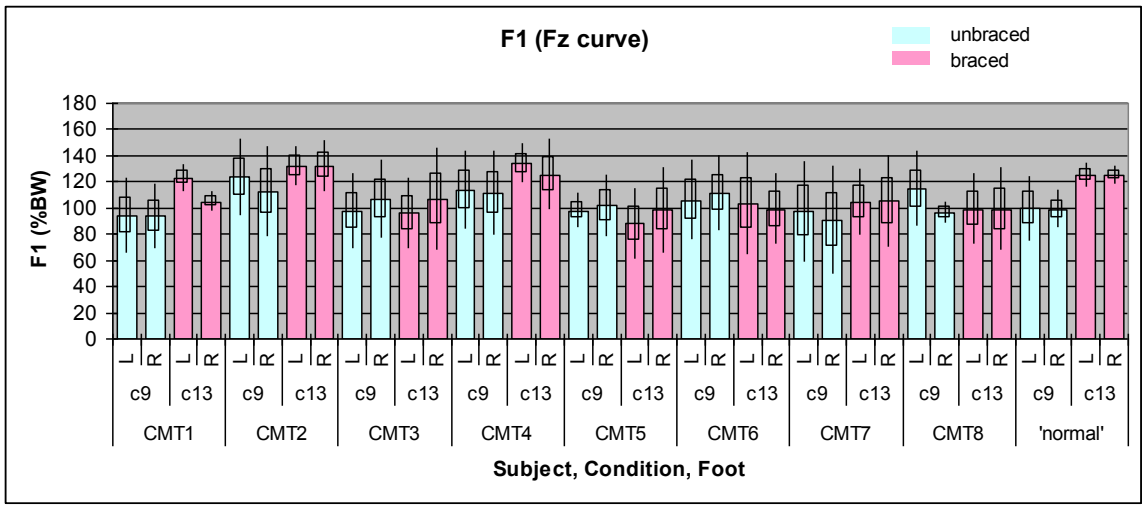

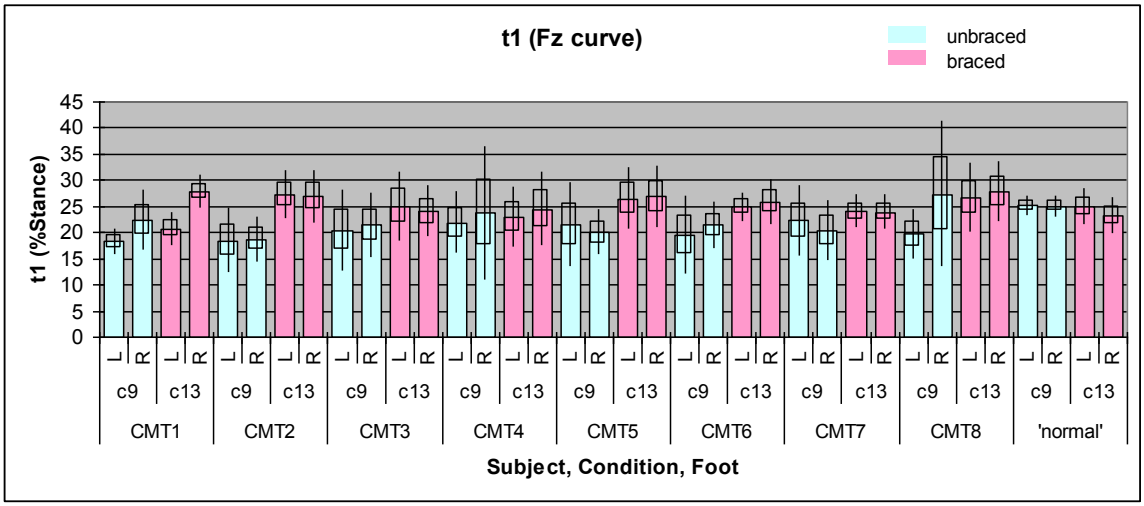
t1 (Fz curve)
unbraced
braced
t1 (%Stance)
45
40
35
30
25
20
15
10
5
0
L R L R L R L R L R L R L R L R L R L R L R L R L R L R L R L R L R L R
c9 c13 c9 c13 c9 c13 c9 c13 c9 c13 c9 c13 c9 c13 c9 c13 c9 c13 c9 c13
CMT1 CMT2 CMT3 CMT4 CMT5 CMT6 CMT7 CMT8 'normal'
Subject, Condition, Foot

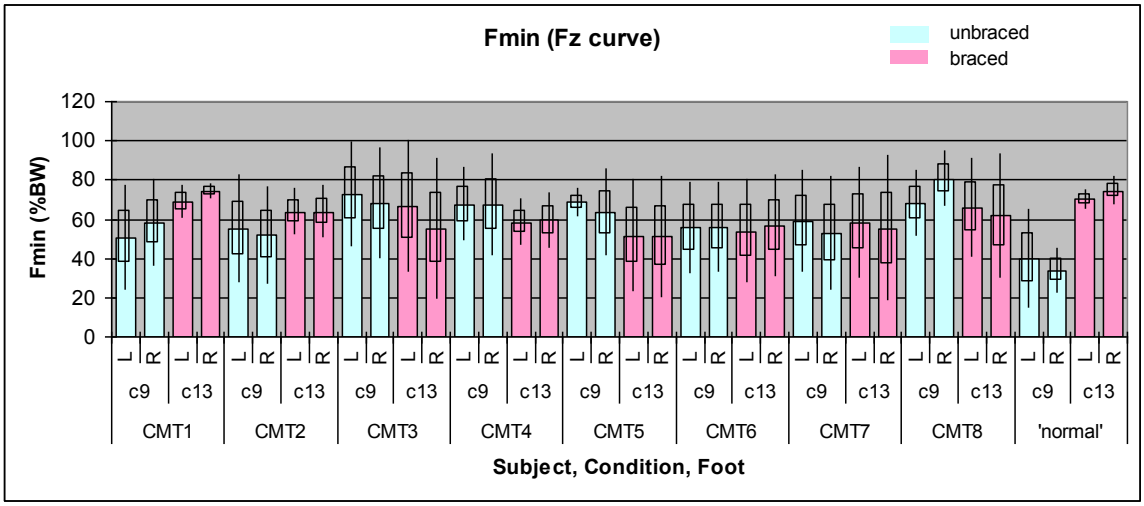
Fmin (Fz curve)
unbraced
braced
Fmin (%BW)
120
100
80
60
40
20
0
L R L R L R L R L R L R L R L R L R L R L R L R L R L R L R L R L R L R
c9 c13 c9 c13 c9 c13 c9 c13 c9 c13 c9 c13 c9 c13 c9 c13 c9 c13 c9 c13
CMT1 CMT2 CMT3 CMT4 CMT5 CMT6 CMT7 CMT8 'normal'
Subject, Condition, Foot

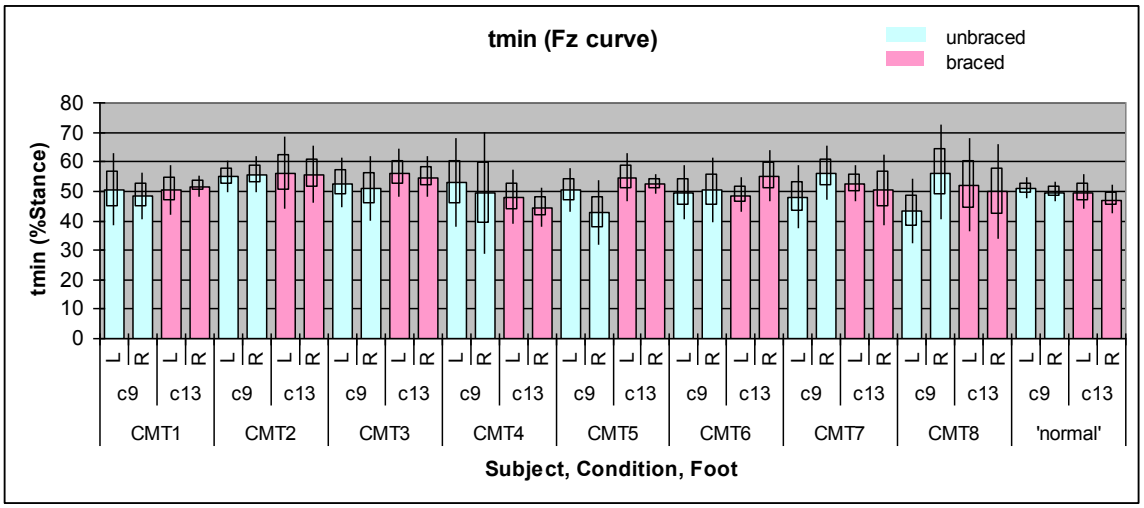
tmin (Fz curve)
unbraced
braced
tmin (%Stance)
80
70
60
50
40
30
20
10
0
L R L R L R L R L R L R L R L R L R L R L R L R L R L R L R L R L R L R
c9 c13 c9 c13 c9 c13 c9 c13 c9 c13 c9 c13 c9 c13 c9 c13 c9 c13 c9 c13
CMT1 CMT2 CMT3 CMT4 CMT5 CMT6 CMT7 CMT8 'normal'
Subject, Condition, Foot

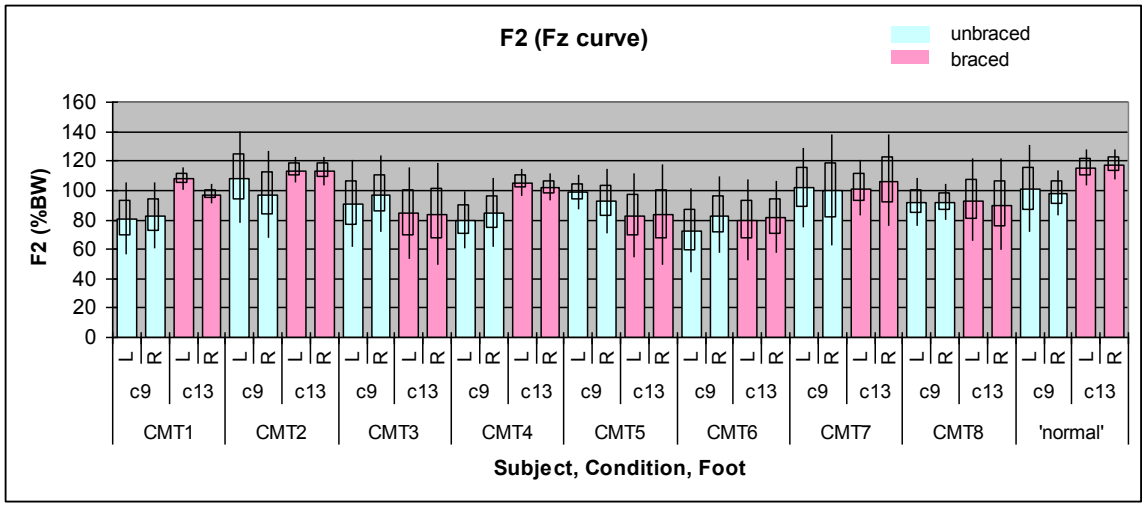
F2 (Fz curve)
unbraced
braced
F2 (%BW)
160
140
120
100
80
60
40
20
0
L R L R L R L R L R L R L R L R L R L R L R L R L R L R L R L R L R L R L R
c9 c13 c9 c13 c9 c13 c9 c13 c9 c13 c9 c13 c9 c13 c9 c13 c9 c13
CMT1 CMT2 CMT3 CMT4 CMT5 CMT6 CMT7 CMT8 'normal'
Subject, Condition, Foot

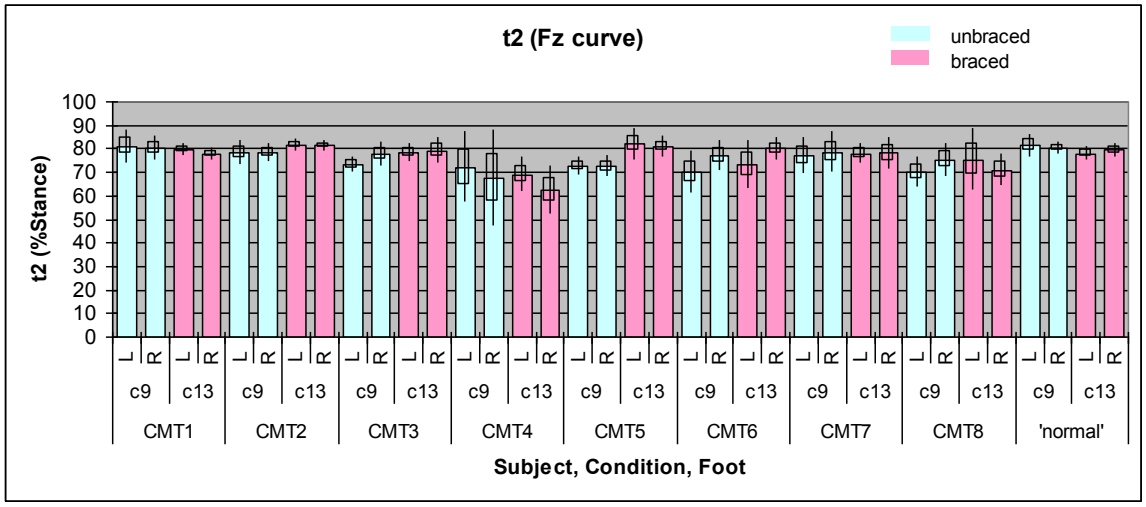
t2 (Fz curve)
unbraced
braced
t2 (%Stance)
100
90
80
70
60
50
40
30
20
10
0
L R L R L R L R L R L R L R L R L R L R L R L R L R L R L R L R L R L R L R
c9 c13 c9 c13 c9 c13 c9 c13 c9 c13 c9 c13 c9 c13 c9 c13 c9 c13
CMT1 CMT2 CMT3 CMT4 CMT5 CMT6 CMT7 CMT8 'normal'
Subject, Condition, Foot

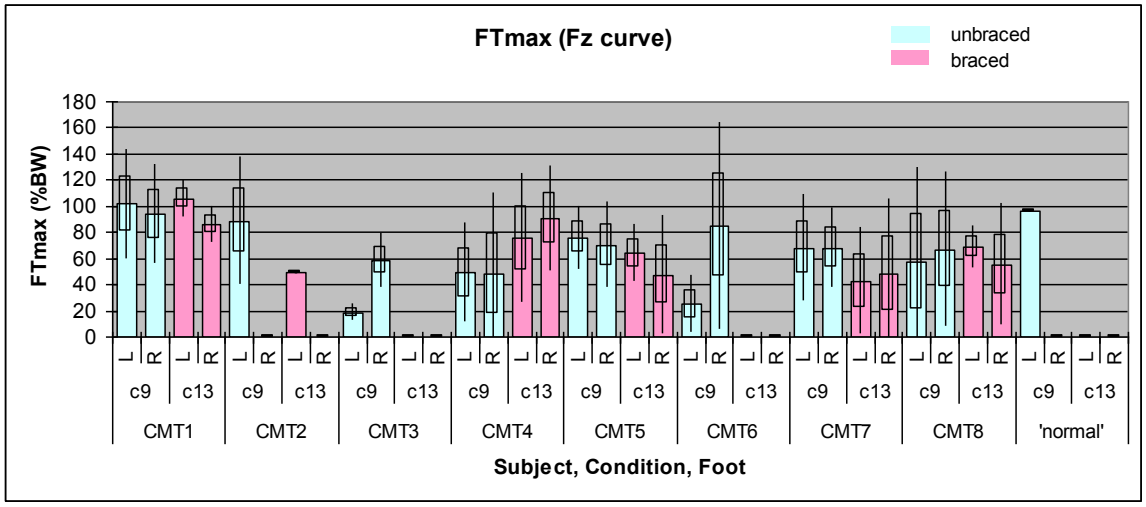
FTmax (Fz curve)
unbraced
braced
FTmax (%BW)
180
160
140
120
100
80
60
40
20
0
L R L R L R L R L R L R L R L R L R L R L R L R L R L R L R L R L R L R L R
c9 c13 c9 c13 c9 c13 c9 c13 c9 c13 c9 c13 c9 c13 c9 c13 c9 c13
CMT1 CMT2 CMT3 CMT4 CMT5 CMT6 CMT7 CMT8 'normal'
Subject, Condition, Foot

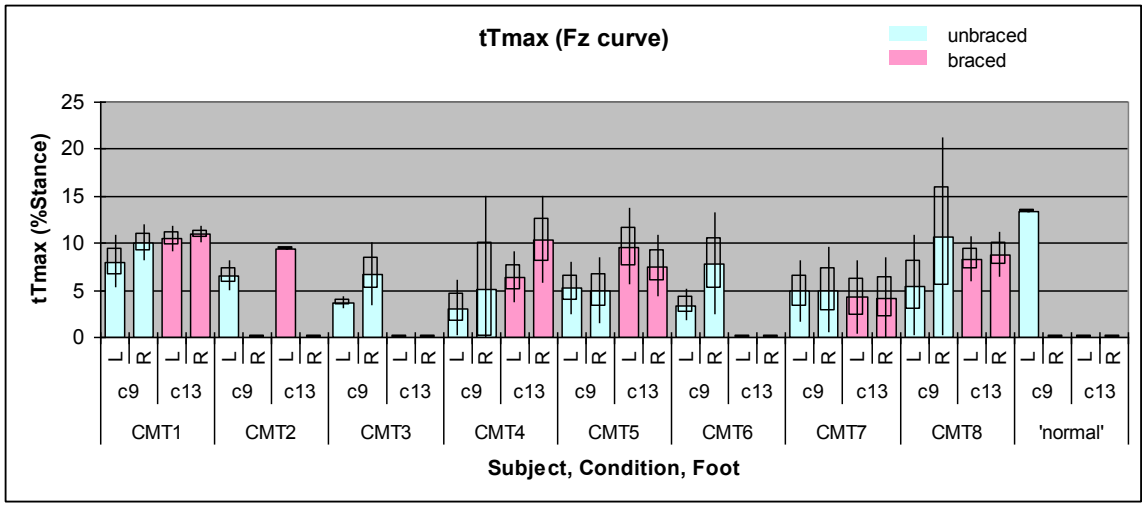
tTmax (Fz curve)
unbraced
braced
tTmax (%Stance)
25
20
15
10
5
0
L R L R L R L R L R L R L R L R L R L R L R L R L R L R L R L R L R L R
c9 c13 c9 c13 c9 c13 c9 c13 c9 c13 c9 c13 c9 c13 c9 c13 c9 c13
CMT1 CMT2 CMT3 CMT4 CMT5 CMT6 CMT7 CMT8 'normal'
Subject, Condition, Foot

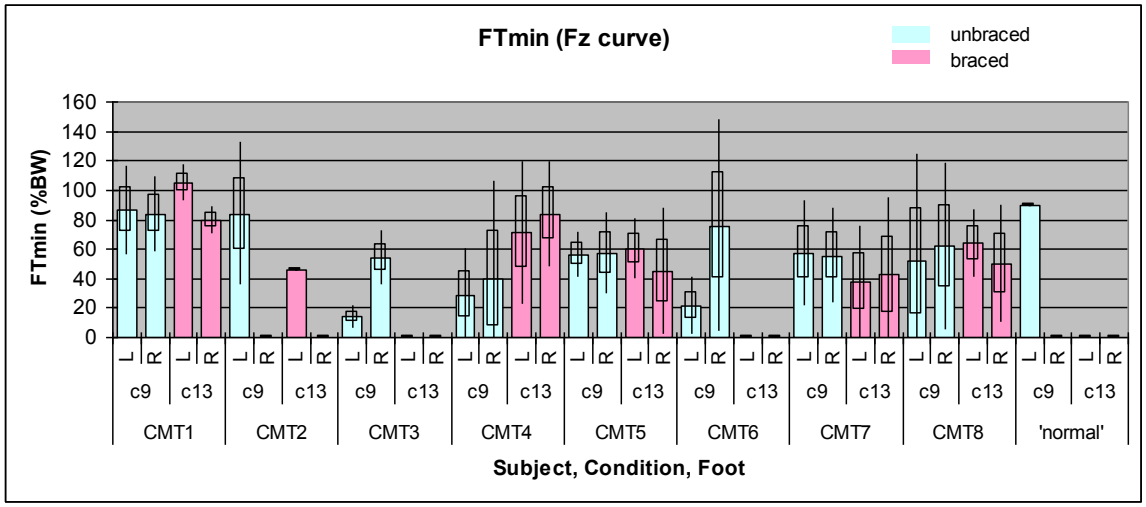
FTmin (Fz curve)
unbraced
braced
FTmin (%BW)
160
140
120
100
80
60
40
20
0
L R L R L R L R L R L R L R L R L R L R L R L R L R L R L R L R L R L R
c9 c13 c9 c13 c9 c13 c9 c13 c9 c13 c9 c13 c9 c13 c9 c13 c9 c13
CMT1 CMT2 CMT3 CMT4 CMT5 CMT6 CMT7 CMT8 'normal'
Subject, Condition, Foot

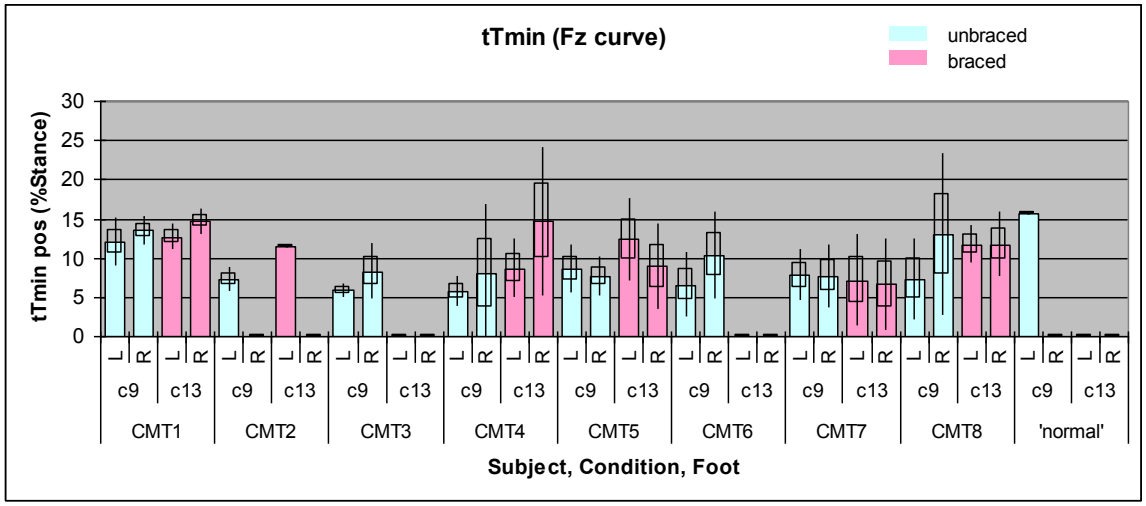
tTmin (Fz curve)
unbraced
braced
tTmin pos (%Stance)
30
25
20
15
10
5
0
L R L R L R L R L R L R L R L R L R L R L R L R L R L R L R L R L R L R
c9 c13 c9 c13 c9 c13 c9 c13 c9 c13 c9 c13 c9 c13 c9 c13 c9 c13
CMT1 CMT2 CMT3 CMT4 CMT5 CMT6 CMT7 CMT8 'normal'
Subject, Condition, Foot

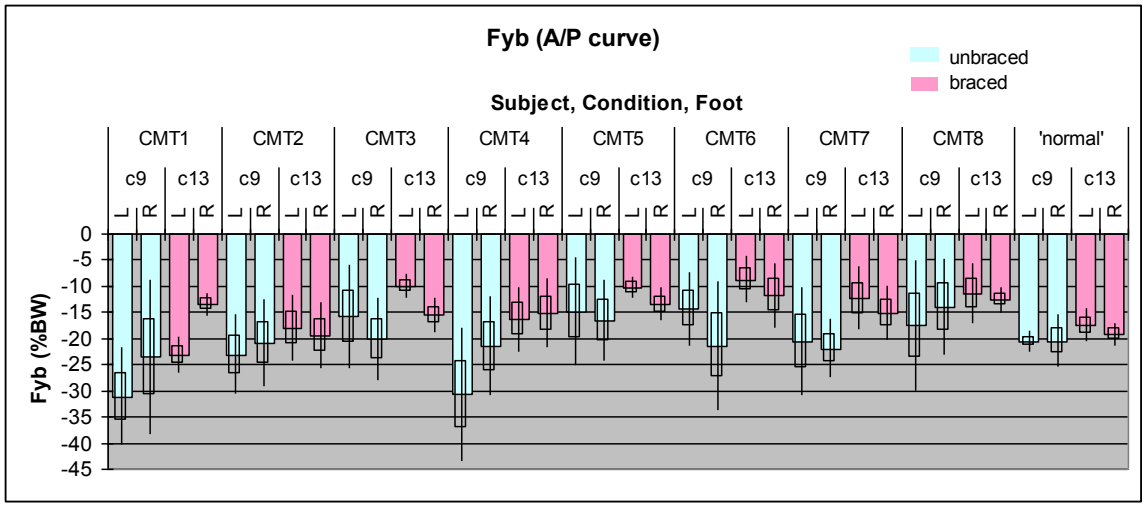
Fyb (A/P curve)
unbraced
braced
Subject, Condition, Foot
CMT1
CMT2
CMT3
CMT4
CMT5
CMT6
CMT7
CMT8
'normal'
c9
c13
L
R
Fyb (%BW)
0
-5
-10
-15
-20
-25
-30
-35
-40
-45

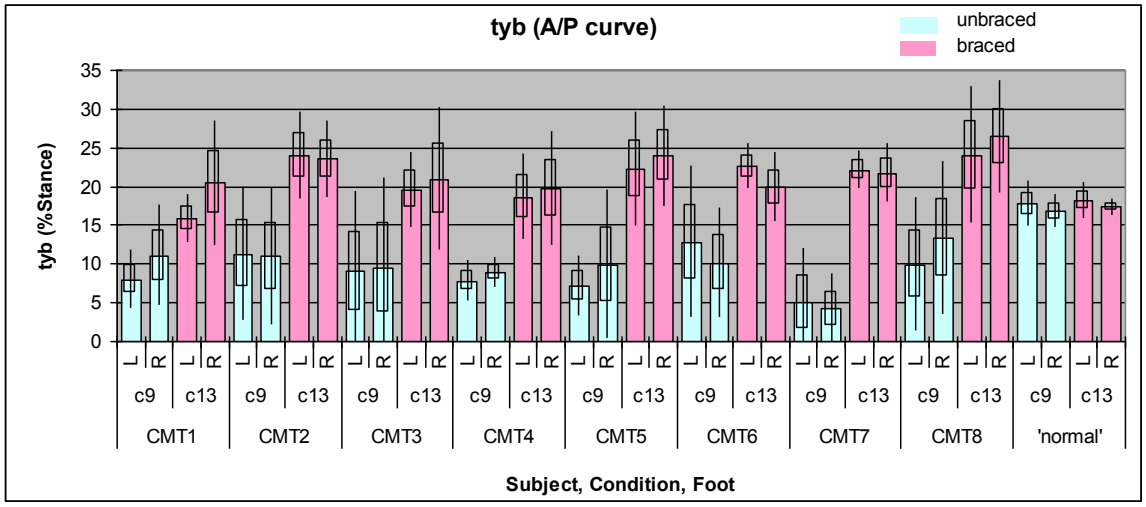
tyb (A/P curve)
unbraced
braced
tyb (%Stance)
35
30
25
20
15
10
5
0
CMT1
CMT2
CMT3
CMT4
CMT5
CMT6
CMT7
CMT8
'normal'
c9
c13
L
R
Subject, Condition, Foot

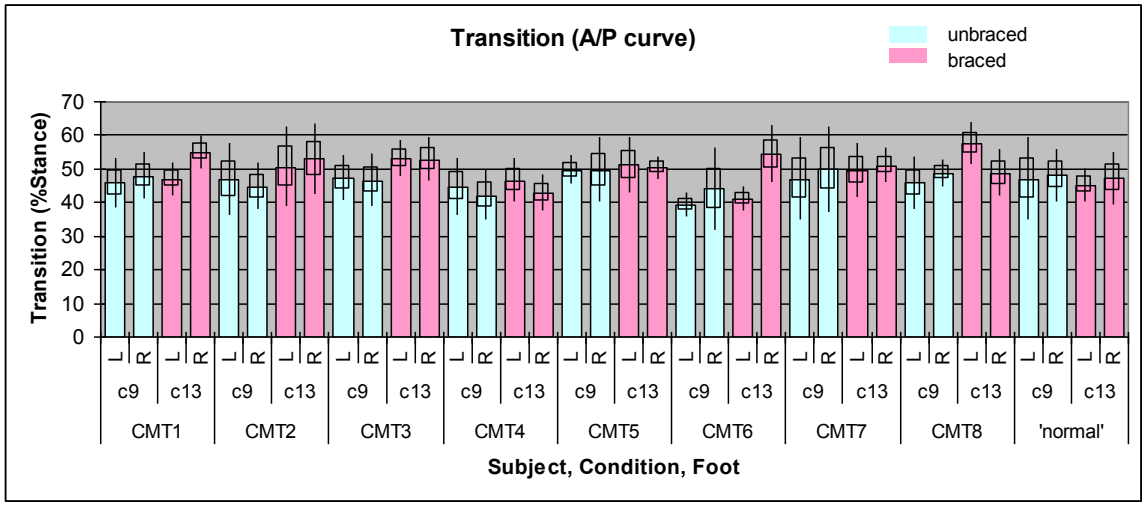
Transition (A/P curve)
unbraced
braced
Transition (%Stance)
70
60
50
40
30
20
10
0
CMT1
CMT2
CMT3
CMT4
CMT5
CMT6
CMT7
CMT8
'normal'
c9
c13
L
R
Subject, Condition, Foot

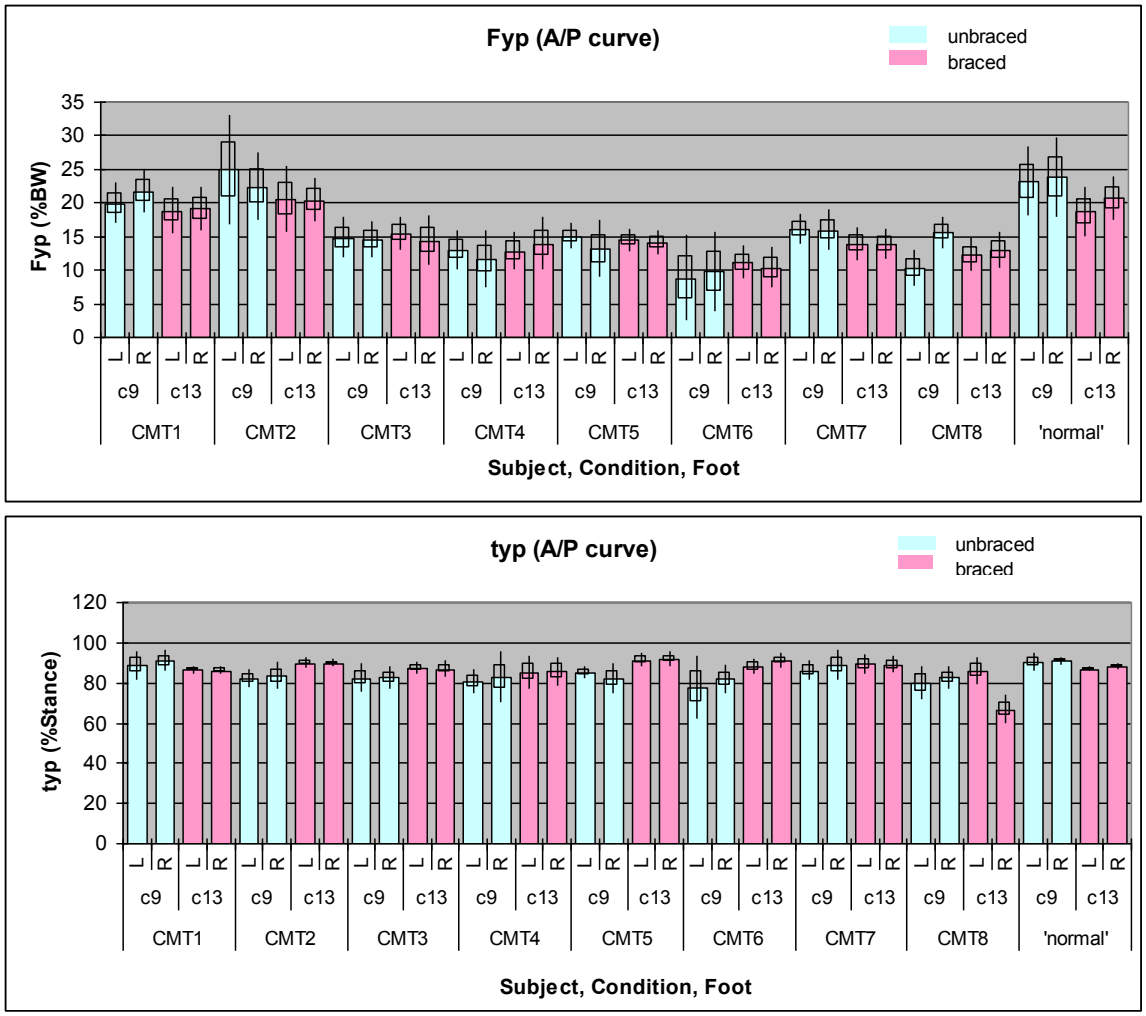

‘normal’ Subject (Conditions 1 through 16)

Shown in this section are graphs of the averages and standard deviations for the force (F_y and F_z) and temporal parameters for the ‘normal’ subject. All sixteen conditions are shown. Conditions 1 through 4 are pre-adaptation unbraced with 0%BW, 5%BW, 10%BW, and 15%BW added. Conditions 5 through 8 are pre-adaptation braced (HELIOS) with 0%BW, 5%BW, 10%BW, and 15%BW added. Conditions 9 through 12 are post-adaptation unbraced with 0%BW, 5%BW, 10%BW, and 15%BW added. Conditions 13 through 16 are post-adaptation braced (HELIOS) with 0%BW, 5%BW, 10%BW, and 15%BW added.

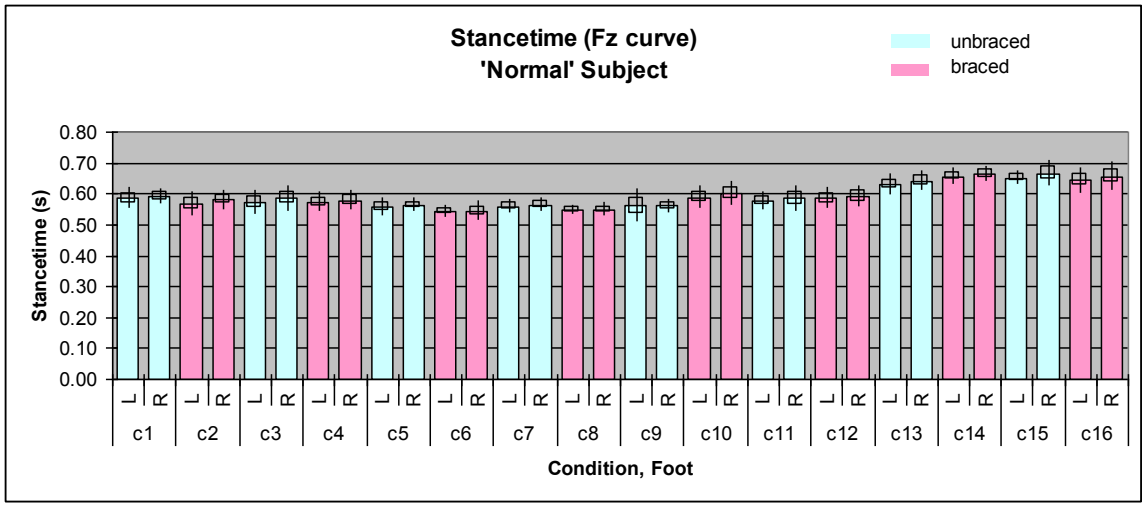
Stancetime (Fz curve)
'Normal' Subject
unbraced
braced
Stancetime (s)
0.80
0.70
0.60
0.50
0.40
0.30
0.20
0.10
0.00
L R
c1 c2 c3 c4 c5 c6 c7 c8 c9 c10 c11 c12 c13 c14 c15 c16
Condition, Foot

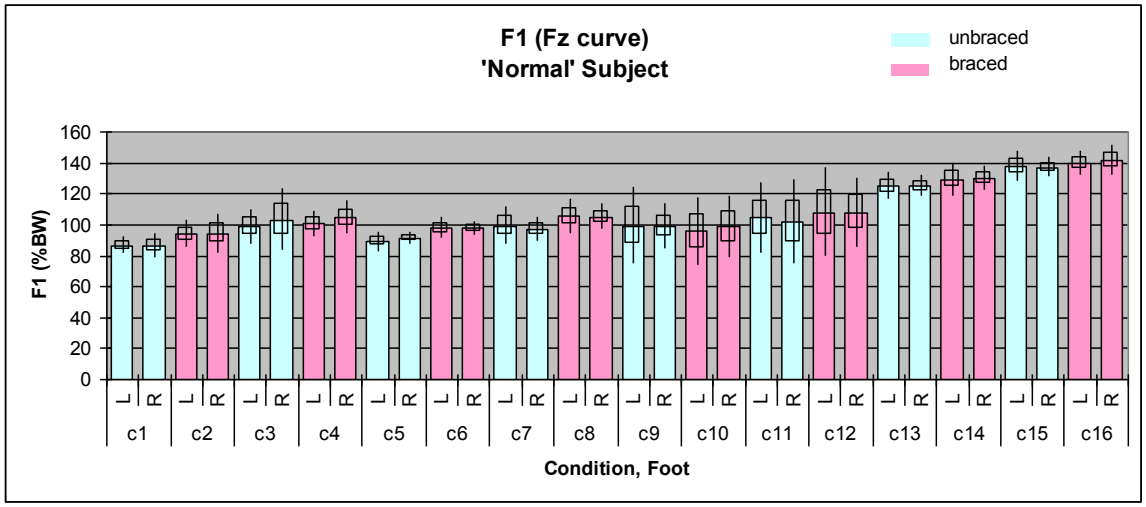
F1 (Fz curve)
'Normal' Subject
unbraced
braced
F1 (%BW)
160
140
120
100
80
60
40
20
0
L R
c1 c2 c3 c4 c5 c6 c7 c8 c9 c10 c11 c12 c13 c14 c15 c16
Condition, Foot

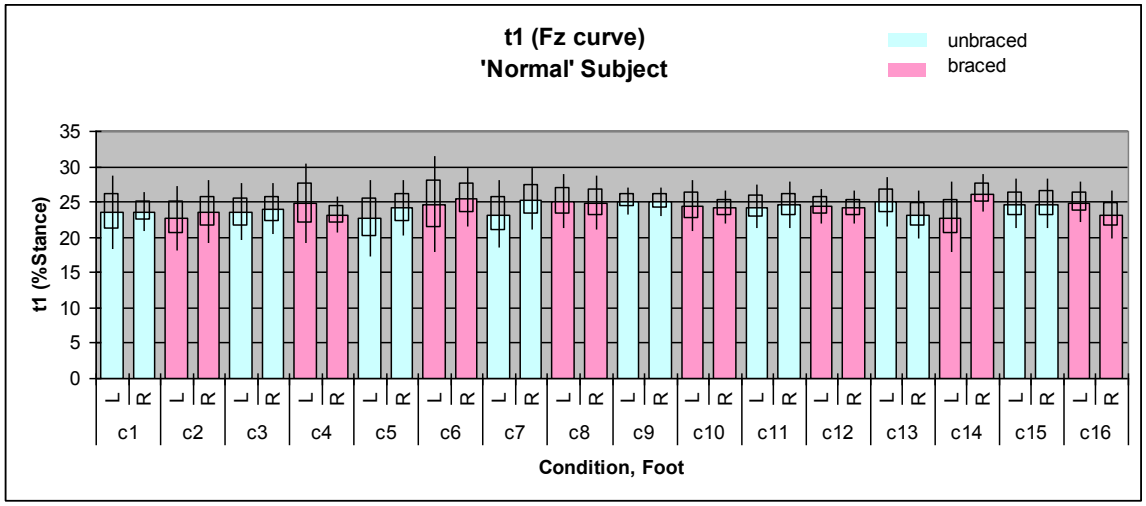
t1 (Fz curve)
'Normal' Subject
unbraced
braced
t1 (%Stance)
35
30
25
20
15
10
5
0
L R
c1 c2 c3 c4 c5 c6 c7 c8 c9 c10 c11 c12 c13 c14 c15 c16
Condition, Foot

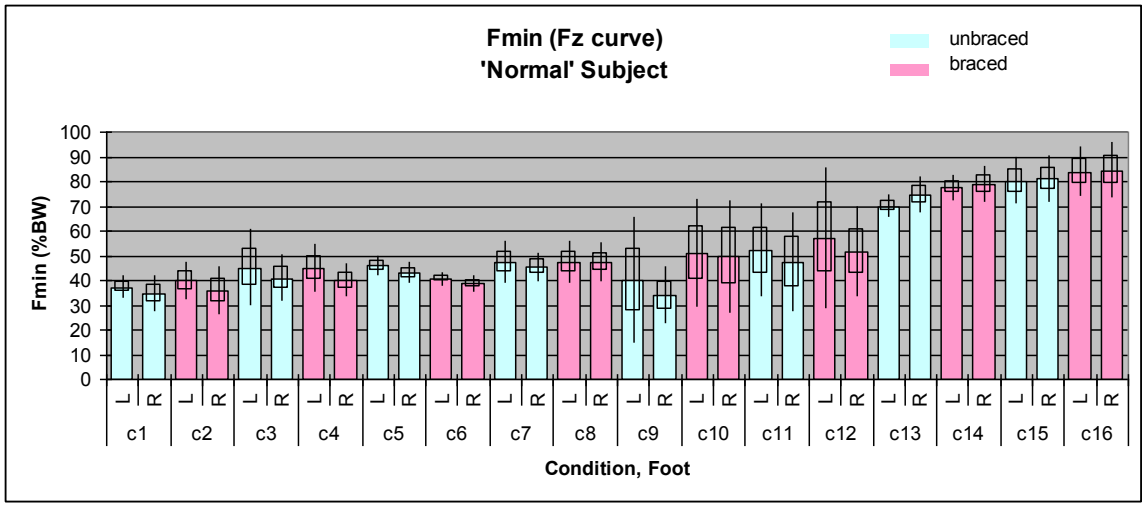
Fmin (Fz curve)
'Normal' Subject
unbraced
braced
Fmin (%BW)
100
90
80
70
60
50
40
30
20
10
0
L
R
c1
c2
c3
c4
c5
c6
c7
c8
c9
c10
c11
c12
c13
c14
c15
c16
Condition, Foot

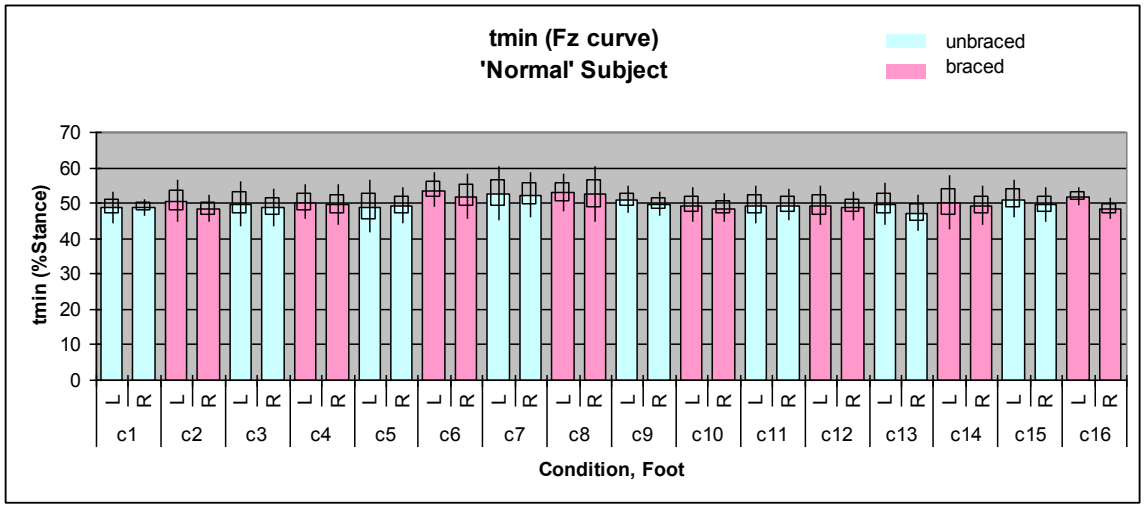
tmin (Fz curve)
'Normal' Subject
unbraced
braced
tmin (%Stance)
70
60
50
40
30
20
10
0
L
R
c1
c2
c3
c4
c5
c6
c7
c8
c9
c10
c11
c12
c13
c14
c15
c16
Condition, Foot

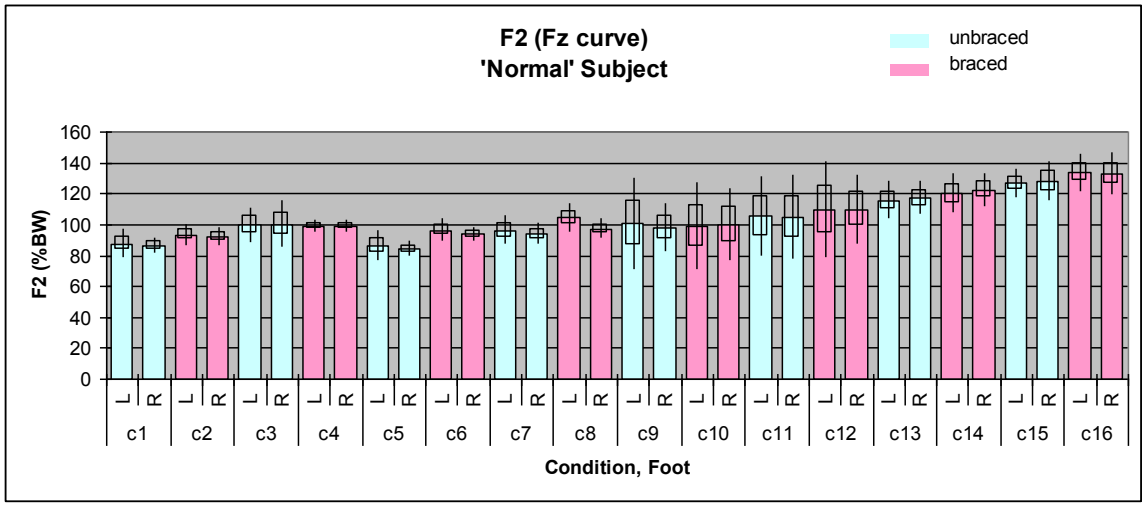
F2 (Fz curve)
'Normal' Subject
unbraced
braced
F2 (%BW)
160
140
120
100
80
60
40
20
0
L
R
c1
c2
c3
c4
c5
c6
c7
c8
c9
c10
c11
c12
c13
c14
c15
c16
Condition, Foot

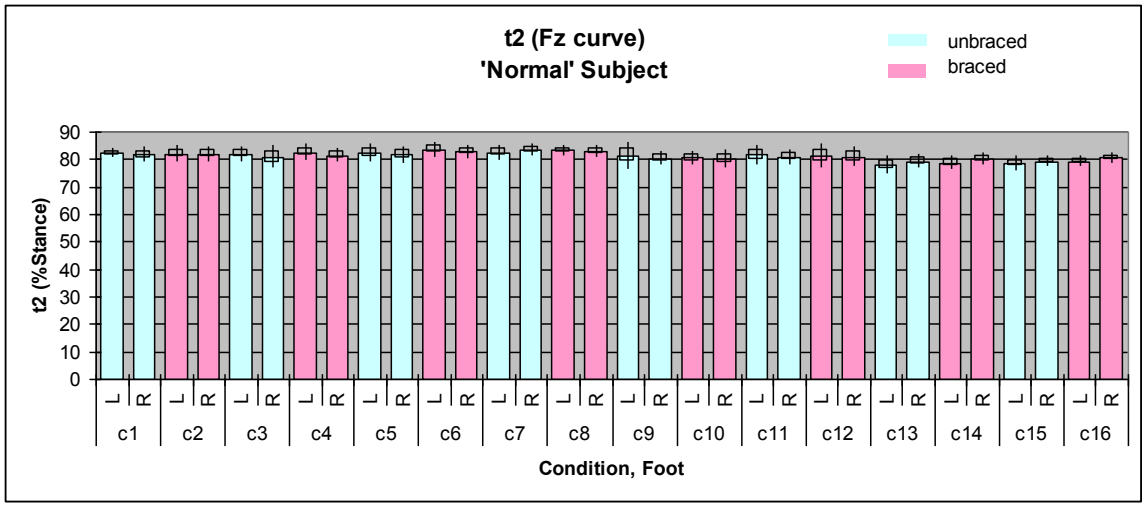
t2 (Fz curve)
'Normal' Subject
unbraced
braced
t2 (%Stance)
90
80
70
60
50
40
30
20
10
0
L
R
c1
c2
c3
c4
c5
c6
c7
c8
c9
c10
c11
c12
c13
c14
c15
c16
Condition, Foot

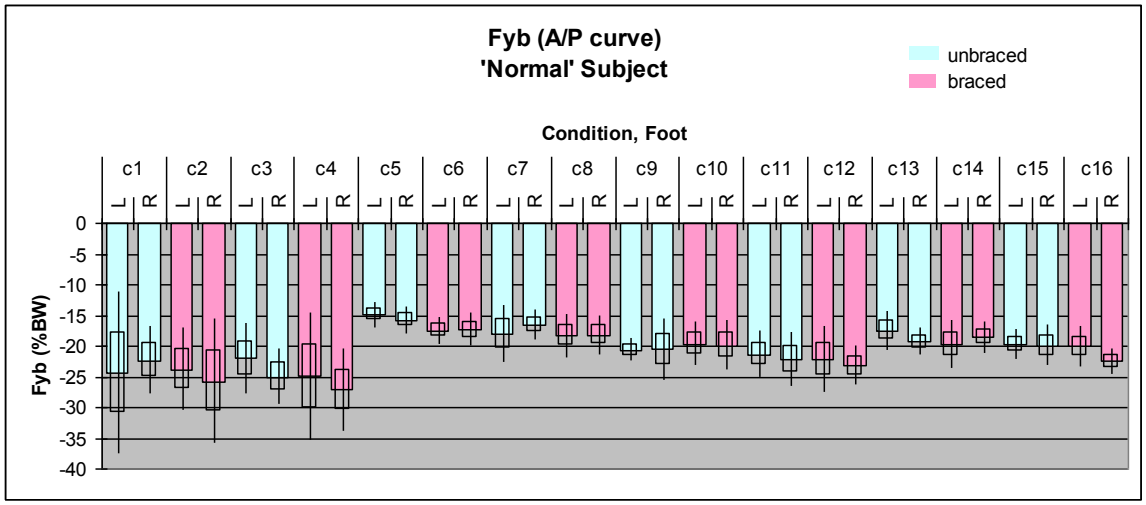
Fyb (A/P curve)
'Normal' Subject
unbraced
braced
Condition, Foot
Fyb (%BW)
0
-5
-10
-15
-20
-25
-30
-35
-40

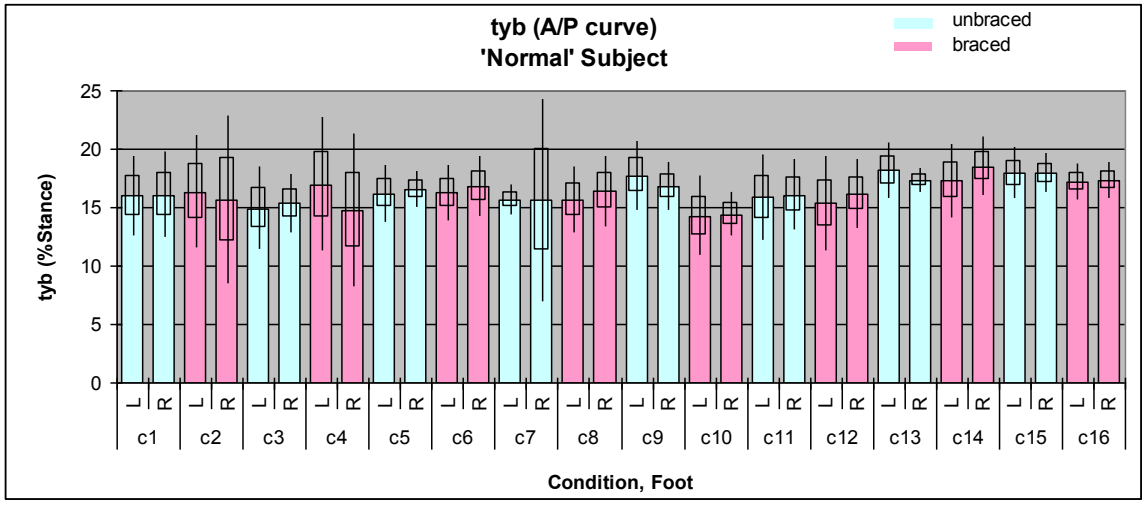
tyb (A/P curve)
'Normal' Subject
unbraced
braced
tyb (%Stance)
25
20
15
10
5
0
Condition, Foot

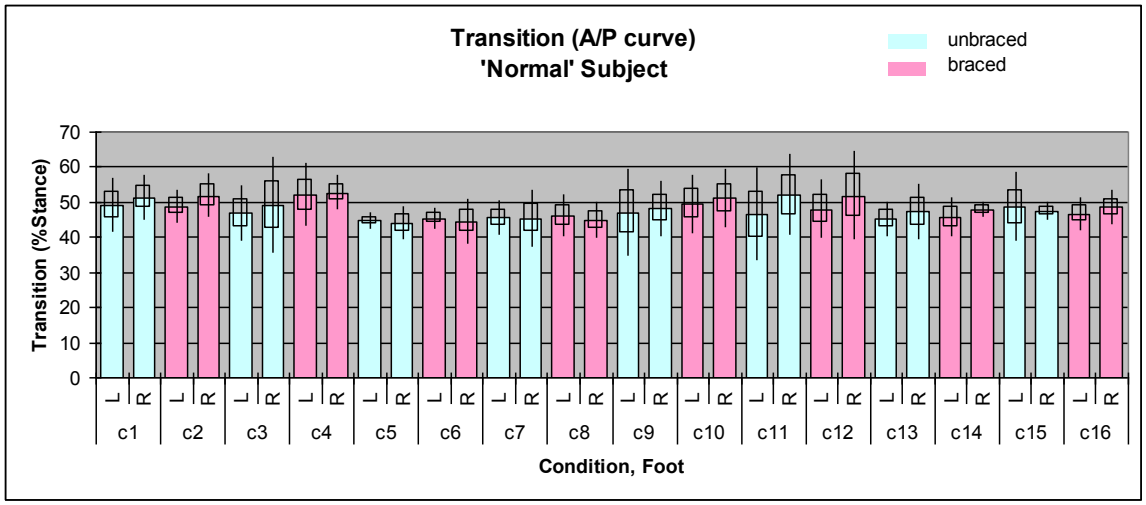
Transition (A/P curve)
'Normal' Subject
unbraced
braced
Transition (%Stance)
70
60
50
40
30
20
10
0
L R
c1 c2 c3 c4 c5 c6 c7 c8 c9 c10 c11 c12 c13 c14 c15 c16
Condition, Foot

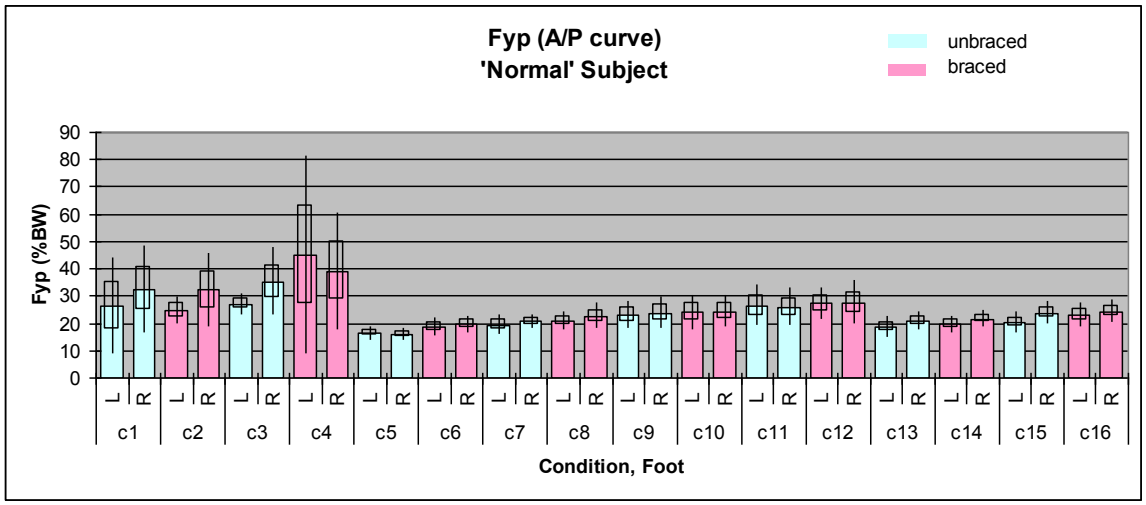
Fyp (A/P curve)
'Normal' Subject
unbraced
braced
Fyp (%BW)
90
80
70
60
50
40
30
20
10
0
L R
c1 c2 c3 c4 c5 c6 c7 c8 c9 c10 c11 c12 c13 c14 c15 c16
Condition, Foot

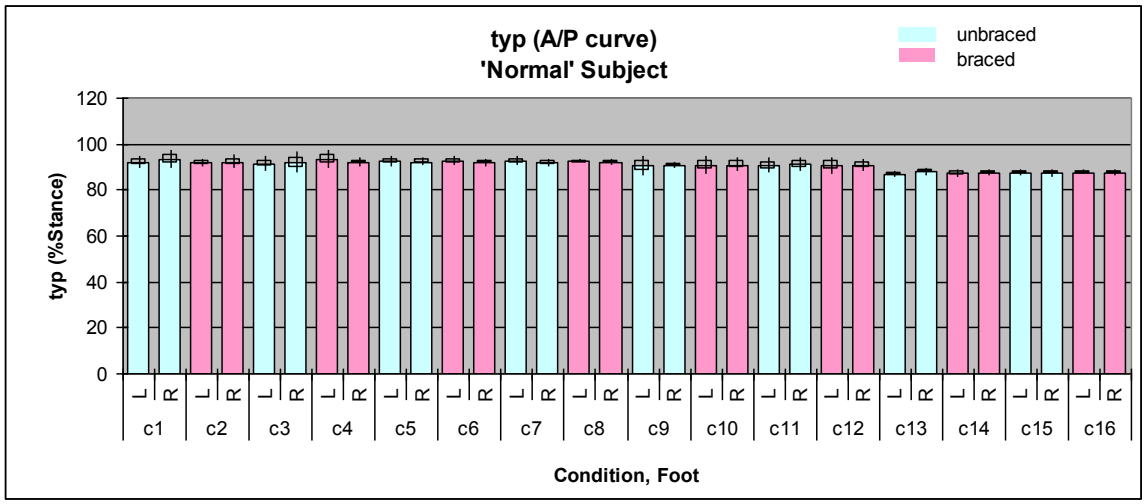
typ (A/P curve)
'Normal' Subject
unbraced
braced
typ (%Stance)
120
100
80
60
40
20
0
L R
c1 c2 c3 c4 c5 c6 c7 c8 c9 c10 c11 c12 c13 c14 c15 c16
Condition, Foot

APPENDIX D

BRACE GEOMETRY

CMT1, Left (Brace 7)

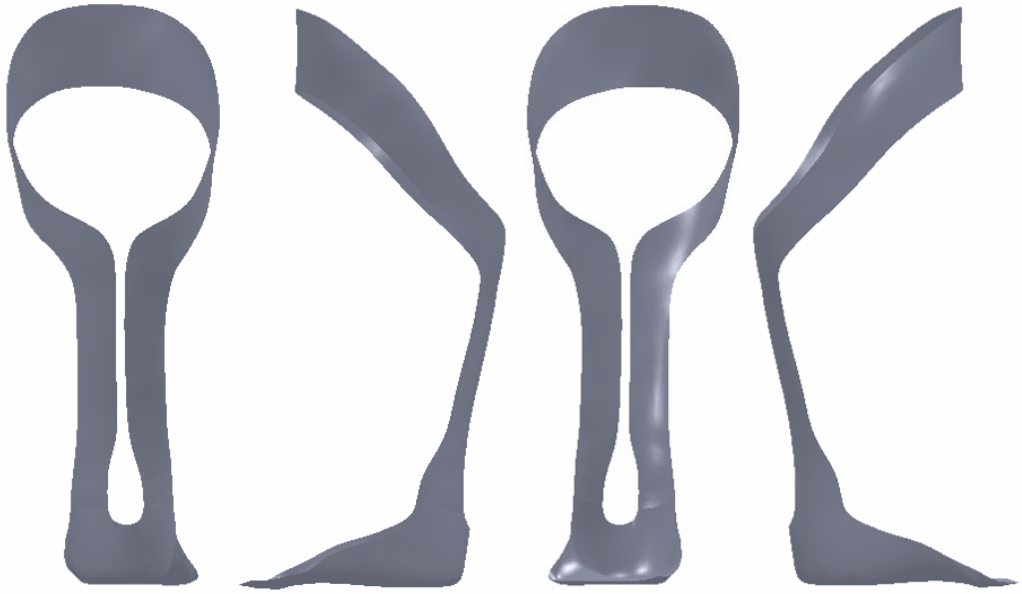

CMT1, Right (Brace 8)

CMT2, Left (Brace 5)

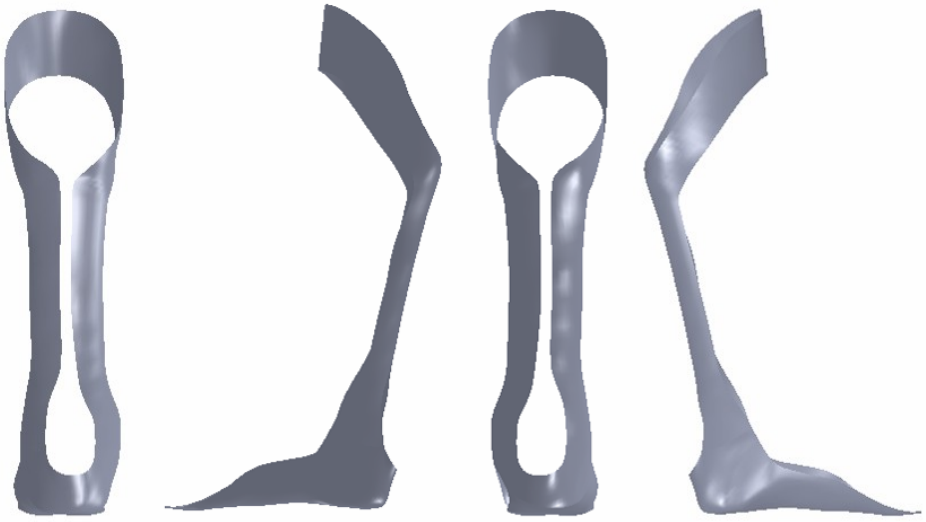

CMT2, Right (Brace 6)

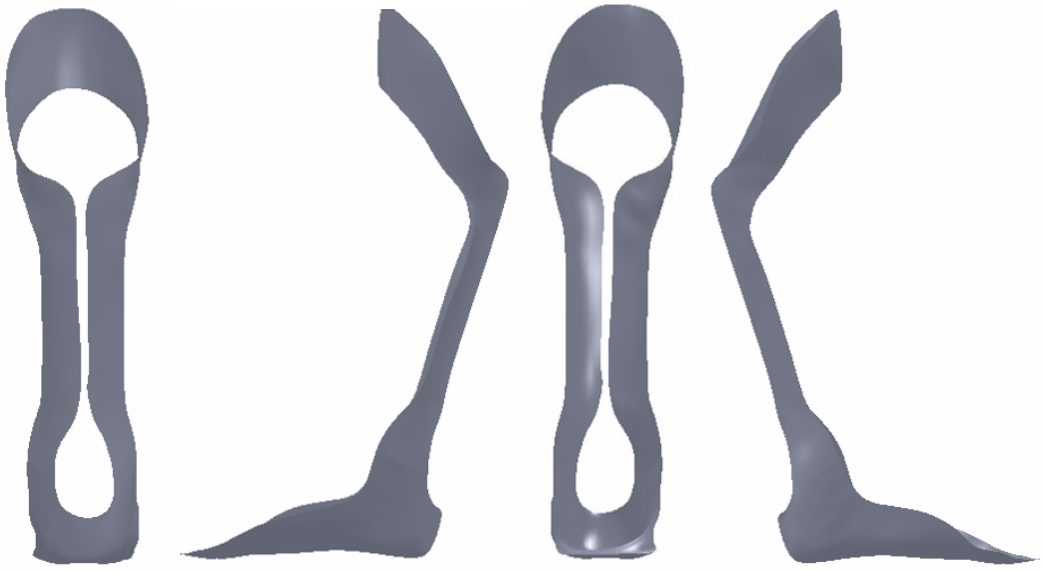

CMT4, Left (Brace 3)

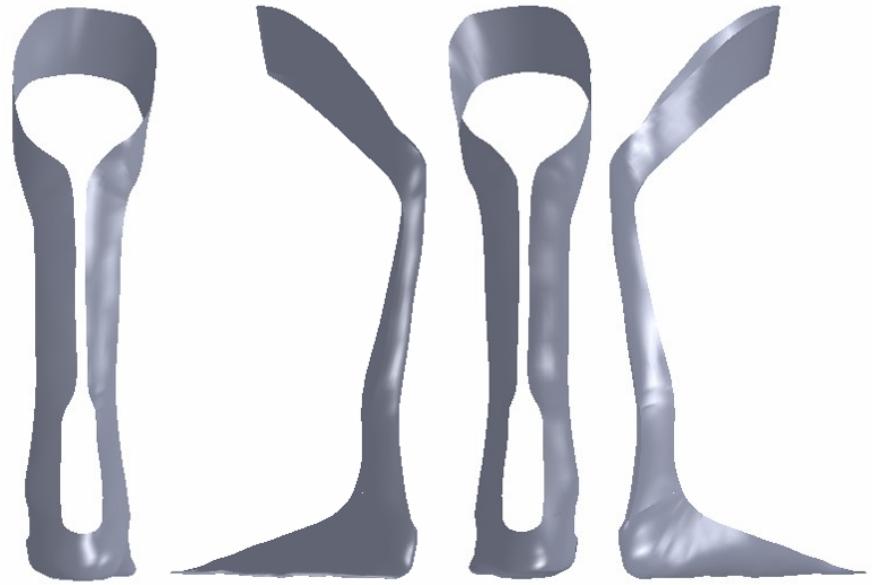

CMT4, Right (Brace 4)

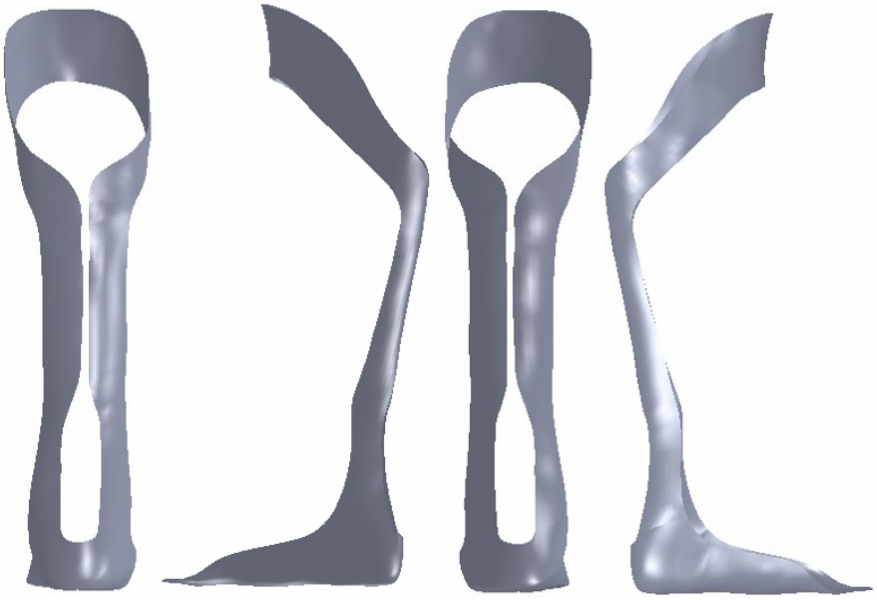

‘Normal’ Subject, Left (Brace 1)

‘Normal’ Subject, Right (Brace 2)

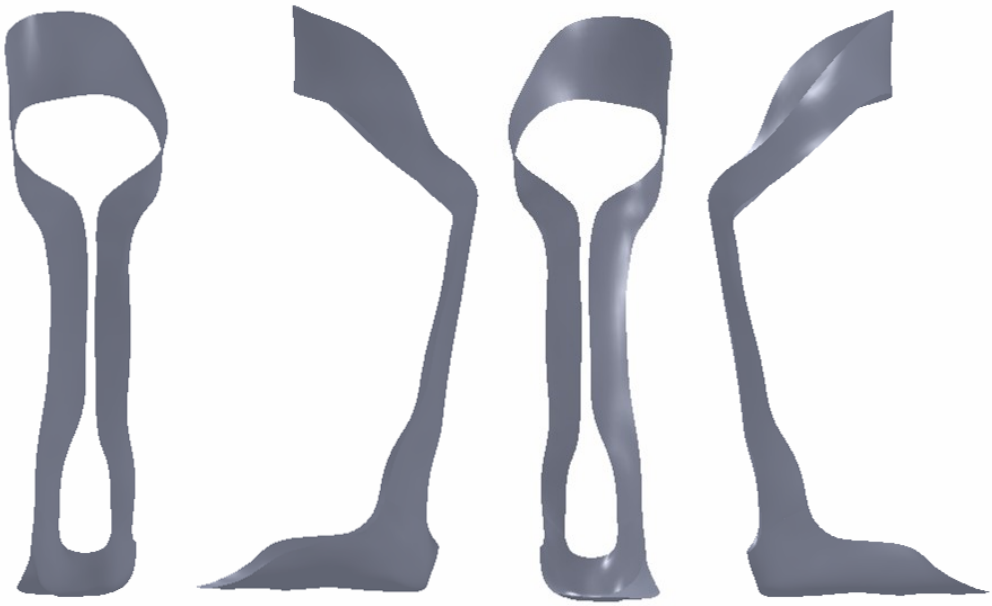

APPENDIX E

HUMAN MOTION STRAIN DATA PEAKS AND TEMPORAL PARAMETERS

All Instrumented Subjects (Condition 13)

Shown in this section are graphs of the average gage strain data during human motion for the peaks and temporal parameters for all instrumented subjects. Condition 13 is post-test braced with the HELIOS.

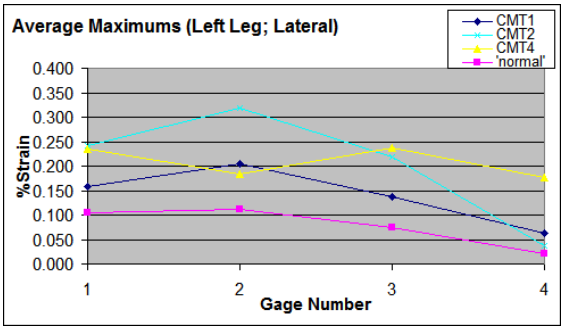

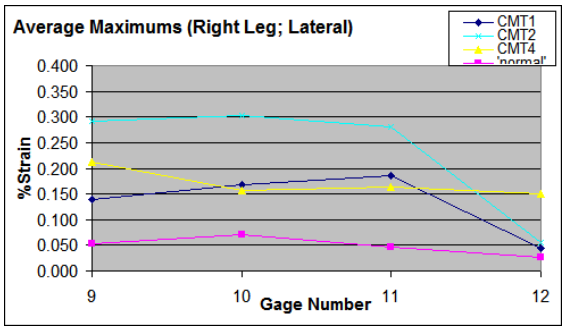

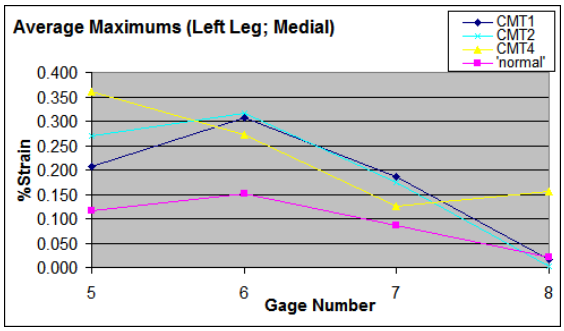

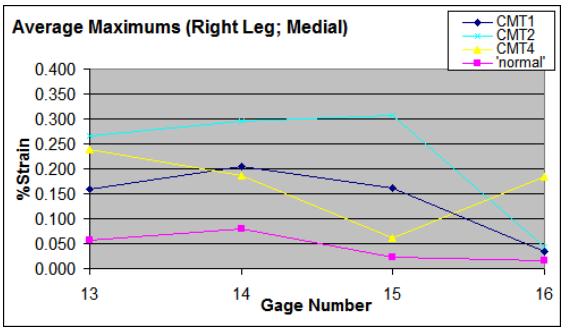

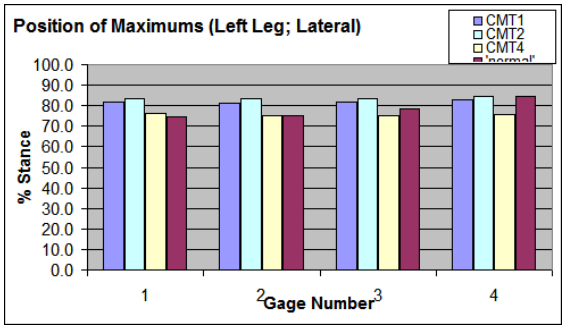
Position of Maximums (Left Leg; Lateral)
CMT1
CMT2
CMT4
'normal'
% Stance
100.0
90.0
80.0
70.0
60.0
50.0
40.0
30.0
20.0
10.0
0.0
1
2
3
4
Gage Number

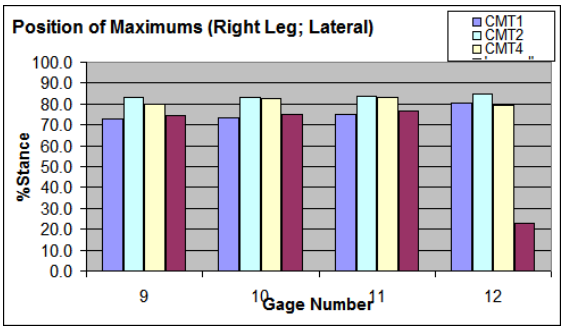
Position of Maximums (Right Leg; Lateral)
CMT1
CMT2
CMT4
%Stance
100.0
90.0
80.0
70.0
60.0
50.0
40.0
30.0
20.0
10.0
0.0
9
10
11
12
Gage Number

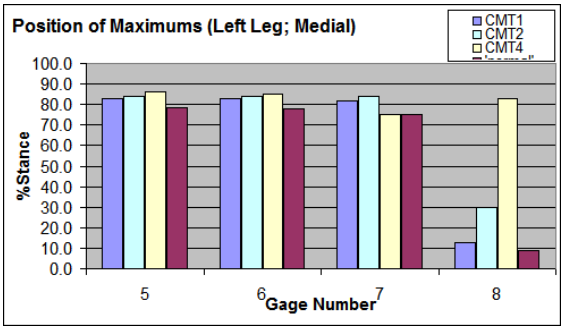
Position of Maximums (Left Leg; Medial)
CMT1
CMT2
CMT4
'normal'
%Stance
100.0
90.0
80.0
70.0
60.0
50.0
40.0
30.0
20.0
10.0
0.0
5
6
7
8
Gage Number

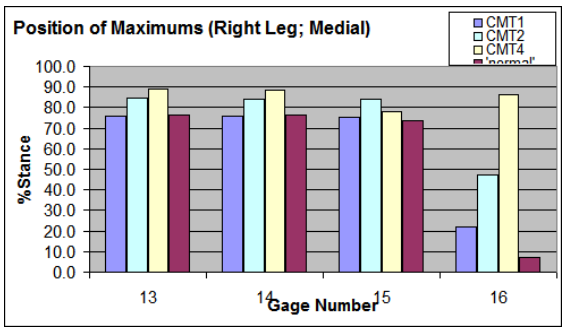
Position of Maximums (Right Leg; Medial)
CMT1
CMT2
CMT4
'normal'
%Stance
100.0
90.0
80.0
70.0
60.0
50.0
40.0
30.0
20.0
10.0
0.0
13
14
15
16
Gage Number

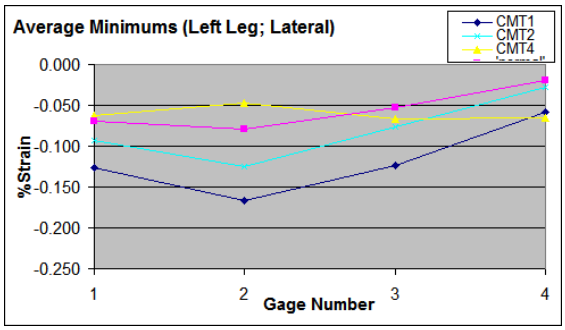
Average Minimums (Left Leg; Lateral)
CMT1
CMT2
CMT4
'normal'
%Strain
0.000
-0.050
-0.100
-0.150
-0.200
-0.250
1
2
3
4
Gage Number

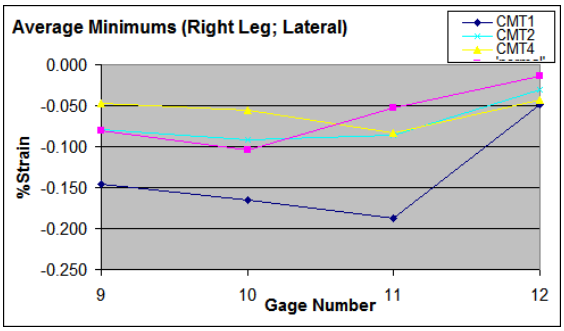
Average Minimums (Right Leg; Lateral)
CMT1
CMT2
CMT4
'normal'
%Strain
0.000
-0.050
-0.100
-0.150
-0.200
-0.250
9
10
11
12
Gage Number

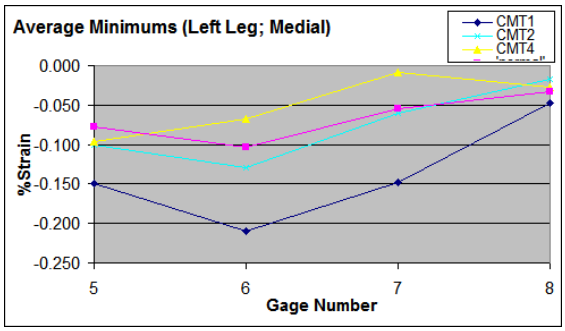
Average Minimums (Left Leg; Medial)
CMT1
CMT2
CMT4
'normal'
%Strain
0.000
-0.050
-0.100
-0.150
-0.200
-0.250
5
6
7
8
Gage Number

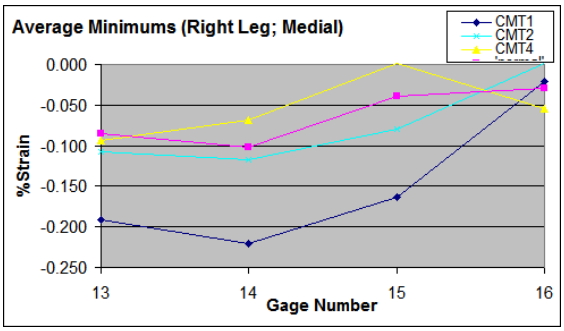
Average Minimums (Right Leg; Medial)
CMT1
CMT2
CMT4
'normal'
%Strain
0.000
-0.050
-0.100
-0.150
-0.200
-0.250
13
14
15
16
Gage Number

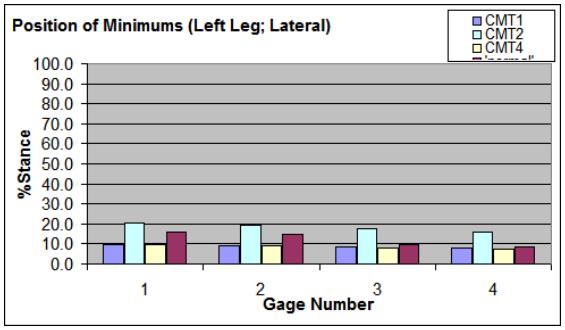
Position of Minimums (Left Leg; Lateral)
CMT1
CMT2
CMT4
%Stance
100.0
90.0
80.0
70.0
60.0
50.0
40.0
30.0
20.0
10.0
0.0
1
2
3
4
Gage Number

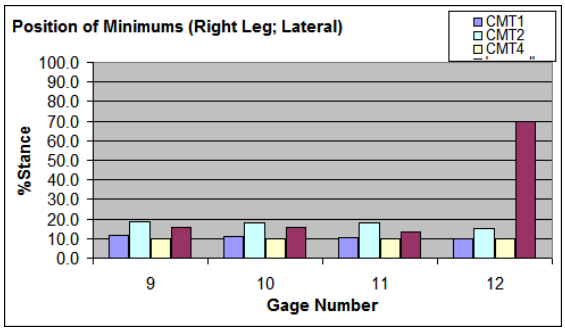
Position of Minimums (Right Leg; Lateral)
CMT1
CMT2
CMT4
%Stance
100.0
90.0
80.0
70.0
60.0
50.0
40.0
30.0
20.0
10.0
0.0
9
10
11
12
Gage Number

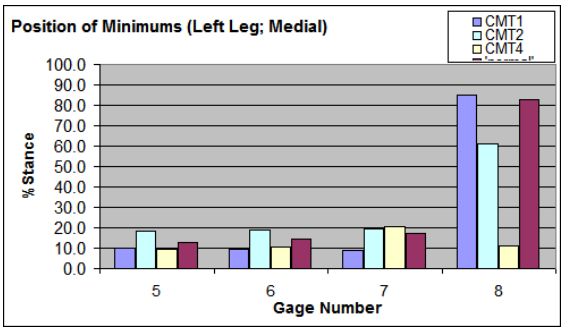
Position of Minimums (Left Leg; Medial)
CMT1
CMT2
CMT4
% Stance
100.0
90.0
80.0
70.0
60.0
50.0
40.0
30.0
20.0
10.0
0.0
5
6
7
8
Gage Number

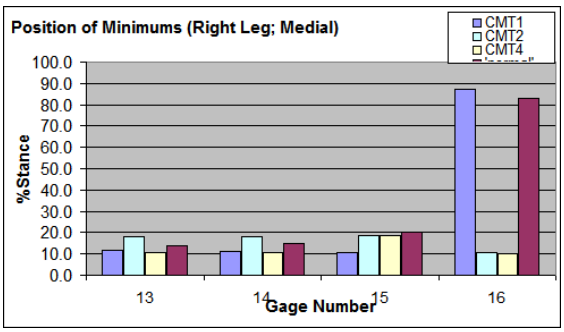
Position of Minimums (Right Leg; Medial)
CMT1
CMT2
CMT4
%Stance
100.0
90.0
80.0
70.0
60.0
50.0
40.0
30.0
20.0
10.0
0.0
13
14
15
16
Gage Number

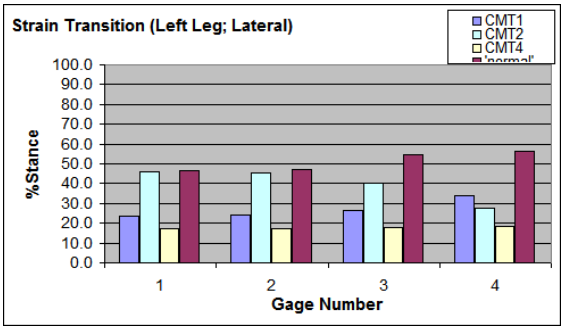
Strain Transition (Left Leg; Lateral)
CMT1
CMT2
CMT4
%Stance
100.0
90.0
80.0
70.0
60.0
50.0
40.0
30.0
20.0
10.0
0.0
1
2
3
4
Gage Number

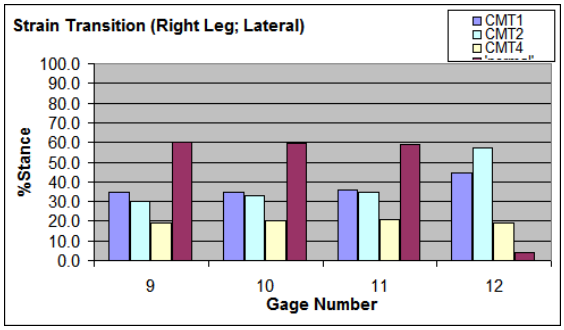
Strain Transition (Right Leg; Lateral)
CMT1
CMT2
CMT4
%Stance
100.0
90.0
80.0
70.0
60.0
50.0
40.0
30.0
20.0
10.0
0.0
9
10
11
12
Gage Number

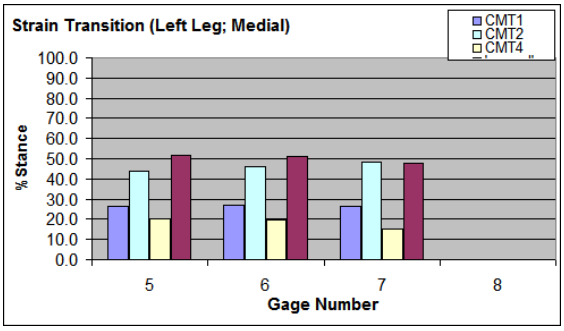
Strain Transition (Left Leg; Medial)
CMT1
CMT2
CMT4
% Stance
100.0
90.0
80.0
70.0
60.0
50.0
40.0
30.0
20.0
10.0
0.0
5
6
7
8
Gage Number

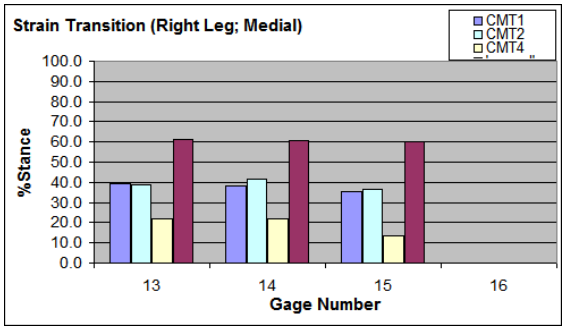
Strain Transition (Right Leg; Medial)
CMT1
CMT2
CMT4
%Stance
100.0
90.0
80.0
70.0
60.0
50.0
40.0
30.0
20.0
10.0
0.0
13
14
15
16
Gage Number

’normal’ Subject (Condition 13, 14, 15, and 16)

Shown in this section are graphs of the average gage strain data during human motion for the peaks and temporal parameters for the ‘normal’ subject. Conditions 13 through 16 are post-adaptation braced (HELIOS) with 0%BW, 5%BW, 10%BW, and 15%BW added.

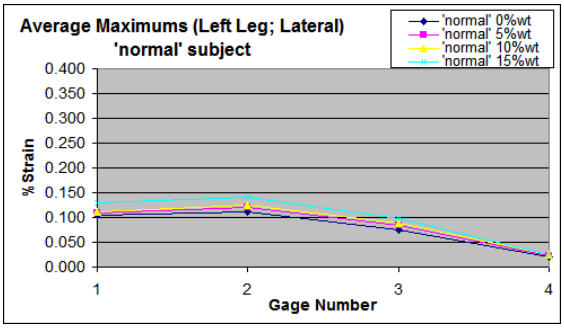

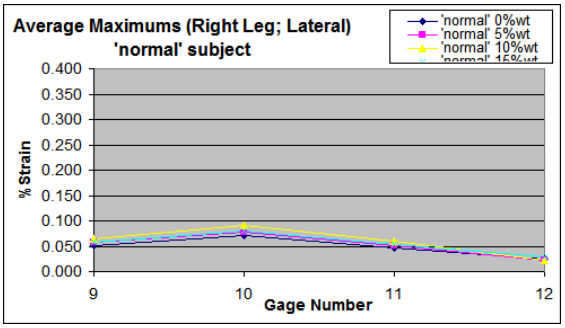

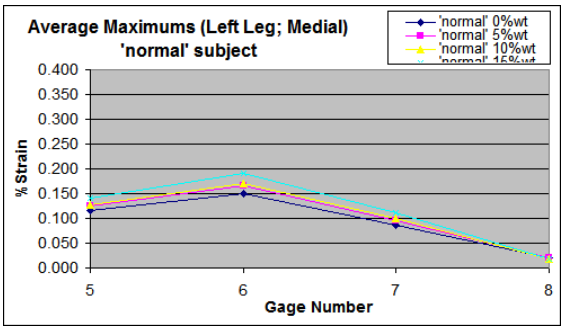

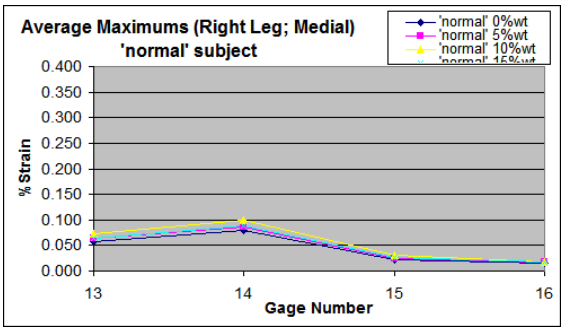

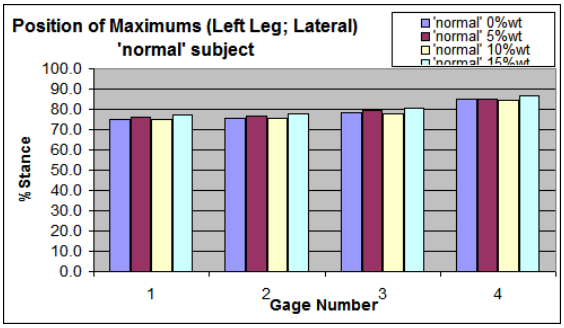
Position of Maximums (Left Leg; Lateral)
'normal' subject
'normal' 0%wt
'normal' 5%wt
'normal' 10%wt
% Stance
Gage Number

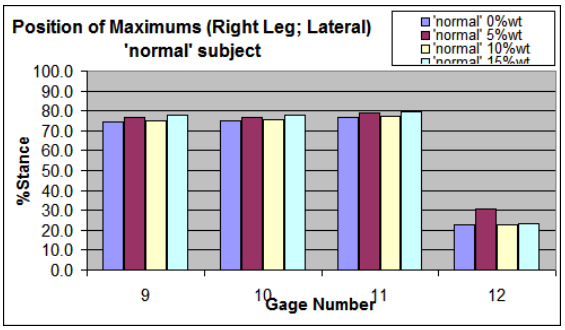
Position of Maximums (Right Leg; Lateral)
'normal' subject
'normal' 0%wt
'normal' 5%wt
'normal' 10%wt
%Stance
Gage Number

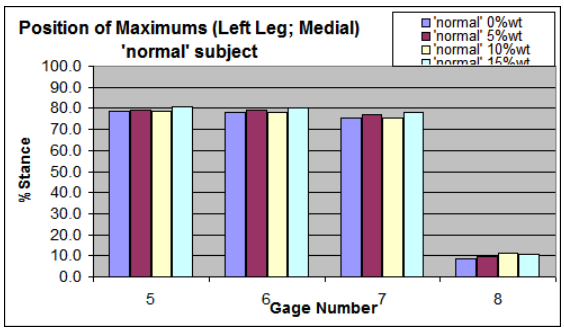
Position of Maximums (Left Leg; Medial)
'normal' subject
'normal' 0%wt
'normal' 5%wt
'normal' 10%wt
% Stance
Gage Number

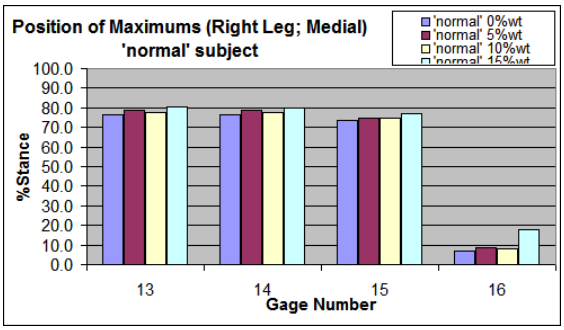
Position of Maximums (Right Leg; Medial)
'normal' subject
'normal' 0%wt
'normal' 5%wt
'normal' 10%wt
%Stance
Gage Number

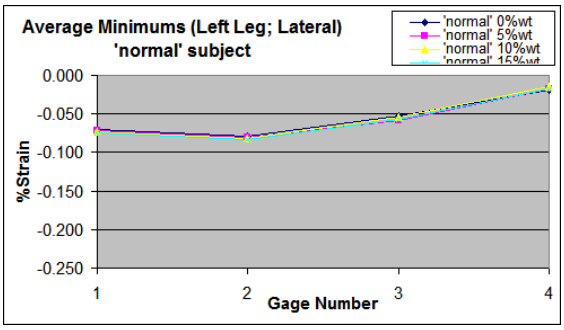
Average Minimums (Left Leg; Lateral)
'normal' subject
'normal' 0%wt
'normal' 5%wt
'normal' 10%wt
%Strain
Gage Number

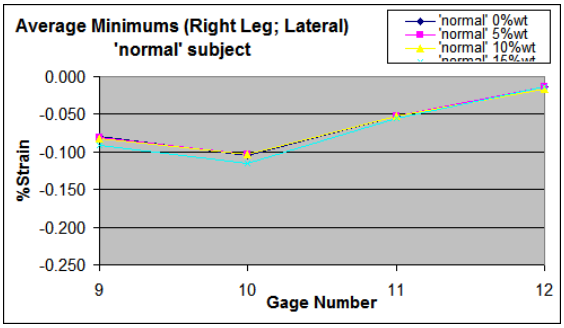
Average Minimums (Right Leg; Lateral)
'normal' subject
'normal' 0%wt
'normal' 5%wt
'normal' 10%wt
%Strain
Gage Number

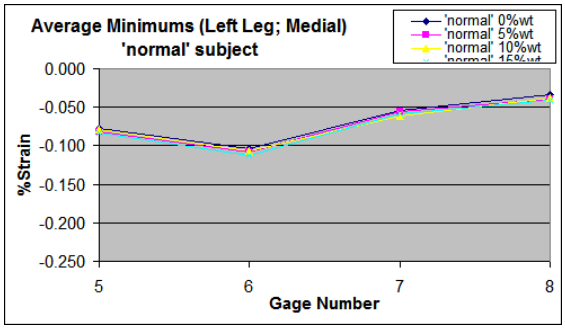
Average Minimums (Left Leg; Medial)
'normal' subject
'normal' 0%wt
'normal' 5%wt
'normal' 10%wt
%Strain
Gage Number

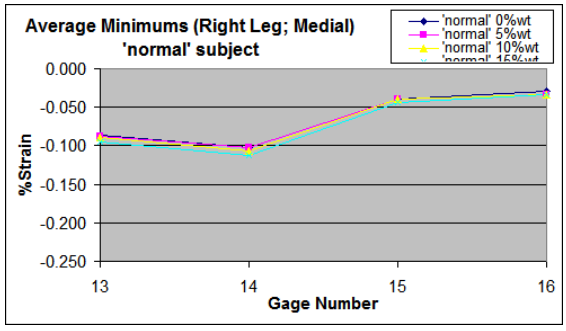
Average Minimums (Right Leg; Medial)
'normal' subject
'normal' 0%wt
'normal' 5%wt
'normal' 10%wt
%Strain
Gage Number

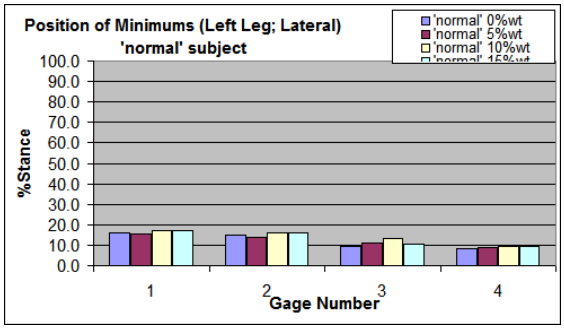
Position of Minimums (Left Leg; Lateral)
'normal' subject
'normal' 0%wt
'normal' 5%wt
'normal' 10%wt
%Stance
Gage Number

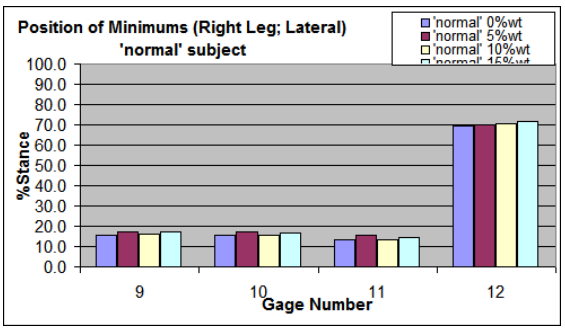
Position of Minimums (Right Leg; Lateral)
'normal' subject
'normal' 0%wt
'normal' 5%wt
'normal' 10%wt
%Stance
Gage Number

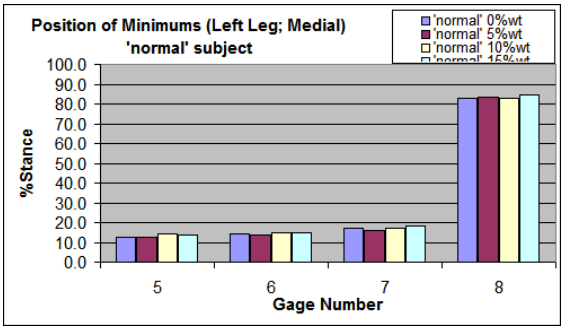
Position of Minimums (Left Leg; Medial)
'normal' subject
'normal' 0%wt
'normal' 5%wt
'normal' 10%wt
%Stance
Gage Number

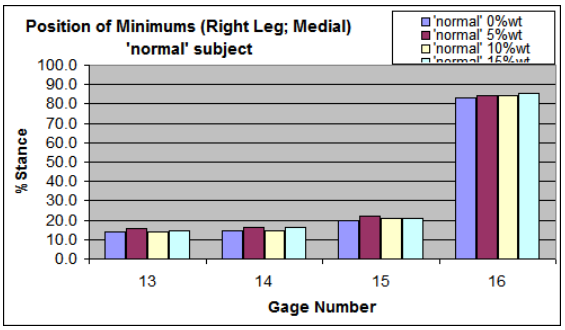
Position of Minimums (Right Leg; Medial)
'normal' subject
'normal' 0%wt
'normal' 5%wt
'normal' 10%wt
% Stance
Gage Number

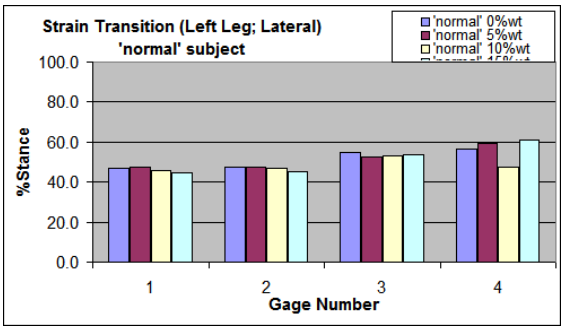
Strain Transition (Left Leg; Lateral)
'normal' subject
'normal' 0%wt
'normal' 5%wt
'normal' 10%wt
%Stance
Gage Number

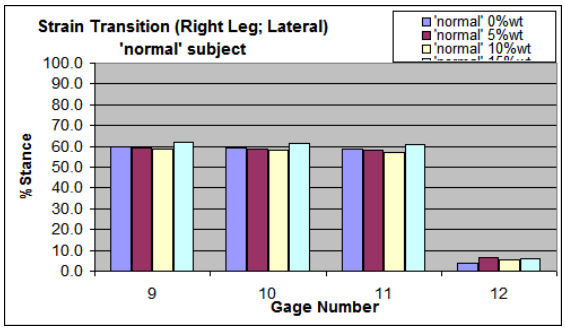
Strain Transition (Right Leg; Lateral)
'normal' subject
'normal' 0%wt
'normal' 5%wt
'normal' 10%wt
% Stance
Gage Number

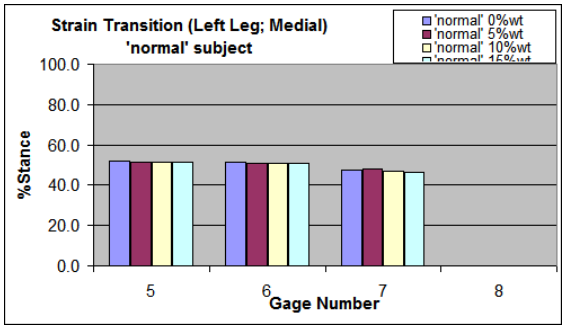
Strain Transition (Left Leg; Medial)
'normal' subject
'normal' 0%wt
'normal' 5%wt
'normal' 10%wt
%Stance
Gage Number

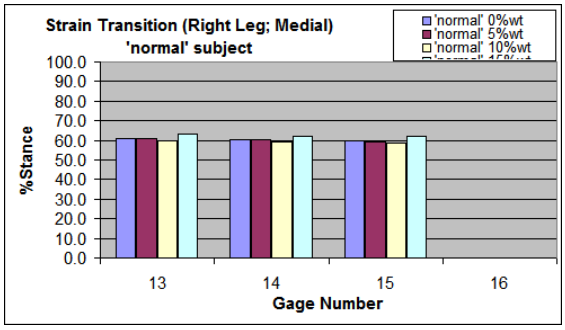
Strain Transition (Right Leg; Medial)
'normal' subject
'normal' 0%wt
'normal' 5%wt
'normal' 10%wt
%Stance
Gage Number

‘normal’ Subject (Conditions 13 through 16)

Shown in this section are graphs of the average maximum and minimum gage strain data during human motion for the ‘normal’ subject. Conditions 13 through 16 are post-adaptation braced (HELIOS) with 0%BW, 5%BW, 10%BW, and 15%BW added.

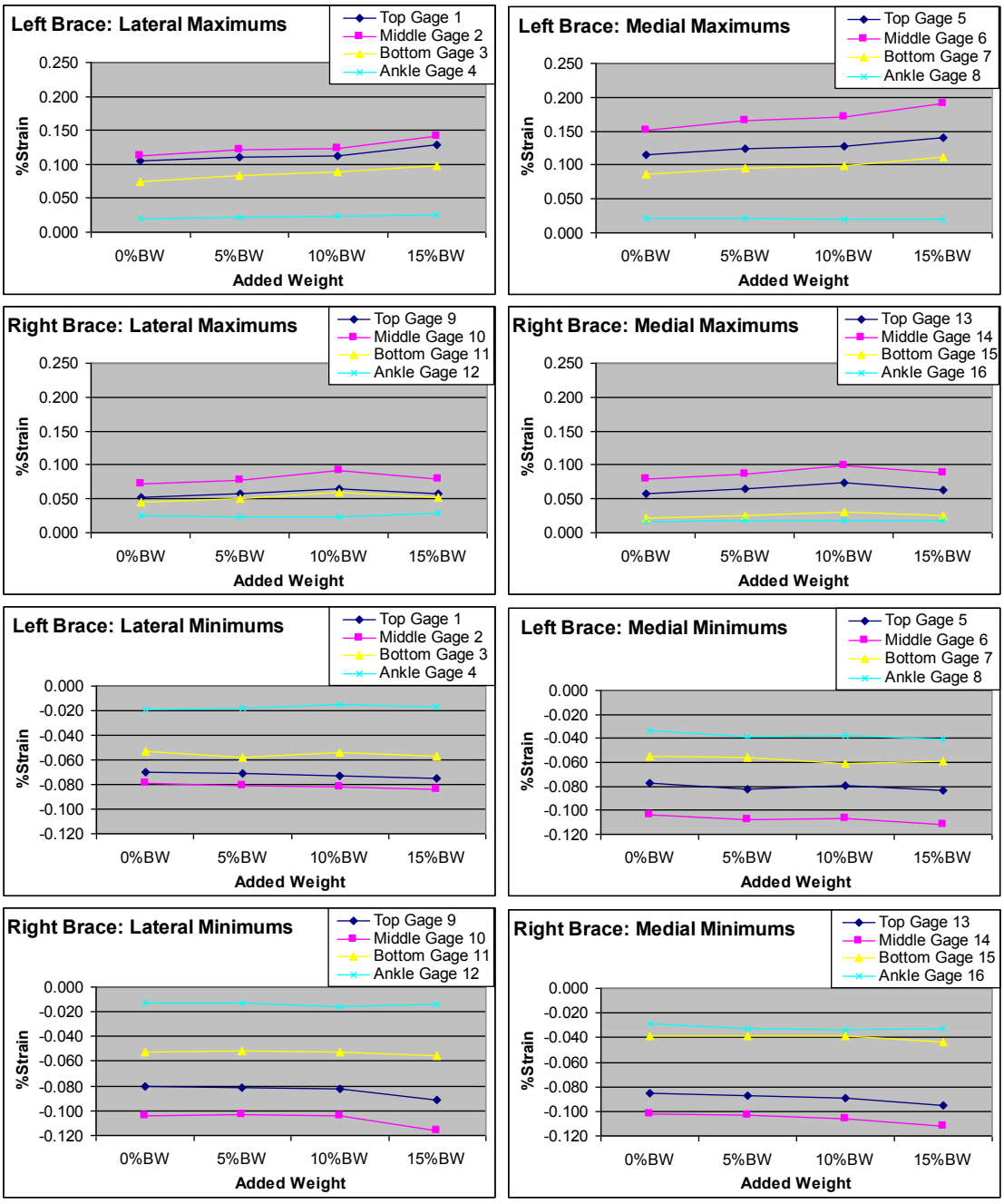

APPENDIX F

HUMAN MOTION TEMPORAL COMPARISONS

BETWEEN GRF AND STRAIN DATA

GRF Temporal Parameters- All Instrumented Subjects (Condition 13)

Shown in this section are graphs of the average GRF temporal parameters. Condition 13 is post-test braced with the HELIOS.

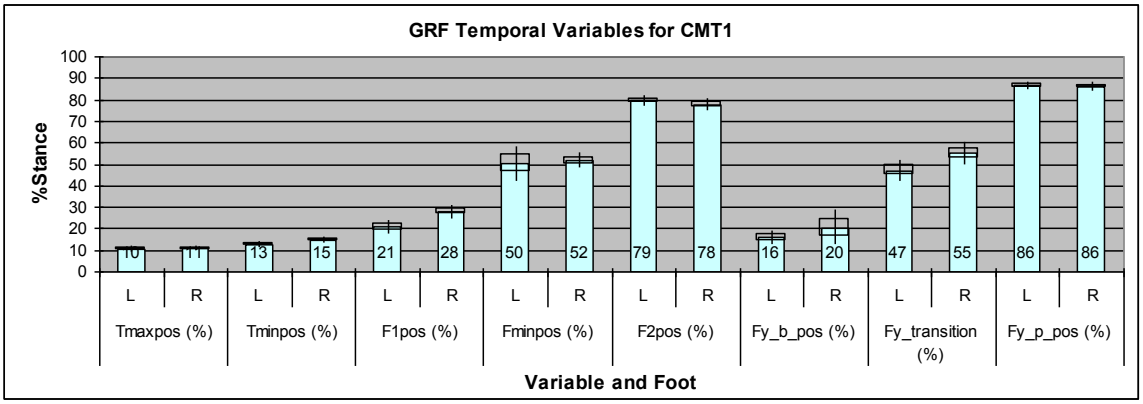

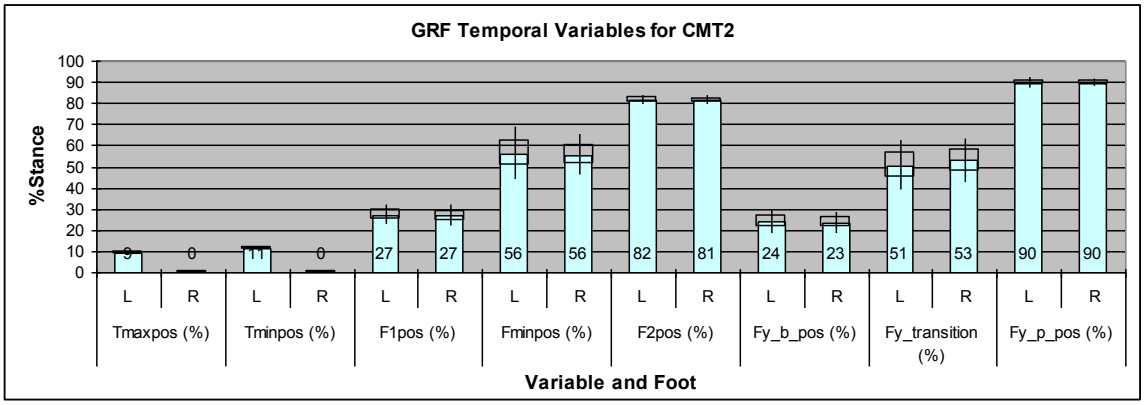

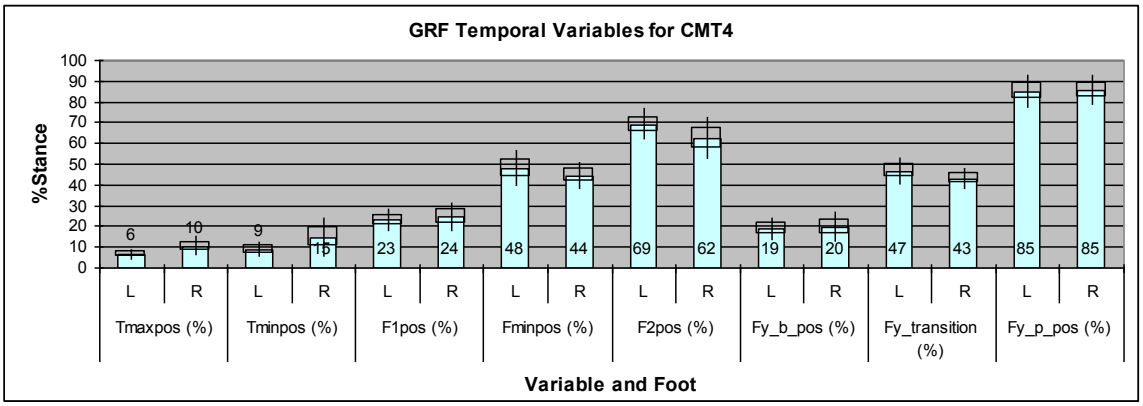

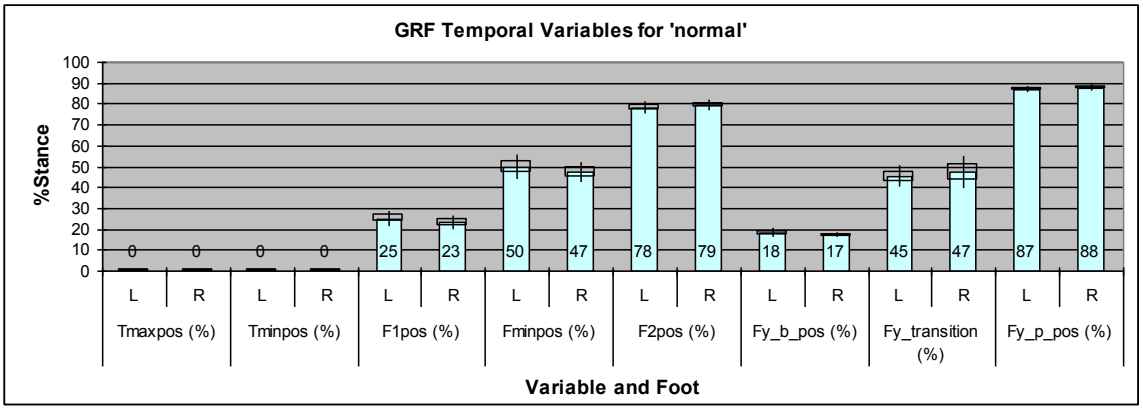

Strain Gage Temporal Parameters- All Instrumented Subjects (Condition 13)

Shown in this section are graphs of the average gage strain temporal variables for the maximums, strain transitions, and minimums. Condition 13 is post-test braced with the HELIOS.

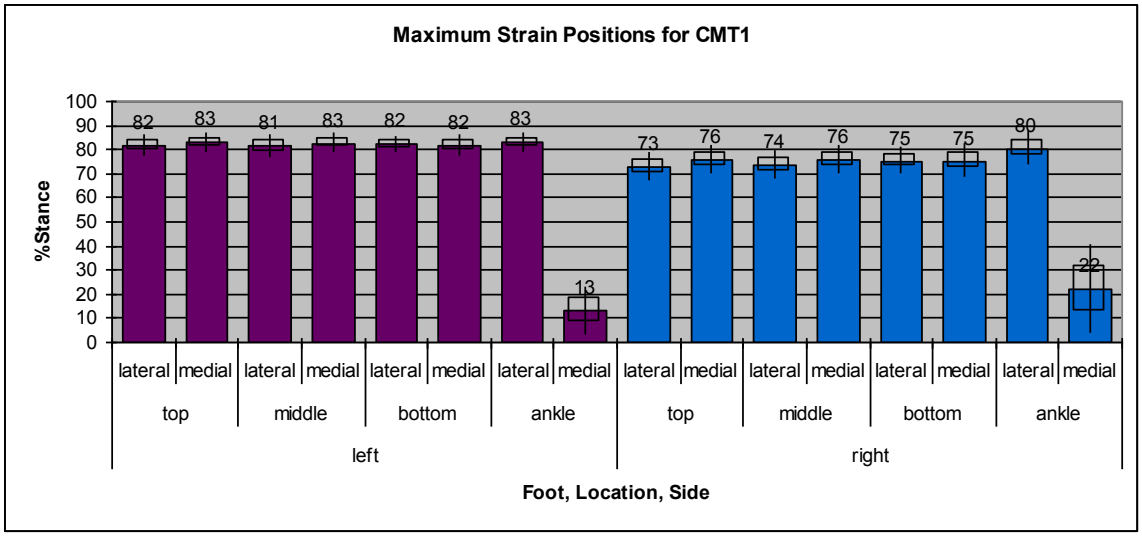
Maximum Strain Positions for CMT1
%Stance
100
90
80
70
60
50
40
30
20
10
0
82 83 81 83 82 82 83 13 73 76 74 76 75 75 80 22
lateral medial lateral medial lateral medial lateral medial lateral medial lateral medial lateral medial lateral medial
top middle bottom ankle top middle bottom ankle
left right
Foot, Location, Side

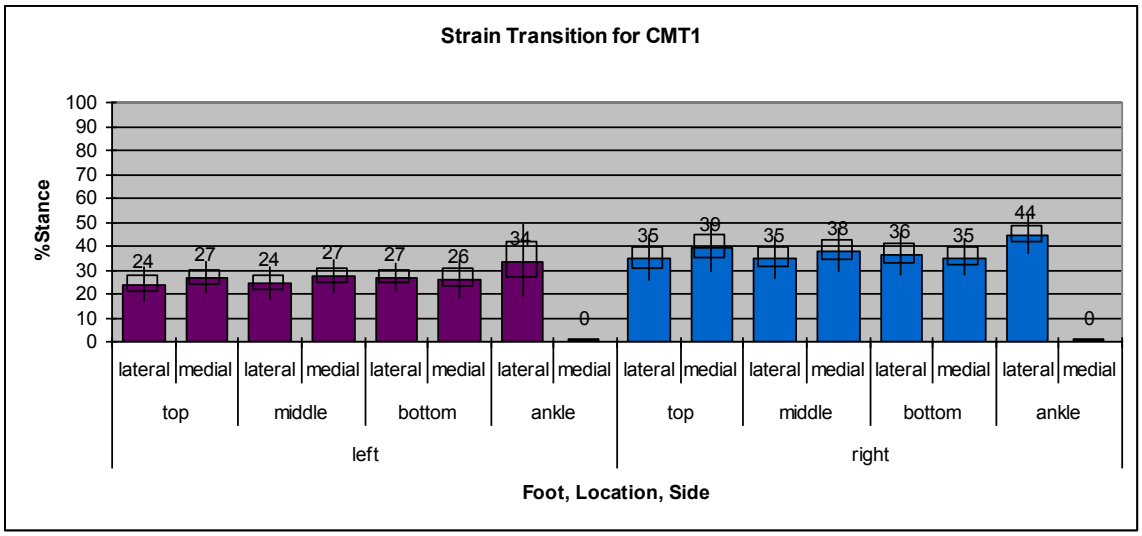
Strain Transition for CMT1
%Stance
100
90
80
70
60
50
40
30
20
10
0
24 27 24 27 27 26 34 0 35 39 35 38 36 35 44 0
lateral medial lateral medial lateral medial lateral medial lateral medial lateral medial lateral medial lateral medial
top middle bottom ankle top middle bottom ankle
left right
Foot, Location, Side

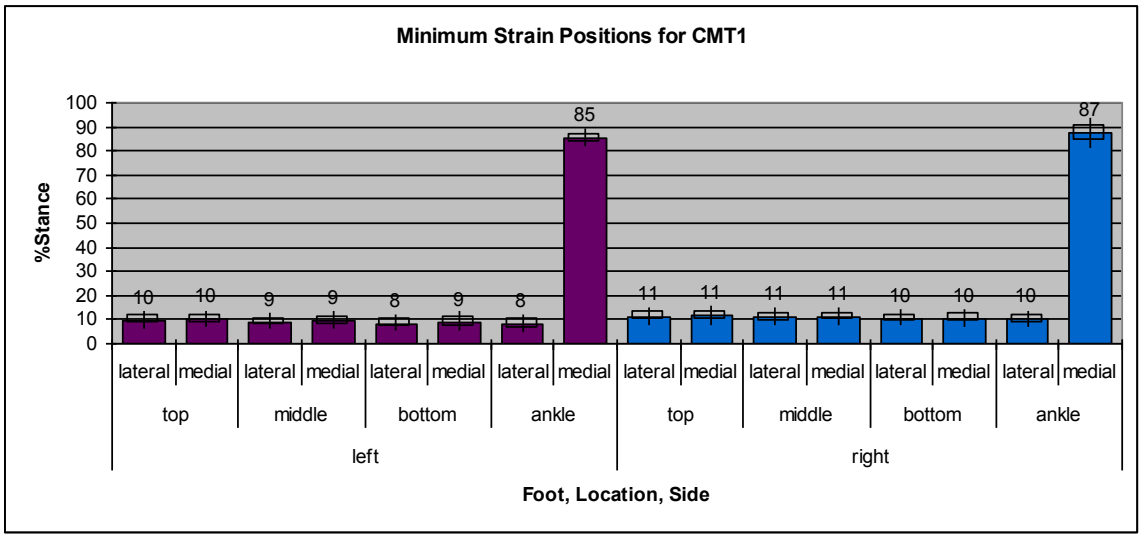
Minimum Strain Positions for CMT1
%Stance
100
90
80
70
60
50
40
30
20
10
0
10 10 9 9 8 9 8 85 11 11 11 11 10 10 10 87
lateral medial lateral medial lateral medial lateral medial lateral medial lateral medial lateral medial lateral medial
top middle bottom ankle top middle bottom ankle
left right
Foot, Location, Side

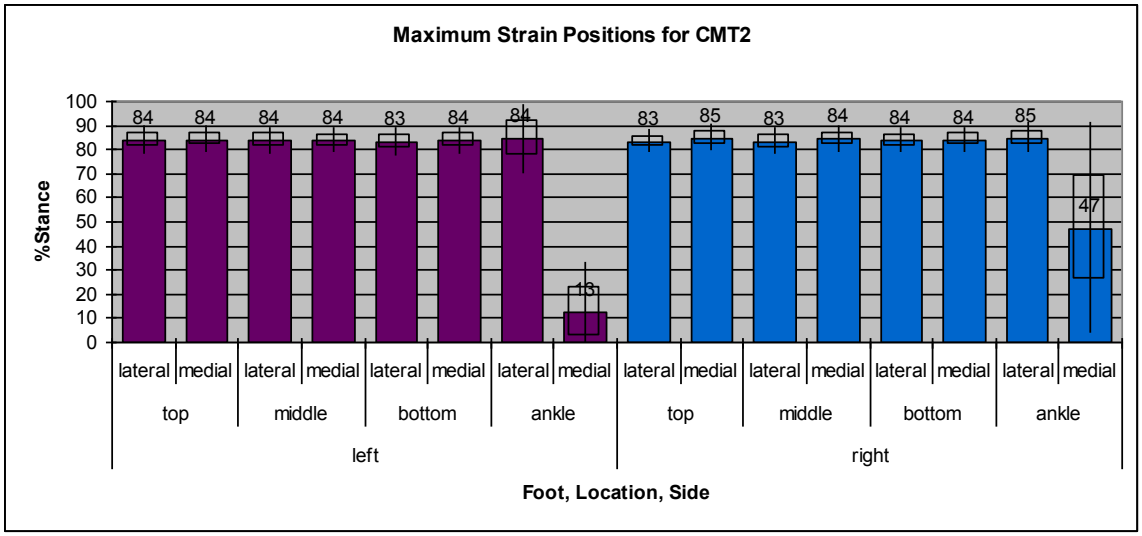
Maximum Strain Positions for CMT2
%Stance
100
90
80
70
60
50
40
30
20
10
0
84 84 84 84 83 84 84 13 83 85 83 84 84 84 85 47
lateral medial lateral medial lateral medial lateral medial lateral medial lateral medial lateral medial lateral medial
top middle bottom ankle top middle bottom ankle
left right
Foot, Location, Side

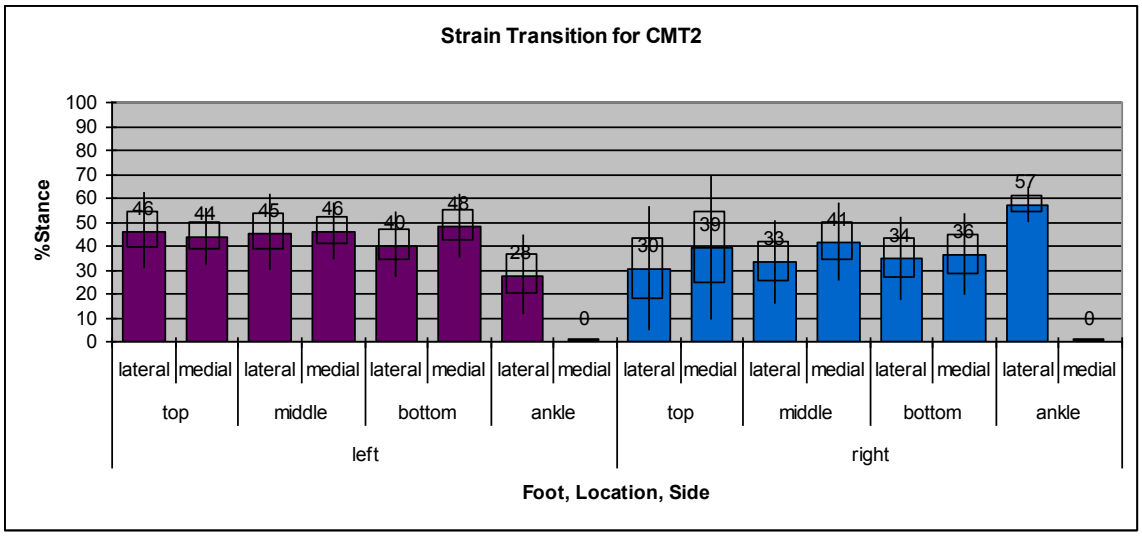
Strain Transition for CMT2
%Stance
100
90
80
70
60
50
40
30
20
10
0
46 44 45 46 40 48 28 0 30 39 33 41 34 36 57 0
lateral medial lateral medial lateral medial lateral medial lateral medial lateral medial lateral medial lateral medial
top middle bottom ankle top middle bottom ankle
left right
Foot, Location, Side

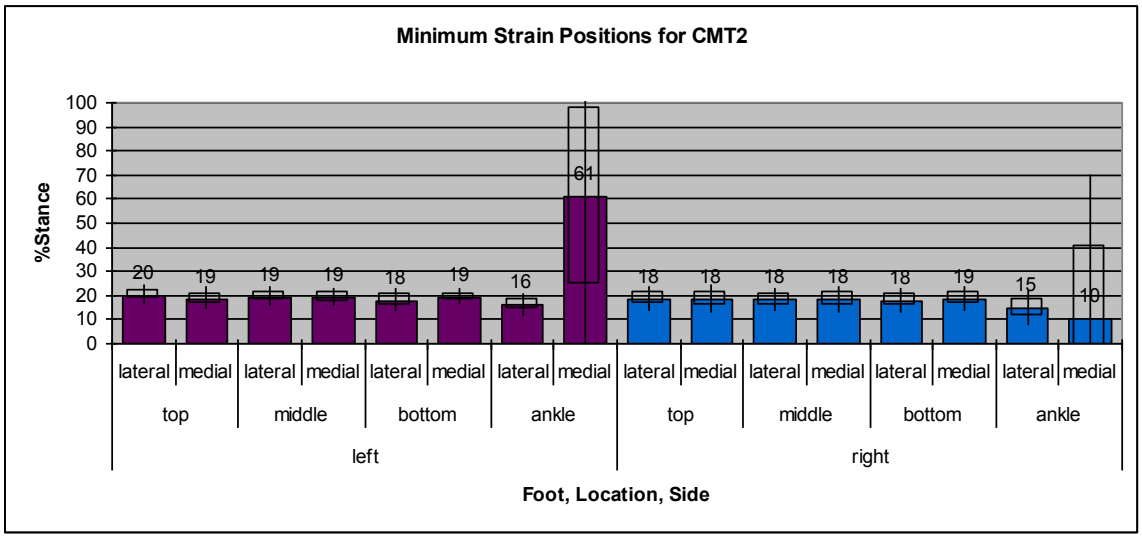
Minimum Strain Positions for CMT2
%Stance
100
90
80
70
60
50
40
30
20
10
0
20 19 19 19 18 19 16 61 18 18 18 18 18 19 15 10
lateral medial lateral medial lateral medial lateral medial lateral medial lateral medial lateral medial lateral medial
top middle bottom ankle top middle bottom ankle
left right
Foot, Location, Side

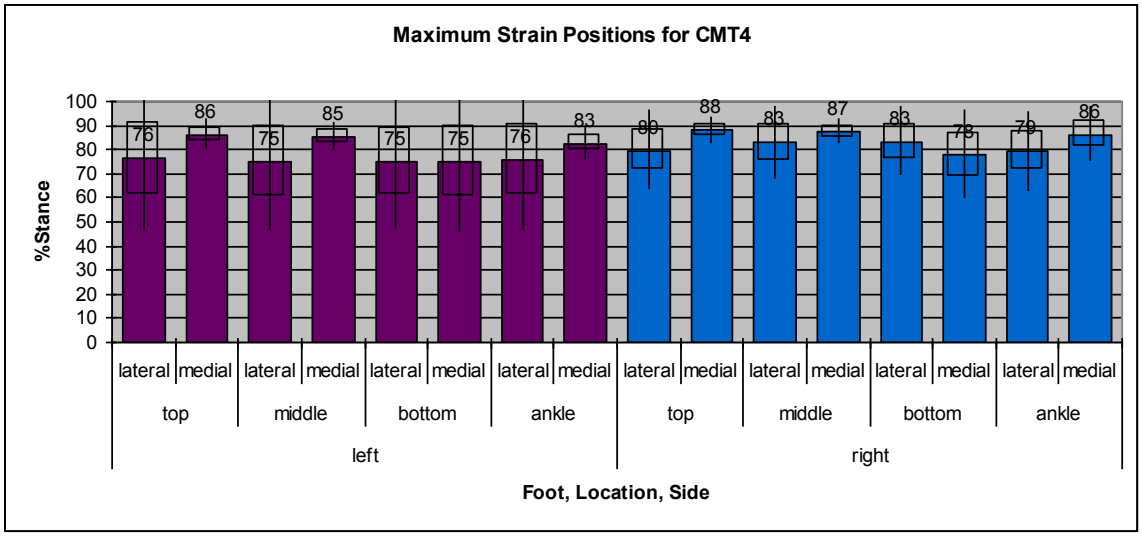
Maximum Strain Positions for CMT4
%Stance
100
90
80
70
60
50
40
30
20
10
0
76
86
75
85
75
75
76
83
80
88
83
87
83
78
79
86
lateral
medial
top
middle
bottom
ankle
left
right
Foot, Location, Side

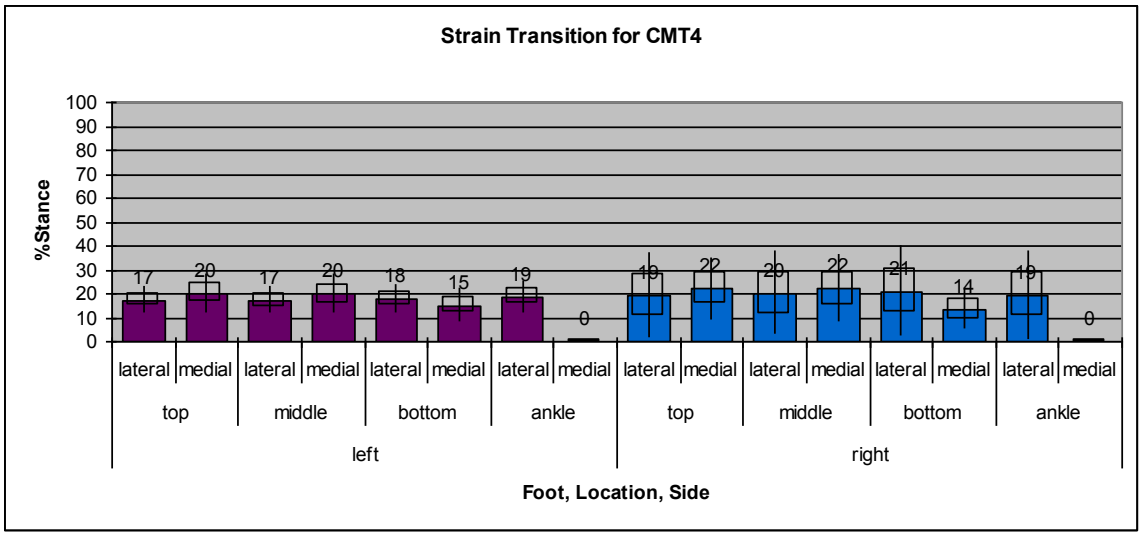
Strain Transition for CMT4
%Stance
100
90
80
70
60
50
40
30
20
10
0
17
20
17
20
18
15
19
0
19
22
20
22
21
14
19
0
lateral
medial
top
middle
bottom
ankle
left
right
Foot, Location, Side

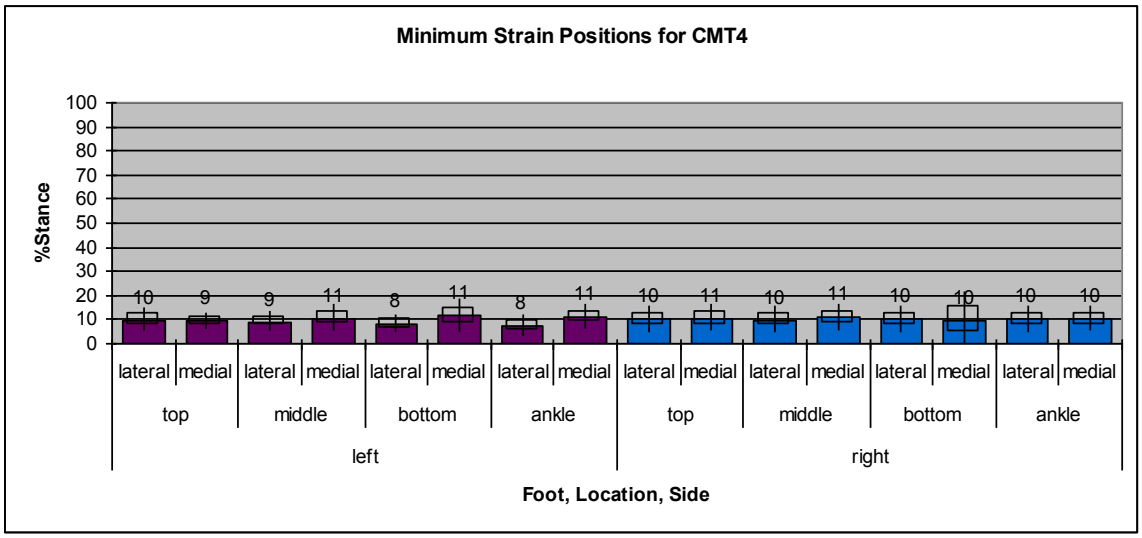
Minimum Strain Positions for CMT4
%Stance
100
90
80
70
60
50
40
30
20
10
0
10
9
9
11
8
11
8
11
10
11
10
11
10
10
10
10
lateral
medial
top
middle
bottom
ankle
left
right
Foot, Location, Side

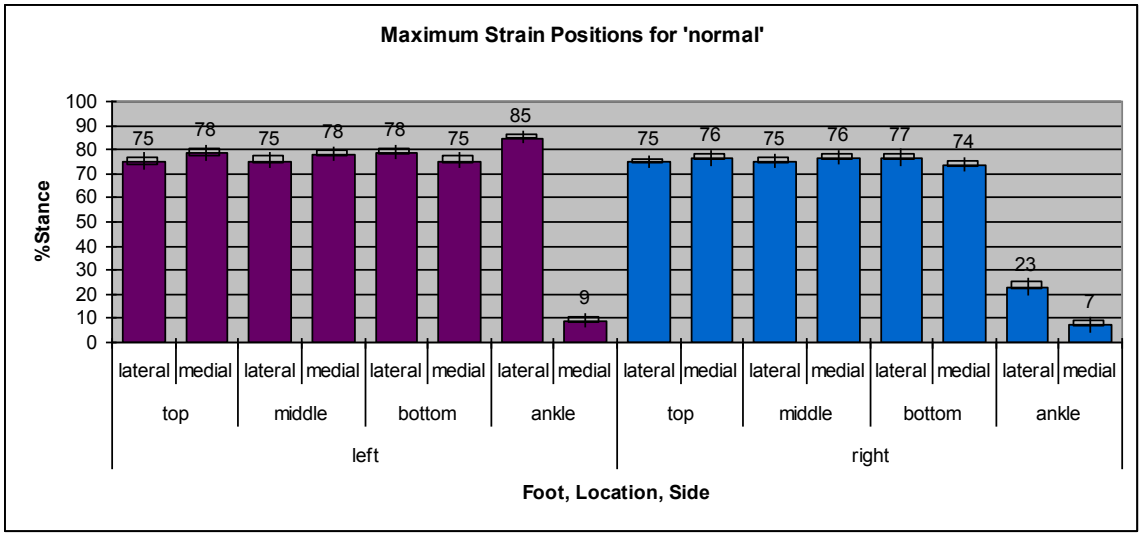
Maximum Strain Positions for 'normal'
%Stance
100
90
80
70
60
50
40
30
20
10
0
75 78 75 78 78 75 85 9 75 76 75 76 77 74 23 7
lateral medial lateral medial lateral medial lateral medial lateral medial lateral medial lateral medial lateral medial
top middle bottom ankle top middle bottom ankle
left right
Foot, Location, Side

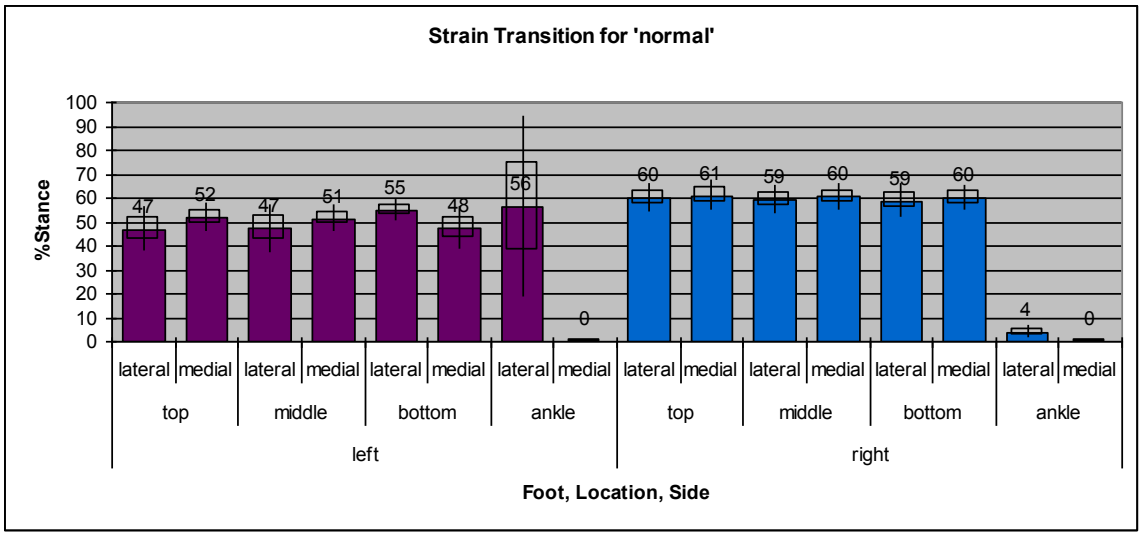
Strain Transition for 'normal'
%Stance
100
90
80
70
60
50
40
30
20
10
0
47 52 47 51 55 48 56 0 60 61 59 60 59 60 4 0
lateral medial lateral medial lateral medial lateral medial lateral medial lateral medial lateral medial lateral medial
top middle bottom ankle top middle bottom ankle
left right
Foot, Location, Side

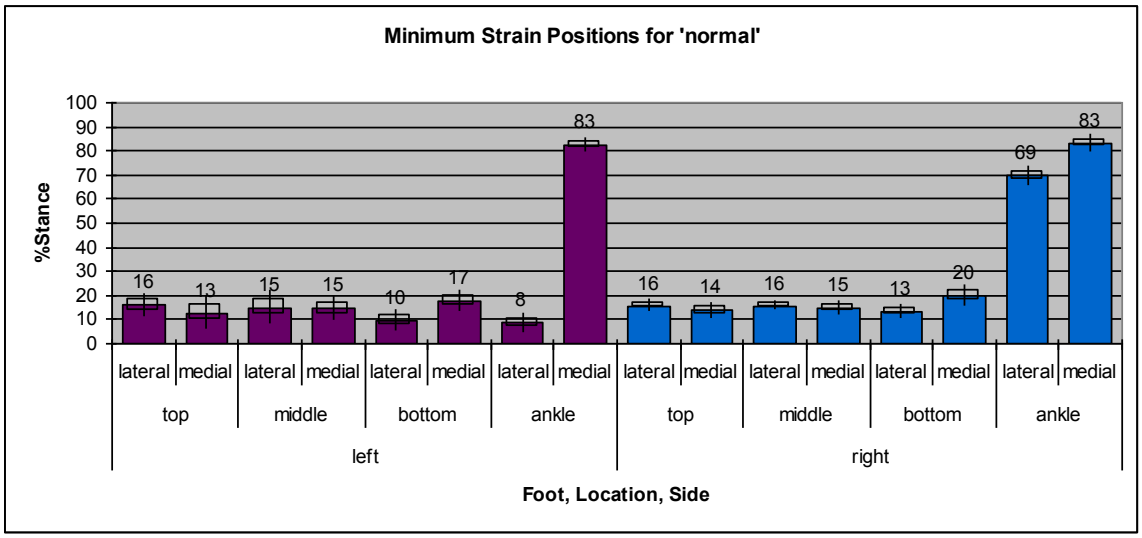
Minimum Strain Positions for 'normal'
%Stance
100
90
80
70
60
50
40
30
20
10
0
16 13 15 15 10 17 8 83 16 14 16 15 13 20 69 83
lateral medial lateral medial lateral medial lateral medial lateral medial lateral medial lateral medial lateral medial
top middle bottom ankle top middle bottom ankle
left right
Foot, Location, Side

APPENDIX G

FEA CONTOURS FOR STATIC LINEAR ANALYSIS

Condition 1: Small Angle Properties/ Small Angle Thicknesses

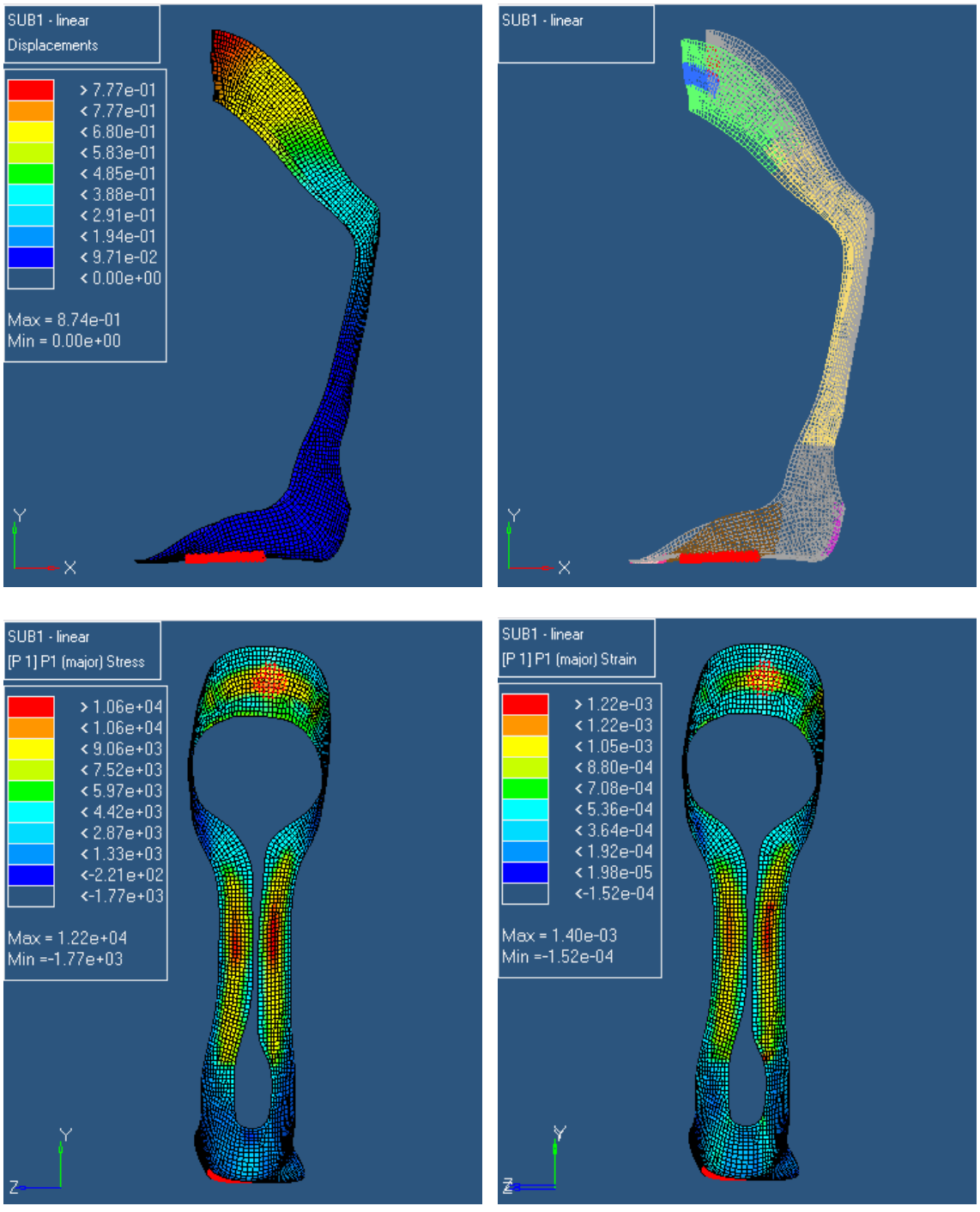

Condition 2: Small Angle Properties/ Original Angle Thicknesses

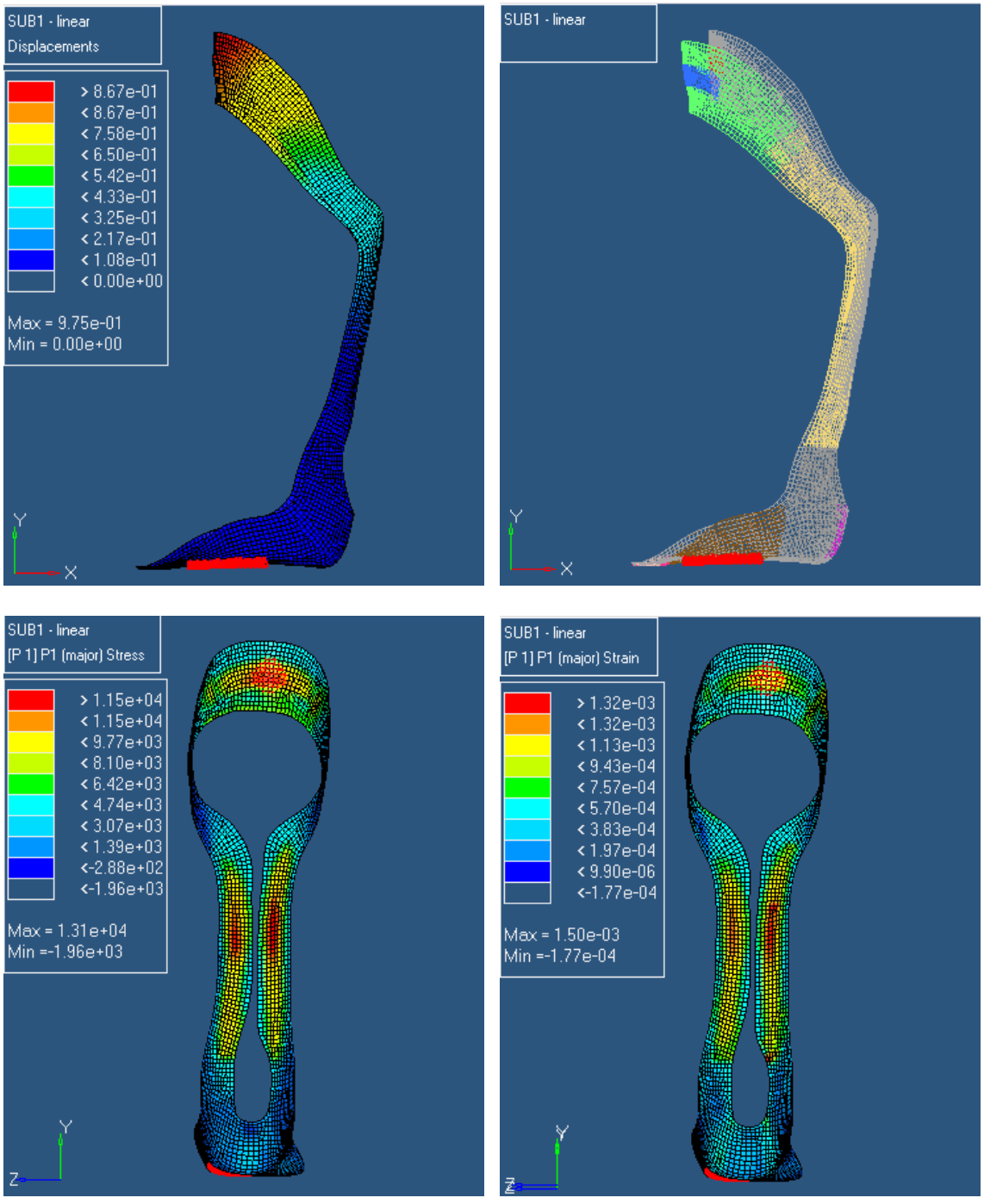

Condition 3: Original Angle Properties/ Original Angle Thicknesses

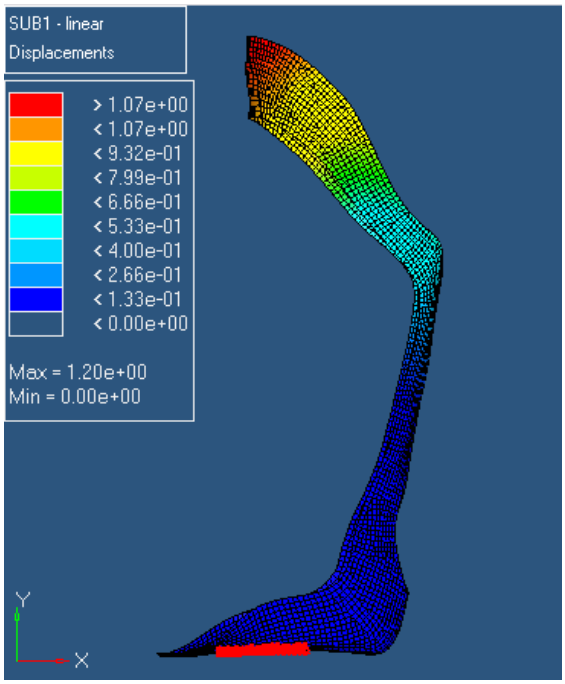

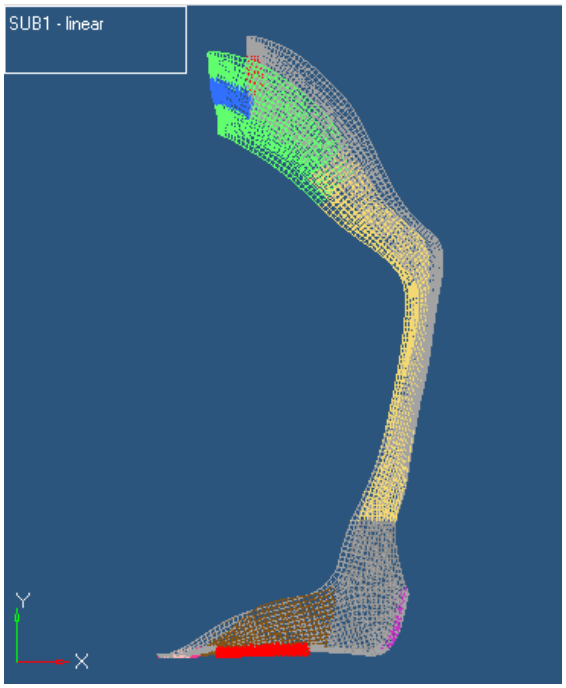

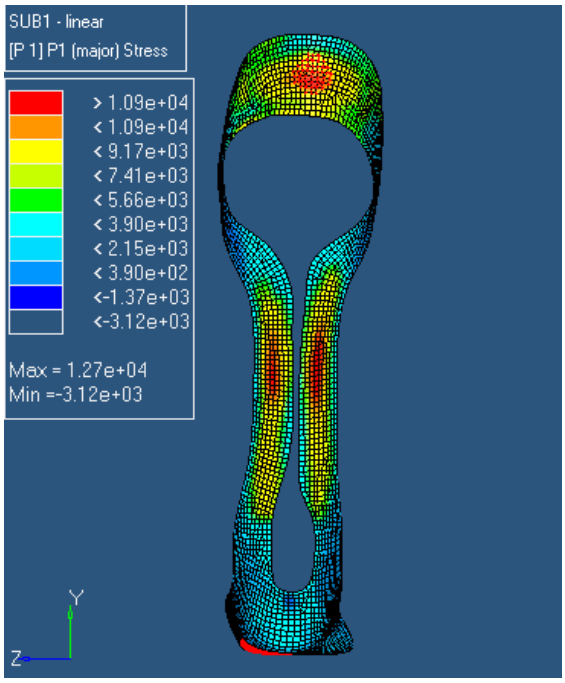

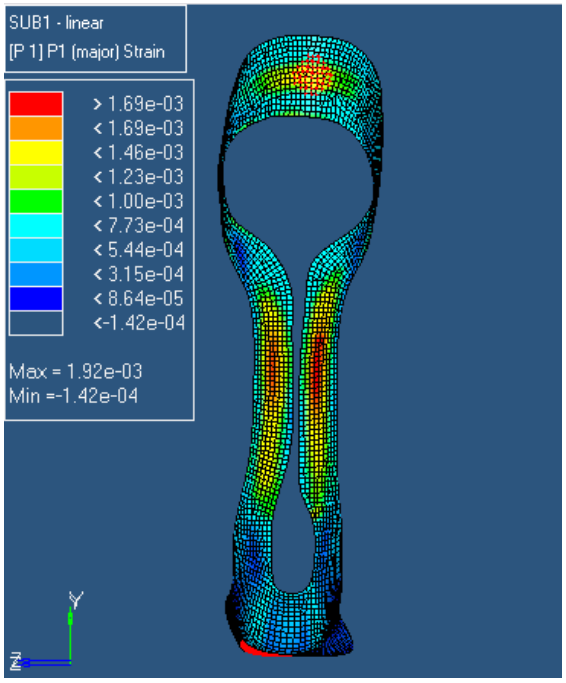

Condition 4: Large Angle Properties/ Original Angle Thicknesses

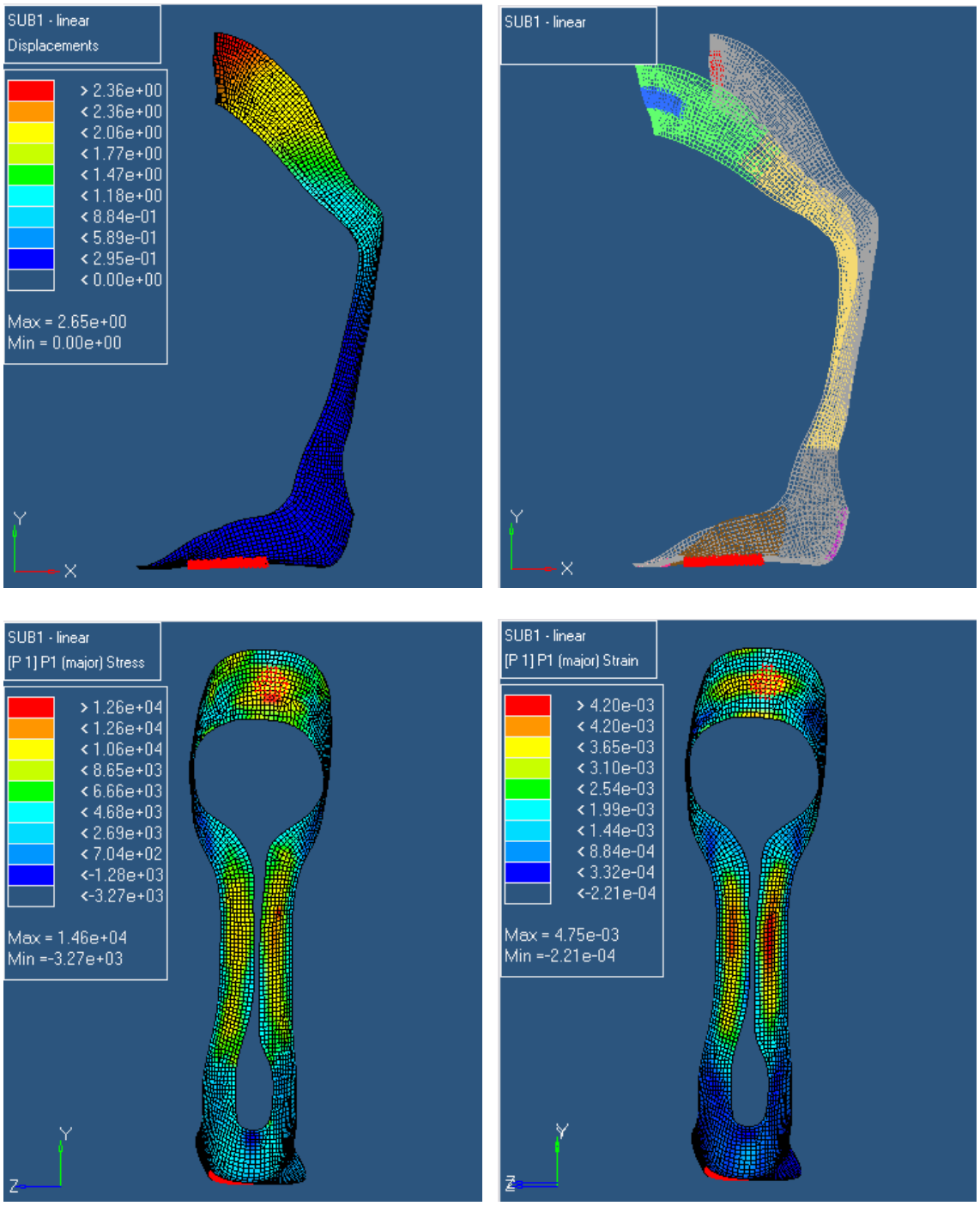

Condition 5: Large Angle Properties/ Large Angle Thicknesses

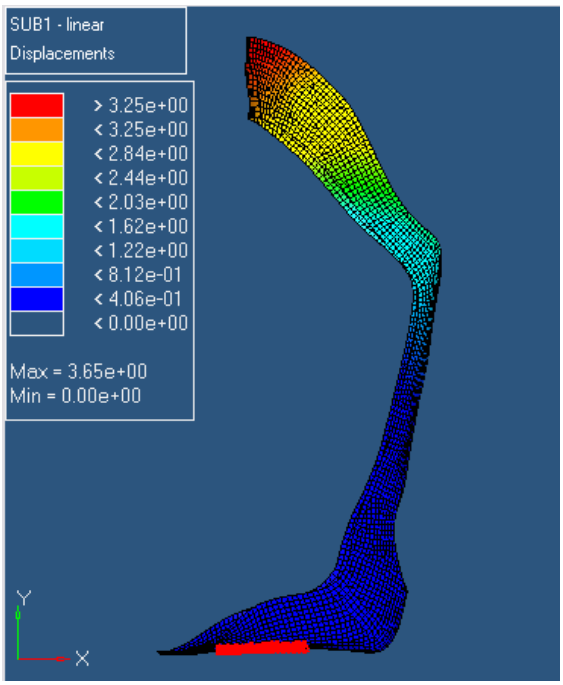

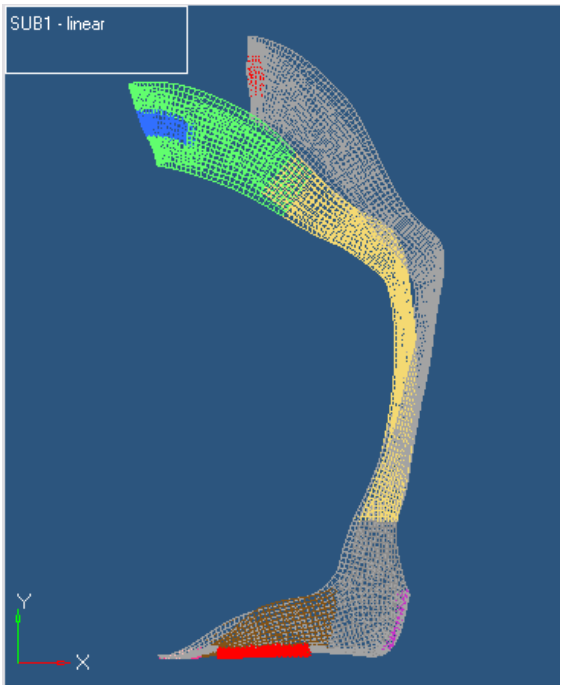

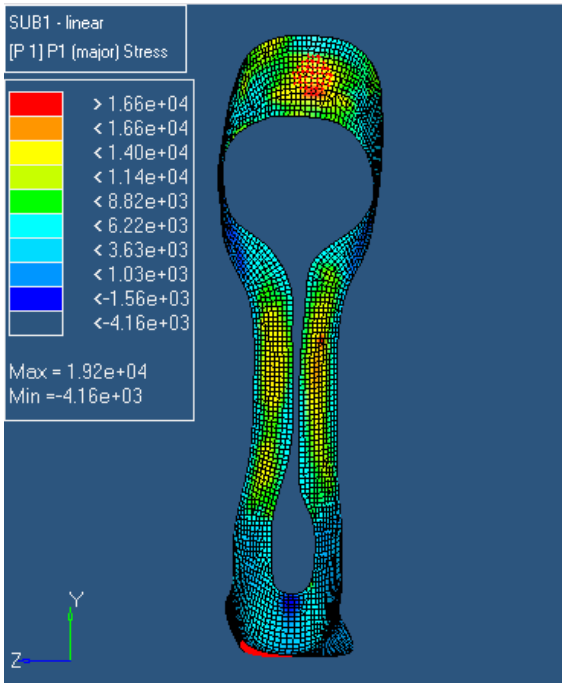

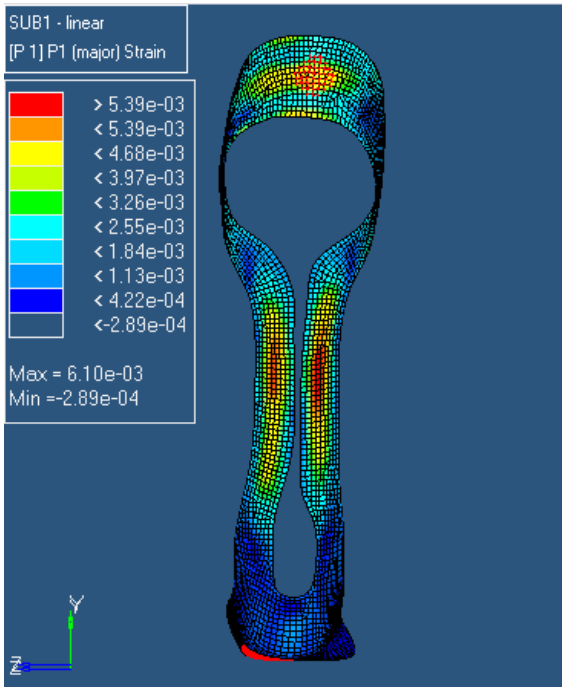

APPENDIX H

LS-DYNA CONTROL CARDS FOR STATIC NONLINEAR ANALYSIS

Control cards for explicit solution

```
*CONTROL_TERMINATION
$$  ENDTIM    ENDCYC     DTMIN    ENDENG    ENDMAS
     554.0
*CONTROL_TIMESTEP
$$  DTINIT    TSSFAC      ISDO    TSLIMT     DT2MS      LCTM     ERODE     MSIST
               0.9                            8e-6
*CONTROL_HOURGLASS
$$     IHQ        QH
         1       0.1
*CONTROL_ENERGY
$$    HGEN      RWEN    SLNTEN     RYLEN
         2
*DATABASE_NODFOR
$$      DT
       6.0
*DATABASE_NODAL_FORCE_GROUP
$$    NSID
       100
*SET_NODE_LIST
$$    NSID
       100
$$    NID1      NID2
      4107      4103
*DATABASE_ELOUT
$$      DT
       6.0
*DATABASE_NODOUT
$$      DT
       6.0
*DATABASE_GLSTAT_MASS_PROPERTIES
$$      DT
       6.0
*DATABASE_MATSUM
$$      DT
       6.0
*DATABASE_SSSTAT_MASS_PROPERTIES
$$      DT
       6.0
*DATABASE_EXTENT_SSSTAT
$$   PSID1
       101
*SET_PART_LIST
$$     SID
       101
$$    PID1      PID2      PID3      PID4      PID5      PID6      PID7      PID8
         1         2         3         4         5         6         7         8
*DATABASE_BINARY_D3PLOT
$$ DT/CYCL      LCDT      BEAM     NPLTC
       6.0
$$   IOOPT
         0
*DATABASE_EXTENT_BINARY
$$   NEIPH     NEIPS    MAXINT    STRFLG    SIGFLG    EPSFLG    RLTFLG    ENGFLG
                            3         1
$$  CMPFLG    IEVERP    BEAMIP     DCOMP      SHGE     STSSZ    N3THDT    IALEMAT

$$ NINTSLD   PKP_SEN    SCLP               MSSCL     THERM
```

Control cards for implict solution

```
*CONTROL_TERMINATION
$$  ENDTIM    ENDCYC     DTMIN    ENDENG    ENDMAS
         1
*CONTROL_IMPLICIT_GENERAL
$$  IMFLAG       DT0    IMFLAG      NSBS       IGS     CNSTN      FORM
         1       0.1
*CONTROL_IMPLICIT_SOLUTION
$$  NSOLVR    ILIMIT    MAXREF     DCTOL     ECTOL     RCTOL     LSTOL
         2         0         0       0.0       0.0       0.0       0.0
$$   DNORM    DIVERG     ISTIF   NLPRINT    NLNORM   D3ITCTL
                                        1
*CONTROL_IMPLICIT_EIGENVALUE
$$    NEIG    CENTER     LFLAG    LFTEND     RFLAG    RHTEND    EIGMTH    SHFSCL
         0
$$   ISOLD     IBEAM    ISHELL   ITSHELL
                           16
*CONTROL_IMPLICIT_AUTO
$$   IAUTO    ITEOPT    ITEWIN     DTMIN     DTMAX
         1        15         5   1.0E-04       1.0
*CONTROL_HOURGLASS
$$     IHQ        QH
         1       0.1
*CONTROL_ENERGY
$$    HGEN      RWEN    SLNTEN     RYLEN
         2
*DATABASE_NODFOR
$$      DT
       0.1
*DATABASE_NODAL_FORCE_GROUP
$$    NSID
       100
*SET_NODE_LIST
$$     SID
       100
$$    NID1      NID2      NID3      NID4      NID5      NID6
      4107      4103      3186      2647      2956      3802
*DATABASE_ELOUT
$$      DT
       0.1
*DATABASE_NODOUT
$$      DT
       0.1
*DATABASE_GLSTAT
$$      DT
       0.1
*DATABASE_MATSUM
$$      DT
       0.1
*DATABASE_BINARY_D3PLOT
$$ DT/CYCL      LCDT      BEAM     NPLTC
       0.1
$$   IOOPT
         0
*DATABASE_EXTENT_BINARY
$$   NEIPH     NEIPS    MAXINT    STRFLG    SIGFLG    EPSFLG    RLTFLG    ENGFLG
                             3         1
$$  CMPFLG    IEVERP    BEAMIP     DCOMP      SHGE     STSSZ    N3THDT    IALEMAT

$$ NINTSLD   PKP_SEN    SCLP               MSSCL     THERM
```

REFERENCES

1. Newman CJ, Walsh M, O'Sullivan R, Jenkinson A, Bennett D, Lynch B, O'Brien T, "The characteristics of gait in charcot-marie-tooth disease types I and II", *Gait and Posture,* 26(1): 120-127, 2007.

2. Winter DA, Biomechanics and Motor Control of Human Movement, 3rd ed, Hoboken, New Jersey, John Wiley, 2005.

3. Kirtley C, Clinical Gait Analysis, Washington, DC, Churchill Livingstone Elsevier, 2006.

4. Giakas G and Baltzopoulos V, "Time and frequency domain analysis of ground reaction forces during walking: an investigation of variability and symmetry", *Gait and Posture,* 5: 189-197, 1997.

5. Juvinall RC, Marshek KM, Fundamentals of machine component design, 3rd ed, New York, John Wiley and Sons, Inc, 2000.

6. Buschbacher L, Rehabilitation of patients with peripheral neuropathies, Philadelphia, WB Saunders, 1996.

7. Atlas of stress-strain curves, 2nd edition, ASM International, Materials Park, OH, 2002.

8. Diani J, Brieu M, Gilormini P, "Observation and modeling of the anisotropic visco-hyperelastic behavior of a rubberlike material", *International Journal of Solids and Structures*, 43: 3044-3056, 2006.

9. Hafner BJ, Sanders JE, Czerniecki JM, Fergason J, "Transtibial energy-storage-and-return prosthetic devices: A review of energy concepts and a proposed nomenclature", *Journal of Rehabilitation Research and Development*, 39(1): 1-11, 2002.

10. Hanson DE, Hawley M, Houlton R, Chitanvis K, Rae P, Orler EB, Wrobleski, DA, "Stress softening experiments in silica-filled polydimethylsiloxane", *Polymer*, 46(24): 10989-10995, 2005.

11. Loew R, Meier P, "Simulation of reiterated mechanical load of silicone rubber", *Finite Elements in Analysis and Design*, 43: 453-462, 2007.

12. Ariyama T, Kaneko K, "A constitutive theory for polypropylene in cyclic deformation", *Polymer Engineering and Science*, 35(18), 1995.

13. Krzypow DJ, Rimnac CM, "Cyclic steady state stress-strain behavior of UHMW polyethylene", *Biomaterials 21*, 2081-2087, 2000.

14. Zrida M, Laurent H, Rio G, Pimbert S, Grolleau V, Masmoudi N, Bradai C, “Experimental and numerical study of polypropylene behavior using an hyper-visco-hysteresis constitutive law”, *Computational Materials Science*, 45: 516-527, 2009.

15. Tsuji N, Kubomura K, “Non-linear compression stress-strain curve of pitch-based high modulus carbon fibre composites and structural responses”, *Journal of Materials Science*, 27: 3782-3788, 1992.

16. Mallick PK, Fiber-reinforced composites, New York, Marcel Dekker, Inc, 1993.

17. Wang Y, Zhang L, Cheng L, Ma Junqiang, Zhang W, “Tensile performance and damage evolution of a 2.D C/SiC composite characterized by acoustic emission”, *Applications of Composite Materials*, 15: 183-188, 2008.

18. Shokrieh MM, Rezaei D, “Analysis and optimization of a composite leaf spring”, *Composite Structures*, 60: 317-325, 2003.

19. Yu WJ, Kim HC, “Double tapered FRP beam for automotive suspension leaf spring”, *Composite Structures*, 9: 279-300, 1988.

20. Lo KH, Mccusker JJ, Gottenberg WG, “Composite leaf spring for tank trailer suspensions”, *Journal of reinforced plastics and composites*, 6, 1987.

21. Young P, De Jongh P, Stogbauer F, et al., "Treatment for Charcot-Marie-Tooth disease", *Cochrane Database Syst Rev*, 1: CD006052, 2008.

22. Danielsson A, Sunnerhagen KS, "Energy expenditure in stroke subjects walking with a carbon composite ankle foot orthosis", *Journal of Rehabilitation Medicine*, 36(4): 165-8, 2004.

23. Brehm MA, Beelen A, Doorenbosch CAM, et al., "Effect of carbon-composite knee-ankle-foot orthoses on walking efficiency and gait in former polio patients", *Journal of Rehabilitation Medicine*, 39(8): 651-7, 2007.

24. Sheffler LR, Hennessey MT, Knutson JS, et al., "Functional effect of an ankle foot orthosis on gait in multiple sclerosis: a pilot study", *American Journal of Physical Medicine and Rehabilitation*, 87(1): 26-32, 2008.

25. Bean J, Walsh A, Frontera W, "Brace modification improves aerobic performance in Charcot-Marie-Tooth disease: A single-subject design", *American Journal of Physical Medicine and Rehabilitation*, 80(8): 578-582, 2001.

26. Ezenwa BN, Hinderer S, Shy M, "Gait improvement in CMT patients with orthotic devices", *Proceedings of the First Joint BMES/EMBS Conference Serving Humanity*, Advancing Technology, Oct 13-16, Atlanta, GA USA p638, 1999.

27. Otto J, "Prefabricated orthoses: their place in the O&P industry", *O&P Business News*, 11(9): 21-29, 2002.

28. Smits J, "Appropriate patient selection for a carbon composite dynamic response AFO", Orthopadie-Technik Quarterly, English edition II, pp7-11, 2004.

29. Singerman R, Hoy DJ, Mansour J, "Design changes in ankle-foot orthosis intended to alter stiffness also alter orthosis kinematics", *Journal of Prosthetics and Orthotics*, 11(3): 48–56, 1999.

30. Hill JT, Fenwick AL, "A fibreglass-epoxy drop-foot brace", *Orthotics and Prosthetics*, 22(3): 1-8, 1968.

31. Lunsford T, Ramm T, Miller J, "Viscoelastic properties of plastic pediatric AFOs", *Journal of Prosthetics and Orthotics*, 6(1): 3, 1994.

32. Chu T, "Determination of peak stress on polypropylene ankle-foot orthoses due to weight change using strain gage technology", *Experimental Techniques*, 24(2): 28–30, 2000.

33. Wan YZ, Zak G, Naumann S, Redekop S, Slywynska I, Jiang Y, "Study of 2.5D glass-fabric-reinforced light-curable resin composites for orthotic applications", *Composites Science and Technology*, 67(13): 2739-2746, Oct, 2007.

34. Yamamoto S, Ebina M, Iwasaki M, Kubo S, Kawai H, and Kawai H, "Comparative study of mechanical characteristics of plastic AFOs", *Journal of Prosthetics and Orthotics*, 5(2): 259–264, 1993.

35. Sumiya T, Suzuki Y and Kasahara T, "Stiffness control in posterior-type plastic ankle-foot orthoses: effect of ankle trimline, Part 2: orthosis characteristics and orthosis/ patient matching", *Prosthetics and Orthotics International*, 20(2): 132-137, 1996.

36. Lee YS, Choi KJ, Cho KH, Choi YJ, Lim HK, Kim BO, "Plastic ankle foot orthosis for hemiplegics and structural analysis", *Key Engineering Materials*, 326-328(I): 855-858, 2006.

37. Chu TA, Feng R, "Determination of stress distribution in various ankle-foot orthoses: experimental stress analysis", *J Prosthet Orthot*, 10: 11-16, 1998.

38. Abu-Hasaballah KS, Nowak MD, Cooper PD, "Enhanced solid ankle-foot orthosis design: Real-time contact pressures evaluation and finite element analysis", *American Society of Mechanical Engineers, Bioengineering Division (Publication) BED*, 36: 285-286, 1997.

39. Klasson B, Convery P and Raschke S, "Test apparatus for the measurement of the flexibility of ankle-foot orthoses in planes other than the loaded plane", *Prosthetics and Orthotics International*, 22(1): 45-53, 1998.

40. Polliack AA, Swanson C, Landsberger SE, et al., "Development of a testing apparatus for structural stiffness evaluation of ankle-foot orthoses", *Journal of Prosthetics and Orthotics*, 13: 74-82, 2001.

41. Chu T, "Experimental validation on finite element stress analysis of a polymeric orthotic device", *Annual International Conference of the IEEE Engineering in Medicine and Biology*, 17(2): 1259–1260, 1995.

42. Chu TM, Reddy NP, Padovan J, "Three-dimensional finite element stress analysis of the polypropylene, ankle-foot orthosis: static analysis", *Medical Engineering and Physics*, 17(5): 372-379, 1995.

43. Syngellakis S, Arnold MA, Rassoulian J, "Assessment of the non-linear behavior of plastic ankle foot orthoses by the finite element method", *Proceedings of the Institution of Mechanical Engineers*, 214(H): 527, 2000.

44. Chu T, Reddy N P, and Padovan J, "Stress distribution in the ankle-foot orthosis used to correct pathological gait", *Journal of Rehabilitation Research and Development*, 32(4): 349–360, 1995.

45. Actis RL, Ventura LB, Smith KE, Commean PK, Lott DJ, Pilgram TK, Mueller MJ, "Numerical simulation of the plantar pressure distribution in the diabetic foot during the push-off stance", *Medical and Biological Engineering and Computing*, 44(8): 653-663, 2006.

46. Tak-Man Cheung J, Zhang M, An KN, "Effects of plantar fascia stiffness on the biomechanical responses of the ankle-foot complex", *Clinical Biomechanics*, 19(8): 839-846, 2004.

47. Budhabhatti SP, Erdemir, "Finite element modeling of the first ray of the foot: a tool for the design of interventions", *Journal of Biomechanical Engineering*, 129(5): 750-6, 2007.

48. Stallard J, McLeod N, Woollam PJ, Miller K, "Reciprocal walking orthosis with composite material body brace: Initial development", *Proceedings of the Institution of Mechanical* Engineers, Part H: Journal of Engineering in Medicine, 217(5): 385-392, 2003.

49. Woollam PJ, Dominy J, McCleod N, et al., "Feasibility study on a composite material construction technique for highly stressed components in reciprocal walking orthoses for paraplegic patients", *J Eng Med*, 213H: 355-360, 1999.

50. Granata C, DeLollis A, Campo G, Piancastelli L, Merlini L, "Analysis, design and development of a carbon fibre reinforced plastic knee-ankle-foot orthosis prototype for myopathic patients", *Proceedings of the Institution of Mechanical Engineers*, Part H: Journal of Engineering in Medicine, 204(2): 91-96, 1990.

51. Faustini MC, Neptune RR, Crawford RH, Stanhope SJ, "Manufacture of passive dynamic ankle-foot orthoses using selective laser sintering", *IEEE Transactions of Biomedical Engineering*, 55(2): 784-790, February, 2008.

52. Hafner BJ, Sanders JE, Czerniecki J, Fergason J, "Energy storage and return prostheses: does patient perception correlate with biomechanical analysis?", *Clinical Biomechanics,* 17(5): 325-344, 2002.

53. Bates BT, James CR, Dufek JS, "Single-Subject Analysis", Innovative Analyses of Human Movement, Stergiou N, ed, Champaign, IL, 2004, pp 3-28.

54. Frank F, Ruoff A, "A method of measuring poisson's ratio of fibers", *Textile Research Journal*, 28(3): 213-7, 1958.

55. "The engineering toolbox", 2005. Web. 27 July, 2010.

56. Lempriere BM, "Poisson's Ratio in Orthotropic Materials", *AIAA Journal*, 6(11), November, 1968.

57. Hallquist J, "LS-DYNA keyword user's manual", Livermore Software Technology Corporation, version 971, January, 2007.

58. Hansen AH, Childress DS, Miff SC, Gard SA, Mesplay KP, "The human ankle during walking: implications for design of biomimetic ankle prostheses", *Journal of Biomechanics*, 37: 1467-1474, 2004.

59. Don R, Serrao M, Vinci P, Ranavolo A, Cacchio A, Ioppolo F, Paoloni M, Procaccianti R, Frascarelli F, DeSantis F, Pierelli F, Frascarelli M, Santilli V, "Foot drop and plantar flexion failure determine different gait strategies in Charcot-Marie-Tooth patients", Clinical Biomechanics, 22:905-916, 2007.

VITA

Graduate College
University of Nevada, Las Vegas

Michelle Cameron Hawkins

Degrees:

Bachelor of Science, Mechanical Engineering, 2001 (Magna Cum Laude)
University of Nevada, Las Vegas

Master of Science, Mechanical Engineering, 2003
University of Nevada, Las Vegas

Special Honors and Awards:

Harold J. and Mayme Stocker Scholarship, Fall 1998 to Spring 2003
Tau Beta Pi, Nevada Beta, President-2001 to 2002
Tau Beta Pi, Student Member of the Year, 2001 and 2002
Tau Beta Pi, R.H. Nagel Most Improved Chapter Award, 2002
Engineer Intern (EI#0T3999), December 2000

Publications:

B. O'Toole, **M Hawkins**, E Neumann, M Warner, "Strain Analysis of a Composite Ankle-Foot Orthosis (AFO)," *World Journal of Engineering*, 2009, 757-758.

B. O'Toole, **M Hawkins**, E Neumann, M Warner, "Strain Analysis of a Composite Ankle-Foot Orthosis (AFO)," *17th International Conference on Composites/Nano Engineering*, Honolulu, HI.

M. Hawkins, B. O'Toole, D. Jackovich, "Cell Morphology and Mechanical Properties of Rigid Polyurethane Foam," *Journal of Cellular Plastics*, Vol. 41, No. 3, May 2005, 267-285.

D. Jackovich, B. O'Toole, **M. Hawkins**, and L. Sapochak, "Temperature and Mold Size Effects on Physical and Mechanical Properties in a Polyurethane Foam," *Journal of Cellular Plastics*, Vol. 41, No.2, Mar 2005, 153-168.

B. O'Toole, **M. Hawkins**, D. Jackovich, "Cell Morphology, Density, and Mechanical Property Relations in a Rigid Polyurethane Foam," *Proceedings of the API Polyurethanes Conference*, Las Vegas, NV, Oct 18-20, 2004.

M. Nelson (Hawkins), "The Relationship of Cell Morphology, Density, and Mechanical Properties in a Rigid Polyurethane Foam," Masters Thesis, University of Nevada Las Vegas, Dec 2003.

B. O'Toole, **M. Nelson (Hawkins)**, M. Mullin, D. Jackovich, R. Mohan, L. Sapochak, D. Fogarty, F. Bennicasa, "Correlation of Processing Temperature, Density Gradients, and Mechanical Properties in a Molded Polyurethane Foam System," *Proceedings of the SPE Annual Technical Conference*, May 5-9, 2002.

B. O'Toole, M. Mullin, **M. Nelson (Hawkins)**, D. Jackovich, R. Mohan, "Effect of Mold Size on the Average Density and Density Gradients in a Polyurethane

Foam System," *Proceedings of the SPE Annual Technical Conference*, May 5-9, 2002.

Dissertation Title: Experimental and Computational Analysis of an Energy Storage Composite Ankle Foot Orthosis

Dissertation Examination Committee:
Co-Chairperson, Dr. Brendan O'Toole, Ph. D.
Co-Chairperson, Dr. Edward Neumann, Ph. D.
Committee Member, Dr. Mohamed Trabia, Ph. D.
Committee Member, Dr. Woosoon Yim, Ph. D.
Graduate Faculty Representative, Dr. Janet Dufek, Ph. D.